Interfacial and bulk friction-inducted dissipation in composites

Olga Smerdova

N° ordre : **2012-24** Année **2012**

Thèse de l'Université de Lyon

délivrée par **L'Ecole Centrale de Lyon**

Spécialité : **Mécanique** de l'Ecole Doctorale **MEGA**

en co-tutelle avec

Bauman Moscow State Technical University

Soutenue publiquement le 17 Septembre 2012 à Lyon

par

Mlle Olga SMERDOVA

Interfacial and bulk friction-induced dissipation in composites

préparée au **Laboratoire de Tribologie et Dynamique des Systèmes**

Composition du jury :

D.R.	Alain Le Bot	CNRS - LTDS Lyon	Directeur de Thèse
Prof	Boris Sarbayev	MSTU Bauman - Moscou	Directeur de Thèse
C.R.	Juliette Cayer-Barrioz	CNRS - LTDS Lyon	Directrice de Thèse
D.R.	Antoine Chateauminois	CNRS - ESPCI Paris	Rapporteur
Prof	Alexander Gouskov	MSTU Bauman - Moscou	Rapporteur
D.R.	Roland Seguela	INSA - Lyon	Président
Prof	Christian Gauthier	ICS - Strasbourg	Examinateur
Prof	Grigoriy Panovko	MSTU Bauman - Moscou	Examinateur
M.d.C.	Michelle Salvia	LTDS - Ecole Centrale de Lyon	Membre Invitée
M.d.C.	Vincent Semet	INL - UCB Lyon	Membre Invité

На алтарь науки...

Abstract/Résumé

An investigation of interfacial and bulk friction-induced dissipation in model epoxy-based composite materials reinforced with carbon fillers, as well as pure epoxy, is a challenge of this PhD thesis. While the interfacial dissipation depends mostly on surface properties of very thin material layer, the bulk dissipation involves high volume deformations.

Firstly, an experimental friction investigation on carbon fibre- and carbon nanopearl-reinforced epoxies of different filler volume friction under soft tribological conditions is carried out. In order to understand the results, a generalized frictional law for interfacial friction between two composites is proposed. It is based on Bowden and Tabor theory applied to multimaterial contact and requires a contact in-plane geometry parameter and local friction coefficients. Depending on applied assumption, effective shear stress or effective hardness for all composite phases, it results in direct or inverse proportionality frictional law. These analytical results complete and explain the experimentally obtained tendencies: the direct law should be applied to the composite/epoxy contact, while the inverse law is valid for the composite/composite contact.

The second part of the experimental work deals with pure epoxy and carbon fibre-reinforced epoxy under severe tribological conditions. It aims to investigate bulk frictional dissipation and associated wear. A two-scale approach is established, which consists in calculation of macro parameters, such as wear rate, dissipated frictional energy, friction coefficient and relative contact temperature rise, and their coupling with damaged surface observations. This approach allows us to distinguish several wear modes, as two-body and three-body abrasion, adhesion, fatigue and thermal effects, and to associate their appearance and evolution to macro parameters. In contrast to pure epoxy, carbon fibre-reinforced epoxy tends to be more wear resistant.

Keywords: *polymer composites; carbon; dissipation; dry friction; polymer friction; polymer wear.*

L'enjeu de ce travail concerne la dissipation interfaciale et volumique induite par le frottement dans les matériaux composites modèles á base d'époxy renforcée par du carbone, ainsi que dans l'époxy pure. Alors que la dissipation interfaciale dépend surtout des propriétés d'une couche mince de surface, la dissipation volumique induit des déformations de volume importantes.

Dans un premier temps, nous avons effectué une étude expérimentale de frottement sur les résines époxy renforcées par des fibres et des nanoperles de carbone en différentes concentrations sous des conditions tribologiques faibles. Afin de comprendre les résultats obtenus, une loi de frottement généralisée pour le frottement interfacial entre deux composites a été proposée. Basée sur la théorie de Bowden et Tabor et appliquée au contact des composites, elle requiert un paramètre géométrique de contact et des coefficients de frottement locaux. En fonction de l'hypothèse appliquée, la contrainte de cisaillement ou la dureté effective pour toutes les phases du composite, elle découle sur une loi de proportionnalité directe ou inverse. Ces résultats analytiques complètent et expliquent les tendances obtenues expérimentalement : la loi directe doit être appliquée pour le contact composite/époxy, tandis que la loi inverse est valide pour le contact composite/composite.

La deuxième partie du travail expérimental est consacrée á l'étude sur l'époxy pure et celle renforcée par des fibres de carbone sous des conditions tribologiques plus sévères. Son objectif est d'étudier la dissipation volumique et l'usure associée. Dans ce cadre, une approche multi-échelle est établie, qui consiste d'abord á calculer les paramètres macroscopiques, comme le taux d'usure, l'énergie dissipée par le frottement, le coefficient de frottement et l'augmentation de la température. Ces paramètres sont ensuite couplés avec les observations des surfaces endommagées. Cette approche nous permet de distinguer plusieurs régimes d'usure, i.e. l'abrasion á deux et trois corps, l'adhésion, la fatigue et les effets thermiques, et associer leur apparence et leur évolution avec les paramètres macroscopiques. Contrairement á l'époxy pure, le composite renforcé par des fibres de carbone s'avère être plus résistant á l'usure.

Mots clés : *composites à base de polymère; carbone; dissipation; frottement sec; frottement des polymères; usure des polymères.*

Acknowledgements/Remerciements

 

Ce travail de thèse a été réalisé en co-tutelle franco-russe entre le Laboratoire de Tribologie et Dynamique des Systèmes (LTDS) de l'Ecole Centrale de Lyon et Bauman Moscow State Technical University (BMSTU).

Travailler au sein du LTDS a complètement changé le cap de ma vie et l'a remplie de sens, de nombreuses nouvelles connaissances et de savoir-faire, d'ambitions, d'amis et d'amour. Ce n'est que par chance et par hasard que je suis arrivée en France, qui est devenue mon chez moi, pour travailler dans ce laboratoire. Sans cette opportunité et la chance de rencontrer des gens formidables sur ma route, je ne serais jamais arrivée à cette carrière scientifique internationale que je réalise aujourd'hui avec grand plaisir. Et je tiens à remercier les personnes qui y ont contribué, ci-dessous, par ordre chronologique.

D'abord mon directeur de thèse russe monsieur Boris SARBAYEV, qui m'a offert cette chance unique de faire une thèse en co-tutelle avec la France, qui m'a encouragé à tenter ma chance malgré les nombreux obstacles qui me paraissaient insurmontables, et supporté les démarches administratives du côté russe.

Спасибо, Борис Сафиулович, за этот уникальный шанс работать во Франции и за Ваши ободрения в преодолении препятствий, которые мне казались непреодолимыми, и поддержку со всеми административными проблемами с российской стороны. Вы были абсолютно правы, "Не боги горшки обжигают".

La personne qui m'a accueillie en France est mon deuxième directeur de thèse monsieur Alain LE BOT. Je ne connaissais rien ni personne dans ce pays et ce laboratoire. De plus, je ne parlais pas français et ne comprenais donc rien autour de moi. Si je ne suis pas repartie pour toujours après les deux premiers mois, c'est surtout grâce à lui et son accueil chaleureux. Je veux le remercier pour cela, ainsi que pour sa confiance, sa patience et bien entendu ses connaissances scientifiques et son aide précieuse dans les parties expérimentales et théoriques de mon travail.

Une autre personne qui a assuré mon accueil et mon intégration dans la vie du laboratoire est Boyko STOIMENOV. C'est une personne formidable avec qui j'ai passé des centaines d'heures de discussions sur tous les sujets possibles, une personne qui a introduit le monde fascinant de la recherche pour moi et m'a donné le goût pour le travail scientifique, qui a facilité et suivi ma transition vers ma nouvelle vie, qui a été et reste toujours un grand exemple et un grand frère pour moi.

Concernant mon intégration sociale au laboratoire, je ne peux pas ne pas mentionner une personne grâce à qui j'ai commencé à parler français et aux français. Cette personne est Samuel MAMBINGO-DOUMBE, qui a fait beaucoup d'efforts et passé du temps pour que je m'y sente bien, à qui je dois une grande partie de ma réussite, et à qui je souhaite toujours le meilleur.

Quand j'ai trouvé ma place dans la vie sociale française, il a fallu agir sur le champ scientifique. C'est à ce moment là que ma troisième directrice de thèse madame Juliette CAYER-BARRIOZ m'a tendu la main. Mon travail et mon développement professionnel se sont passés côte à côte avec Juliette. Sa confiance en moi, ses encouragements et sa contribution à ma carrière scientifique sont inestimables. C'est grâce à sa disponibilité et l'envie de travailler avec moi à toute heure possible, que ce travail de thèse à été fini dans des délais raisonnables. Son enthousiasme, son efficacité au travail et sa manière de travailler, sa curiosité et ses qualités humaines font d'elle un grand exemple à suivre pour moi. Tout cela, ainsi que son intérêt pour le football et la gastronomie internationale et ses connaissances en langue russe, ont contribué à renforcer notre amitié que j'espère garder pour longtemps.

D'une manière générale, j'apprécie beaucoup la liberté et la confiance que tous mes directeurs de thèse m'ont laissées dans mon travail.

Je voudrais aussi remercier monsieur Denis MAZUYER, directeur du LTDS, pour son accueil dans le laboratoire et pour les discussions et ses conseils scientifiques qui ont apporté beaucoup dans les résultats présentés au dernier chapitre.

Je suis également très reconnaissante envers madame Michelle SALVIA, qui m'a donné de bons conseils scientifiques pour mon travail et surtout la possibilité de m'impliquer dans l'enseignement qui m'a ouvert de nouveaux horizons.

Un grand merci à monsieur Vincent Semet et son doctorant Marcel QUATRESOUS de l'INL de Lyon qui m'ont fourni des nanoperles de carbone et aidé dans la fabrication de composites renforcés par ces particules fines.

Je remercie beaucoup madame Anne Rubin de l'ICS de Strasbourg pour son étroite collaboration, sa volonté de travailler avec nous, sa disponibilité et, plus précisément, pour les manips de nanoindentation et de frottement à l'échelle microscopique.

Avec l'aide précieuse de tous ces gens, voilà, nous arrivons au jour de ma soutenance ! Je voudrais remercier très chaleureusement mes deux rapporteurs messieurs Antoine CHATEAUMINOIS et Alexandre GOUSKOV, qui ont pris soin d'examiner soigneusement mon travail et de donner leur précieux avis. Je remercie également tous les examinateurs du mon grand jury de thèse : messieurs Roland SEGUELA, Christian GAUTHIER, Grigoriy PANOVKO, Vincent SEMET et madame Michelle SALVIA pour les discussions scientifiques intéressantes et enrichissantes.

Et enfin, je veux dire un grand merci à tous les gens du LTDS et de l'ECL avec qui j'ai travaillé et passé de nombreux moments chaleureux. Merci à Gerard MEILLE pour les observations MEB, à Roberto VIARGOULU pour la profilométrie, un grand merci à Mathieu GUIBERT pour son aide dans les manips de tribologie et pour l'introduction à Labview, à Mohamadou DIEW pour la formation sur le tribomètre linéaire, merci à Didier ROUX pour la fabrication des pièces dans les plus courts délais possibles, merci au secrétariat et à l'administration du LTDS et de l'ECL. Et bien sûr merci à tous mes amis que j'ai rencontrés pendant cette période de thèse : Anton, Imène, Vanessa, Kény, Leslie, FiPi, Minori, Gaëtan, Christine, Gaylord, Zelie, Flo, Romain, Paule, Svetlana et beaucoup d'autres. J'ai encore un merci particulier à Julian pour son énorme soutien pendant la période de rédaction et sa grande patience, qui m'ont été nécessaires pour finaliser ce travail.

Nomenclature

α_i	Surface fraction of i phase of composite, -
γ	Shear strain, Pa
δ	Coefficient of partition of frictional heat, -
$tan\ \delta$	Loss tangent, -
$\Delta\theta$	Flash temperature rise, °C
$\Delta\theta_{av}$	Average flash temperature rise, °C
ΔM	Mass loss, g
ε	Mean strain rate, -
η	Surface density of asperities, -
θ	Average slope of asperities, -
θ_w	Coefficient of proportion between EP and AW modes of Axèn model, -
θ_b	Bulk temperature, °C
μ	Friction coefficient, -
μ_{adh}	Adhesive component of frictional coefficient, -
μ_{pl}	Ploughing component of frictional coefficient, -
μ_{def}	Deformation component of frictional coefficient, -
μ_i	Interfacial frictional coefficient, -
μ_s	Static friction coefficient, -
μ_k	kinetic friction coefficient, -
μ_{av}	Average friction coefficient, -
ν	Poisson's ratio, -
ρ	Density, kg/m^3
σ_a	Standard deviation of asperity heights distribution, -
σ	Shear stress, Pa
σ_{soft}	Yield pressure of softest material, Pa
σ_Y	Yield limit, Pa
τ	Shear stress, Pa
τ_{soft}	Shear stress of softer material, Pa
τ^*	Effective shear stress, Pa
ϕ^*	Standardized height distribution, -
$\phi(z)dz$	Probability that asperity height is between z and $z + dz$, -
φ	Fibre orientation angle, deg
χ	Thermal diffusivity, m^2/s
ψ	Plasticity index, -

a	Contact size, m
a_e	First ellipse semi-axis, m
a_w	Coefficient of mass/kinematic length dependence, g/mm
A	Contact area, m^2
A_r	Real contact area, m^2
A_n	Normalized contact area, -
A_w	Worn area, m^2
$A(h)$	Chord of the cut fibre, m
b	Contact width, m
b_e	Second ellipse semi-axis, m
c_e	Equivalent contact radius of ellipse, m
c_p	Specific heat capacity, J/kg K
d	Depth of indentation or surfaces separation, m
d_f	Fibre diameter, m
d_m	Distance between two adjacent fibres, m
D	Characteristic size of a contact, m
f	Sliding frequency, Hz
F	Frictional force, N
F_{adh}	Adhesive component of frictional force, N
F_{pl}	Ploughing component of frictional force, N
$F_1(e)$, $F_2(e)$	Correlation functions of the eccentricity, -
G	Shear modulus, Pa
E	Young's modulus, Pa
E^*	Effective Young's modulus, Pa
E_d	Dissipated frictional energy, J
h	Depth of dissipation zone, m
H	Hardness, Pa
H^*	Effective hardness, Pa
i, s, x, y, z	Variables, -
k	Thermal conductivity, W/m K
k_w	Wear coefficient, -
l	Sliding distance, m
L_k	Kinematic length, m
L_P	Peclet number, -
M_c	Mass concentration, -
n	Number of contact spots, -
N	Number of fibres in composite volume, -
N_{cycle}	Number of sliding cycles, -
p	Contact pressure, Pa
p_0	Average pressure, Pa
$p(h)$	Density probability function, -
P	Normal force, N
q	Quantity of heat per surface unity, W
r	Distance from contact center, m

R	Radius, m
R', R''	Radii of curvature, m
R_a	Average roughness, μm
R_q	RMS roughness, μm
R_{sk}	Skewness, -
R_{ku}	Kurtosis, -
t	Time, s
t_c	Contact time, s
t_{exp}	Total duration of frictional experiment, s
t_d	Time of heat propagation in the bulk on distance b, s
V	Sliding speed, m/s
V_f	Filler volume fraction, -
V_m	Matrix volume fraction, -
V_{wear}	Volume of wear, m^3
w	Groove track width, m
W	Wear rate, m^3/m
W_q	RMS waviness, μm
W_{sk}	Skewness waviness, -
W_{ku}	Kurtosis waviness, -
W_s	Specific wear rate, m^3/m N

Contents

Introduction

Over the last decades, composite materials have found more and more applications in several fields of industry, from the aerospace brunch to sports and leisure equipment. This interest is due to a combination of a large range of excellent mechanical and thermal properties associated with a low weight. Since a unidirectional fibre-reinforced composite layer is anisotropic, the properties of multilayer composite materials vary depending on orientation of layers and can be calculated before their manufacturing. This flexibility and orientation of properties make possible to replace metals in many standard applications with identical strength characteristics, to gain in mass and, eventually, thermal and chemical resistance. Furthermore, the reinforcement of polymers by small particles or short fibres significantly improves their mechanical characteristics, without decreasing other properties. Although many analytical and numerical models for composite mechanical characteristics have been developed and successfully used by engineers all over the world, their frictional properties seem to be less investigated and understood.

Empirical laws of mixture are usually used for friction and wear coefficient in practice. However, a general understanding of the problem is missing. From a scientific point of view, the problem of frictional dissipation in multimaterial contacts remains a big challenge, because a combination of surface and bulk mechanical, thermal, chemical, structural, geometrical and other properties of each composite component and their interface must interfere. Moreover, the problem is multiscale: while final friction and wear coefficients are defined for macrosize composite, the origins of dissipation processes lie in nano- and microscale structural features and interactions. An attempt to clarify this problem on model carbon-reinforced epoxy composites is made in this work. Therefore, the understanding of friction-induced dissipation process and involved friction and wear mechanisms in polymer composites is the main aim of this study. An approach consisting in the separation of interfacial and bulk dissipations for polymer friction is adopted for this polymer composite study, and two independent investigations are carried out.

Chapter 1 presents a literature survey of main advances in our subject. It is divided in three parts. The first part covers fundamentals of dry friction and sliding contact. It discusses the main theories and models of elastic and plastic, static and sliding contact and the problem of real contact area definition. The second part is focused on the features of polymer and composite friction and wear with a short review of main wear mechanisms and laws. The third part presents a synthesis of experimentally observed effects on friction and wear of unidirectional carbon fibre-reinforced epoxy. The aims and implementation of this PhD work are established on the basis of this literature review.

Chapter 2 describes the materials used in this study. It starts with the explanation of atomic and microscale structure of carbon fillers. Carbon fibre-reinforced epoxy composites and carbon nanopearl-reinforced epoxy composites of different filler volume fraction were manufactured for this study. The process of manufacturing, as well as morphology, surface and bulk mechanical properties and topography, are presented and characterized for these composite materials.

Chapter 3 presents an experimental study of interfacial frictional dissipation in dif-

ferent configurations between two composites and pure epoxy. Frictional experiments at macro and microscale are carried out. Firstly, the effect of normal load and sliding speed is studied, and then optimal conditions for interfacial friction are established. The contribution of carbon fillers to the composite friction, as well as friction of individual carbon fibres, are investigated.

The results of this experimental study and the literature review inspired us to propose an analytical model of the interfacial friction of composites, which is presented in *Chapter 4*. A review of the currently available models of composite friction starts this chapter. It is followed by an establishment of generalized friction law for composites with its hypotheses and assumptions, and its successive successful application to the contact between two composites and pure epoxy in different combinations. All theoretical results are compared to the results of the experimental study and discussed.

The last *Chapter 5* covers an experimental study of bulk friction dissipation in carbon fibre-reinforced epoxy and pure epoxy. A two-scale approach is established, and an investigation of mass loss, friction coefficients, frictional energy dissipation, worn area, contact temperature distributions is carried out for epoxy/epoxy, epoxy/CFRE and CFRE/CFRE sliding contact under severe tribological conditions. These results are associated with observed wear mechanisms for each material couple leading us to propose and discuss a retrospective of wear history.

Chapter 1

Theoretical and experimental basis

This chapter presents theoretical and experimental background for our study of frictional dissipation in carbon composites. It is organized by the following manner. Firstly, the main theories and models of dry friction and sliding contact are presented, such as the empirical frictional laws of da Vinci, Amontons and Coulomb, the real contact area observations and models of Hertz, Archard and Greenwood-Williamson, and the broadly used Bowden and Tabor's adhesive theory of friction. Further, the features of frictional dissipation in polymers and composites are discussed and several wear mechanisms are presented. It is followed by a literature review of experimental observations of the influence of different factors on friction and wear of carbon fibre-reinforced epoxy. Finally, the aims and methodology of our work are established and presented as a conclusion of this chapter.

Contents

1.1 Fundamentals of dry friction and sliding contact

1.1.1 Origins: da Vinci, Amontons and Coulomb's empirical friction laws

The phenomenon of friction has been studied since the first Leonardo da Vinci experiments at the beginning of XVI century. His original drawings of experiment are presented in Fig. 1.1. He found that the frictional force did not depend on the apparent contact area and was proportional to the normal load. The coefficient of proportionality was identical for all contacts and equal to 1/4 [1]. These two conclusions were refund and published in 1699 by Amontons [2], who, in turn, observed that the coefficient of friction for all materials and conditions was equal to 1/3. Since da Vinci's works have been lost for centuries, these two friction laws are usually attributed to Amontons. However, these frictional laws became appreciated only after Coulomb's vast experimental study of friction effects, published in 1821 [3]. Coulomb carried out friction experiments between different kind of woods and metals under lubricated and dry conditions. He supplemented Amontons' laws with his observations regarding sliding velocity effect and static friction. Hence, the basic frictional laws, named from Amontons or Coulomb, are usually formulated as following:

1. The frictional force does not depend on the apparent area of contact.
2. The frictional force is proportional to the normal load.

Therefore, the friction coefficient μ is defined as a ratio between frictional F and normal P forces:

$$\mu = \frac{F}{P} \tag{1.1}$$

There is a tendency to add a third 'Coulomb' frictional law: The kinetic frictional force does not depend on the velocity. In fact, Coulomb's work [3] states that it is true only for a particular contact type. His experimental evidences will be presented further.

1.1.2 Static and kinetic frictional forces definition by Coulomb

Coulombs defines the *static friction* as a force resisting to motion between contacting solids and the *kinetic friction* as a force required to maintain sliding. He experimentally observed that

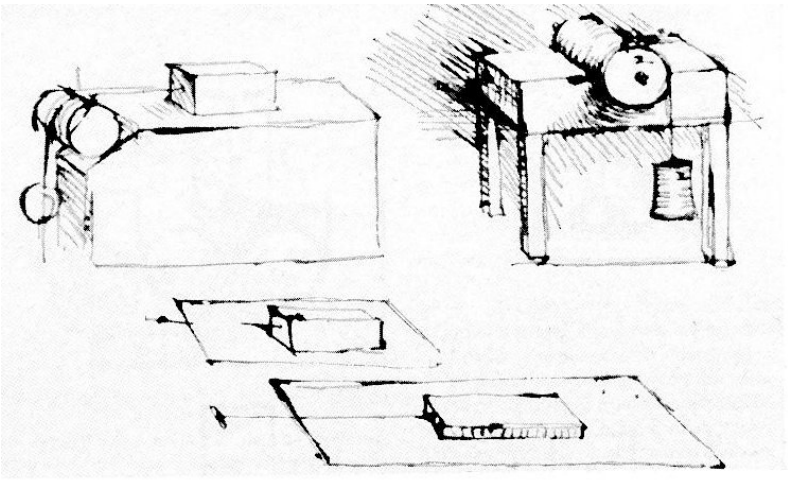

Figure 1.1: Leonardo Da Vinci tribometers [1]

- for wood/wood frictional pair, the static frictional force increased with the rest time and had a maximum in some minutes delay. The static friction coefficient was much higher than the kinetic one $\mu_s > \mu_k$. For instance, for oak/oak contact the ratio between static and kinetic friction coefficients was 4.3. Kinetic friction coefficient did not depend on sliding velocity.

- For metal/metal contact, no dependance of friction with the rest time and $\mu_s \approx \mu_k$ was observed. No effect of the sliding velocity was detected either.

- However, the observations of metal/wood dry friction were very different from the two previous cases: the maximum of static friction force occurred only after some days rest, $\mu_s > \mu_k$, and sliding velocity had a great influence on the frictional force. While the velocity increases in the geometrical progression, the friction increases in the arithmetic one.

These observations allowed Coulomb to suppose that friction was induced by interactions between surface asperities. He represented contacting surfaces as two brushes, as in Fig. 1.2, and explained friction phenomena of wood by penetration of the surfaces into each other due to the flexibility of its fibres. It is contrary to metals, whose surfaces are not flexible and, consequently, do not change with the rest time. Therefore, the static friction is a force required to overcome the formed junctions, which depends on the depth of penetration or the rest time. In the case of wood/metal friction, wood fibres meeting the metal inequalities can bend as springs. The number of these bending and relaxations depends on the velocity.

Since friction arises from overcoming surface asperities, both static and kinetic forces are proportional to the load, and the friction coefficient depends only on the average slope θ of the asperities

$$\mu = \tan\theta \tag{1.2}$$

(a) (b)

Figure 1.2: Coulomb's representation of wood (a) and metals (b) contact [3]

In reality, the Amontons-Coulomb's laws, being valid for a majority of cases, present limitations. The fact that friction coefficient is independent of the normal load is only true for contacts where real contact area is much lower than the apparent one, as for hard metals. For soft metals and, especially, for polymer or elastomer friction coefficient can vary dramatically with normal load. For instance, the frictional force for the contact of teflon/steel is hardly proportional to the normal force, it is rather $F \propto P^{0.85}$ [4].

1.1.3 Real contact area of static and sliding contact

1.1.3.1 Experimental observations

Bowden, Lieben [5] and Tabor [6] carried out numerous experiments of friction between a wide range of metals. During their experiments, they measured local contact temperature, friction forces and electrical conductance of the contact. This permitted them to calculate the real contact area. They compared contact areas from microscopic observation of the imprints with those calculated from electrical conductance assuming plastic flow or elastic deformations. For both stationary and sliding contact, they observed

- A curvature of the surface does not affect the conductance (and contact area), and the conductance for rough surfaces is of the same order of magnitude as for flat surfaces.

- The real contact area is much lower and nearly independent of the apparent area, but depends on normal load. For instance, the conductance measurements, with an assumption of 10 contact bridges for any load, conclude that a load of 300 kg on 21 cm^2 corresponds to real contact of 1/130 of the apparent area, while for 3 kg on the same surface it is about 1/170000.

- The variations of conductance (and of real contact area) with load is in better agreement with the theory of plastic rather than elastic deformation, which implies that the real contact area (and frictional force) is directly proportional to the normal load.

- The average value of conductance (and real contact area) during sliding is similar to the one observed for the stationary contact, though an instantaneous value of conductance was highly fluctuating synchronously with friction instabilities.

- Friction and real contact area fluctuations during sliding exhibit different tendencies for 3 types of contact: low-melting metal on high-melting metal, high-melting metal on low-melting metal and two similar metals.

1.1.3.2 Hertz theory: Contact of smooth elastic solids

The first theoretical solution for purely elastic contact of two solids was proposed by Hertz in 1882, when he was 23 years old [7]. His optical observations of interference fringes in a contact between two glass lenses inspired him to create his model of elastic contact. He studied the contact between two non-conforming elastic perfectly smooth bodies in several geometrical configurations without friction.

Contact of rigid sphere and elastic half-space

He started with the problem of a rigid sphere squeezed with the force P into an elastic half-space, see Fig. 1.3 [8,9]. The restriction of contact geometry is that the size of solids and their relative radii of curvature are much bigger than significant dimension of the contact. The contact area is circular and described by the radius a and the depth of indentation d, which are equal to

$$a = \left(\frac{3PR}{4E^*}\right)^{1/3} \tag{1.3}$$

$$d = \frac{a^2}{R} = \left(\frac{9P^2}{16RE^{*2}}\right)^{1/3} \tag{1.4}$$

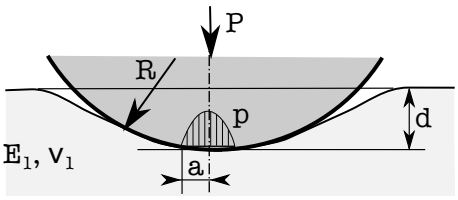

Figure 1.3: A rigid sphere in contact with an elastic half-space

The pressure distribution is parabolic with a maximum in the center. Thus the pressure in the distance r from the contact center is equal [10]

$$p(r) = \frac{3}{2}p_0\left[1 - \left(\frac{r}{a}\right)^2\right]^{1/2} \tag{1.5}$$

where $p_0 = P/\pi a^2$ is the average pressure.

In the case, when one body is rigid, the elastic constant E^* is equal to

$$E^* = \frac{E_1}{1-\nu_1^2} \tag{1.6}$$

where E is the Young modulus, and ν is the Poisson ratio for the elastic material of the half-space. An image of such a contact made by the photoelasticy method is shown

in Fig. 1.4 (a). The stress distributions are seen by different colors within transparent photoelastic materials under polarized light.

Eqs. 1.3−1.5 are applicable to different geometrical configurations with little modifications. For example, one can consider two spheres, crossed cylinders or two cylinders with parallel axes.

Contact of two elastic spheres

For the contact between two elastic spheres, as in Fig. 1.4 (b), the radius R from Eqs. 1.3−1.5 is a relative curvature of two spheres of the radii R_1 and R_2:

$$\frac{1}{R} = \frac{1}{R_1} + \frac{1}{R_2} \tag{1.7}$$

This solution is valid for both positive and negative radii of solids [8]. The effective Young's modulus E^* is calculated from the Young moduli E_1, E_2 and Poisson's ratios ν_1, ν_2 of two solids:

$$\frac{1}{E^*} = \frac{1-\nu_1^2}{E_1} + \frac{1-\nu_2^2}{E_2} \tag{1.8}$$

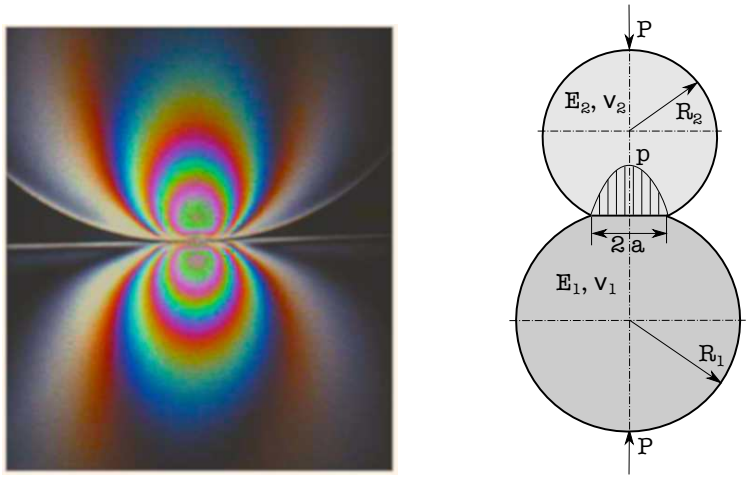

(a) **(b)**

Figure 1.4: a) Photoelasticity image: isochromatics give the isocontours of Tresca stresses [11]; b) Elastic deformation and pressure distribution between two elastic spheres

General case of elastic contact

Based on his interference fringes observations, Hertz supposed that the contact area is an ellipse [9]. If the deformed solid has radii of curvature R' and R'', the equivalent contact radius c_e, which depends on ellipse semi-axes a_e and b_e as $c_e = \sqrt{a_e b_e}$, is equal to

$$c_e = \left(\frac{3PR_e}{4E^*}\right)^{1/3} F_1(e) \tag{1.9}$$

where $R_e = \sqrt{R'R''}$ is the equivalent relative curvature. The depth of indentation d is

equal to

$$d = \left(\frac{9P^2}{16E^{*2}R_e}\right)^{1/3} F_2(e) \tag{1.10}$$

$F_1(e)$, $F_2(e)$ are the functions of the eccentricity $e = \sqrt{1 - b_e^2/a_e^2}$, when $b_e < a_e$. They play the role of correlation factors for Eqs. 1.9−1.12 with regards to Eqs. 1.3−1.5 for the contact of two spheres.

The pressure distribution is semi-ellipsoidal:

$$p(x, y) = p_0 \sqrt{1 - \left(\frac{x}{a_e}\right)^2 - \left(\frac{y}{b_e}\right)^2} \tag{1.11}$$

The maximum pressure is given by

$$p_0 = \left(\frac{6PE^{*2}}{\pi^3 R_e^2}\right)^{1/3} (F_1(e))^{-2/3} \tag{1.12}$$

Beginning of plastic flow

When the pressure exceeds the yield limit σ_Y of the softer material, the deformations are not elastic anymore. Plastic flow starts when the mean pressure is $p_0 = 1.1\sigma_Y$ in the point Z situated in the depth of $0.5a$, as shown in Fig. 1.5. With an increase of the load, the plastic region grows, and the mean pressure becomes $p_0 \approx 3\sigma_Y$. With further load growth, the mean pressure remains constant, while the area of plastic deformation increases.

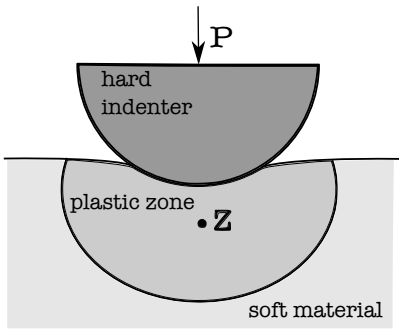

Figure 1.5: Plastic deformation of a soft plane by the hard sphere. Z is the point of the onset of plasticity

1.1.3.3 Archard model: transition from the single Hertz elastic contact to multiple asperities contact

Real surfaces of solids are never smooth, but are covered with numerous asperities. Archard [13,14] reasoned that the proportionality of Hertz contact area to $P^{2/3}$ mismatched to Amontons's law of direct proportionality between friction and normal forces. Therefore, it is more likely that all the asperities in contact deform plastically and the contact area

becomes $A_r = P/H$, where H is the hardness of the softest material in contact.

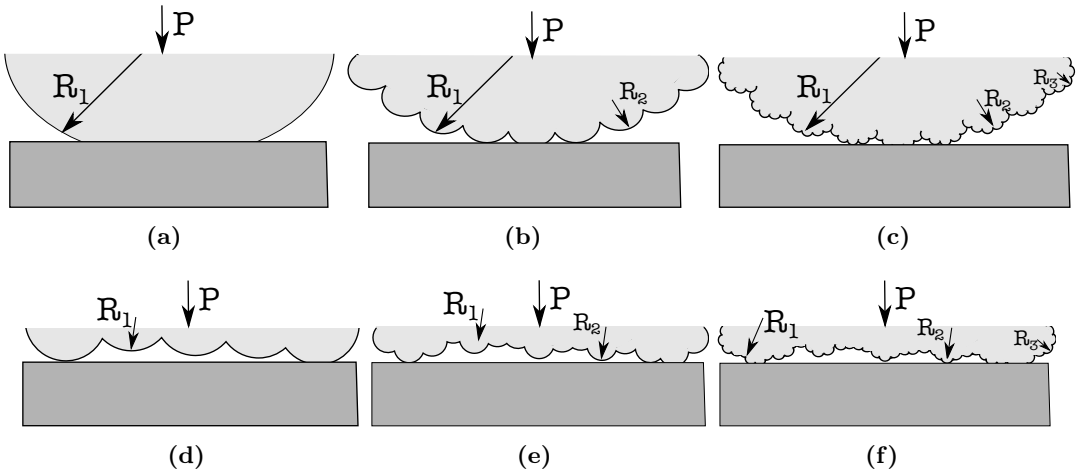

Figure 1.6: Archard's contact models. The relation between the contact area and normal force are (a) $A_r \propto P^{2/3}$, (b) $A_r \propto P^{8/9}$, (c) $A_r \propto P^{26/27}$, (d) $A_r \propto P^{4/5}$, (e) $A_r \propto P^{14/15}$, (f) $A_r \propto P^{44/45}$ [13]

He studied some cases of elastic contact, starting with the contact of a sphere covered by spherical asperities of identical radius and a smooth flat surface under the load P (Fig.1.6(a)). Then, he complicated this model by covering each asperity with smaller ones (Fig.1.6(b)), and more smaller ones (Fig.1.6(c)). On the other hand, he supposes that real flat surfaces are always slightly undulated. This allows him to represent a flat surface as a plane covered by spheres (Fig.1.6(d)), which, in turn, are covered by smaller spheres (Fig.1.6(e)), etc.

Based on Hertz solution for sphere/plane elastic contact, Eq. 1.3, Archard calculated the relationship between the contact area and the normal load for all these cases, as it is given in this figure legend. He obtained that the contact area varied from $A_r \propto P^{2/3}$ in the case Fig. 1.6 (a) to $A_r \propto P^{44/45}$ in the case Fig. 1.6 (f).

Therefore, by this geometrical reasoning, Archard concluded that the contact area is proportional to the normal load.

1.1.3.4 Greenwood-Williamson model of rough contact and plasticity index

Random distribution of asperities

Greenwood and Williamson [12] considered the contact between a smooth rigid plane and a nominally flat deformable rough surface covered with round tip asperities of the same radius R, as in Fig. 1.7. The basic assumption of this theory is that the deformation of each asperity is independent of that of its neighbours. The heights of asperities have a random distribution, the probability that asperity height is between z and $z + dz$ is $\phi(z)dz$. Accepting that each asperity deforms elastically according to Hertz model, the authors calculated the number of contact spots n, the total contact area A_r and the total load P in general case. They introduce new variables normalized by the standard

deviation of asperity height distribution σ_a, such as $s = z/\sigma_a$ and $\phi^*(s)ds = \phi(z)dz$. Thus, $\phi^*(s) = \sigma\ \phi(\sigma s)$ and

$$n = \eta A_n \int_{d/\sigma_a}^{\infty} \phi^*(s)ds \tag{1.13}$$

$$A_r = \pi\eta A_n R\sigma_a \int_{d/\sigma_a}^{\infty} (s - d/\sigma_a)\phi^*(s)ds \tag{1.14}$$

$$P = \frac{4}{3}\eta A_n E^* R^{1/2}\sigma_a^{3/2} \int_{d/\sigma_a}^{\infty} (s - d/\sigma_a)^{3/2}\phi^*(s)ds \tag{1.15}$$

where d is the separation, A_n is the nominal contact area, η is the surface density of asperities, E^* is the effective Young modulus.

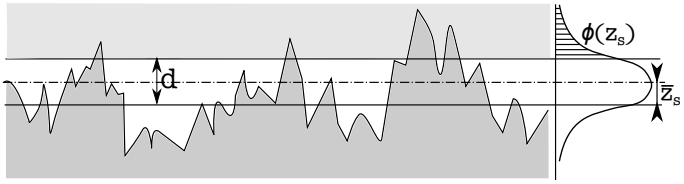

Figure 1.7: Contact of a randomly rough surface with a smooth flat

Exponential distribution of asperities

Firstly, the authors applied these equations to an exponential height distribution, representative of 25% of all surfaces. They obtained

$$n = \eta A_n e^{-d/\sigma_a} \tag{1.16}$$

$$A_r = \pi\eta R\sigma_a A_n e^{-d/\sigma_a} \tag{1.17}$$

$$P = \pi^{1/2}\eta R\sigma_a A_n E^*(\sigma_a/R)^{1/2} e^{-d/\sigma_a} \tag{1.18}$$

These equations show that although the number of contact spots is proportional to the load, their average size is load-independent.

Gaussian distribution of asperities

Since the most of engineering surfaces present a Gaussian distribution of asperity heights, this is the next case studied by Greenwood and Williamson:

$$\phi^*(s) = \frac{1}{\sqrt{2\pi}} e^{-s^2/2} \tag{1.19}$$

They numerically calculated the integrals for Eqs. 1.13-1.15 and found that the results were close to those obtained using exponential distribution.

Beginning of plastic flow. Plasticity index

The second major contribution of Greenwood and Williamson is an introduction of the plasticity index ψ combining both material and topographic properties. It can be defined as

$$\psi = \frac{E^*}{H}\sqrt{\frac{\sigma_a}{R}} \tag{1.20}$$

where H is the material hardness. If $\psi < 0.6$ the contact deformations can be considered as purely elastic for all asperities until very high applied load, and Eqs. 1.13−1.15 characterize the contact geometry and the load distribution. If $\psi > 1$ there is a plastic flow of asperities even under low loads and the contact area is proportional to applied load P obeying the law $A = P/H$. Moreover, the surface treatments, such as abrading and polishing, reduce the plasticity index and can shift the contact to the elastic deformation zone.

Contact of two rough surfaces The contact of two rough surfaces with the height distributions ϕ and ϕ' and their standard deviations σ_{as} and σ'_{as} is equivalent to the case of the contact between a rough surface and a smooth plane with the following effective parameters:

$$\sigma_a^* = \sqrt{\sigma_a^2 + \sigma_a'^2} \tag{1.21}$$

The mechanical characteristics are defined by Eq. 1.6 for the effective Young modulus and by

$$H^* = min(H, H') \tag{1.22}$$

for the effective hardness.

The sliding real contact area is usually considered equal to the static one. This is more or less true depending on material, as, for example, it was experimentally observed in section 1.1.3.1 for metals.

Therefore, this model concludes that the origin of the proportionality of the contact area to the load of Amontons' law is not the plastic flow of asperity contact, but a statistics of surface roughness [15]. Being the first model of rough contact based on statistical method, Greenwood-Williamson model marks the beginning of a creation of the multitude of new statistical contact models.

1.1.4 Bowden and Tabor adhesive friction theory

According to Bowden and Tabor, friction is not only a surface process but involves the material in the depth of thousands of atomic layer, and therefore depends on bulk characteristics. Due to the great difference between apparent and real contact area, the real contact spots undergo very high local pressures and deform plastically, which induces welding and junctions formation. The total frictional force F arises from two different mechanisms: the shear of the established adhesive junctions in the real contact area spots F_{adh} and the ploughing of a softer surface by hard asperities of another one F_{pl}:

$$F = F_{adh} + F_{pl} \tag{1.23}$$

- *Adhesive force.* Adhesive component is affected mainly by real surface area, surface energy, intermolecular interactions and surface contamination. The total real area of these junctions under normal load P is equal to

$$A_r = \frac{P}{\sigma_{soft}} \tag{1.24}$$

where σ_{soft} is the yield pressure of the softer metal. To shear these adhesive junctions the tangential force F_{adh}, proportional to the critical interfacial shear strength τ_i, is required:

$$F_{adh} = A_r \tau_i = \frac{P \tau_i}{\sigma_{soft}} \tag{1.25}$$

- *Ploughing force.* During sliding the asperities of the hardest material deform the surface of the softest one. This component is affected mainly by the topographical characteristics of the hardest surface and hardness and mechanical properties of softest material. If we suppose a hard hemisphere with the radius R, which moves and deforms a soft plane with the track width w, see Fig. 1.8, this component of tangential force will be equal to the cross-section of the grooved track A multiplied by the mean pressure p_0 required to displace the softest material from the front of the slider:

$$F_{pl} = A \cdot p_0 = \frac{w^3}{12R} p_0 \tag{1.26}$$

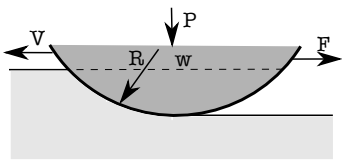

Figure 1.8: Deformation of a soft metal by a hard moving hemisphere

According to Bowden and Tabor, a correlation between these two components depends on materials in contact:

- for *relatively hard metals* the ploughing component is negligible, and $F \approx F_{adh}$. The shearing often occurs not on the interface, but in the bulk of metal, thus the critical shear strength τ_i is the shear strength of the softest metal τ_{soft}. This means that friction coefficient depends only on the physical characteristics of softest metal in contact:

$$\mu = \frac{F}{P} = \frac{\tau_{soft}}{\sigma_{soft}} \tag{1.27}$$

- for soft materials, as *polymers and rubbers, or well lubricated surfaces*, ploughing could be of the same order as adhesion, and both constitutions need be considered. Moreover because of the visco-elastic nature of polymers, the area of contact depends significantly on sliding speed and the time of loading. The experiments of Bowden and Tabor showed that for low speeds the frictional behavior of polymers can be described by the adhesive component of frictional force F_{adh}. However, under high speeds, the temperature arises in the contact and melting occurs. Therefore, friction is defined by molten surface film properties and can not be described using only the adhesive component.

1.1.5 Three component model for friction coefficient

Suh and Sin [16] proposed a new friction model issued from their experiments on metals, alternative to Bowden and Tabor's model. This model considers an influence of sliding distance or time on the evolution of friction coefficient. Three basic mechanisms are responsible for friction and constitute the total friction coefficient:

$$\mu = \mu_{adh} + \mu_{pl} + \mu_{def} \tag{1.28}$$

where μ_{adh} is the component from the adhesion between flat surfaces, μ_{pl} is the component from the ploughing by wear particles or hard surface asperities and μ_{def} is the component from the deformation of asperities. The deformation component is mostly responsible for the static friction coefficient because the asperities deform before sliding initiates and less during the delamination wear process. Two other components define dynamic friction coefficient and increase during sliding, but the proportion between these frictional components can change with time of sliding.

1.2 Dissipation by friction and wear in polymers

1.2.1 Concept of interfacial and bulk frictional dissipation

The frictional energy in polymers is dissipated differently in the region close to the contact and in the bulk of material [17,18]. Therefore the energy dissipation in these two regions, named interfacial and bulk region (see Fig. 1.9), occurs by different mechanisms. Distinguished by the zone of action, these two components of friction force are not supposed to interact one with another.

- In the *interfacial zone*, a key parameter is the interfacial shear strength τ_i. The thickness of this zone for organic polymers is between 10 and 100 nm. Static and dynamic frictional forces are adhesive and obey Bowden and Tabor's theory (see Eq. (1.25)). The interfacial friction coefficient is equal to

$$\mu_i = \frac{\tau_0}{\sigma_Y} + \alpha \tag{1.29}$$

  where σ_Y is the yield stress, α and τ_0 are experimental constants. The experiments on film and bulk polymers [17] show that the pressure coefficient α is rather similar for bulk and interfacial shear, and only τ_0 makes the difference between them. At high loads $\mu_i \approx \alpha$.

  The interfacial shear strength is in the logarithmic proportion with the mean strain rate,

$$\tau_i \propto \ln \varepsilon$$

  where $\varepsilon = V/h$, V is the sliding speed, and h is the depth of a dissipation zone. In addition, it varies exponentially with the contact time,

$$\tau_i \propto e^{t_c}$$

where $t_c = D/V$ and D is the characteristic size of a contact.

- The dissipation in the *bulk zone* is governed by its plastic or viscoelastic deformation and it corresponds to the ploughing component of Bowden and Tabor's theory (see Eq. (1.26)). This component is important in rolling or well-lubricated sliding friction. For viscoelastic bulk dissipation of sliding or rolling sphere of the radius R under the load P, the friction coefficient is

$$\mu_b \approx \frac{\pi}{2}\sqrt[3]{\frac{P}{E^* R^2}}\tan\delta \tag{1.30}$$

where E^* is the effective Young's modulus (see Eq. 1.6), $\tan\delta$ is the loss tangent.

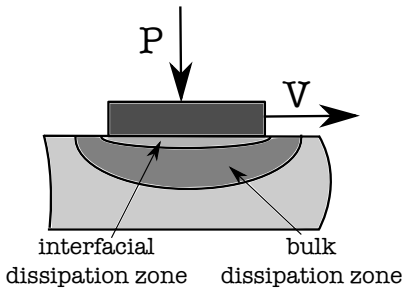

Figure 1.9: Interfacial and bulk regions of energy dissipation in polymer under normal load and sliding conditions

Friction and wear of polymers differ a lot depending on the polymer nature: thermosetting, thermoplastic or elastomer, and particularly on the chemical structure. For instance, PTFE is famous for its ability to form a transfer layer, which lubricates the contact and significantly diminishes the friction. On the other hand, during the sliding of some other polymers, such as UHDPE, there is no transfer layer formation, and, consequently, friction is much higher [20].

1.2.2 General wear mechanisms and laws

There are a number of wear mechanisms and their consequences, which gives rise to a number of wear classifications [21–24]. Here are some examples: abrasive wear, adhesive wear, fatigue wear, erosive wear, cavitation wear, tribochemical wear, corrosive and oxidative wear *etc.* The difficulty relies on the fact that these mechanisms are often coupled and it is not easy to recognize and separate the damage caused by one or another mechanism. Furthermore, there is no universal characteristic parameter of wear, and one or several of the following can be used:

- Volume of worn material, $[mm^3]$
- Mass of worn material, $[g]$
- Depth of the wear track, $[mm]$

- Wear rate, calculated as the quantity of wear per time, [mm^3/s, g/s or mm/s]
- Wear rate, calculated as the quantity of wear per sliding distance unit, [mm^2, g/mm or unitless]
- Wear rate, calculated as the quantity of wear per number of cycles, [mm^3, g or mm]

In addition to the problem of interacting mechanisms, many external and internal factors affect wear. Therefore, it difficult to establish a universal wear law. A review [22] of all wear papers (5466 surveyed papers) published in the journal Wear and the Wear of Material conferences between 1957 and 1992 illustrates well this problem. The authors collected very interesting statistics: up to 1992, more than 300 empirical or theoretical laws of wear, including more than 100 parameters, appeared. The average number of parameters per equation is 4.8. The most famous and one of the oldest wear law is the law of Archard [14]. He considered the hypothesis of plasticized contact, i.e. $A_r = P/H$, and defined volume of wear V_{wear} and wear rate W as following:

$$V_{wear} = k_w A_r l = k_w \frac{Pl}{H} \tag{1.31}$$

$$W = \frac{V_{wear}}{l} = k_w \frac{P}{H} \tag{1.32}$$

where k_w is the wear coefficient varying from 10^{-3} to 10^{-7} for different materials, H is the hardness of the surface which is worn away, l is the relative sliding distance between the materials and P is the normal force. Coefficient k_w is the probability of wear event on the real contact area, it does not depend on normal load or sliding speed. Another equation for wear rate, proposed by Archard is

$$\frac{dh}{dt} = k_w PV \tag{1.33}$$

where PV is the product of the pressure and the sliding speed and h is the depth of the wear track. These laws were established from experimental observations and hold for many tested materials. Archard [25] also observed that wear rate is independent of the apparent area of contact.

In the following section we will briefly describe three main wear mechanisms, which are supposed to act in dry sliding friction of polymer composites: adhesive, abrasive and fatigue wear.

1.2.2.1 Adhesive wear

This type of wear is important when the surfaces are not separated by lubrication or contaminant layers. It is also sensitive to the surface roughness and hardness: the surfaces of low hardness present higher adhesion. Van der Waals forces are supposed to play a crucial role in the adhesion between polymers [23]. Adhesive wear can cause cracks of asperities of brittle material or large plastic deformations of ductile material, as it is depicted on Fig. 1.10. If particles detached from one surface remains attached to another,

they gradually form a *transfer film*. Adhesive wear can cause severe surface damage because of a possibility of seizure and high fluctuating friction coefficients.

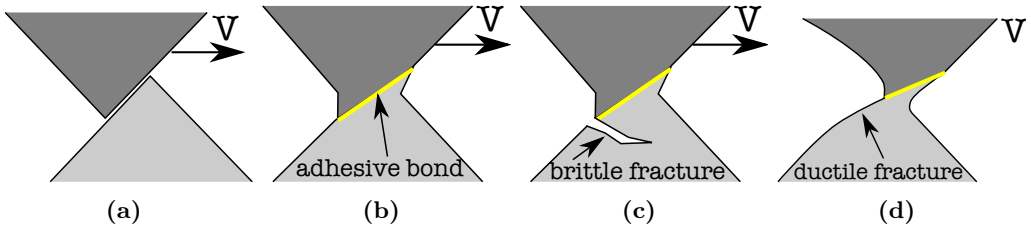

Figure 1.10: Adhesive sliding contact of asperities: (a) before the contact, (b) adhesive bond formation, (c) brittle and (d) ductile fracture during asperity separation

1.2.2.2 Abrasive wear

A key parameter in abrasive wear is material hardness, because this wear mechanism occurs when one material grooves the other, softest one, *two-body abrasive wear*, or when hard particles jam between two surfaces, *three-body abrasive wear*. Several mechanisms are grouped by the name of abrasive wear, namely cutting, fracture, fatigue by repeated plugging and grain pull-out, as schematically depicted in Fig. 1.11.

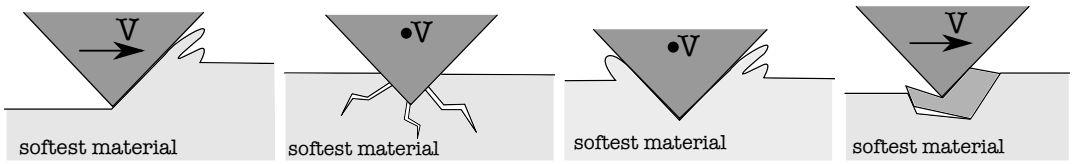

Figure 1.11: Mechanisms of abrasive wear: (a) cutting, (b) fracture, (c) fatigue by repeated ploughing, (d) grain pull-out

Cutting is caused by ploughing of hard or sharp asperity into soft material, cutting it if the material is ductile and causing fractures if the material is brittle. If the sliding asperities are blunt, the ductile counterface will be deformed repeatedly and wear debris are formed due to *fatigue*. The last mechanism presented in Fig. 1.11 is grain pull-out: it occurs in heterogeneous materials with weak bonding between phases.

Polymers usually have high resistance to abrasive wear by blunt asperities. However because of their low hardness, a probability of abrasive wear by sharp asperities of counter-body is high.

1.2.2.3 Surface fatigue wear

This type of wear is caused by material deformation beneath the surface, and is particularly important under reciprocated sliding. Under many passes of slider the plastic deformations

accumulate under the surface of fixed surface. This initiates cracks formation and detachment of wear debris. This process, illustrated in Fig. 1.13, starts beneath the surface and is not visible before the debris formation. Many materials contain imperfections, such as voids and other material inclusions. This favors the crack initiation in the bulk material. This idea was developed in the delimitation theory of wear [26] and verified in many experimental works: heterogeneous materials with many inclusions exhibit higher wear rate than homogeneous materials.

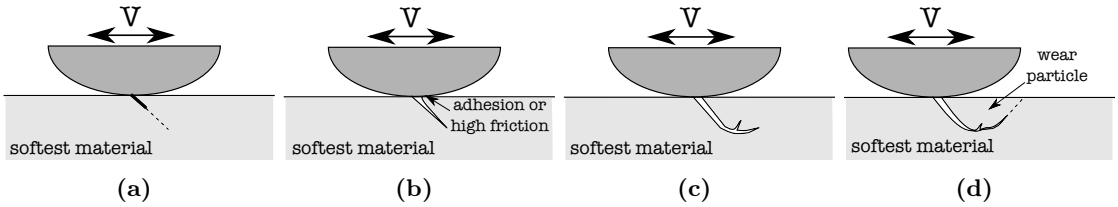

Figure 1.12: Fatigue wear: (a) crack initiation, (b) primary crack propagation, (c) secondary crack initiation, (d) secondary crack propagation and formation of wear particle [23]

1.2.2.4 Melting wear

Since the contact temperatures are often very high, a melting of one or both contacting surfaces can occur. This is especially important for polymers, whose melting point is usually low. When a polymer surface layer melts, it can be noticed by dramatic fall of friction force, because the liquid polymer layer lubricates the contact. At the same time, the wear rate quickly grows, because new polymer layers are involved in the frictional process. The contact temperature does not grow infinitely, it stabilizes when it reaches the polymer melting point. The additional generated frictional heat dissipates into deeper polymer layers, melting new areas.

On the other hand, contact temperature growth can cause a polymer state transition from solid to rubber-like. This affects its friction coefficient, wear rate and mechanical properties, as well as the mechanisms of dissipation.

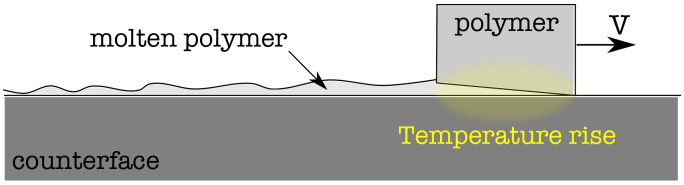

Figure 1.13: Melting wear mechanism [23]

1.2.3 Features of polymer wear

Polymers often form a transfer film, which lubricates the contact, decrease the friction and influence the wear. Polymeric surfaces rubbing against metal experience a break-in period, followed by a steady state linear wear regime and a severe wear regime [27]. In the early stage of rubbing the roughness and contamination of surfaces play the crucial role. However, surface finish has no influence on steady linear wear, because after the transfer film formation, an equilibrium is established between two surfaces. At this stage, wear and friction are rather stable, and wear rate is low. Little by little, energy is accumulated during sliding. If it is not removed from contact, a critical temperature on polymer surface is reached, and the polymer starts to melt or char, which leads to dramatical wear. As experiments [27] show, this critical temperature could be much higher than crystalline melting point or softening point of polymer. After the transfer film removal, the polymer generates a new layer, which detaches according to the similar mechanism, but much faster. The difference between wear rate of the tenacious and temporary film removal could reach more than 2000 times.

The nature of transfer film is different depending on polymer nature. For instance, PTFE and polyethylene form smooth and thin film of about 0.5 μm, while some other polymers produce thick and discontinuous film. Particles of this layer regularly wear out from the contact during sliding, causing drops in friction. The dust particles or other contamination can seriously influence the transfer layer formation and the wear process. If the surfaces are clean and the transfer film is firmly attached to the metal surface, the polymer can resist to more severe sliding.

Not only polymer, but also metal produces wear debris under sliding of polymer/metal contact. This means that the transfer layer does not grow by successive addition, but by a turbulence of wear particles of both surfaces occurring continuously at least at the run-in stage.

The criterion usually used to quantify the polymer wear severity is a PV limit, the product of normal load or pressure and sliding velocity, above which the polymer can not be used as wear part due to softening, melting or high deformations. It is defined experimentally for each material and geometrical configuration under certain temperature.

1.2.4 Composite wear mechanisms

Composite wear mechanisms depend on fibre orientation [23]. Wear process of parallel and antiparallel orientations are similar: The fibres and matrix are worn out until a depth of a half of fibre diameter, and, then, fibres break and form wear debris (smaller for antiparallel than for parallel orientation). The matrix wear debris is fine and might form a transfer layer. The normal orientation causes small wear rate, because bent fibres remain attached in the matrix and resist longer. However, the risk of seizure exists.

The variation of composite wear mechanisms due to elimination or capture of composite wear debris in the contact is highlighted in [28, 29], where unidirectional carbon fibre epoxy composite covered by grooves of the width of 100 μm, the depth of 250 μm and the spacing of 200 μm, parallel to the fibre direction are fabricated and compared in terms of friction and wear with similar but continuous composite. Grooves on the composite surface

favor wear debris elimination from the contact, which results in lower friction and wear rate. Wear mechanisms for continuous and grooved composite surface are different. The compacted wear debris, remained in the contact, penetrates between fibres and matrix and provokes the debonding and the breakage of fibres. However, when it is eliminated from the contact zone, mainly polishing of fibres by harder asperities of counterface occurs. It is seen in Fig. 1.14 (a-d), worn out fibres are shown on Fig. 1.14 (a) and (c), while broken fibres are presented in Fig. 1.14 (b) and (d).

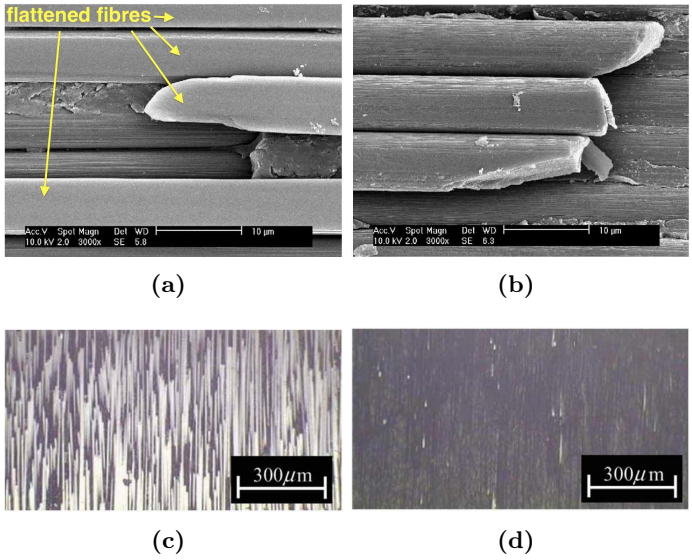

Figure 1.14: Worn out flat carbon fibres (a, c) under 3.4 MPa and broken round carbon fibres (b, d) under 10.7 MPa [28]

1.3 Experimental observations of carbon fibre reinforced epoxy friction and wear

Many friction and wear experiments with unidirectional carbon fibre reinforced epoxies against different metals have been carried out. Some general tendencies concerning effects of different parameters on friction coefficients and wear rates are presented in this section. However, it should be noticed that the observations of different authors often contradict one another and usually no general conclusions can be assessed.

Each paragraph divides into two parts: effect on friction coefficient μ and effect on wear rate W or wear volume V_{wear}. HM and HS designate high modulus and high strength carbon fibres, respectively, while composite always means carbon fiber reinforced epoxy composite.

1.3.1 Material effect

a) Graphite friction and wear

The allotropes of carbon can have very different frictional and wear behavior. Due to its lamellar structure, graphite is capable to form a transfer layer, lubricating the contact. It has a high level of interlayer bonding energy and is not a low shear strength lamellar material [31]. The contact lubrication occurs only in air atmosphere reducing the bonding energy of near surface layers, probably because of the interaction of the unpaired electron of oxygen molecule and the π-electron of graphite, or due to the absorption of water vapor.

Against metal surfaces, graphite usually wears by abrasion [32], which makes the roughness of the opposite surface important. For instance, an experimental study on friction and wear of graphite against tool steel and silicon nitride confirm the importance of the counterface roughness on the transfer layer formation [33]. Two wear mechanisms are distinguished: wear by transfer of graphite to the hard slider with its subsequent removal, and fatigue cracking of the graphite surface with further coalescence of cracks and detaching of wear particles.

On the other hand, less graphitized forms of carbon, as HS carbon fibres, are rather hard and, instead of softening the sliding contact, they can abrade counterface material and provoke higher wear and friction.

When graphitic or nongraphitic carbons rub against themselves, the friction coefficient is low. However, under some critical combination of sliding speed, load and ambient temperature, the contact temperature becomes too high ($> 500^\circ$ C for nongraphitic carbon and $\approx 150 - 180^\circ$ C for graphite) and the friction coefficient increases in several times, while the wear rate grows in several orders [34–36]. Under less severe sliding conditions, friction and wear rate of nongraphitic carbon exhibits large variations with time. Increasing speed induces a decrease in the friction coefficient, but does not influence the wear rate. However, both the friction coefficient and the wear rate increase with raising temperature. This change is more pronounced for graphitic materials.

b) The effect of the nature of carbon fibres

The experiments show that friction and wear of CFRP are very different according to the type of carbon fibers considered: high strength or high modulus. There is a macroscopic peeling-off of the carbon fibres from epoxy resin in HS carbon fibre composite [37]. High-modulus carbon fibers have the ability of transfer film formation, which favors a smoothing of the composite surface and affects the friction coefficient and the wear rate.

On the other hand, the friction and wear of the composite are defined mainly by the reinforcement [38]: polyester, polyimide, polypropylene and epoxy matrices reinforced by HS or HM carbon fibres exhibit similar friction and wear behavior under the same conditions.

- The friction coefficient of high strength carbon fibre composite is generally higher than the one of high modulus carbon fibre composites [37,38]. The type of thermosetting matrix has no influence on the friction coefficient of HM and HS carbon fibre composites.

$$\boldsymbol{\mu_{HS} > \mu_{HM}}$$

- While according to [37], high strength carbon fibre composites possesses a better

wear resistance, other authors observed opposite results [38]. The type of thermosetting matrix has no influence on the wear rate.

$$\boldsymbol{W_{HS} \overset{?}{\gtrless} W_{HM}}$$

1.3.2 Fibre orientation effect

There are three principal orientations for unidirectional composite: parallel P (sometimes called longitudinal), antiparallel AP (sometimes called transversal) and normal N. It means the orientation of composite fibres with regard to sliding direction. The mechanisms of composite surface damage are different according to fibre orientation:

- in parallel orientation, the fibres are damaged by pushing, bending, buckling or pulling;

- in antiparallel orientation, the damage is caused by bending of fibres;

- in normal orientation, the damage of both surfaces is caused, firstly, by ploughing of counterface by stiff carbon fibres, and by abrasion of both surfaces after generation of fibre debris [39]. In all the cases, the origin of cracking is at the fibre-matrix interface, where the debonding of the fibres is initiated.

- According to [40], for HM carbon fibre composite $\mu_N < \mu_P < \mu_{AP}$. The values of friction coefficient in the fibre orientations between normal and transversal orientations (30° and 45° to the composite surface) monotonly increase. Another study [41] reports that under two loads and four different sliding speeds, friction coefficients in P orientation is always smaller than in AP orientation, $\mu_P < \mu_{AP}$. The effect of fibre orientation on the friction coefficients of HM fibres composite against sapphire changes with sliding velocity: under 2 m/s $\mu_{AP} < \mu_P < \mu_N$, but under 3.5 and 7 m/s they invert $\mu_N < \mu_P < \mu_{AP}$ [42]. Fibre orientation has no effect on the friction coefficient of HS carbon fibres composite under scratching by Vicker's indenter [43].

$$\boldsymbol{\mu_N \overset{?}{\gtrless} \mu_P \overset{?}{\gtrless} \mu_{AP}}$$

- For HM carbon fibre composite against steel, the highest wear is observed in the normal orientation, when the lowest wear is in the antiparallel orientation $W_{AP} < W_P < W_N$ [39]. However other authors [40] under similar conditions observed that $W_N < W_P < W_{AP}$. The wear rate in the fibre orientations between normal and transversal orientations (30° and 45° to the composite surface) monotonly increases. According to [41] the wear volume in P direction is lower than in AP direction, $W_P < W_{AP}$. The friction tests with the HM carbon fibres composite in 0°, 30°, 45°, 60°, 75° and 90° orientations [44] reveal a strong dependence of wear rate on the composite orientation, and its maximum corresponds to 30°. Wear rates of HM fibres composite against sapphire disk are highest for normal orientation and lowest for anti-parallel orientation $W_{AP} < W_P < W_N$ [42]. Friedrich and Reinicke [45] in their review reported that the relation of the wear rates of carbon fibre reinforced epoxy depending on fibre orientation is $W_P < W_N < W_{AP}$. The better

wear resistance of normal and parallel orientations with regards to antiparallel orientation were observed by [46] for both HS and HM composites $W_N \approx W_P < W_{AP}$.

$$\boldsymbol{W_N \overset{?}{\geqslant} W_P \overset{?}{\geqslant} W_{AP}}$$

1.3.3 Fibre volume fraction effect

According to [47], less volume fraction of fibres leads to contact heating, higher adhesion, break of the transfer film, and surface damage. Since the thermal conductivity of epoxy is not high, the heat localizes and stores in the frictional zone. The addition of carbon fibers increases the thermal conductivity of the composite, which helps to draw aside the heat from the friction zone.

- Friction coefficient drops dramatically with carbon fibre addition (2.5 times for 15 % of carbon fiber content) [47]. The ratio between friction coefficients of 82 % and 67 % of carbon fibres composites changes with the increase of the pressure. An initial higher friction of 67 % of carbon fibres composite becomes lower under the pressure higher than 8 MPa [28] . Friction coefficient decreases gradually with fibre volume friction increase according to [46], which describes the experiments with fibre volume fractions from 40 % to 72 % in three orientations.

$$\boldsymbol{\mu_{lowVf} \overset{?}{>} \mu_{highVf}}$$

- The wear rate decreases simultaneously with the friction coefficient and reaches the minimum at $50-70$ % of fibers. If the fibre volume fraction exceeds 70 %, the conditions for polymer film formation on fibers are broken, defects inside the composite appear, which results in small wear increase [47]. Other authors [37] observed, that wear volume diminishes with the increase of volume fraction of HS carbon fibres composite, but it has no effect on the wear of HM carbon fibre composite. The wear rate of 82 % of carbon fibres composite is higher than the one of 67 % composite [28].

$$\boldsymbol{W_{Vf<50-70\%} \overset{?}{>} W_{Vf=50-70\%} \overset{?}{<} W_{Vf>50-70\%}}$$

1.3.4 Counterface hardness and roughness effect

a) Counterface roughness

- Steady state friction coefficient of HM carbon fibre composite is independent of roughness of the counterface material, because the transfer film between two surfaces in contact is formed rather quickly [38].

$$\boldsymbol{\mu_{lowRa} \approx \mu_{highRa}}\ (HM)$$

- Wear of both HS and HM carbon fibre composites increases with the counterface roughness growth, though for HM composite it occurs faster [38]. Steady state

wear rate of HM carbon fibre composite increases on 1-2 order for the counterface roughnesses from 0.05 to 1.1 μm, while for HS carbon fibre composite it remains almost the same.

$$W_{lowRa} < W_{highRa}$$

b) Counterface hardness effect

- Friction coefficient of the composite is 2-3 times lower against harder metals than against softer metals [47]. Other authors [38] observed that the friction coefficients of the HM carbon fibres composite against 17 metals and alloys with hardnesses from 58 ± 2 to 2000 VPN are rather equal. The effect of counterface hardness on the friction coefficient of HS carbon fibres composites is not so clear: up to 500 VPN the friction coefficient is high and similar, for $500 - 1000$ VPN for some materials the tendency is the same, when for others the friction coefficient is 2.5 times lower and does not depend on the counterface hardness, upper than 1000 VPN the tendency of low friction coefficient continues. Moreover, a thin transfer film was observed in the cases of low friction.

$$\mu_{soft} \overset{?}{\gtrless} \mu_{hard}$$

- The values of wear volume of the composite are similar against gold, mild steel and chromium [48]. Among 17 metals and alloys [38] rubbing against HM carbon fibres composites only gold, copper, Al alloy and titanium did not provoke transfer film formation and display high values of wear rate. In other cases, wear rate was rather similar. There are large variations in the wear rates of HS carbon fibre composites against the metals of different hardness.

$$W_{soft} \overset{?}{\gtrless} W_{hard}$$

1.3.5 Sliding speed and load effect

- Under four sliding speeds, the friction coefficient is smaller under light load and increase with the speed growth. It is less sensitive to the variation of load than to the sliding velocity [41].

$$\mu_{lowV} < \mu_{highV} \; ; \quad \mu_{lowN} < \mu_{highN}$$

- Wear volume increases with sliding speed increase for HM and HS carbon fibre composites with different fibre volume fraction, but this dependence is not always linear [37, 49]. According to [41] wear volume increases linearly with the increase of sliding speed and with normal load. In an experiment with HM carbon composite against sapphire disk [42], the wear rates exhibit a minimum value at an intermediate velocity for three orientations, the effect of velocity is more remarkable for the normal orientation.

$$W_{lowV} \overset{?}{<} W_{highV} \; ; \quad W_{lowN} < W_{highN}$$

The contact temperature of HM fibres composite contact with an optically flat sapphire disk was measured with an infrared microscope [42], the increase of surface temperature with sliding velocity until a certain value was observed for three fibre orientations. The further increase of the sliding velocity does not change this value of the contact temperature about 110°, which roughly corresponds to the glass temperature of epoxy.

1.3.6 Environment effect

The carbon fibre reinforced polymers friction is highly influenced by water presence in the contact. The mechanism is similar to the one of the graphite friction, explained before. The interruption of transfer layer formation causes frictional variations and dramatically affects wear and friction values. Higher temperatures favor polymer matrix melting and high wear.

- The friction coefficient of HS and HM carbon fibre composites descends with temperature rise until about $200°C$ and reascends with further heating [48]. The steady state friction coefficients in the atmosphere with high humidity are higher for any fibre orientation and sliding speed of HM composite [49].

$$\boldsymbol{\mu_{humid} > \mu_{dry}}$$

- A temperature increase until $300°C$ causes a rapid increase of wear rate [48]. High atmosphere humidity significantly decreases the wear of HM composite [49].

$$\boldsymbol{W_{humid} < W_{dry}\ ;\ \ W_{lowT} < W_{highT}}$$

1.4 Conclusions and methodology of this study

This literature review of experimental works on carbon fibre-reinforced epoxy friction and wear clearly shows that:

- There is a lack of information about friction between composites and composite/soft material. The experiments with composite are usually carried out against metal (steel) counterface;
- The experimental observations from different works are often contradictory, which makes difficult to draw conclusions and understand general tendencies;
- The mechanisms of frictional dissipation and wear of composites are sophisticated and change during the sliding process, which makes difficult, and maybe impossible, to create a theory applicable to the whole process.

Therefore, in our work, we are interested in the frictional dissipation in composite/composite and composite/epoxy sliding contact. The approach of the separation of interfacial and bulk levels of frictional dissipation is adopted for our polymer composite study. The both levels will be investigated experimentally on model polymer composite materials

reinforced with carbon fibres or carbon nanopearls. The equivalent experiments on pure epoxy will be carried out in order to trace the influence of carbon reinforcement.

The experiments on interfacial dissipation study will be carried out under low normal loads and sliding velocities in order to avoid surface damage and bulk dissipation. The aim of these experiments is to understand how the nature, content, shape and distribution of fillers affect the frictional energy dissipation of polymer. Further, an analytical model of interfacial friction between composites, based on the theoretical background given in Section 1 of this chapter, will be developed and applied to the studied experimentally composite contacts.

Finally, the bulk frictional dissipation of composites will be investigated by means of application of severe tribological conditions, i.e. normal load and sliding speed. A special attention will be paid to a study of wear mechanisms, which are expected under such conditions. The wear mechanisms and laws presented in section 2 of this chapter will be looked for and discussed, respectively, for composite and pure epoxy contacts. An attempt to associate the frictional energy dissipation with the initiation and development of these mechanisms will be made.

Chapter 2

Polymer composites reinforced with carbon fillers

The literature review highlights the lack of knowledge regarding the interfacial dissipation of composites, as defined by Tabor for polymers. Besides, it reveals the wide variety of bulk friction and wear mechanisms observed according to the nature of the matrix and of the filler. In this PhD work, we will focus on fundamental dissipation mechanisms at stake at the interface and in the bulk. For this investigation, we will use model composite systems. The main requirement is a sharp contrast of tribological properties between the matrix and the filler, as well as a range of filler shapes in order to investigate a possible anisotropy effect. In this context, epoxy matrix has emerged as a natural candidate. On the other hand, carbon reinforcement is widely used and exists in various shapes and sizes. Therefore, our choice of model composite systems was oriented towards carbon reinforced epoxy composites. Namely,

- Pure epoxy;
- Carbon fibre-reinforced epoxy composites of 34, 52 and 62 % of fibre volume fraction;
- Carbon nanopearl-reinforced epoxy composites of 1, 15, 28 and 35 % of nanopearl mass fraction.

From a tribological point of view, a material study requires consideration of its structure from atomic to macro structure, because all scales influence its frictional behavior. Therefore, we start this chapter with an overview from nano to micro structure of carbon fillers and their physical and mechanical properties. Along with carbon fibres and carbon nanopearls, used for our composite reinforcement, carbon blacks are presented in this section due to their better state of knowledge and similarity to nanopearls.

Furthermore, this chapter successively presents two model composites with their manufacture processes and discusses these composites morphologies. Composite surface topography and mechanical properties are also characterized and presented in this chapter.

Contents

2.1 Carbon fillers

2.1.1 Crystalline and amorphous forms of carbon

Carbon has several crystalline forms, such as graphite, diamond, fullerenes and nanotubes, and many transitional amorphous and partially crystalline forms, such as fibres, films, membranes, glassy carbon, pyrolytic carbon and others. Basically, carbon has 4 electrons on the outer orbit and is able to create sp, sp^2 and sp^3 atomic bonds (Fig. 2.1). The sp-hybridisation relates to linear polymer chain of $(-C \equiv C-)_n$ or $(= C = C = C =)_n$ that is called carbine. Carbon atoms of sp^2-hybridisation form a lamellar graphite structure, while tetrahedrons of carbon atoms of sp^3-hybridisation form a diamond structure.

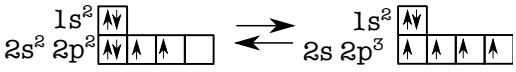

Figure 2.1: Hybridization of carbon

Graphite is the carbon crystalline form found in nature. This is one of the first materials studied with X-rays, which revealed the parallel planes of carbon atoms in graphite structure. A distance between these layers (see Fig. 2.2(a)) is equal to 0.335 nm. In each layer, called graphene, carbon atoms form a network of regular hexagons with $C-C$ distance of 0.142 nm. An energy of carbon-carbon bonding in the layer is 420...460 $kJ/mole$, while an energy of interlayer bonding is equal to 42 $kJ/mole$. In 1924, Bernal [50] proposed an idealized model of graphite structure (Fig. 2.2(a)), which has been accepted by

other scientists. This is a lamellar structure, where each layer is formed by carbon atom hexagons, and each atom is located exactly above the centre of the hexagon of an adjacent layer. The graphene layers alternate in the 3D structure of graphite.

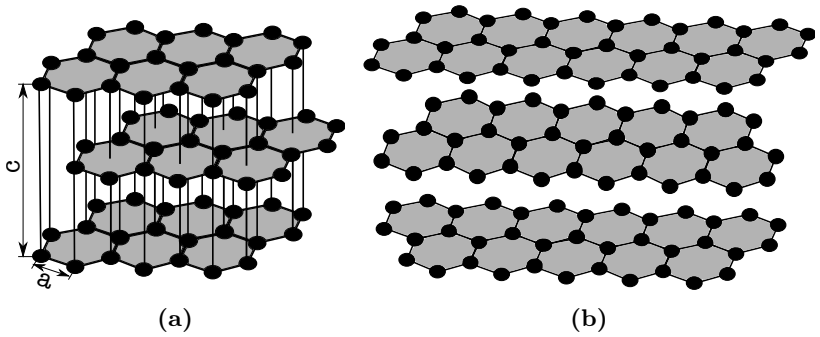

Figure 2.2: Atomic structure of (a) graphite, (b) turbostratic carbon

Such a structure implies a strong anisotropy of physical and mechanical properties. However, real graphite materials consist of graphite flakes oriented randomly, which leads to the general isotropy of a macrostructure.

Carbon fibres, as well as cokes are the products of thermic transformation of polymers or glassy carbon. They are considered as a transition form of carbon: they contain areas of different carbon structures. The transition form of carbon is composed of turbostratic structure and amorphous carbon. Turbostratic structure resembles the graphite structure: it is also formed by parallel hexagonal lattice planes of carbon atoms. But the relative positions of carbon atoms in adjacent layers are random, see Fig. 2.2(b).

2.1.2 Carbon fibre: from micro- to nanostructure

2.1.2.1 Morphology and types of carbon fibres

The morphology and structure of carbon fibres is defined by a precursor, polymer chains orientation and the heat treatment conditions [51]. They exhibit the effect of shape memory, which means that they keep the shape of the precursor fibres. The most common precursor materials are PolyAcriloNytrile (PAN), rayon and pitch. Fibre cross-section shape is set by the manufacturer and depends on the precursor material and extrusion process. It can be round, hollow, square, triangular or have bean- or star-like shape. For instance, PAN fibres, depending on manufacture method have round or bean-shape cross-section, while carbon fibres produced from rayon often have star-like shape [52, 53]. Several examples of carbon fibre cross-sections are presented in Fig. 2.3 using Scanning Electron Microscopy (SEM).

The surface roughness of carbon fibres is also defined by the precursor material and manufacture procedure. Generally, pitch-based fibres exhibit relatively smooth surface, while star-shape fibres are very rough. Only produced from synthetic fibres, carbon fibres

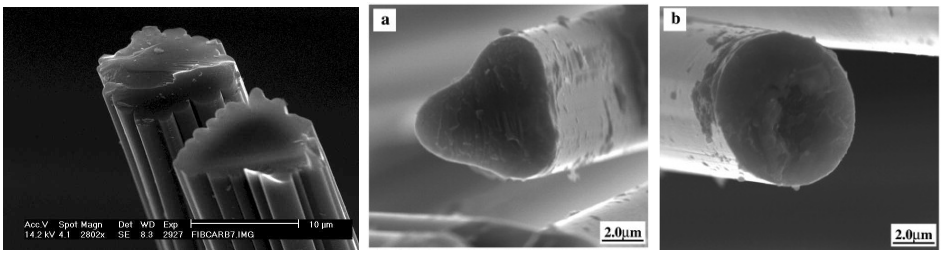

(a) (b) (c)

Figure 2.3: SEM observation of amorphous: (a) star-shape carbon fibres [54] (b) triangle carbon fibre of $E = 115\ GPa$ [55] and (c) round carbon fibre of $E = 102\ GPa$ [55]

have a micro-fibrillar structure and present anisotropic properties. The other types of precursor give an isotropic structure of carbon fibre. Moreover, the density of fibre structure is not uniform: they contain micro- and macro-defects and pores.

Usually carbon fibres are classified onto 3 types, distinguished by maximal heat treatment temperature. They manifest distinct mechanical and tribological properties. These 3 types, the temperature conditions of manufacturing and their main differences in terms of mechanical characteristics are presented in Table 2.1.

Carbon fibre type	**Heat treatment temperature, °C**	**Crystalline orientation**	**Rupture strength** MPa	**Young's modulus** GPa	**Carbon contain, % mass**
Type I High modulus (graphitic fibre)	> 1500	Mainly parallel to the fibre axis	2000-3000	350-700	$> 99\%$
Type II High strength (carbon fibre)	800-1500	Mainly parallel to the fibre axis	3000-7000	200-300	$91\% - 98\%$
Type III (isotropic) Low modulus Medium strength	< 800	Random	 500-1000 1000-2000	 30-50 50-150	$< 90\%$

Table 2.1: Classification of carbon fibres [56, 57]

2.1.2.2 Models of carbon fibre structure

Although, the majority of scientists agree that carbon fibres contain mostly turbostratic structure, several models of carbon fibre structure coexist. Some of them will be presented below in this section.

Ribbon-like structures. A model of carbon fibre structure based on small-angle X-ray scattering and electron microscopy observations was proposed by Watt and Johnson and

schematized by Ruland [58]. This structural model includes an alternate of straight and bent parts of fibrils, forming a stretch network. The crystallites are arranged in chains inside the fibrils of about 50 nm diameter. The voids in this structure are long ($20 - 30$ nm) and thin (average cross-section $1 - 2$ nm), mostly oriented in the fibre axis direction. A basic structure unit is ribbon-like turbostratic carbon layer.

Using Tunnel Electron Microscopy (TEM) technique to examine high-modulus fibres, Diefendorf and Tokarsky found the wrinkled ribbon structure in carbon fibres. The thickness of these ribbons are from 13 to 20 layers, and their width is between 4 and 9 nm. In spite of the evidence of the fibrils in carbon fibre structure, it is more preferable to present crystallite packing as ribbon-like structure, because the torsional rigidity of fibre is not low, as it could be expected if the fibril was a structural unit. A number of observations with dark-field microscopy, X-ray wide-angle scattering and transmission electron microscopy of pitch, rayon and PAN-based carbon fibres of different treatment temperatures confirm the presence of slightly undulating ribbons of sp^2-carbon, as the basic structural unit.

A model for both HM and HS fibre structure was proposed by Oberlin. According to him, HM fibres have aromatic layers with a larger transverse radius of curvature, which decreases from the periphery to the centre of the fibre, while the HS fibres have aromatic layers with a smaller but uniform radius of curvature.

Some studies [57] of carbon fibres after different stages of oxidation and heat treatment showed a lamellar structure in fibre. The formation of this structure is a function of the graphitization temperature. The lamellar phase has a ribbon width of 230 nm, while for fibrillar structure this value is less than 10 nm. Jonhson et al. [59] suppose that the fibrillar structure gradually changes into the lamellar one as the preferred orientation becomes stronger. Many studies showed that both fibrillar and lamellar structures exist simultaneously in carbon fibre.

Circumferential-Radial or onion-skin model and 3D models. By examining with optical microscopy PAN-based carbon fibres produced under different conditions, Knibbs [60] identified three types of fibre cross-section. The first type shows some layers with circumferential preferred orientation in outer zone and a randomly oriented inner zone. The inner zone of the second type is radially oriented, while the outer is also circumferential. Finally, all layers of the third structure have a circumferential preferred orientation. It was found that high temperature treatment does not influence the preferred orientation, but only the crystalline alignment.

SEM observations of carbon fibres after etching in oxygen plasma allowed Barnett and Norr [61] to conclude that a carbon fibre consists of a more etch-resistant central region, a less etch-resistant outer ring and the radial ridges and valleys between them. Based on these observations for Modmor I carbon fibre they proposed the macrostructure model, but admitted that other fibres may not necessarily have all these structure elements.

A three-dimensional carbon fibre model confirmed by optical, SEM and X-ray diffraction studies for fibres from different precursors was constructed by Diefendorf and Tokarsky [62]. Fig. 2.4 presents this model for the rayon-based fibre structure, which consists of randomly oriented microfibrils, and for two PAN-based carbon fibres, which have a more complex internal radial structure.

Fig. 2.5 reveals the difference in carbon fibre structure correlated to their elastic

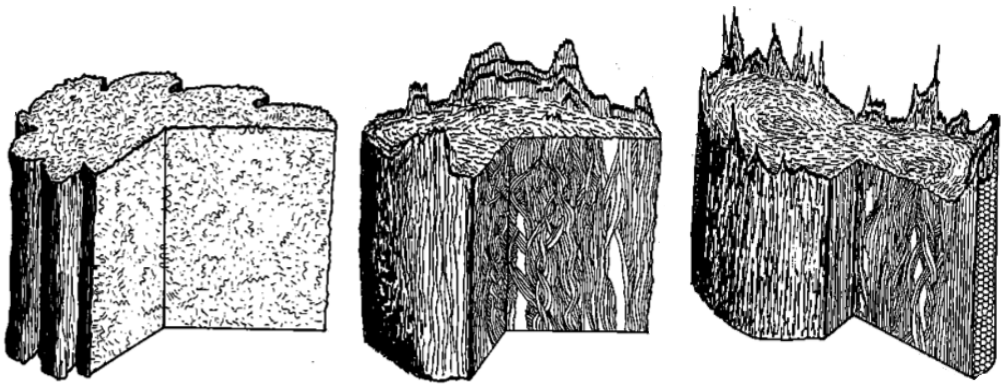

(a) (b) (c)

Figure 2.4: Diefendorf and Tokarsky's three-dimensional models [62] for (a) Rayon-based Wyb carbon fibre, (b) PAN-based Fortrail 4y carbon fibre, (c) PAN–based *CS-1* carbon fibre

moduli. The SEM photos are given from the left to the right in the order from the lowest Young's modulus of $E = 377\ GPa$ to the highest Young's modulus $E = 950\ GPa$. One can notice that the carbon fibre structure becomes more arranged, lamellar or fibrillar, with the increase of elastic modulus [54, 55].

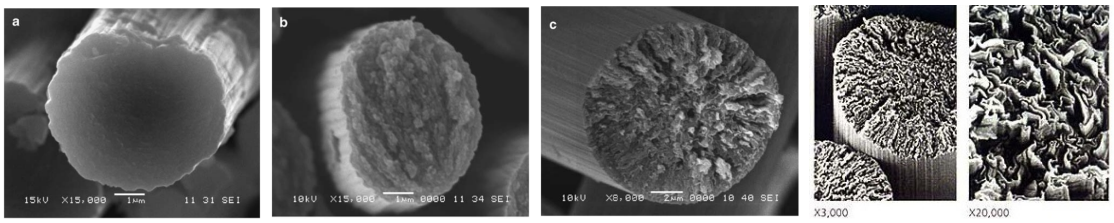

(a) (b) (c) (d)

Figure 2.5: SEM photos of: (a-c) High modulus carbon fibres of $E = 377\ GPa$, $E = 436\ GPa$ and $E = 640\ GPa$, respectively [63]; (d) Ultra high modulus carbon fibres *Granoc* ® of $E = 950\ GPa$ [64]

2.1.2.3 Physical and mechanical properties of carbon fibres. *Hextow*® *AS*4 carbon fibres

In comparison to other fibres used in composite industry, carbon fibres have extremely high values of elastic modulus and strength, chemical and thermal stability, low linear thermal expansion coefficient (CLTE), specific tribological properties, high thermal and electrical conductivity. Several typical characteristics of carbon and graphite fibres are shown in Table 2.2.

In this work, the fibres, selected to reinforce our composite samples, are *HexTow*® *AS*4

Type of fibre	Density, g/cm^3	Specific area, m^2/g	CLTE $\cdot 10^{-6}$, K^{-1}
Graphite fibre (Type I)	$1.8 - 2.15$	$0.15 - 3$	-1.5 – 2.5
Carbon fibre (Type II, III)	$1.4 - 1.8$	$1 - 1000$	-1.5 – 1.5

Type of fibre	Specific electrical resistivity $\cdot 10^5$, Omm	Thermal conductivity, $W/(m \cdot K)$	Specific heat J/(kg K)
Graphite fibre (Type I)	$0.3 - 1$	$1.7 - 2.0$	0.6
Carbon fibre (Type II, III)	$1 - 70$	$0.8 - 1.6$	0.8

Table 2.2: Typical physical properties of carbon and graphite fibres [56]

carbon fibres. These continuous fibres are produced from PAN precursor fibres. They are characterized by high strength and strain. Several mechanical and physical properties of these fibres are presented in Table 2.3. Optical observations are also shown in Fig. 2.6.

Density, g/cm^3	Filament diameter, μm	Carbon content, %	Tensile strength, MPa	Tensile modulus (Chord $6000 - 1000$), GPa	Ultimate elongation at failure, %
1.79	6.5	94	4.43	231	1.8

Table 2.3: Carbon fibre $HexTow^{®}AS4$ properties [65]

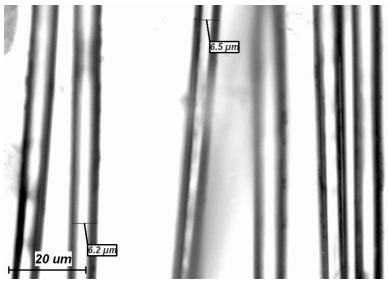

Figure 2.6: Carbon fibres $HexTow^{®}AS4$ by optical microscopy

2.1.3 Carbon black

Carbon black is the name of the large range of carbon compounds, produced by oil furnace, lampblack, channel, thermal or acetylene processes [59]. Carbon black has many applications, mostly as a filler for rubbers and polymers. Its properties, such as electrical and thermal conductivity, color, aging (UV protection), reinforcement as well as low cost, lead to use it in tyre, wire and cables, electrical isolators, *etc.*

The temperature of its formation is usually between 700 and 2500 °C. Like carbon fibres, they have an amorphous core enveloped by parallel, but disoriented graphene layers,

which put them into the class of turbostratic carbons, see Fig. 2.7. The crystalline fraction and orientation of graphene layers both depend on temperature of treatment. Due to aggregation phenomena, several structural levels are distinguished for carbon black. The first level is constituted from elementary particles, small spheres, paracrystalline, inseparable components of an aggregate. Their diameter varies from some dozens to some hundreds of nanometers. These particles form secondary structures, referred to as aggregates, a discrete, rigid colloidal entity that is the smallest dispersible unit; it is composed of extensively coalesced particles. The particle is separable from the aggregate only by fracturing. The aggregates form agglomerates. While particles and aggregates are formed by covalent bonds, the organization of agglomerates results from Van der Waals bonds. The carbon black can contain sulfur, oxygen, hydrogen or nitrogen, depending on the fabrication process and precursor. Its physical properties vary largely and highly depend on the fabrication process.

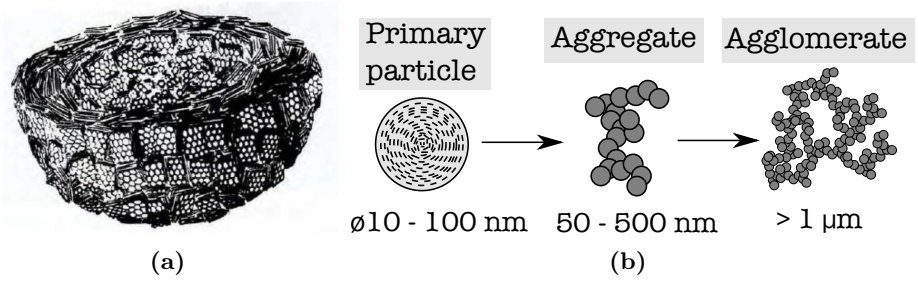

Figure 2.7: (a) Model of carbon black particle composed of graphene plates [66] (b) Agglomerate structure of carbon black

2.1.4 Carbon nanopearl

Carbon nanopearls (CNP) are monodispersed spherical particles, which form a foam-like macrostructure of continuous 3D chains analogous to strings of pearls [67].

Carbon nanopearls, used as a filler for our composite materials, are provided by Institute of Nanotechnology of Lyon (INL). Fig. 2.8 shows a nanopearl foam manufactured by chemical vapor deposition process. The features of this process and main physical properties of the nanopearls are described in the paper of Levesque et al. [67] and their patent on this manufacture method [68]. These particles are synthesized using Ni nano cluster catalysis at only 700 °C. The diameter of particles described in the patent is about 150 nm. However, the particles used in our study are from the next generation and have a diameter of 90 nm. A polydispersity is estimated at about 85 %. The highly bent nanopearl strings can reach a length of ten microns. Fig. 2.9, adopted from [67], shows HRTEM images of carbon nanopearls, which demonstrate their spherical shape. This high magnification image also shows carbon flakes of $2-6$ nm size covering the nanopearl surface with an interfringe distance of 0.47 nm. The diffraction pattern, inset in the right image, indicates the mixture of amorphous and crystalline carbon species, which was confirmed by Raman spectroscopy measurements.

The advantages of these nanopearls compared to carbon black are low cost, relative simplicity of fabrication and monodispersity and purity of particles, as well as field emission properties.

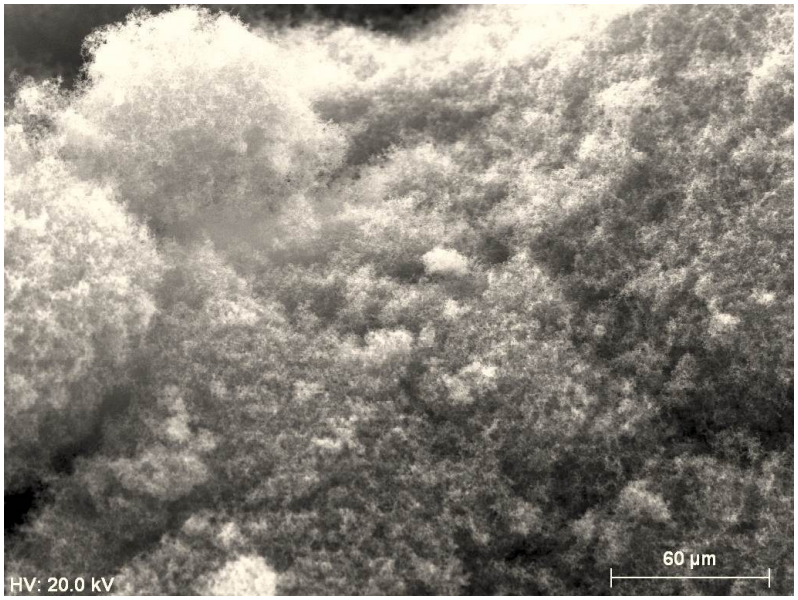

Figure 2.8: SEM image of the carbon-nanopearls foam-like structure

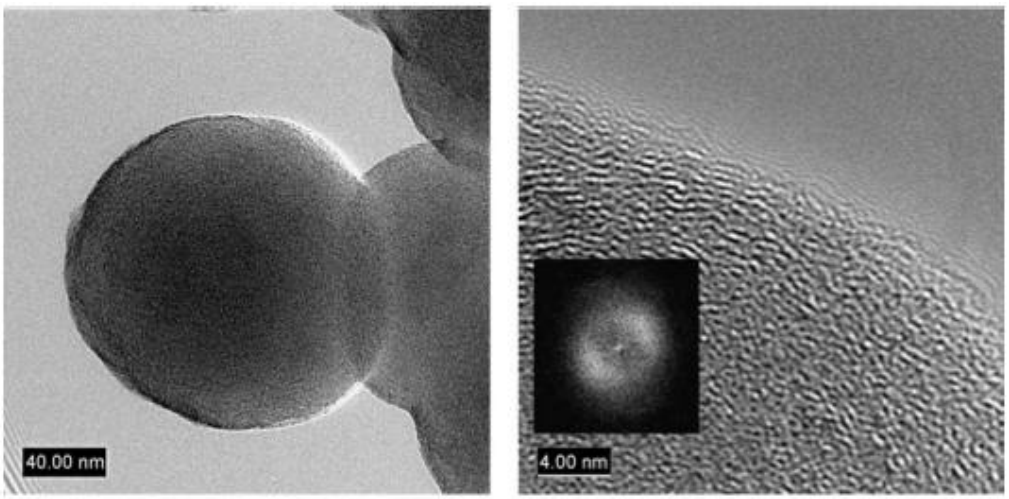

Figure 2.9: HRTEM images of the carbon nanopearls, adopted from [67]

2.2 Carbon fibre-reinforced epoxies (CFRE)

In this section, we successively present pure epoxy and CFRE composites with their macroscopic physical and mechanical properties; their surface preparation and topographical properties and, finally, their surface mechanical properties, measured by nanoindentation at the laboratory ICS of Strasbourg.

2.2.1 Epoxy resin as a matrix. $HexPly^{®}M10.1$ epoxy resin.

The matrix, principal component of any composite material, provides the integrity of composite, fixes a shape to final product and relative positions of reinforcing fibres. It also distributes the applied load between fibres into material bulk and provides its redistribution if several fibres are ruptured. The strength properties of the matrix become crucial either under shear loading, or tensile/compressive loading of composite in transversal fibre orientation, or submitted to cyclic loads.

Matrix material can have the same nature as reinforced material, for instance carbon, ceramic, metallic matrix. However, the majority of fibre-reinforced composites are manufactured on basis of polymers. Two major groups of polymers, thermosetting and thermoplastic, with completely different thermal behavior, can be considered in composite design.

Thermoplastic polymers, semi-crystalline and amorphous, are characterized by the ability to change reversibly their phase state from liquid to solid with temperature, without material destruction. Their mechanical characteristics are not inferior to these of cured thermosettings, while their chemical resistance and leaktightness often exceed those of thermosettings. Their disadvantages as composite matrix are the strong dependence of mechanical properties on temperature, low heat resistance and manufacture problems caused by high viscosity of the molten state [69]. Thermoplastic resins are generally less expensive than thermosettings.

Thermosetting resins are synthetic polymers, which are stored in liquid state before the composite impregnation process. The curing of the majority of thermosetting resin with a hardener or catalyzer is necessary to create cross-linked three-dimensional polymer chains. The final product is infusible and insoluble polymer, incapable to further phase transition. Cured thermosetting plastics have higher values of hardness, heat resistance, elastic modulus, fatigue strength and lower linear thermal expansion coefficient than thermoplastics. This set of properties gives them more applications as composite matrix material.

Epoxy resin, which we use as composite matrix in our study, is a thermosetting polymer. In addition to already mentioned thermosetting properties, it has high adhesion and high resistance to humidity and radioactive emission. One of the disadvantages of epoxy resin is a relatively low heat resistance resulting in a dramatic loss of strength at near glass temperature [69]. Table 2.4 presents several typical physical and mechanical properties of cured epoxy.

$HexPly^{®}M10.1$ epoxy resin is used as a matrix for manufacturing of carbon fibre-reinforced composites presented further. It is a formulated epoxy resin, suitable for low pressure moulding processes. The range of processing temperature of this epoxy resin is

Tensile strength, MPa	**Compressive strength**, MPa	**Young's modulus,** GPa	**Poisson's coefficient** °C	**Elongation** %
$35-100$	$90-160$	$2.4-4.2$	0.4	$2-9$
Volume shrinkage	**CLTE** $\cdot 10^5$**,** K^{-1}	**Glass temperature,** ° C	**Thermal conductivity,** W/(m K)	
$1-5$	$4.8-8.0$	120	0.19	

Table 2.4: Order of magnitude of physical and mechanical properties of cured epoxy [56, 69, 70]

from 85° C up to 150° C at pressure between 0.9 and 5 bar. It has high fatigue resistance and a long pot-life at room temperature. Nominal density of this resin is 1.20 g/cm^3 [71].

2.2.2 On the importance of fibre-matrix interface

The interface between composite components is responsible for its global mechanical properties, because it is the most probable area of material rupture and it transfers a load from matrix to fibres. The fibre-matrix interface can be studied at two levels [72]. At the molecular level, the interaction is determined by chemical structures of fibres and matrix and is due to Van der Waals forces, acid-base interactions and chemical bonds. At the level of single fibres, the fibre-matrix interaction is usually described in terms of load transfer parameters, as bond strength, interfacial shear stress, critical energy release rate, *etc.* Interphase is often considered to have properties differing from those of fibre and matrix [73].

In order to increase fibre-matrix adhesion, a surface layer is weaker than carbon fibre core, can be removed from the carbon fibres by oxidation, usually with acid. After this treatment, there are reactive groups, such as $-COOH$, $-CHO$ and $=CO$, on the fibre surface that permit easy chemical bonding with polymer matrix [74].

There are a number of fibre-matrix interface characterisation tests, such as single fibre pull-out test (and its variations as microbond test or three-fibre test) or push-out test, fragmentation test, Broutman test, *etc.* For carbon fibre reinforced polymers, because of ductility of their matrix and brittleness of the fibres, the most adequate test is the fragmentation test [74]. Another method to characterize fibre-matrix interface is to study damping properties of composite material. An interfacial bonding is defined by Dynamic Mechanical Analysis testing, and associated with damping coefficient $\tan\delta$ [75].

For instance, the single fibre pull-out experiments [74] with carbon fibre (sized AS1 graphite fibres) reinforced epoxy resin show, that interfacial shear stresses at the instant a fibre emerged from matrix are from about 9 to 13 MPa, coefficients of friction vary from 0.42 to 0.58 and shear strength of the interphase, estimated from the slope of maximal force causing bond failure versus embedded length, is from 33 MPa to 56 MPa. These values change with cure temperature of epoxy resin from 60°C to 135°C.

2.2.3 Prepreg $HexPly$® and multilayer unidirectional composite CFRE 62%

The unidirectional composite samples for our frictional study were manufactured from $HexPly$®M10/38%/UD300/CHS prepreg. It is a unidirectional high strength carbon fibre/epoxy prepreg. Its name carries information about its components: $M10$ is the epoxy resin type; 38 % is the resin content by weight; UD300 means 300 g of fibres per 1 m^2 of prepreg and *CHS* represents high strength carbon fibre reinforcement. Tables 2.5 and 2.6 present physical and mechanical properties, relatively, given by the data sheet of this prepreg. Photos of two composite samples produced from this prepreg are shown in Fig. 2.11 (e, f). These samples will be referred to as CFRE 62% in this thesis.

Areal weight, g/m^2	**Cured ply thickness,** mm	**Fibre volume,** %	**Resin weight content,** %	**Laminate density,** g/cm^3	**Glass transition temperature,** $°C$
484	0.322	52.4	38	1.57	120

Table 2.5: Nominal physical properties of $HexPly$® M10/38%/UD300/CHS prepreg [76]

Tensile strength, MPa	**Tensile modulus,** GPa	**Compressive strength,** MPa	**Compressive modulus,** GPa	**Flexural strength,** MPa	**Flexural modulus,** GPa	**ILSS,** MPa
1700	130	1250	110	1400	127	80

Table 2.6: Mechanical properties of $HexPly$® M10/38%/UD300/CHS prepreg [76]

2.2.4 Intermediate fibre volume fraction composites

The samples of intermediate fibre volume fractions were manufactured by a third company from AS4 carbon fibres and M10.1 epoxy resin. They contain unidirectional carbon fibre layers of about 0.5 mm thickness immersed into epoxy, see Fig. 2.10. The resulting structure is highly heterogeneous in volume, as well as on surface perpendicular to fibre layer due to misalignment of fibre layers. Fibre volume fraction of these composites was provided by the manufacturer and is equal to 34 and 52 % for two composite types.

The sample overview photos in Fig. 2.11 clearly shows the dark zones of pure epoxy and grey zones of carbon fibre hanks exposing on the surface. The percentage of pure epoxy zones on the surface is estimated from the overview surface photos by means of the software *ImageJ*. A grey color threshold is imposed and the areas of upper and lower color zones are calculated. Hence, on macroscale, the circular CFRE 34% sample has about 35 % of epoxy, and the circular CFRE 52% sample has about 16 % epoxy on the surface.

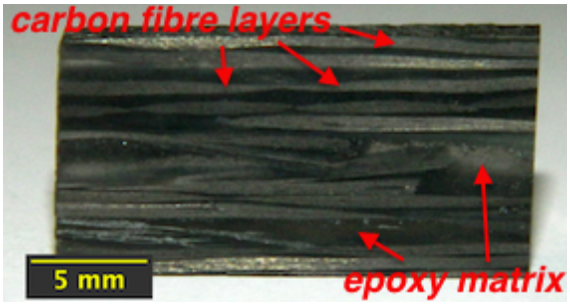

Figure 2.10: Cross-section of intermediate volume fraction composite material: transparent epoxy filled by the layers of fibre tissues

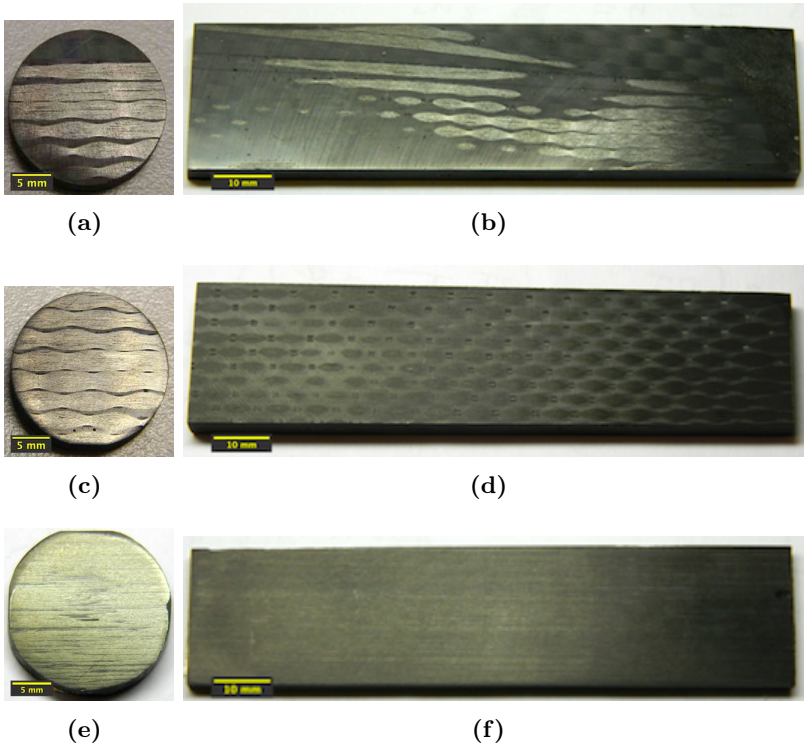

Figure 2.11: Carbon fibre-reinforced epoxies of (a, b) 34% (CFRE 34%), (c, d) 52% (CFRE 52%), (e, f) 62% (CFRE 62%)fibre volume fraction

2.2.5 Composite and epoxy surface preparation and topography

All manufactured composite material and pure epoxy operating surfaces are prepared using a similar protocol. Surface grinding with abrasive papers is performed on the polishing machine Presi Mecapol P220U. The speed of grinding is regulated by user and can reach 400 rpm on 200 mm diameter plate. The procedure of grinding is carried out manually: sample holding and pressure supply and its distribution onto the sample surface are controlled by operator hands. A jet water spray system continuously supplies the water to the sample/abrasive paper contact to prevent sample overheating and evacuate wear particles. The abrasive silicon papers P600, P1200, P2400 and P4000 are successively used for each sample surface. The duration of the procedure is adapted for each initial material surface: generally, it is longest for CFRE composites and shortest for pure epoxy surfaces.

There are many experimental techniques of rough surface measurements. The choice of experimental technique must be based on the expected surface characteristics. In our case of ground composite and epoxy surfaces, the tactile profilometry is sufficient. A profile of any rough surface is decomposed on primary, waviness and roughness profiles. The definitions of main standard roughness characteristics, which are equivalent to the characteristics of waviness profile after the filter application, are presented in Table 2.7.

Name and symbol	Definition	Formula
Average roughness R_a	Average absolute deviation from mean line over one sampling length	$R_a = \frac{1}{n}\sum_{i=1}^{n} \lvert y_i \rvert$
RMS roughness R_q	Root mean square deviation from profile mean line over sampling length	$R_q = \sqrt{\frac{1}{n}\sum_{i=1}^{n} y_i^2}$
Skewness R_{sk}	Third central moment of profile amplitude probability density function, measured over sample length	$R_{sk} = \frac{1}{nR_q^3}\sum_{i=1}^{n} y_i^3$
Kurtosis R_{ku}	Fourth central moment of profile amplitude probability density function, measured over sampling length	$R_{ku} = \frac{1}{nR_q^4}\sum_{i=1}^{n} y_i^4$

Table 2.7: Standard roughness characteristics. y_i defines the height of i-point relatively the mean line [77]

The surface profile map of CFRE 62% composite is measured with Dektak 150 Surface Profiler of Veeco Instruments Inc. in order to verify the homogeneity of surface topography after polishing. An example of 3D map of polished CFRE 62% surface, measured on the 1×1 mm area with the step of 200 nm and a distance between adjacent profiles of 1 μm, is presented in Fig. 2.12. The stylus of 12.5 μm tip radius is used for these measurements. The surface characteristics on the left of the surface map image are calculated by Veeco software. This surface map reveals, that the polishing does not smooth the whole composite surface: polished carbon fibres apparently protrude from the matrix as $1 - 1.5$ μm.

The surface of pure epoxy samples is homogeneous. Moreover, taking into account large surface of our samples, several individual profiles are measured in different places in order to evaluate more accurately the surface statistic, than with a local surface map. The

individual surface profiles are measured with Surfascan Somicronic tactile profilometer with the stylus of 2.5 μm radius tip and the step of 4 μm. Fig. 2.13 (a) presents an example of the measured profile of pure epoxy sample, while its roughness and waviness characteristics, together with those of CFRE 62% composite surface, are reported in Table 2.8.

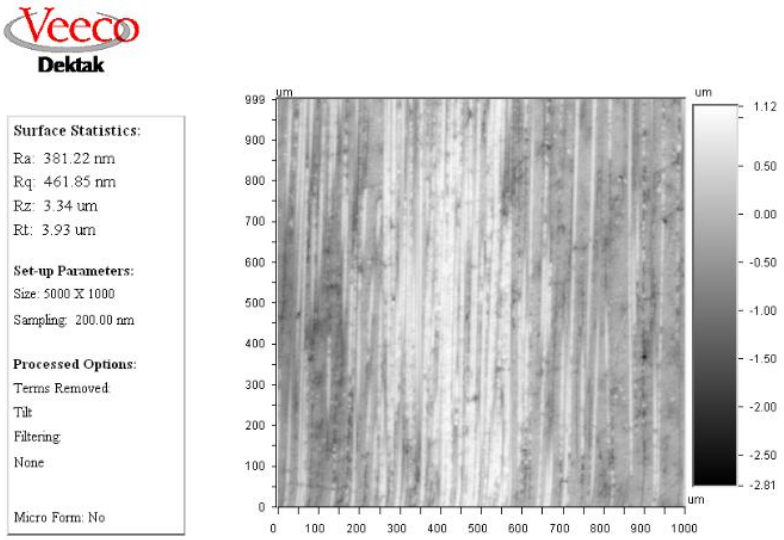

Figure 2.12: Surface map of CFRE 62% sample 1×1 mm area

Due to the high heterogeneity of the surfaces of CFRE 34% and CFRE 52% (see photos of surfaces Fig. 2.11) the average waviness and roughness characteristics for these surfaces are meaningless. Two examples of CFRE 52% surface profiles are presented in Fig. 2.13 (b, c). The smooth zones of surface on Fig. 2.13 (b) corresponds to pure epoxy zones, while the rough protuberances represent carbon fibre hanks. The profile of Fig. 2.13 (c) is taken along the fibre direction on the center of a fibre hank. It clearly shows that fibre hanks protrude from the matrix. The knots of fibre hanks are covered by matrix, as it is seen on Fig. 2.11 (c) surface photo.

Material	***Rq***, μm	***Rsk***	***Rku***
Pure epoxy	0.07 ± 0.003	-1.03 ± 0.433	7.84 ± 2.205
CFRE 62%	0.53 ± 0.074	-0.48 ± 0.114	3.34 ± 0.309
	Wq, μm	***Wsk***	***Wku***
Pure epoxy	0.05 ± 0.001	-1.00 ± 0.569	4.27 ± 1.052
CFRE 62%	0.42 ± 0.108	0.01 ± 0.750	2.98 ± 0.672

Table 2.8: Surface characteristics of track samples based on 3 measurements for each material type (ISO4287)

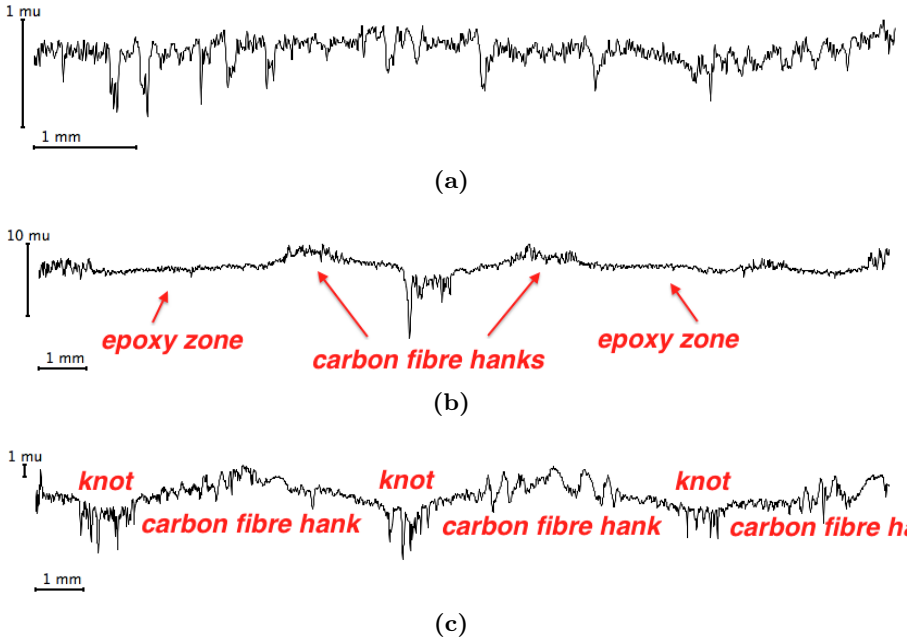

Figure 2.13: Typical examples of surface profiles of (a) pure epoxy, (b) CFRE 52% across fibre direction, (c) CFRE 52% along fibre direction centered in a fibre hank

2.2.6 Composite and epoxy surface mechanical properties. Nanoindentation

Measurements of surface mechanical properties with nanoindentation technique were carried out by Dr Anne Rubin from Institut Charles Sadron (ICS) of Strasbourg. The nanoindentation test consists in the penetration of tested material specimen with a hard indenter of specified shape. The known geometry of the indenter along with the measured penetration depth gives the contact area, which, together with the measured full load, provide the material hardness. The elastic modulus can be calculated from the initial elastic part of the unloading curve.

Pure epoxy and carbon fibre-reinforced epoxy of 62% of fibres were tested in order to study the influence of reinforcement on local mechanical properties of fibres and epoxy matrix. The tests were carried out on the CSM Ultra Nanoindentation Tester with Berkovitch indenter tip under ambient environmental conditions. The penetration velocity of loading and unloading for these static indentation tests is 10 mN/min, or 2 μm/s, in terms of displacement. A pause of 20 seconds is made after total loading for all indentations.

The imprint of the indentation tip into the pure epoxy, which demonstrates visco-elastic polymer nature by recovering of indentation sides, is shown in Fig. 2.14 (a). The curves of force vs penetration, corresponding for three indentations into pure epoxy, are presented on Fig. 2.15 (a). The visco-elastic nature of polymer can be also noticed from the polymer deformation during the pause after total loading, while its visco-elasto-plastic behavior is seen from the large hysteresis loop of loading-unloading. We observe, that under the applied force of 10 mN, the measured penetration depth in pure epoxy is

about 1500 nm. These measurements, treated by the Oliver and Pharr method [78], give an elastic modulus of 4.5 ± 0.1 GPa and a hardness of 256.7 ± 8 MPa.

The points of indentation into CFRE composite material are marked by red numbers on the microscopic image of the examined area in Fig. 2.14(b). The minimal distance between the indentations is 20 μm. Fig. 2.15 (b) and (c) present the curves for indentations into epoxy matrix and a carbon fibre, respectively. The behavior of epoxy matrix is similar to that of pure epoxy. The larger dispersion is explained by a closeness of carbon fibres beneath the surface to indentation points, which influences the measurement. The elastic modulus of 6 ± 0.4 GPa and the hardness of 241.2 ± 42 MPa are found for epoxy matrix zone.

In contrast to epoxy, carbon fibre deformations are purely elastic. They demonstrate no hysteresis loop and a higher rigidity. In this case, the force of 10 mN causes a penetration depth of about 500 nm. The calculated transversal elastic modulus of carbon fibre is 20.7 ± 1.4 GPa, while its hardness is equal to 4401.4 ± 325.4 MPa. The values of hardness and elastic moduli of pure epoxy and epoxy matrix and carbon fibre of composite material are summarized in Table 2.9.

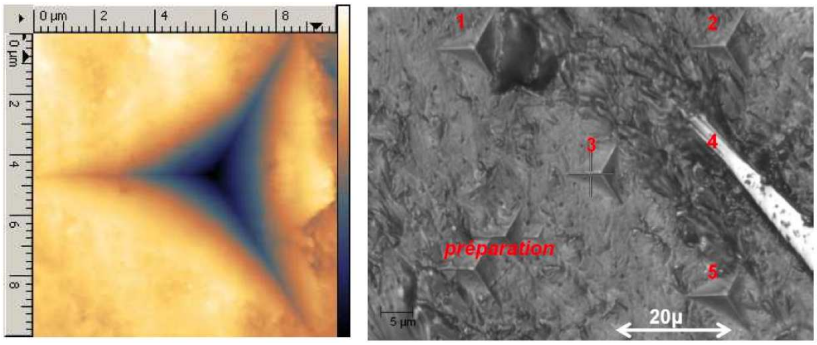

(a) **(b)**

Figure 2.14: Residual impressions after nanoindentation test on (a) pure epoxy and (b) carbon fibre-reinforced epoxy

Material	Hardness, MPa	Elastic modulus, GPa	Poisson's ratio
Pure epoxy	256.7 ± 8	4.5 ± 0.1	0.4
Epoxy matrix (composite)	241.2 ± 42	6 ± 0.4	0.3
Carbon fibre (composite)	4401.4 ± 325.4	20.7 ± 1.4	0.3

Table 2.9: Surface mechanical properties measured by nanoindentation and Poisson's ratios used for their calculation

The value of measured carbon fibre transverse modulus can be compared with the similar measurements of [63]. The authors performed nano indentations with a Berkovitch indenter by a dynamic/continuous stiffness measurement method with a frequency of 70 Hz. They tested three high modulus carbon fibre-reinforced epoxy composites, with the

longitudinal tensile modulus of fibres of 377, 436 and 640 GPa. SEM images of these fibres have been presented before, in Fig. 2.5. The measured transversal elastic moduli of these fibres are of 15 ± 4.9, 14 ± 5.7, 10.7 ± 3.1 GPa, respectively. Taking into account this dropping tendency of transversal modulus with an increase of longitudinal modulus, our value of 20 ± 1.4 GPa seems to be absolutely reasonable for carbon fibres of 231 GPa of longitudinal modulus. The same authors found a value of 4.5 ± 0.1 GPa for elastic modulus of epoxy matrix, which perfectly coincide with our value for pure epoxy, but is less than our value for epoxy matrix. As we said before, it must be due to a proximity of fibres beneath the epoxy surface.

2.3 Carbon nanopearl-reinforced epoxies (CNPRE)

This section focuses on carbon nanopearl-reinforced epoxy composites, their manufacturing and properties. Thus, it starts with a brief epoxy resin description, as this epoxy is not similar to that used for CFRE composites. Then, it presents the manufacturing method and a morphology of produced composite samples. It ends with surface characterization and observations of these composites.

2.3.1 *R&G Faserverbundwerkstoffe* epoxy resin

For manufacturing of these composite samples, we used R&G Faserverbundwerkstoffe GmbH epoxy resin L, a bisphenol A/F resin, and its hardener L, a modified cycloaliphatic polyamine. This hardener required processing time of 40 min at 20°C per 100 g of mixture, curing time for 1 mm laminate is 24 h at 20°C. Mixing ratio of hardener and resin is 40 : 100 by weight. The mechanical properties of epoxy resin cured for 7 days at room temperature, as provided in the data sheet, are given in Table 2.10.

Tensile strength, MPa	**Compressive strength,** MPa	**Tensile modulus,** GPa	**Flexural strength,** MPa
62	118	2.65	98
Heat distortion temperature, $°C$	**Elongation at break,** %	**Impact strength,** kJ/m^2	
65	4.5	25	

Table 2.10: Mechanical properties of cured epoxy resin R&G with hardener L (cured 7 days at room temperature) [79]

2.3.2 Composite manufacture method

The carbon nanopearl-reinforced composites are manually manufactured by moulding method. This process involves several stages: a design and fabrication of a mould and a fabrication of composite and epoxy specimens.

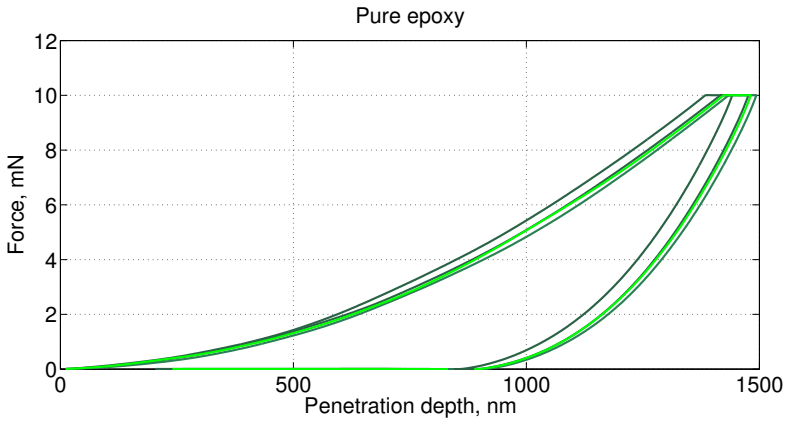

(a)

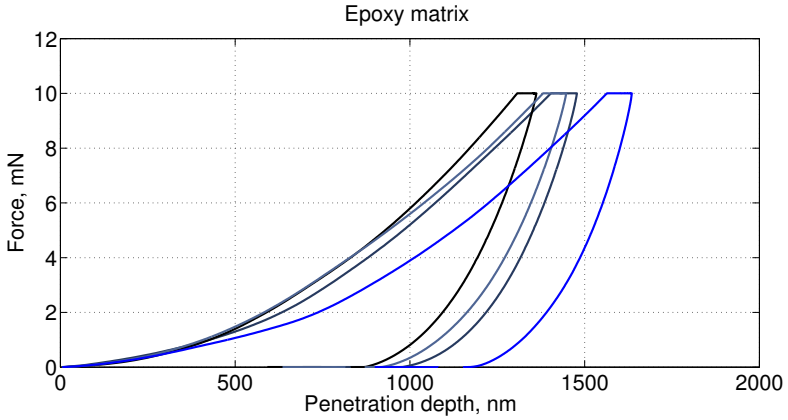

(b)

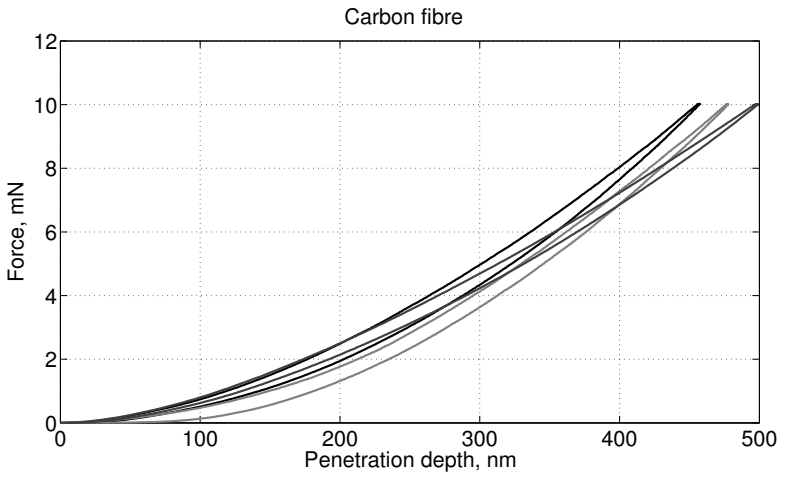

(c)

Figure 2.15: Compliance curves for (a) pure epoxy, (b) epoxy zone and (c) carbon fibre zone of CFRE 62% surface

The mould is produced from PolyDiMethylSiloxane (PDMS) produced by Sylgard company. PDMS is a transparent flexible silicon-based organic polymer, which needs a curing agent to cross-link. Fabrication process of PDMS mould is described in detail in Annex 2. The cured PDMS mould with inserted objects is presented in Fig. 2.16. This design of the mould permits us to produce two rectangular and three cylindrical specimens, simultaneously, in order to ensure a similar nanopearl concentration in both rubbed specimens and repeatability of the results.

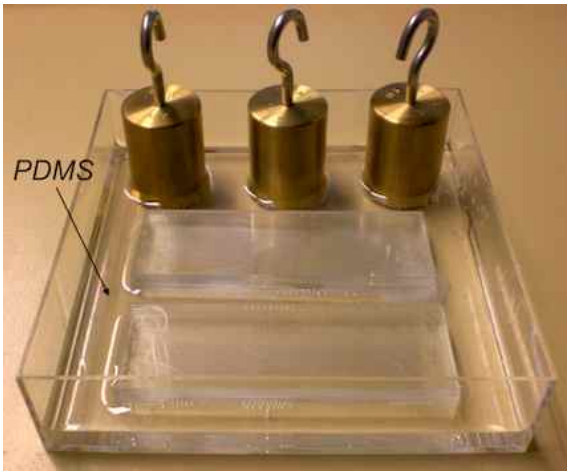

Figure 2.16: PDMS mould containing the objects to form the cavities for composite samples

Carbon nanopearl-reinforced epoxy composite of four CNP mass concentration and pure epoxy samples are manufactured by the similar technique in this mould. Mass concentration M_c of CNPs is calculated by $M_c = M_{CNP}/(M_{CNP} + M_{ep})$, where M_{CNP} and M_{ep} are the masses of CNPs and epoxy, respectively. Manufacture process for nanopearl-reinforced composites required similar facilities as for PDMS mould fabrication, and involves following steps:

1. Pour the epoxy resin into the plastic cup placed onto the balance;
2. Add the hardener in proportions for 100 parts of resin, 40 parts of hardener by weight and manually stir the mixture with the laboratory spatula for 3 minutes;
3. Add CNPs in a desirable mass proportion, stirring continuously the mixture for 5 minutes;
4. Pour the mixture of epoxy-nanopearls into the PDMS mould;
5. Put the mould into the desiccator, close it and connect to the vacuum pump. Leave to degas for 30 minutes;
6. Take out the mould from the desiccator and put it into the furnace at 60°C for 2 hours.

7. Take out the mould with cured samples from the furnace, let it cool down and carefully take out the samples.

The procedure of curing pure epoxy sample is identical to the described above, without CNP addition. The examples of freshly demoulded CNPRE composite samples with untreated surfaces are presented in Fig. 2.17.

(a) (b)

Figure 2.17: Freshly demoulded samples of CNPRE 1% composite. The samples of 15, 28 and 35 % are visually similar

2.3.3 Morphology of CNP-reinforced composites

Four composite materials with CNP mass concentrations of 1%, 15%, 28% and 35%, as well as pure epoxy samples, were produced. High porosity is observed for composites with CNP mass concentration more than 1%. Examples of composite surfaces are presented in Fig. 2.18. The porosity of composite surface is calculated by image treatment technique, using ImageJ software. As for carbon fibre-reinforced composites, the threshold of grey color on the surface is imposed and the percentage of black pixels, corresponding to the composite surface area, is calculated by the software.

Two examples of composite surface porosity, CNPRE 15% and CNPRE 28% surfaces, are given by SEM image in Fig. 2.19. The surfaces of these samples are also studied in high magnification (x23200) by SEM, see Fig. 2.20. The nanopearls are clearly distinguished on both surfaces, with an obvious prevalence of their fraction on the surface of CNPRE 28% sample. A sample of CNPRE 35% was cracked into two parts and covered by a thin gold layer in order to study the fracture. Fig. 2.21 presents a global view of this fracture, confirming a porosity of composite volume, and a high magnification (x20000) SEM image of this fracture. The spherical protuberances, corresponding to nanopearls, have diameter of $110 - 250$nm, which means that carbon nanopearls of 90 nm diameter are covered by epoxy layer (and this gold layer).

The density of carbon nanopearl-reinforced composites and pure epoxy are calculated from measured volume and mass of the manufactured samples and presented in Table 2.11.

2.3.4 Composite surface preparation, topography and observation

The rubbing surfaces of CNPRE composites were prepared by the similar grinding procedure as those of carbon fibre-reinforced composites.

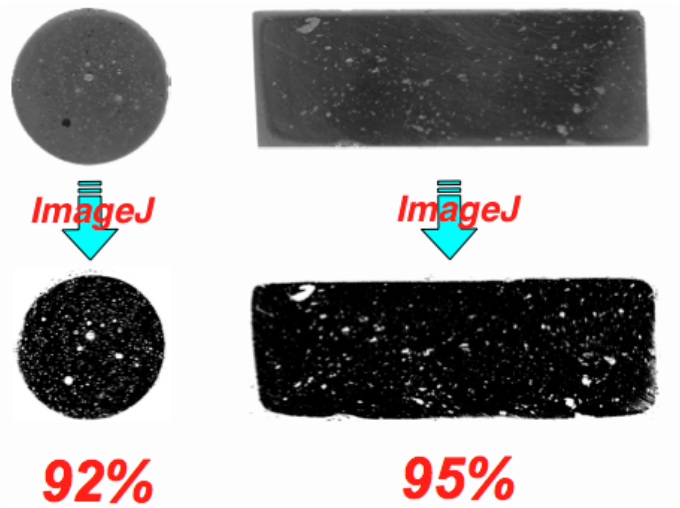

Figure 2.18: Surfaces of CNPRE 15% composite with surface area percentages, deduced by the image treatment technique

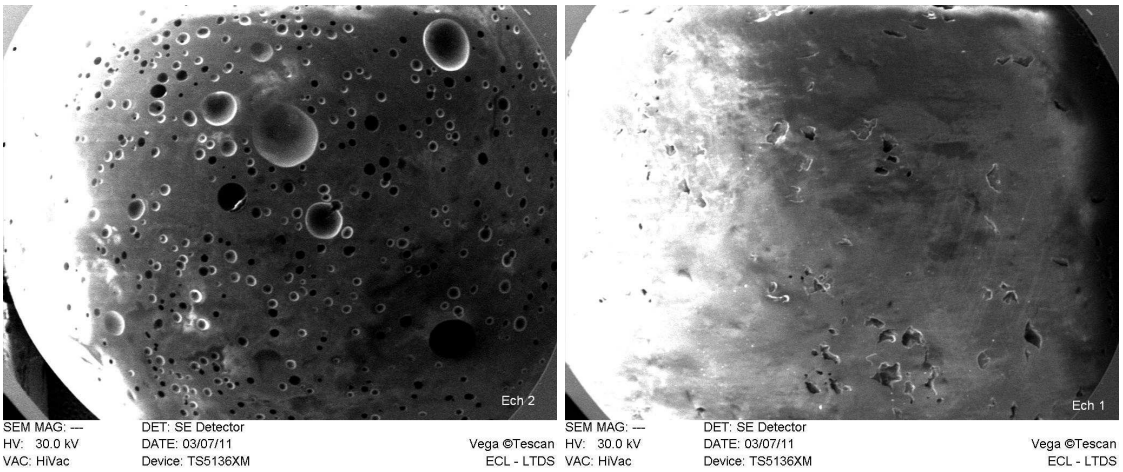

(a) **(b)**

Figure 2.19: Global views of (a) CNPRE 15% surface and (b) CNPRE 28% surface taken by scanning electron microscope

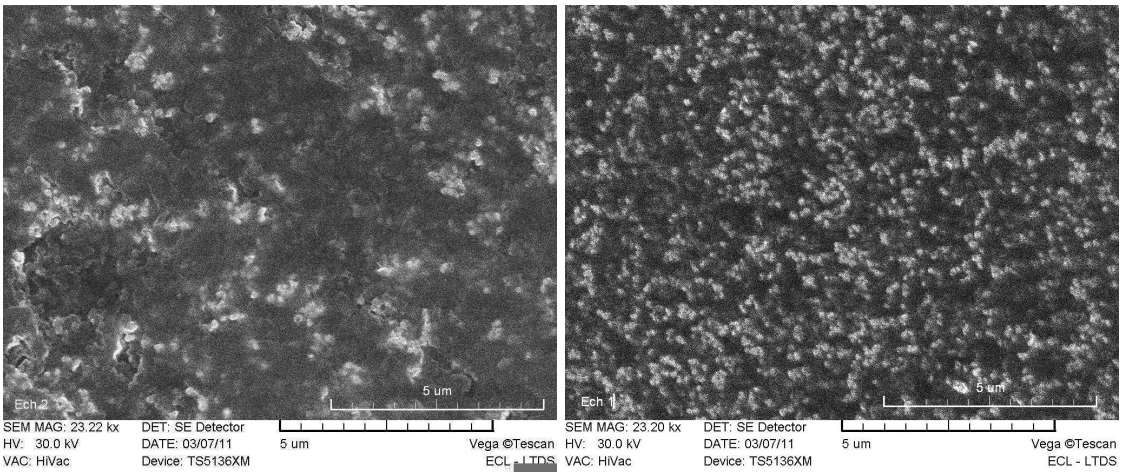

(a) **(b)**

Figure 2.20: High magnification (x23200) of (a) CNPRE 15% surface and (b) CNPRE 28% surface taken by scanning electron microscope

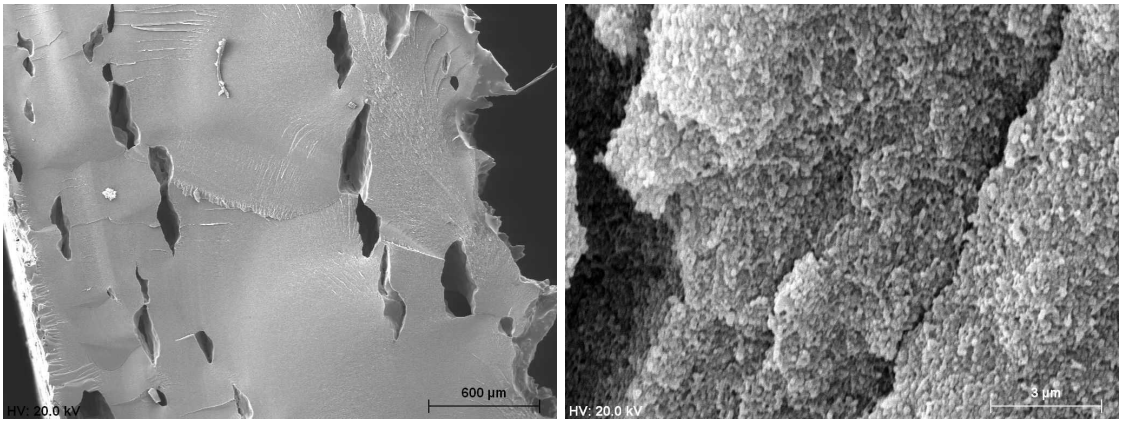

(a) **(b)**

Figure 2.21: (a) Global view of golden CNPRE 35% fracture and (b) high magnification (x20000) view of golden CNPRE 35% fracture taken by scanning electron microscope

Composite	**Average porosity, %**	**Volume,** cm^3	**Mass,** g	**Average density,** g/cm^3
Neat epoxy	0	5.73 (0.87)	6.49 (0.97)	1.12
CNPRE 1%	0	8.71 (1.50)	9.76 (1.68)	1.12
CNPRE 15%	5 (8)	7.17 (1.40)	8.24 (1.70)	1.18
CNPRE 28%	5 (10)	6.84 (1.65)	8.29 (2.20)	1.27
CNPRE 35%	3 (13)	7.23 (1.54)	9.99 (2.24)	1.42

Table 2.11: Measured volume and mass of carbon nanopearl-reinforced and neat epoxy tracks (and sliders) and calculated average composites densities

CNPRE with carbon nanopearl content higher than 1% present high level of porosity, which makes impossible and useless the surface profile measurements and calculation of topographic characteristics. However, CNPRE 1% composite is relatively even and homogeneous at microscopic scale. Therefore, as for pure epoxy, several individual profiles taken in different surface areas are more representative of the surface statistic, than a local surface map. Fig. 2.22 presents an example of the measured profile of CNPRE 1% sample, while its roughness and waviness characteristics are presented in Table 2.12.

Rq, μm	***Rsk***	***Rku***	***Wq***, μm	***Wsk***	***Wku***
0.07 ± 0.001	2.36 ± 1.266	24.82 ± 14.06	0.23 ± 0.030	1.26 ± 2.166	11.24 ± 10.75

Table 2.12: Surface characteristics of CNPRE 1% track sample based on 3 measurements for each material type (ISO4287)

Figure 2.22: Typical example of surface profile of CNPRE 1% composite

2.4 Synthesis

To conclude this chapter, we will summarize the main characteristics and properties of composite materials presented before. Their main points of difference and similarity are presented in Table 2.13.

Composite	**CFRE**	**CNPRE**
Matrix material	Epoxy	Epoxy
Carbon filler	Fibre	Nanopearl
Atomic structure of filler	Turbostratic graphene planes around amorphous center	Turbostratic graphene planes around amorphous core
Filler shape	Long cylinder	Aggregate of spherical particles
Characteristic size of filler	$\varnothing$ 7 μm Length: some mm−m	Particle: $\varnothing$ 90 nm Agregates length: μm−mm
Filler concentration	34, 52, 62 % in volume	1, 15, 28, 35 % in mass
Anisotropy	Anisotropic	Isotropic
Surface state	CFRE 34, 52 %: heterogeneous CFRE 62%: homogeneous, but rough ($R_q = 0.53\mu$m)	CNPRE 15, 28, 35 %: porous CNPRE 1%: smooth ($R_q = 0.07\mu$m)
Hardness	$H_{CF} \approx 4400$ MPa, $H_{ep} \approx 240$MPa	–
Elastic modulus	$E_{CF} \approx 20.7$ GPa, $E_{ep} \approx 6$ GPa	–

Table 2.13: Main differences and similarities of CFRE and CNPRE composites

Chapter 3

Interfacial frictional dissipation: experimental study

As it was shown in Chapter 1, interfacial and bulk zones of frictional dissipation in polymers are distinguished. However, the interfacial friction component is independent on the mechanical properties of composite [80]. It takes place at the composite surface and is determined by the interfacial shear stress. In this context, the term 'surface' means a layer of $10 - 100$ nm, as it consists in various composite phases.

This chapter presents an experimental study of interfacial friction carried out on carbon fibre–reinforced epoxy and carbon nanopearl-reinforced epoxy composites, as well as pure epoxy, described in Chapter 2. The key condition for such a study is an absence of surface damage. This can be reached by applying low pressures, which means a use of large surfaces and low normal loads. Presented in Chapter 1 literature review on carbon-fibre-reinforced epoxy friction reveals that it is sensible to many factors. However, the general tendencies are not clear and change from one experiment to another. Moreover, neither frictional behavior between two composites has been studied enough, nor the aspect of interfacial friction of composites has been evaluated. Therefore, a preliminary study of normal load and sliding velocity effect was carried out in order to establish sliding conditions preventing surface damage. The aim of this chapter is to analyze experimentally how the fillers contribute to interfacial friction of the polymer matrix. This analysis will be performed by variation of filler content in two composite types. Along with the filler concentration, the effect of fibre orientation will be studied for carbon fibre-reinforced epoxy.

Contents

3.1 Friction at the macroscale

3.1.1 Description of experimental set-up

The experiments presented in this section are carried out on the tribometer RA, shown in Fig. 3.1 and developed in LTDS. It is capable to perform a reciprocating sliding between two plane samples of relatively large surfaces under low loads.

One sample, a track, is glued onto the base plane of the tribometer. The second sample, a slider, slips over the track, its in-plane motion is restricted by a sample holder mounted in a moving part of the tribometer. A brushless servomotor provides the alternative motion of the slider by pushing and pulling it. The rotating velocity of the motor is measured by a decoder and is maintained constant by a feedback loop with electrical variator. The linear sliding velocity varies from few μm/s to approximately 2 m/s. Maximal sliding distance can reach 500 mm.

Device	**Name**	**Principal features**
Brushless servomotor with electrical variator	Danaher AKM22C Servostar 300	Nominal power: 0.57 kW, nominal speed: 8000 min^{-1}, accuracy of the variator: 1 %
Piezoelectric sensor	KISTLER Type 9217A	Stiffness: ≈ 15 N/μm, force range: $-50 - 50$ N, sensitivity: ≈ -98.5 pC/N
Charge amplifier	KISTLER Type 5018A	gain: 5 N/V in the force range $-50 - 50$ N

Table 3.1: List of the tribometer RA components

The normal force is applied by means of a weight put onto the slider and varies from sample weight to approximately 20 N. The tangential, friction force induced by sliding is continuously measured with a piezoelectric sensor mounted in the moving part. A signal from the sensor is amplified by a charge amplifier and interpreted by a data acquisition card of a PC. The list of the commercial components of the tribometer with their principal features is given in Table 3.1.

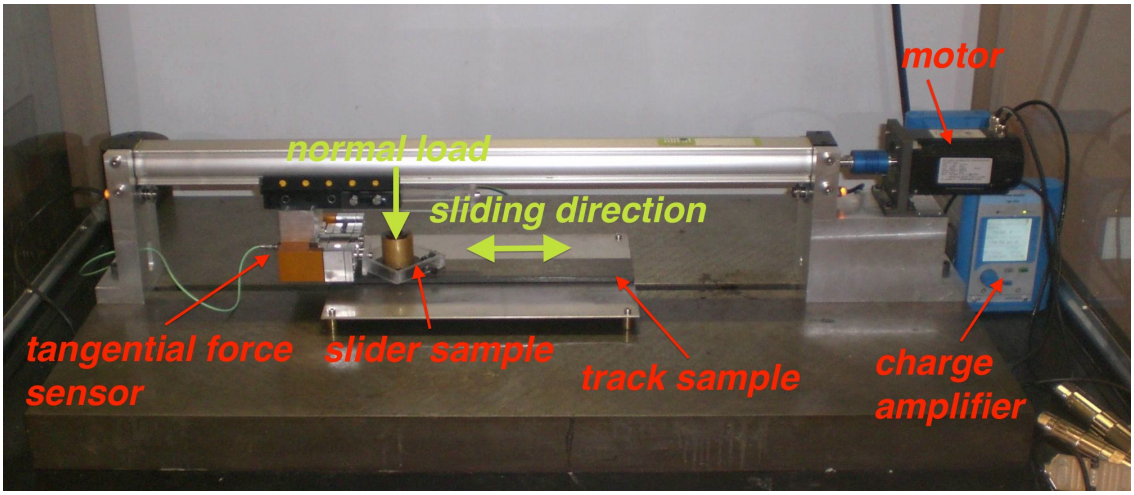

Figure 3.1: The tribometer *RA*

3.1.2 Samples and experimental protocol

The samples, sliders and tracks, of relatively large surfaces were manufactured from all materials presented in Chapter 2 in order to ensure low contact pressure. The rectangular track samples have the dimensions of $80 \pm 2 \times 25 \pm 2 \times 5 \pm 1$ mm^3. The sliders were designed circular, to allow a variation of fibre orientation in carbon fibre–reinforced epoxy. The diameter of their rubbing surface is $\varnothing 20$ mm and their height is 5 ± 1 mm. Thus, the apparent contact area for all experiments is equal to 314 mm^2.

All the samples were polished by the similar procedure described in Chapter 2. Due to the diversity of reinforcing materials and their concentrations, roughness of the composite rubbing surfaces varies from one material to another. The mean roughness characteristics with standard deviations are given in Chapter 2. Before each experiment both surfaces are carefully cleaned with heptane, acetone and propanol-2 successively and finally with a flow of nitrogen. The experiments are carried out under unlubricated conditions in the ambient environment. The ambient humidity ($RH \approx 50 - 60\%$) and room temperature ($T \approx 20 - 25^\circ$ C) are measured during each experiment.

The experiment represents a sequence of reciprocating slips of the slider over the fixed track. The number of passes during one experiment is 50 (the number of cycles is 25). Frictional force is measured continuously during the whole experiment and is recorded into PC memory with the sampling frequency of signal acquisition of 1 kHz, similar for all experiments. The mean friction force is supposed to be equal for two passes of each cycle. Thus, the origin is calculated for each cycle as the mean value between two passes. The sample holder was designed in such a way, that the slider is not strictly fixed, but is rather free and pushed and pulled by sample holder walls. That is why, the friction force signal during each pass is cut off from both ends by 20% and averaged in order to calculate the mean kinetic friction coefficient. It is defined as the ratio of the mean tangential force and a constant normal force for each cycle.

The experiments with CFRE/CFRE, CFRE/epoxy and CNPRE/CNPRE couples were

carried out. The first cycles of sliding for CFRE/CFRE and CNPRE/CNPRE (blue and red curves) with epoxy/epoxy (black curve) as reference under normal load of 2 N and sliding velocity of 10 mm/s are presented respectively in Fig. 3.2(a, b). It is seen from Fig. 3.2(a), that there is a variation of friction force during each pass for epoxy/epoxy couple, while CFRE/CFRE friction is very stable. These variations are observed during all cycles. The friction force of CNPRE/CNPRE couples varies even more, see Fig. 3.2(b), while the friction curve of epoxy/epoxy couple seems to be rather smooth at this scale. Moreover, friction instabilities, which might be related to CNPRE/CNPRE contact stiffness, were often detected during the experiments. The real nature of these instabilities is unknown, but we observe that they are not correlated to surface roughness. Nevertheless, the core of this study lies in a variation of the mean kinetic friction coefficient, which seems slightly affected by this phenomena.

3.1.3 Repeatability of results

The evolution of friction coefficient with time and the repeatability of the results differ depending on the material couples. The scatter of the mean kinetic friction coefficients per cycle for several tests for CFRE 62%/CFRE 62% is presented in Fig. 3.3(a). One can notice, that the friction coefficient of CFRE 62%/CFRE 62% is rather stable for all cycles and varies slightly between the tests. Moreover, similar behavior is observed for all tribological conditions. However, all other pairs - CFRE/CFRE with different fibre volume fraction, CFRE/epoxy, epoxy/epoxy and CNPRE/CNPRE - demonstrate a great dispersion during one test and between several tests. For example, the scatters of mean kinetic friction coefficients per cycle for several tests for epoxy/epoxy and CFRE 62%/epoxy are presented respectively in Fig. 3.3(b, c). This dispersion raises with a severity of the tribological conditions, obviously because of surface damage.

3.1.4 Choice of tribological conditions of interfacial friction

The severity of tribological conditions usually increases a probability of surface damage and wear for any material. It should be reminded, that wearless conditions have to be respected in this experimental study in order to investigate the interfacial friction of composites. High load and low sliding speed favor the formation of junctions between two surfaces, which causes surface damage at the beginning of sliding. On the other hand, low load, as well as high sliding velocity, applied to large surfaces, leads to very small real contact area with short contact life-time and underestimated contact pressure. Moreover, high velocity can cause thermal effects. In order to find a compromise, several tribological conditions are tested and the surfaces of both samples are observed after each experiment aiming to detect possible damage.

3.1.4.1 Epoxy/epoxy contact

An example of friction coefficient increase during one test under the normal load of 10 N, which illustrates a wear influence on epoxy/epoxy friction, is shown in Fig. 3.4. It is clear that this load is too high to study interfacial friction. Inter alia, the friction coefficient of

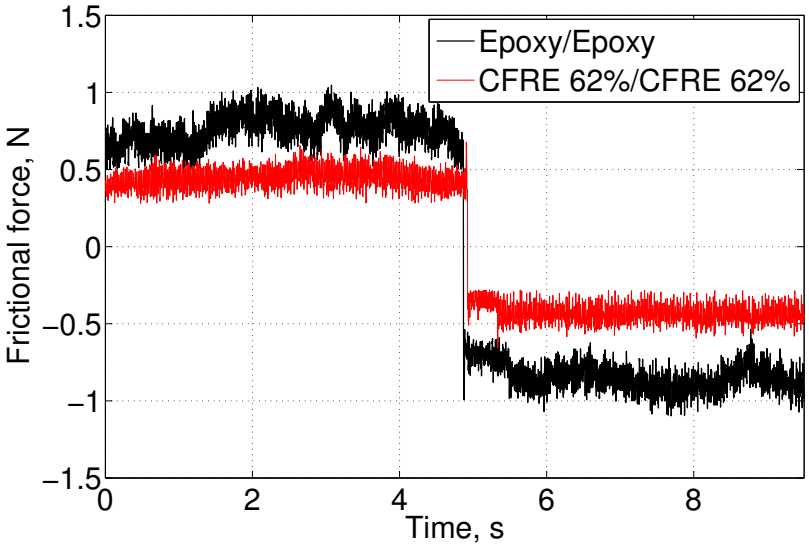

(a)

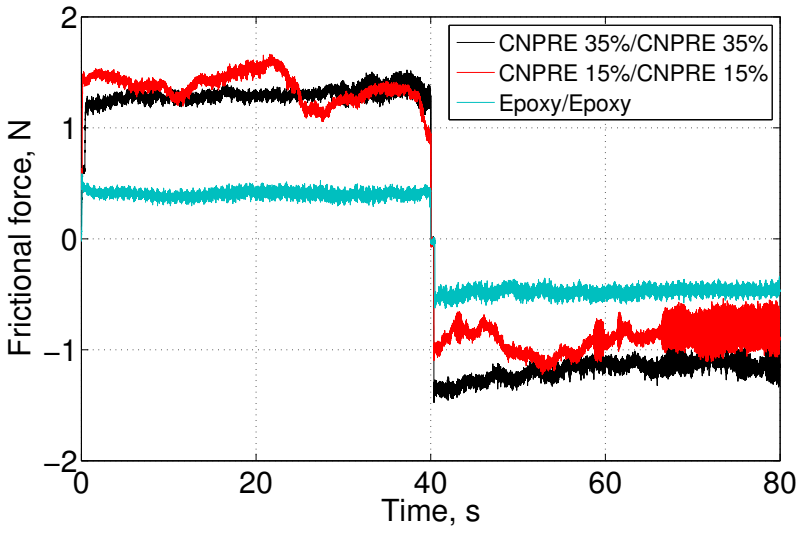

(b)

Figure 3.2: Measured frictional force during first cycle for (a) carbon fibre-reinforced composites and (b) carbon nanopearl-reinforced composites ($N = 2$ N; $V = 10$ mm/s)

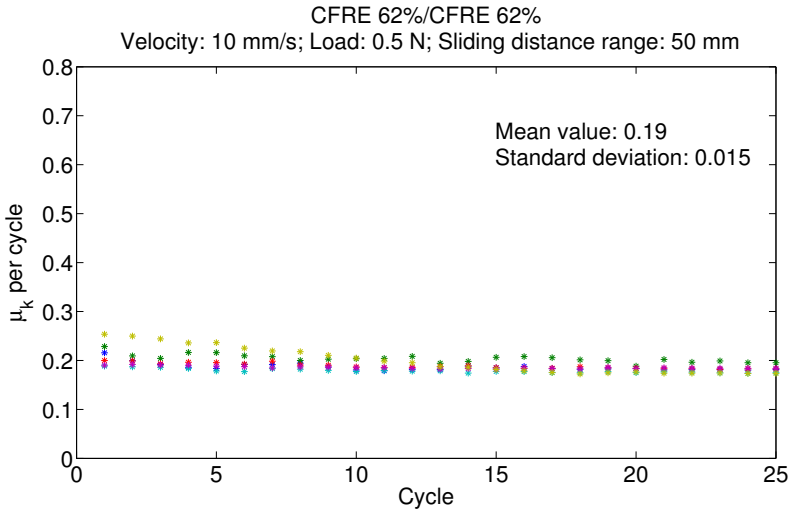

(a)

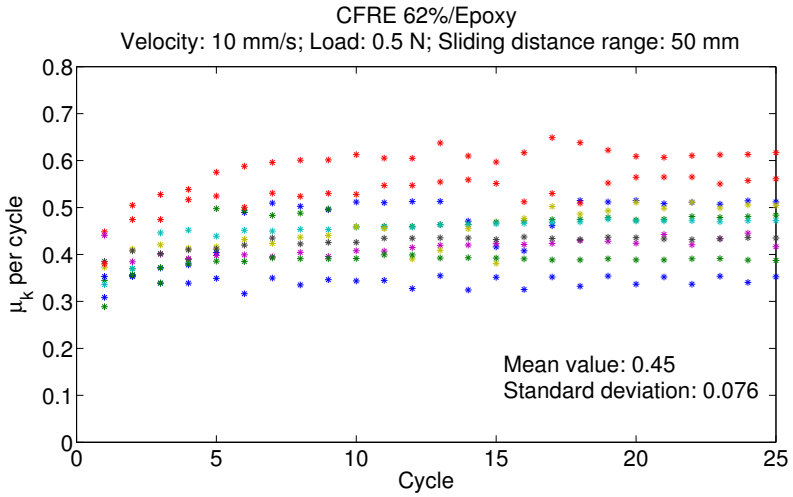

(b)

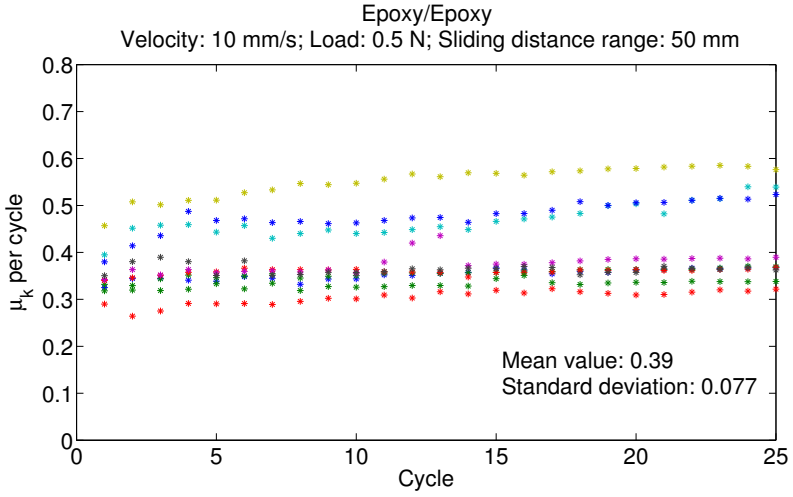

(c)

Figure 3.3: Scatter of mean kinetic friction coefficients for (a) CFRE 62%/CFRE 62%, (b) CFRE 62%/epoxy and (c) epoxy/epoxy (contact pressure $p = 1.6$ kPa; $V = 10$ mm/s). Several tests are presented by different colors

this couple behaves exactly as other polymer couples described in Ch. 1, Sec. (Polymer friction and wear). It exhibits running-in stage, characterized by the increase of wear rate and friction coefficient, which is followed by a period of relatively stable high friction and low wear rate. A verification of possible further increase of wear rate and friction coefficient, predicted by other authors, is not the aim of this experimental study. A detailed experimental study of friction and wear of epoxy couples under severe tribological conditions will be presented in Chapter 5.

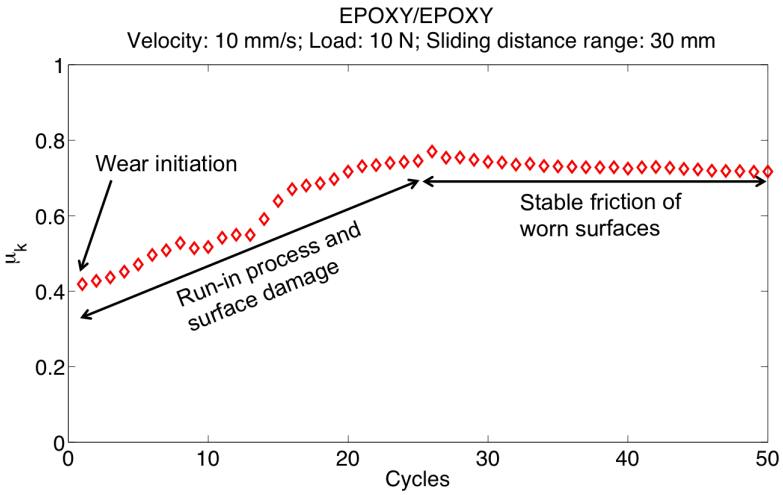

Figure 3.4: Evolution of the kinetic friction coefficient for epoxy/epoxy couple under normal load of 10 N and sliding speed of 10 mm/s

The dependence of the mean kinetic friction coefficient on the normal load in the range of $0.1 - 2$ N, which corresponds to the apparent contact pressure of $0.32 - 6.43$ kPa, is presented in Fig. 3.5(a). It is observed, that friction increases more than two times in this range of forces. It rises dramatically between 0.2 and 0.5 N, probably because of the effect of an expansion of the real contact area, discussed before. Wear of epoxy surfaces is observed under normal loads higher than 2 N. The values of friction coefficients for epoxy/epoxy in this load range are given in Table 2, Annex 1.

The effect of sliding speed on mean kinetic friction coefficient is presented in Fig. 3.5(b). In the range of $1 - 40$ mm/s, the dispersion between the experiments is rather large, but the general tendency is a light diminution of friction with an increase of sliding speed. This tendency can also be explained by the decrease of real contact area with the sliding speed growth. Table 3 of Annex 1 gives the values of friction coefficients for epoxy/epoxy in this sliding speed range.

3.1.4.2 Carbon fibre-reinforced epoxy couples

The similar ranges of sliding speed and normal load are tested on CFRE/CFRE of different fibre contents. The values of mean friction coefficients are presented in Tables 2 and 3 of Annex 1 and plotted in Fig. 3.6(a,b). A light decrease of friction coefficient under higher loads could be explained by the wear of a small amount of epoxy matrix, and the fact that

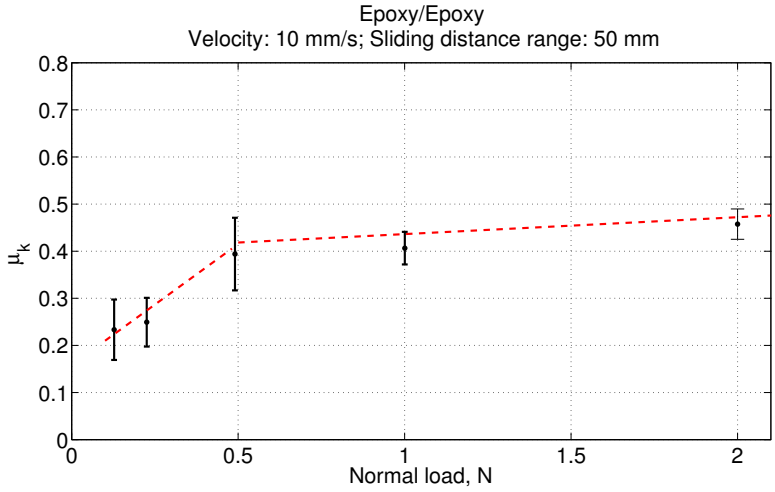

(a)

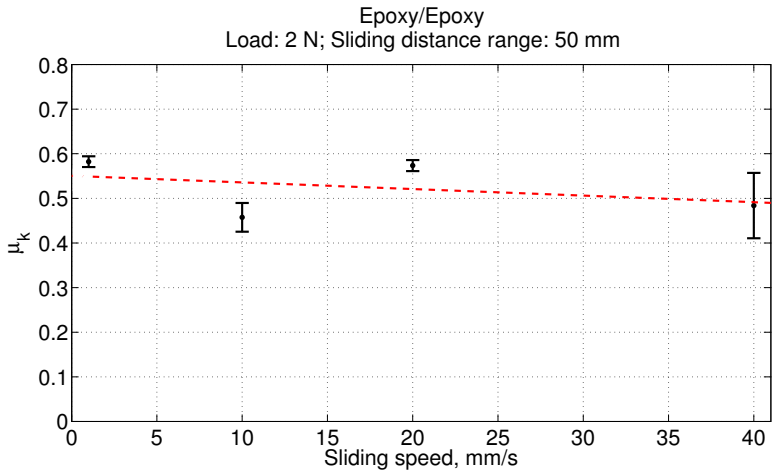

(b)

Figure 3.5: Effect of normal load and sliding velocity on mean kinetic friction coefficient of epoxy/epoxy couple

more fibres are then in contact area.

However, this decrease is rather small and we can consider, that for CFRE 62%/CFRE 62% couple the mean kinetic friction coefficient is independent on both normal load, and sliding speed in the examined ranges. The behavior of CFRE 34%/CFRE 34% and CFRE 52%/CFRE 52% couples is also tested and shows an independence on sliding speed, see Table 3, Annex 1.

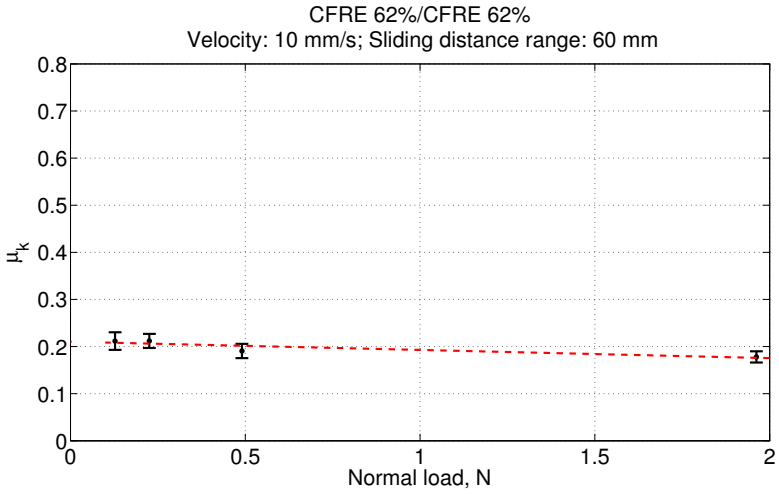

(a)

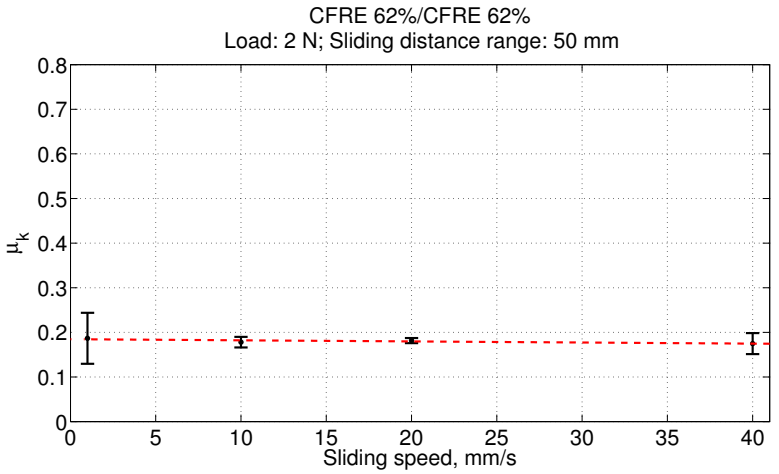

(b)

Figure 3.6: Effect of normal load and sliding speed on friction of CFRE 62%/CFRE 62%

The observed indifference of CFRE interfacial friction under the examined tribological conditions means that, in these composite materials, the reinforcement plays a key role:

- because of its rigidity, the normal loads are not too high and sliding speeds are not too low to change real contact area;
- even if epoxy matrix is worn out, carbon fibres remain in the contact zone, and their friction is low.

3.1.4.3 Carbon nanopearl-reinforced epoxy couples

The effects of normal load and sliding speed on friction coefficient of CNPRE 1%/CNPRE 1% couple, as an example of carbon nanopearl-reinforced composite, are presented in Fig. 3.7(a,b), respectively. The increase of friction coefficient with normal load and its decrease with sliding speed are coherent with the behavior of epoxy/epoxy couple. The level of friction is larger than observed with epoxy/epoxy and CFRE/CFRE. Moreover, as well as for epoxy/epoxy couple, a surface damage and wear are observed under higher loads. This can be explained by the fact, that even if nanoparticles are as rigid as carbon fibres, their size is too small, that they are worn from the surface with epoxy matrix. Therefore, they are incapable to increase the wear resistance of epoxy.

More experimental results of sliding speed effect on friction coefficient for carbon nanopearl-reinforced epoxies of different nanopearl content couples with a comparison with epoxy/epoxy friction are presented in Table 5 of Annex 1. The main tendency is a decrease of friction coefficient for higher speeds for all nanopearl-reinforced composites. This decrease is observed also for epoxy/epoxy friction but for this couple the slope is significantly smaller.

We can notice, that carbon nanopearl-reinforced epoxy is very similar to pure epoxy in its frictional behavior under light tribological conditions. However, this is not the case for carbon fibre-reinforced epoxy, which shows very different friction values and tendencies.

3.1.4.4 Choice of the tribological conditions favorable for interfacial friction study

Based on this investigation of tribological conditions effect on composites and epoxy friction, the conditions favorable to the interfacial friction study of carbon fibre or carbon nanopearl-reinforced epoxies are chosen and reported in Table 3.2. The lower normal loads are recommended for epoxy-involved couples (0.5 N) and carbon nanopearl-reinforced epoxy couples (1 N), while the normal load of 2 N is chosen for CFRE/CFRE couples. The sliding speed of 10 mm/s is similar for the tests on all composite and epoxy couples. These conditions permit us, on the one hand, to minimize the surface damage and wear and, on the other hand, to ensure a relatively large contact area and to estimate the contact pressure more accurately.

	CFRE/epoxy	**CFRE/CFRE**	**CNPRE/CNPRE**
Sliding speed, mm/s	10	10	10
Normal load, N	0.5	2	1
Apparent contact pressure, kPa	1.59	6.37	3.18

Table 3.2: Conditions for interfacial friction study

The following experimental results are obtained under these conditions.

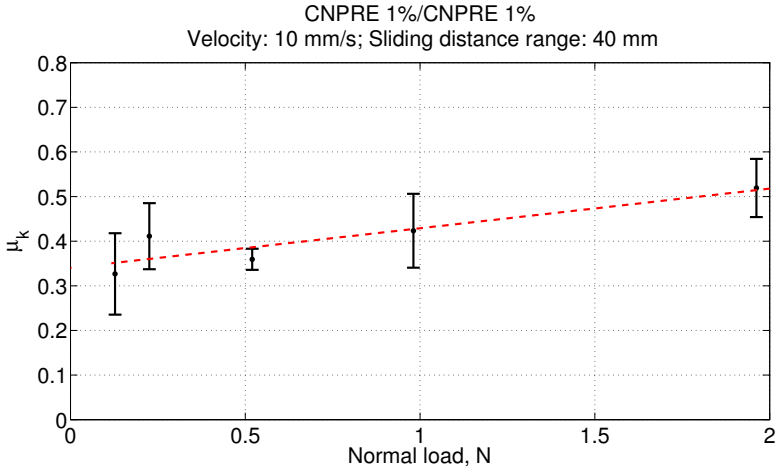

(a)

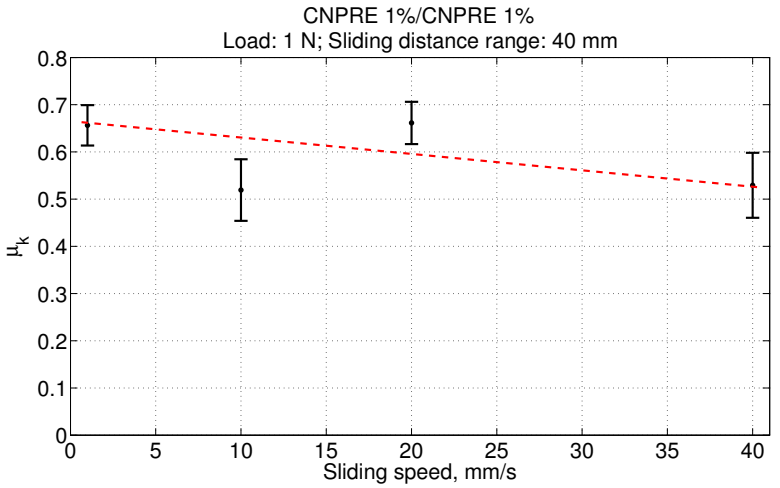

(b)

Figure 3.7: Effect of (a) normal load and (b) sliding speed on friction of CNPRE 1%/CNPRE 1%

3.1.5 Filler contribution to the friction of epoxy composites

3.1.5.1 Carbon fibre volume fraction effect

Reinforcement effect of carbon fibre-reinforced epoxy composites on friction is studied in two configurations: epoxy/CFRE and CFRE/CFRE. The mean kinetic friction coefficients of epoxy/CFRE couples are presented in Fig. 3.8(a). For this contact configuration, the increase of fibre volume content induces an increase of friction coefficient relative to epoxy/epoxy friction, although the difference between the friction coefficients of 34 %, 52 % and 62 % of fibre volume content composites is not appreciable.

Roughly comparing our CFRE/epoxy couples results with published friction coefficients of CFRE/steel couples [28, 46, 81], see Table 3.3, we observe that the tendencies are opposite. This must be due to the severity of sliding conditions and contact pressure, which are higher than these that we used in our interfacial friction study. Along with the hardness of counterface material, they cause surface damage and wear, which modify friction coefficient.

	Sliding speed, mm/s	**Pressure,** kPa	**Carbon fibre volume fraction**	**Friction coefficient**
CFRE/epoxy	10	1.59	0	0.39
			0.34	0.44
			0.52	0.42
			0.62	0.45
CFRE/steel [28]	60	3400	0.67	0.28
			0.82	0.24
CFRE/steel [46, 81]	0.025	193500	0	0.3
			0.40	0.17
			0.50	0.15
			0.68	0.12

Table 3.3: A comparison of CFRE/epoxy couples and CFRE/steel couples [28, 46, 81] frictional behavior

The behavior of friction coefficient of CFRE/CFRE couples compared to that of epoxy/epoxy friction is completely different, see Fig. 3.8 (b). An addition of carbon fibres into both contacting polymers reduces the mean kinetic friction coefficient in more than two times. The lowest friction coefficient is observed for the couple of CFRE 52%/CFRE 52%. However, as in the case of epoxy/CFRE, the friction coefficients between CFRE 34%/CFRE 34%, CFRE 52%/CFRE 52% and CFRE 62%/CFRE 62% differs only slightly.

3.1.5.2 Carbon nanopearl mass content effect

In contrast with the carbon fibre reducing friction effect on epoxy, carbon nanopearls increase the kinetic friction coefficient of epoxy, see Fig. 3.8(c). This friction coefficient rises gradually for all carbon nanopearl composites from CNPRE 1%/CNPRE 1% to CNPRE 35%/CNPRE 35% and reach the value of one and a half of epoxy/epoxy friction

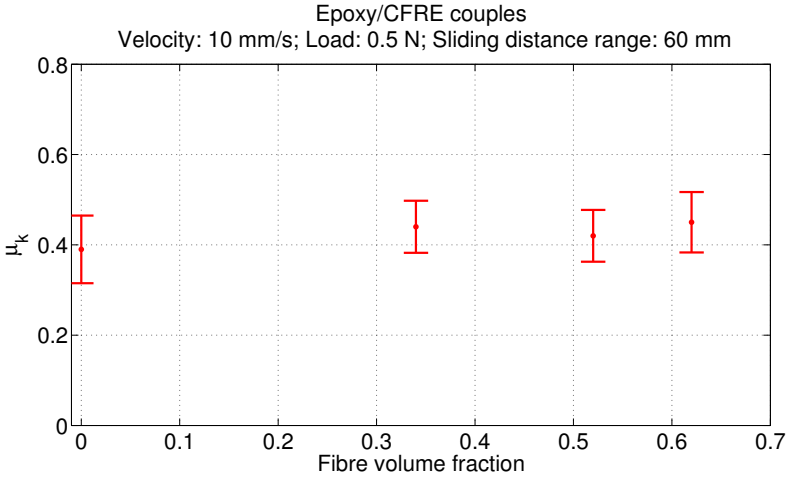

(a)

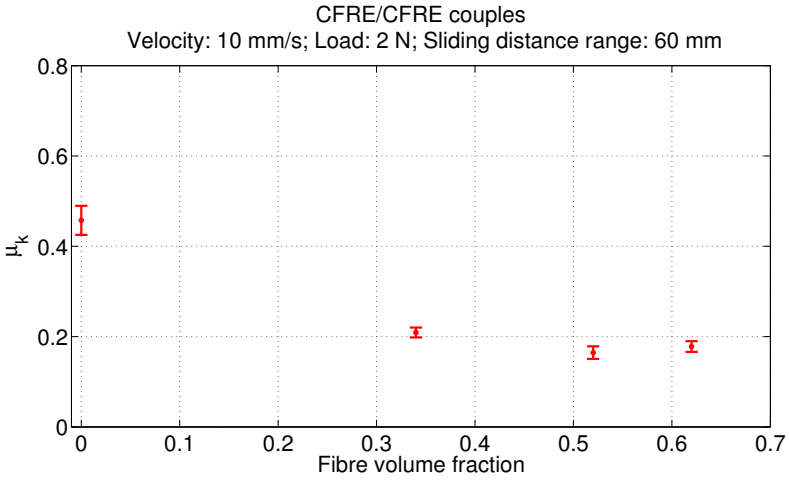

(b)

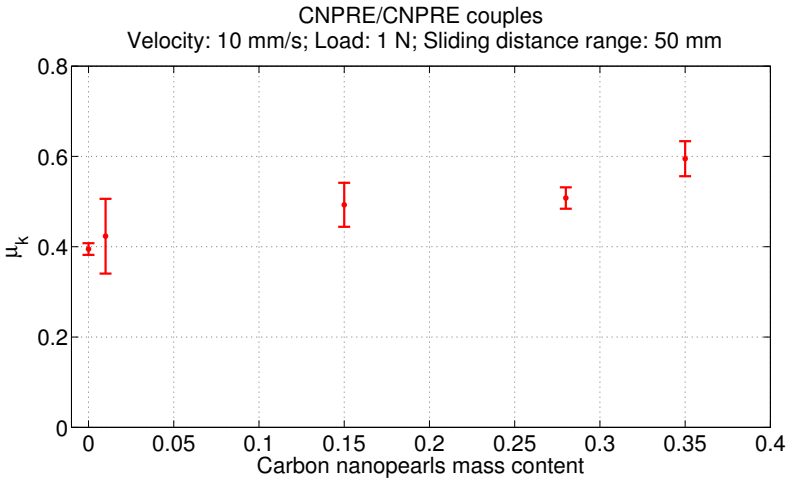

(c)

Figure 3.8: Reinforcement effect on kinetic friction coefficient of epoxy composites: (a) carbon fibre volume fraction for epoxy/CFRE couples; (b) carbon fibre volume fraction for CFRE/CFRE couples; (c) carbon nanopearl mass content for CNPRE/CNPRE couples

coefficient.

We can suppose that after the polishing of composite surface, the nanopearls are cut and can be depicted as in Fig. 2.7 (a) of Chapter 2. In this case, the planes of graphite are oriented perpendicularly to the rubbing surface and jam in sliding contact with the counterface. They may plough a soft epoxy surface, which induces a higher friction force. This effect should be more remarkable in the contact between two cut nanopearls. Thus, the coefficient of friction between two nanopearls is expected to be relatively high.

3.1.5.3 Fibres orientation effect

Along with the reinforcement content effect, the fibre orientation effect is studied for carbon fibre-reinforced epoxy. These tests are realized for CFRE 62%/CFRE 62% configuration under a normal load of 0.5 N and a sliding speed of 10 mm/s. The track samples of 0°, 45° and 90° fibre orientations relative to the velocity vector are used. Furthermore, the circular slider is also rotated in order to vary the total orientation angle. The total orientation angle φ is defined as a sum of two angles between the fibre orientation in each sample and the velocity vector. Therefore, this angle, shown schematically in Fig. 3.9, varies from 0°, when the fibres of two samples are oriented parallel to the sliding direction, to 180°, when both are perpendicular to the sliding direction.

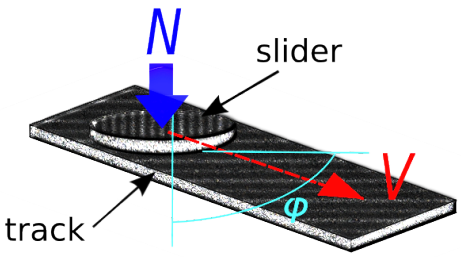

Figure 3.9: Total fibre orientation angle φ between two CFRE samples

Under the light contact pressure of 1.59 kPa, the mean friction coefficient changes slightly: from 0.17 to 0.18, see Fig. 3.10, as a function of the fibre orientation. The greater dispersion of the friction coefficient for φ higher than 0° can be related to the roughness of track samples. Unidirectional fibre-reinforced composite is rougher in the non-parallel to fibre orientation directions. Therefore, when track fibre orientation is different from parallel (90° or 45°), the slider has to overcome higher asperities, leading to a higher friction coefficient. However, under interfacial friction conditions, this effect is not very significant, as $\Delta\mu \approx 0.01$.

3.2 Friction at the microscale

Besides general friction coefficients between composite materials and epoxy, the local friction coefficients are also investigated in this work. This means measurement of friction between two carbon fibre specimens and between carbon fibre and pure epoxy in order

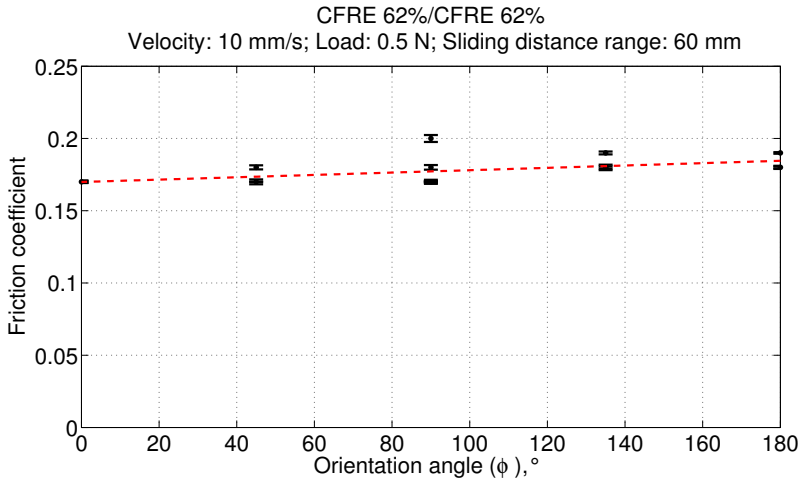

Figure 3.10: Effect of the total fibre orientation angle φ on the mean kinetic friction coefficient

to obtain frictional coefficients of these couples. These experiments are carried out by Dr Anne Rubin of Institut Charles Sadron (ICS), Strasbourg, France.

3.2.1 Experimental setup, protocol and samples

The frictional experiments are carried out on a nano-scratch apparatus from CSM Instruments ®. The spherical glass indentor of millimetric radius $R = 25$ mm is used to rub over the fixed sample, as it is shown in Fig. 3.11. Due to its orientation on nanoscratching, the apparatus can perform sliding passage at nano and micrometer scale and to measure accurately friction and normal forces during the passage. A small contact area of sphere/ plane configuration along with low normal force can give the resulting mean pressure of $0.05 - 2$ MPa. The sliding speed of $V = 30$ μm/s and normal load in the range of $1 - 50$ mN, with the successive steps of 2 mN between 1 and 20 mN and of 5 mN between 20 and 50 mN, are applied in our frictional experiments. The ambient environment $T \approx 25°$, $RH \approx 45\%$ is measured.

Two materials, pure epoxy and carbon fibre, are tested. Firstly, the glass spherical slider is covered with carbon fibres, as shown in Fig. 3.12 (a). The fibres are fixed with a tape attached to the lateral sides of the slider. This carbon fibre slider rubs against the cylindrical pure epoxy sample, used as a slider in the experiments described in the previous section, and against the carbon fibre lock glued to a glass plane, see Fig. 3.12 (b). Both plane samples are fixed on the apparatus base plane. Parallel and perpendicular orientations between two fibre specimens are tested.

3.2.2 Results

The friction force is rather stable during an experiment over a sliding distance of 600 μm. This permits us to calculate the mean friction coefficients for each tested normal load,

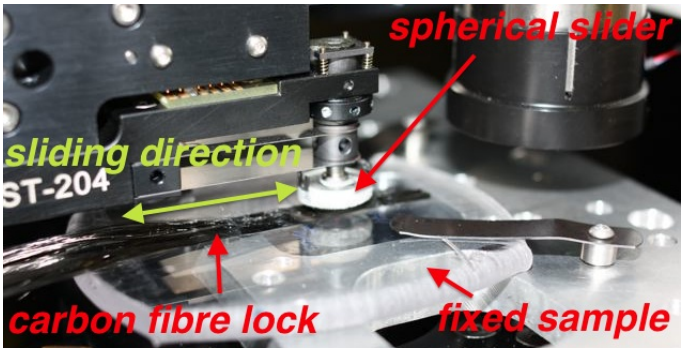

Figure 3.11: View of the nano-scratch apparatus operational zone (by courtesy of Dr Anne Rubin, ICS, Strasbourg)

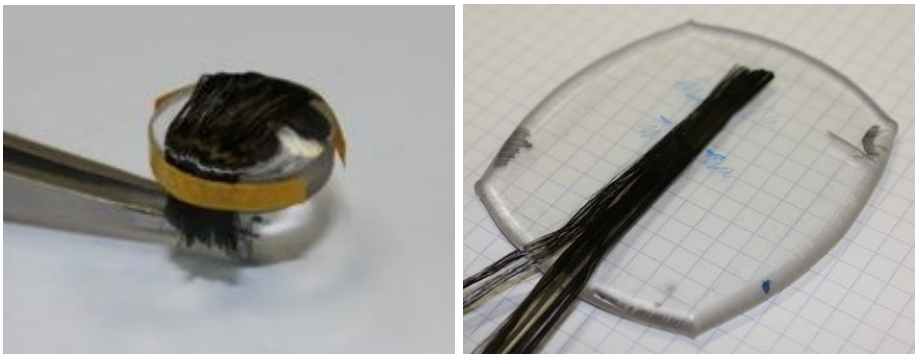

(a) **(b)**

Figure 3.12: Carbon fibre lock (a) Attached to the sphere slider; (b) Glued onto the glass plane (by courtesy of Dr Anne Rubin, ICS, Strasbourg)

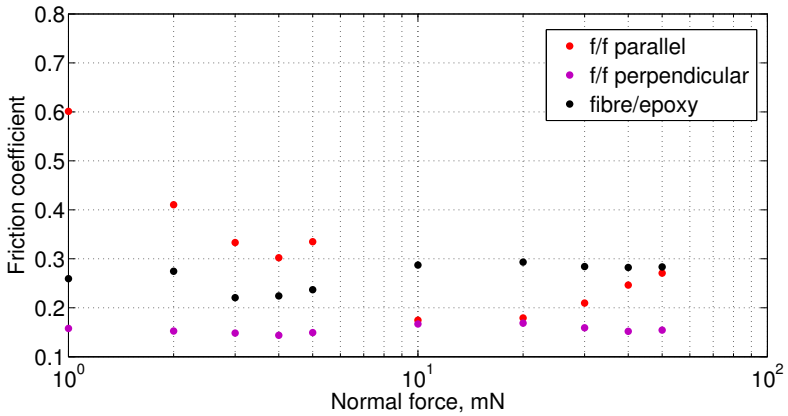

Figure 3.13: Carbon fibre/epoxy and carbon fibre/carbon fibre in parallel and perpendicular orientation friction coefficients depending on applied normal force

which are presented in Fig. 3.13. The variations of friction coefficient with normal load are not significant, except in the case of fibre/fibre configuration in parallel orientation. This might be due to an imperfect alignment between fibres covering the sphere slider and the basal lock of fibres. Mean values of friction coefficients of 0.15 for fibre/fibre and 0.28 for fibre/epoxy are retained from this experimental investigation.

3.2.3 Discussion

These results of epoxy/carbon fibre and carbon fibre/carbon fibre friction coefficients can be compared with the results of Roselman and Tabor [82, 83]. They carried out frictional experiments of individual carbon fibres of two types (high strength and high modulus) against each other and against other materials, including epoxy. The normal load applied in this study is in the range of the order of $10^{-8} - 10^{-2}$ N for carbon fibre/carbon fibre and of the order of $10^{-4} - 10^{-2}$ N for carbon fibre/epoxy. The sliding speed is equal to 3 mm/s. A great effect of normal force on the carbon fibre friction was observed by the authors. Moreover, the friction of high strength fibres is two times higher than for high modulus fibres. In applied normal load range, the friction coefficient of carbon fibre/carbon fibre varies from 0.7 to 0.1. The friction coefficient of carbon fibre/epoxy is reported equal to 0.46.

In order to compare our experimental results with the results of Roselman and Tabor, we will calculate the approximative contact areas and average contact pressures. The considered contact cases and main elastic and geometrical characteristics are given in Fig. 3.14 (a-d). For all cases, we take the elastic characteristics measured by nanoindentation test in Chapter 2: the Young moduli of $E_1 = 20.7$ GPa and $E_2 = 4.5$ GPa and the Poisson coefficients of $\nu = 0.2$ and $\nu = 0.4$ for carbon fibres and epoxy, respectively. The contact geometry, applied theories and resulting mean contact pressures are the following for these four cases:

- Individual fibres contact from [82], see Fig. 3.14 (a). The theory of Hertz for cross-cylinders is applied in this case. The mean contact pressure is in the range $0.26 - 2.54$ GPa under the normal force of $0.01 - 10$ mN.

- Carbon fibre/epoxy plane contact from [83], see Fig. 3.14 (b). The surface of epoxy is considered as covered with a multitude of small spheres, which allows authors to apply Archard's topographic theory for rough contact [84]. Every small contact is considered as Hertzian sphere/plane contact. The mean contact pressure is calculated based on the values for carbon fibre/steel contact of similar surface roughness given in [83] taking into account the difference in elastic characteristics. The mean contact pressure in this case is equal to 117 MPa under a normal force of 0.01 N.

- Covered with carbon fibres sphere/epoxy plane contact, see Fig. 3.14 (c). We consider this contact as carbon sphere/epoxy plane case with the elastic characteristics measured for carbon fibres and epoxy. The Hertz equations for this geometrical configuration is applied. The mean contact pressure is $3.5 - 12.9$ MPa under the normal load of $1 - 50$ mN.

- Covered with carbon fibres sphere/carbon fibres lock plane contact, see Fig. 3.14 (d). This contact case, in the first approximation, can be treated as carbon sphere/carbon plane contact. Thus, the Hertz theory is also applied for this case. The mean contact pressure varies from 1.2 to 4.39 MPa under the normal force range from 1 to 50 mN.

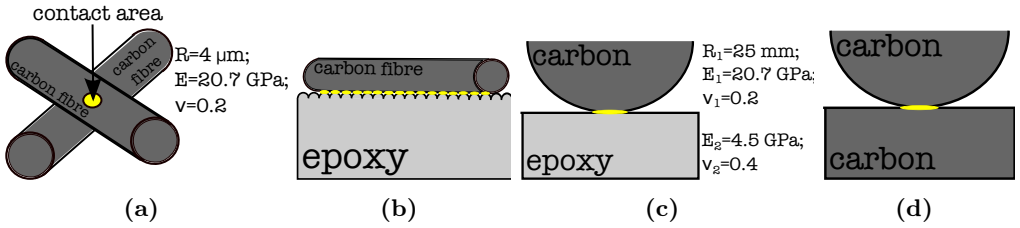

Figure 3.14: Contact schematics considered for contact area and mean pressure calculation

The resulting average contact pressures with corresponding normal load ranges and measured friction coefficients for carbon fibre/carbon fibre and carbon fibre/epoxy contacts are presented in comparative Table 3.4.

Friction couple	**Reference**	**Normal load,** mN	**Average contact pressure, MPa**	**Friction coefficient**
Carbon fibre HS/ carbon fibre HS	Individual fibres [82]	$0.01 - 10$	$260 - 2540$	$0.7 - 0.1$
	Fibre lock, microfriction	$1 - 50$	$1.2 - 4.35$	0.15
Epoxy/ carbon fibre HS	Individual fibres [83]	1	117	0.46
	Fibre lock, microfriction	$1 - 50$	$3.5 - 12.9$	0.28

Table 3.4: Summary of the friction coefficients and load conditions for carbon fibres and epoxy

3.3 Conclusions and arising questions

To summarize the main conclusions from this experimental study, following points should be emphasized:

1. The experimental conditions favorable to interfacial, i.e. damageless, sliding friction were identified and then chosen for epoxy/epoxy, CFRE/epoxy, CFRE/CFRE and CNPRE/CNPRE contacts.

2. The effect of filler addition was studied under established interfacial friction conditions and the following tendencies were observed

- the mean kinetic friction coefficient rises slightly with fibre volume fraction up to 62% for epoxy/CFRE couple;
- the mean kinetic friction coefficient of CFRE/CFRE couples is at least two times lower than its value for epoxy/epoxy couple, and shows a minimum between 0 and 62 % of fibre volume fraction;
- the addition of carbon nanopearls to epoxy monotonously increases the mean kinetic friction coefficient: the highest tested nanopearl mass content of 35 % corresponds to the friction coefficient of one time and a half higher than its value for epoxy/epoxy couple.

3. Under interfacial friction conditions, fibre orientation of two samples does not affect significantly the mean kinetic friction coefficient of CFRE 62%/CFRE 62% couple: for $\varphi = 0° \div 90°$, $\mu = 0.17 \div 0.18$.

4. Friction coefficients of carbon fibre/carbon fibre and carbon fibre/epoxy are measured and compared with those found in literature. The strong dependence of carbon fibre friction coefficient on normal load observed in literature is not confirmed under tested conditions.

These conclusions brings up the following questions:

- Why does the addition of carbon fibres into one polymer of frictional couple increase the friction, while their addition into both contacting polymers causes its dramatic fall?
- Why do carbon fibres and carbon nanopearls change epoxy friction in such a different way?
- What are the mechanisms of friction at stake for composite/polymer and composite/composite contacts?
- How can we predict the friction coefficient of composite material for any reinforcement concentration based on experimental results?

Chapter 4

Interfacial frictional dissipation: analytical model

In order to address the questions raised at the end of the previous chapter, we referred to analytical models currently available to predict and explain the friction of fibre-reinforced composites. Thus, a short presentation of the models of sliding contact of fibre-reinforced plastic starts this chapter. However, these models deal with friction of a composite against a uniphase material, usually much harder. Since no adequate model dealing with the contact between two composites was found, such a model is created in this work and presented further. Based on Bowden and Tabor's theory [85], it is applied to multi materials contact. The application of this model to the contact of CFRE/CFRE, CFRE/epoxy and CNPRE/CNPRE is discussed at the same time, and the results are compared with the experimental observations of Chapter 3.

Contents

4.1 State of the art

In this section we present two analytical models of composite friction against uniphase counterface material from the literature. The first model deals with fibre-reinforced polymer friction, while the second one can be applied to any type and number of composite reinforcement.

4.1.1 Tsukizoe and Ohmae's model

This model [46, 81] for sliding friction between fibre-reinforced polymer against uniphase material issues from the fact, that normal P and frictional force F are distributed between fibres and matrix, designated by indices f and m, respectively

$$P = P_f + P_m$$

$$F = F_f + F_m$$

and lies on following assumptions:

1. Areas of contact for fibres A_f and matrix A_m are proportional to the total contact area A with the fibre and matrix volume coefficients V_f, V_m, respectively: $A_f = V_f A$ and $A_m = V_m A$.

2. If the peeling off of fibres from matrix does not occur, the shear strains of fibres and matrix are equal: $\gamma_f = \gamma_m = \gamma$.

3. Moduli of rigidity of fibres and matrix underneath the contacting surface are equal: $G_f = G_m = G$

Since the shear stress is $\sigma = G\gamma$ and the frictional force is $F = \sigma A$, the frictional force carried by fibres is $F_f = \sigma_f A_f = G_f \gamma_f V_f A$. But the shear strain and the modulus of rigidity are constant, thus $F_f = V_f F$. The frictional force due to the shear of the matrix is similar: $F_m = V_m F$.

The applied normal force $P = F/\mu$ is distributed between fibres and matrix. Hence,

$$\frac{F}{\mu} = \frac{F_f}{\mu_f} + \frac{F_m}{\mu_m} \tag{4.1}$$

where $\mu_f = F/P_f$ and $\mu_m = F/P_m$. Taking into account the contributions of the frictional force due to the fibres and the matrix, the friction coefficient for composite/uniphase counterface contact can be calculated as

$$\frac{1}{\mu} = \frac{V_f}{\mu_f} + \frac{V_m}{\mu_m} \tag{4.2}$$

This equation fits well the experimental results in [46, 81] obtained for polymer composites reinforced by E-glass fibres, HS or HM carbon fibres, stainless steel fibres or aramid fibres under sliding velocity of 25 μm/s and normal load of 1.52 N in contact with flattened stainless steel cone indenter of 0.1 mm diameter (the corresponding pressure is 194 MPa).

The authors claim no damage of the composites under these conditions, which correspond to interfacial friction. Therefore, this equation can be used to describe interfacial friction on composite against uniphase material.

4.1.2 Abrasive friction model of Axén et al

A model of Axén et al [86–88] covers the friction and wear of multiphase materials against abrasive counterface. It is based on Amontons' law for the friction coefficient and Archard's law for the wear resistance. It distinguishes different modes of load distribution between phases and it states that the total frictional force F is a sum of the contributions of each phase

$$F = \sum_{i=1}^{n} \mu_i P_i \tag{4.3}$$

where i is the number of phase. These authors assume that:

1. The phases retain their individual frictional properties, even when part of the composite.
2. The area fractions remain constant during sliding.
3. The phases do not influence the specific wear resistance or friction coefficient of each other.

Three modes of load distribution are proposed by the authors: an equal linear wear rates of the phases (EW) and an equal normal pressure on the phases (EP), constituting upper and lower limits for composite material friction and wear, and an intermediate mode between them (IM). If α_i is the area fraction of phase i, the load carried by this phase in each mode is equal to

$$P_{EPi} = P\alpha_i \tag{4.4}$$

$$P_{EWi} = P\frac{W_{si}}{\sum_{j=1}^{n} \alpha_j W_{sj}}\alpha_i \tag{4.5}$$

$$P_{IMi} = P\left(\theta_w \frac{W_{si}}{\sum_{j=1}^{n} \alpha_j W_{sj}} + (1-\theta_w)\right)\alpha_i \tag{4.6}$$

where W_s is the specific wear resistance and θ_w is the coefficient of proportion between EP and EW modes. From Eqs. 4.3-4.6, the composite friction coefficients for all cases are

$$\mu_{EP} = \sum_{i=1}^{n} \mu_i \alpha_i \tag{4.7}$$

$$\mu_{EW} = \sum_{i=1}^{n} \mu_i \frac{W_{si}}{\sum_{j=1}^{n} \alpha_j W_{sj}}\alpha_i \tag{4.8}$$

$$\mu_{IM} = \sum_{i=1}^{n} \mu_i \left(\theta_w \frac{W_{si}}{\sum_{j=1}^{n} \alpha_j W_{sj}} + (1-\theta_w)\right)\alpha_i \tag{4.9}$$

In the case of two phases composite, like fibre-reinforced polymer, Eqs. 4.7-4.9 reduce to:

$$\mu_{EP} = \mu_f \alpha_f + \mu_m \alpha_m \tag{4.10}$$

$$\mu_{EW} = \mu_f \frac{W_{sf}}{\alpha_f W_{sf} + \alpha_m W_{sm}} \alpha_f + \mu_m \frac{W_{sm}}{\alpha_f W_{sf} + \alpha_m W_{sm}} \alpha_m \tag{4.11}$$

$$\mu_{IM} = \mu_f \left(\theta_w \frac{W_{sf}}{\alpha_f W_{sf} + \alpha_m W_{sm}} + (1 - \theta_w) \right) \alpha_f + \mu_m \left(\theta_w \frac{W_{sm}}{\alpha_f W_{sf} + \alpha_m W_{sm}} + (1 - \theta_w) \right) \alpha_m \tag{4.12}$$

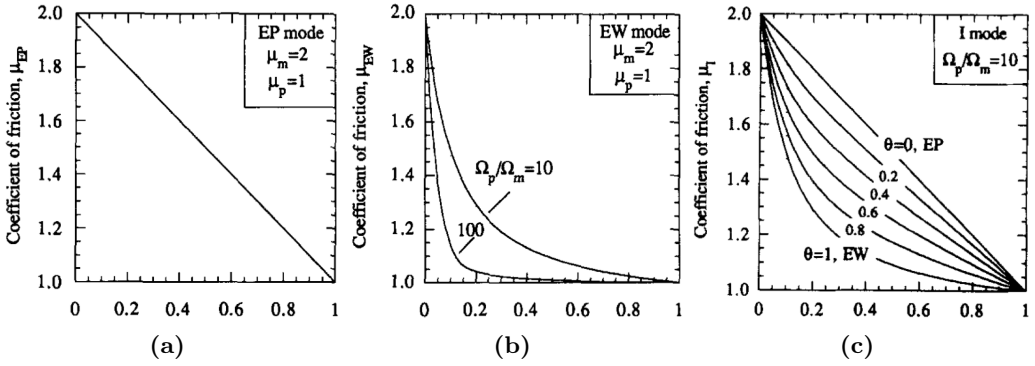

Figure 4.1: Composite friction coefficient for (a) EP mode, (b) EW mode with the variation of specific wear resistance Ω and (c) intermediate mode with the variation of coefficient of proportionality θ [86]

The results of Eqs.4.10-4.12 with a variation of the specific wear resistance and the coefficient of proportionality for different modes are shown in Fig. 4.1 (a-c). In the case of negligible wear, the first mode should dominate and the friction coefficient could be calculated by Eq. 4.10 for equal pressure distribution mode. Therefore, this equation, different from Tsukizoe and Ohmae's Eq. 4.2, may also describe the interfacial friction of composite against uniphase material.

4.2 Generalized friction law for composite/composite interfacial friction

The proposed model is based on Bowden and Tabor [85] adhesion model of friction, described in Chapter 1, and the multi-materials nature of contact between two composites as shown in Fig 4.2. During sliding, the contact area is renewed continuously, but its composition, *i.e.* the proportion between the composite components in the contact remains constant. This assumption relies on the non-occurrence of damage at the interface, which could rarefy a component by removing matter.

Therefore, following hypothesis are imposed:

- wearless and damageless friction
- Coulomb friction for all microscopic contact spots

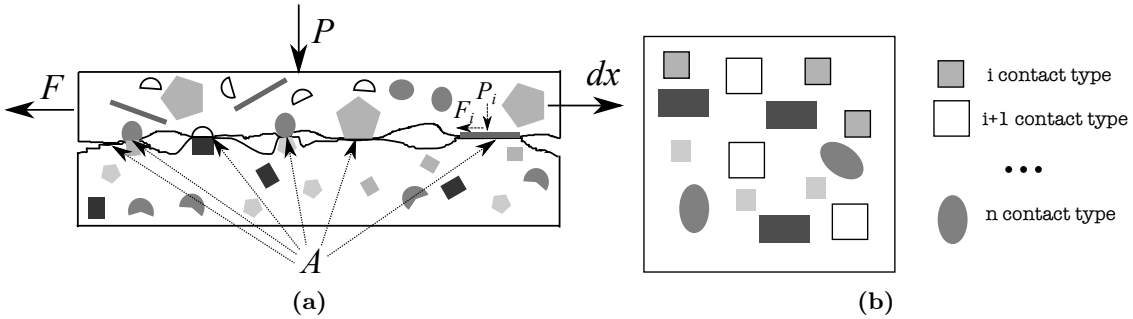

Figure 4.2: Contact area A of two sliding multiphase rough bodies in dx direction under the normal load P inducing the friction force F: (a) side and (b) in-plane views

- uncorrelated friction forces for all microscopic contact spots
- isotropic friction of any couple of components in contact

According to Bowden and Tabor adhesion friction model, the contact of two solids is composed of a multitude of microcontacts forming a real contact area. External normal and tangential forces are distributed over these microcontacts. Since the real area of contact is much lower than the apparent one, the local stresses arising in the microcontacts exceed the yield stress and the hardest asperity penetrates into the softest one. Thus, the normal load for a composite contact, which includes several material couples referred to by the subscript i, see Fig 4.2 (b), is

$$P = \sum_i P_i = \sum_i p_i A_i = \sum_i H_i A_i \tag{4.13}$$

where p_i is the contact pressure, which, in most cases, can be considered as H_i, the hardness of the softest material in couple i; A_i is the total contact area for all i–type contact spots.

The asperities of two materials under the normal load form the junctions. The shear stress arises in the contact until some critical value, when a rupture occurs and the sliding starts. The frictional force is a product of this critical shear stress τ_i and the contact area A_i for each material couple

$$F = \sum_i F_i = \sum_i \tau_i A_i \tag{4.14}$$

According to the Amontons first friction law, the friction coefficient for the composite contact could be written as follows:

$$\mu = \frac{F}{P} = \frac{\sum_i \tau_i A_i}{\sum_i H_i A_i} \tag{4.15}$$

A direct application of this equation is complicated because of the lack of information regarding real contact area and shear stresses. That is why two limit cases are considered below with an additional assumption.

Case 1: The hardness of the materials in contact is assumed to be equal to some

effective hardness, i.e. $H_i = H^*$. Therefore, taking Eq. 4.15 and considering the total real area is $\sum A_i = A$,

$$\mu = \frac{F}{P} = \sum_i \frac{\tau_i}{H^*}\frac{A_i}{A} = \sum_i \alpha_i \mu_i \tag{4.16}$$

where $\mu_i = \tau_i / H^*$ is the friction coefficient of i–type material couple. The contribution coefficient α_i is a surface fraction of all i-type contacts with respect to the total real area of contact between two composites.

Case 2: Another assumption is an equal effective shear stresses for every junction of all material couples $\tau_i = \tau^*$. Thus, Eq. 4.15 reduces to the inverse proportion for the composite friction coefficient:

$$\frac{1}{\mu} = \frac{P}{F} = \sum_i \frac{H_i}{\tau^*}\frac{A_i}{A} = \sum_i \alpha_i \frac{1}{\mu_i} \tag{4.17}$$

where $\mu_i = \tau^* / H_i$ is the friction coefficient for a couple of materials in i–type contact.

To conclude this section, the generalized Bowden and Tabor's model applied to a multiphase contact reduces to one of two composite frictional laws: the proportionality law in Eq. 4.16 and the inverse proportionality law in Eq. 4.17. In both cases, the composite friction coefficient depends only on the partition of contact between phases of two composites and the local friction coefficient between them.

A priori this model can be applied to the contact of composites of any nature, i.e. reinforced by any type, shape and number of fillers if the condition of their uniform distribution in the bulk of composite is respected. Hereafter, we will show its application to both composite/uniphase material and composite/composite sliding contacts, comparing Eqs. 4.16 and 4.17 with experimental results from the previous chapter.

4.3 Local friction coefficients

The proposed analytical model is based on the differentiation of each composite phase contact with counterface material, both to composite and uniphase material. As we have shown in previous section, the local friction coefficients between phases of each material in contact are necessary to calculate the global friction coefficient.

4.3.1 CFRE/CFRE couple

To predict the friction coefficient between two carbon fibre-reinforced epoxy composites three values of friction coefficients - carbon fibre/carbon fibre, carbon fibre/epoxy and epoxy/epoxy - are required.

The epoxy/epoxy friction coefficient was measured in the experimental study, presented in Section 1 of Chapter 3, while the friction coefficients of carbon fibre/carbon fibre and carbon fibre/epoxy frictional couples were measured and discussed in Section 2 of Chapter 3. The choice of local friction coefficients for the model application between composites is made from Table 3.4 on the basis of similar local pressures and sliding speed as discussed. As the local contact pressures in our plane/plane contact are unknown, all values issued

from our experiments and the literature will be tested. The summary of the local friction coefficients is reminded in Table 4.1.

Material couple	Friction coefficient
Carbon fibre/carbon fibre	0.1
	0.15
Epoxy/Carbon fibre	0.46
	0.28
Epoxy/epoxy	0.4
	0.46

Table 4.1: Local friction coefficients used for carbon fibre-reinforced epoxy contacts

4.3.2 CNPRE/CNPRE couple

The local friction coefficients of CNPRE/CNPRE couple are more complicated to obtain experimentally, mostly because of the nanosize of carbon nanopearls, which requires completely different experimental approaches.

Our expectations of high friction of CNPs, discussed in the previous chapter, are confirmed by the experimental work of Hunter et al. [89]. They rubbed silicon disc covered by carbon nanopearls against steel ball in humid (40% RH) and dry (0% RH) air. They observed, that in contrast to graphite, carbon nanopearls reduce the friction only in dry air, when they are compacted by high pressure and form a transfer layer. However, when carbon nanopearls absorb water molecules from humid air, moisture helps to reduce locking between individual nanopearls and prevents agglomerates formation and, consequently, the transfer layer formation. Individual nanopearls do not reduce friction. In our composites, not only the friction experiments are carried out in humid air, but also the fabrication process of addition and mixing of nanopearls into composite. Carbon nanopearls might absorb water molecules already in this stage and will not reduce the friction of our composites.

4.4 Fraction of phases on composite surface

4.4.1 Fibre surface fraction of CFRE

In order to apply our model to the contact of carbon fibre-reinforced epoxies, we must define a composition of the rubbing surface of the composite. The contact plane is considered as a cut parallel to the fibre direction. The problem of calculation of fibre surface fraction from their volume fraction, which is given by the fabrication process, is solved by several approaches represented by two major groups: the probabilistic approach uses random fibre distribution [90, 91], while the deterministic one deals with a representative volume element conception [92].

In this study, a random uniform fibre distribution with round fibres of a constant diameter is chosen. Figure 4.3 shows a cubic element of size a cut out of the composite

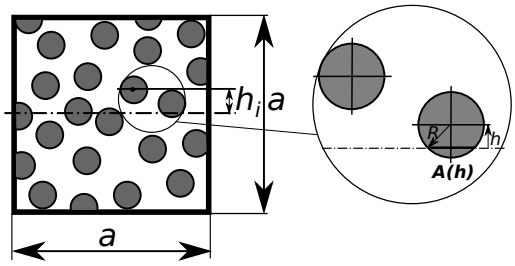

Figure 4.3: Random fibre distribution in the square cross-section of composite of size $a \times a$. $A(h)$ is the chord of the cut fibre i with the radius R, whose centre location is given by the height from the square middle h_i.

and filled of matrix and fibres of radius R. A cutting plane, parallel to the fibre direction, separates this volume into two equal parts. The relative location of the i fibre with respect to this plane is given by its height h_i. Since the fibres are assumed to be uniformly randomly distributed in the volume, the density probability function $p(h)$ is equal to

$$p(h) = \frac{1}{a},\ if\ h \in [-\frac{a}{2}; \frac{a}{2}] \tag{4.18}$$

The middle plane cuts each fibre through a chord $A(h)$, which length depends on the height h by

$$A(h) = \begin{cases} 2\sqrt{R^2 - h^2}, & \text{if } h \in [-R; R]; \\ 0, & \text{otherwise.} \end{cases} \tag{4.19}$$

The expectation of the chord for any fibre from volume a^3 is calculated from Eqs. 4.18 and 4.19 as follows:

$$\langle A(h) \rangle = \int_{-a/2}^{a/2} A(h) p(h)\, dh = \frac{\pi R^2}{a} \tag{4.20}$$

The fibre surface fraction α_f is the sum of all chords $N\langle A \rangle$, where N is the total number of fibres in the volume, divided by the side a of the cutting plane

$$\alpha_f = \frac{N\langle A \rangle}{a} = \frac{N\pi R^2}{a^2} \tag{4.21}$$

Since the fibre volume fraction V_f for the volume a^3 is the ratio of the sum of all fibre sections $N\pi R^2$ enclosed in this volume and the square area a^2. Therefore,

$$\alpha_f = V_f \tag{4.22}$$

Hereby using the probabilistic approach, we can prove that for a uniform random distribution of fibres in a unidirectional fibre–reinforced composite, the fibre surface fraction is equal to the fibre volume fraction.

4.4.2 Nanopearls surface fraction of CNPRE

The problem of a ratio between reinforcement surface and volume fraction is not actual for carbon nanopearl-reinforced composite, because spherical nanopearls are assumed to be distributed uniformly, and from the probabilistic point of view, nanopearls surface fraction is equal to their volume fraction.

However, we need to recalculate the mass content of nanopearls M_c, used in the fabrication process, to the nanopearl volume fraction V_f. Knowing the density of carbon nanopearls ρ_{cnp} and carbon nanopearl-reinforced composite ρ_{comp}, we can calculate nanopearl volume fraction as follows:

$$V_f = \frac{V_{cnp}}{V_{comp}} = \frac{m_{cnp}/\rho_{cnp}}{m_{comp}/\rho_{comp}} = M_c \frac{\rho_{comp}}{\rho_{cnp}} \tag{4.23}$$

The density of carbon nanopearl-reinforced composites was calculated in Chapter 2, see Table 2.11. The density of carbon nanopearls is, a priori, unknown, but we can estimate it. Literature gives a density of carbon nanotubes equal to 1.4 g/cm^3 [93], densities of PAN-based HS and HM carbon fibres of $1.76-1.7$ g/cm^3 and 1.87 g/cm^3 [94], respectively, and the maximal density of graphite of 2.26 g/cm^3 [94]. Based on these values, we suppose the density of carbon nanopearls is close to the density of carbon fibres and equal to 1.8 g/cm^3. Therefore, the volume fractions of carbon nanopearls composites, CNPRE 1%, CNPRE 15%, CNPRE 28% and CNPRE 35%, are calculated by Eq. 4.23 and equal to 0.006, 0.10, 0.20 and 0.28, respectively.

4.5 CFRE/epoxy sliding contact

A first application of our generalized model is the contact of a fibre–reinforced composite with a neat homogeneous material. The composition of the apparent contact area in this case is shown in Fig. 4.4. Two types of contact are distinguished: fibre/counterface material and matrix/counterface material.

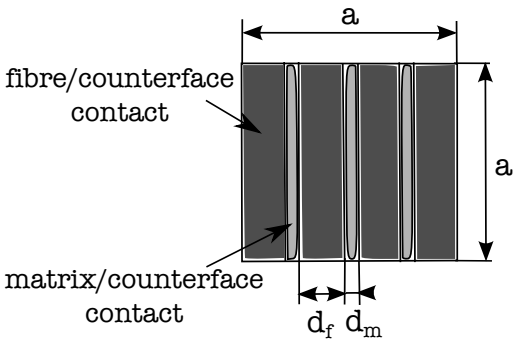

Figure 4.4: Apparent contact between a uniphase material and a FRP with fibre diameter d_f and distance between fibres d_m

In this simple case, designating subscripts c, and ep, respectively, for carbon fibres and epoxy counterface or composite matrix, the contribution coefficients of each contact type

is equal:

$$\begin{cases} \alpha_{epc} = d_f/a = \alpha_f \\ \alpha_{epep} = d_m/a = 1 - \alpha_f \end{cases} \tag{4.24}$$

where d_f is the fibre diameter and d_m is the distance between two adjacent fibres.

Therefore, from Eqs. 4.16, 4.17 and 4.24, the composite friction coefficient can be calculated with one of following equations:

$$\mu = \alpha_f \mu_{epc} + (1 - \alpha_f)\mu_{epep} \tag{4.25}$$

if we adopt the proportionality law, and

$$\frac{1}{\mu} = \frac{\alpha_f}{\mu_{epc}} + \frac{1 - \alpha_f}{\mu_{epep}} \tag{4.26}$$

if we adopt the inverse proportionality law. μ_{epc} and μ_{epep} are the friction coefficients between fibre and counterface materials and matrix and counterface materials, respectively, which are obtained experimentally for each couple of materials.

To apply these two equations to epoxy/carbon fibre-reinforced epoxy contact, we use the values of local friction coefficients from Table 4.1: $\mu_{epep} = 0.4$ for epoxy/epoxy and $\mu_{epc} = 0.46$ or 0.28 for epoxy/carbon fibre friction coefficient. The resulting curves and experimental values from Section 1 are presented in Fig. 4.5. The friction coefficients are plotted versus fibre volume fraction for the experimental results and versus fibre surface fraction for the analytical results. Their equality, proved in Sect. 4.4, permits us to put them on the same abscissa axis.

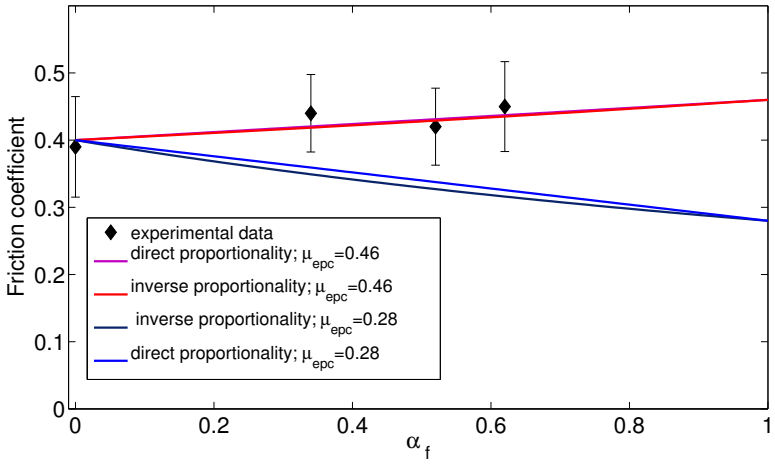

Figure 4.5: Experimental (black points with error bars) and theoretical results corresponding to Eqs. 4.25 and 4.26 (color lines) in case of composite/epoxy contact calculated using the values from Table 4.1. The red line is superimposed on the magenta line

Both equations fit well the experimental results for all CFRE composites using epoxy/carbon fibre friction coefficient of 0.46. However, we observe that a substitution of the

epoxy/carbon fibre friction coefficient of 0.28 gives the wrong tendencies, since the friction coefficient slightly increases with an increase in surface fraction. Besides the validation of composite/uniphase material friction laws, this can be interpreted such as the values of epoxy/epoxy and carbon fibres/epoxy friction coefficients measured for individual fibre [82, 83] and epoxy/epoxy macroscopic friction might be used to calculate the composite friction coefficient. Hence, the hypothesis of uncoupled friction contributions of each component is credible.

The fact, that both direct Eq. 4.16 and inverse Eq. 4.17 proportionality laws are applicable for epoxy/composite friction, can be explained. This validates the assumptions about effective hardness H^* and effective shear stress τ^*. Indeed, in the case of epoxy/composite contact, the hardness used in Eq. 4.16 is similar for epoxy/epoxy and epoxy/carbon contacts, because, according to Bowden and Tabor, we should take the softest material, i.e. epoxy, hardness. Shear stresses for these two contact types, which can be found as $\tau_i = \mu_i H_i$, are also rather similar because of a closeness of their friction coefficients. Therefore, both laws can be used in this specific example.

We should also notice, that fibre surface fractions of composites with 34 and 52% of fibres in volume are obviously not equal to their fibre volume fractions. Nevertheless, keeping in mind the photographs of their surfaces, see Fig. 2.11 (a-d) of Chapter 2, fibre surface fraction must be between 0 and 62%. This shift on the abscissae axis does not affect the validity of our model.

4.6 Composite/composite sliding contact

A more complex case is the contact between two composites, as drawn in Fig. 4.6(a) for sphere- or cylinder-reinforced composite. If two identical carbon fibre- or nanopearl-reinforced composites are in contact, three types of microcontact are distinguished: carbon/carbon (*cc*), carbon/epoxy (*epc*) and epoxy/epoxy (*epep*). According to Eq. 4.16 and 4.17, the composite friction coefficient becomes equal to one of the following equations

$$\mu = \alpha_{cc}\mu_{cc} + 2\alpha_{epc}\mu_{epc} + \alpha_{epep}\mu_{epep} \tag{4.27}$$

according to the proportionality law and,

$$\frac{1}{\mu} = \frac{\alpha_{cc}}{\mu_{cc}} + \frac{2\alpha_{epc}}{\mu_{epc}} + \frac{\alpha_{epep}}{\mu_{epep}} \tag{4.28}$$

according to the inverse proportionality law.

The contribution coefficients α_{cc}, α_{epc} and α_{epep} must be identified for each composite from the contact geometry. We remind, that one of the main assumptions of this model is that, a real microcontact spots distribution is equal to a distribution of the apparent contact area between the phases.

4.6.1 CFRE/CFRE sliding contact

When two identical CFRE are in contact with the angle of orientation between the fibres of two composites φ, the apparent contact area can be depicted as in Fig. 4.6(b). The areas

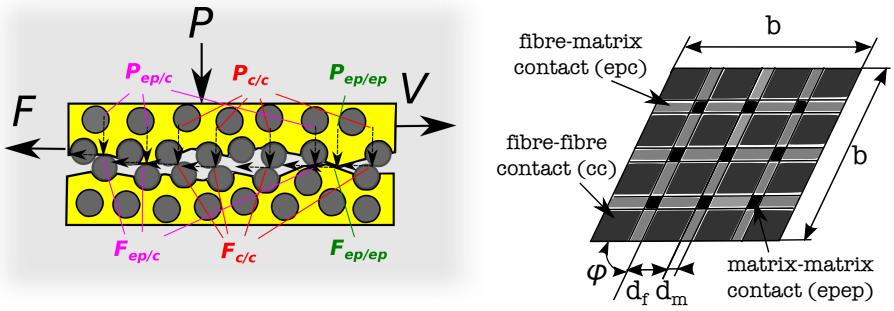

(a) (b)

Figure 4.6: (a) Schematic distribution of forces between phases in fibre or nanopearl-reinforced composite (b) Contact between two similar FRP with an angle φ between fibre directions of two composites with fibre diameter d_f and distance between fibres d_m

of each apparent individual microcontact A_{cc}, A_{epc}, A_{epep} and total apparent contact area A are, respectively, equal to

$$A_{cc} = \frac{d_f^2}{\sin\varphi}; A_{epc} = \frac{d_f d_m}{\sin\varphi}; A_{epep} = \frac{d_m^2}{\sin\varphi}; A = \frac{a^2}{\sin\varphi} \tag{4.29}$$

where d_f is the fibre diameter and d_m is the distance between two adjacent fibres, and $a = d_f + d_m$ is their sum. Thus, the contribution coefficients depend only on fibre surface fraction $\alpha_f = d_f/a$ and are equal to

$$\begin{cases} \alpha_{cc} = \alpha_f^2 \\ \alpha_{epc} = \alpha_f(1-\alpha_f) \\ \alpha_{epep} = (1-\alpha_f)^2 \end{cases} \tag{4.30}$$

Substituting Eq. 4.30 into Eq. 4.27 and 4.28, two equations for composite friction coefficient are obtained:

$$\mu = \alpha_f^2\mu_{cc} + 2\alpha_f(1-\alpha_f)\mu_{epc} + (1-\alpha_f)^2\mu_{epep} \tag{4.31}$$

for the proportionality law and,

$$\frac{1}{\mu} = \frac{\alpha_f^2}{\mu_{cc}} + \frac{2\alpha_f(1-\alpha_f)}{\mu_{epc}} + \frac{(1-\alpha_f)^2}{\mu_{epep}} \tag{4.32}$$

for the inverse proportionality law.

Thus, in the framework of our assumptions, this model reveals an independence of interfacial friction coefficient on the fibre orientation in both composites or their diameter. This conclusion is coherent with the experimental results shown in Fig. 3.10, when a very slight increase of mean friction coefficient $(0.17 \div 0.18)$ was observed for the variation of orientation angle between the fibres of two samples from 0° to 180°.

Figure 4.7 presents the application of the proposed analytical model using the values

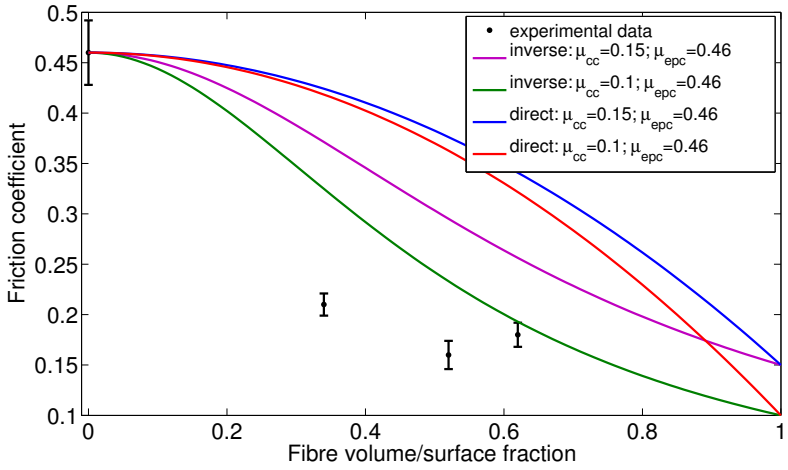

Figure 4.7: Experimental (black points with error bars) and theoretical (color lines) results corresponding to Eq. 4.31 direct and Eq. 4.32 inverse proportionality laws in case of composite/composite contact calculated with values from Table 4.1

of local friction coefficients from Table 4.1 (with $\mu_{epc} = 0.46$ as shown by the CFRE/epoxy friction results) to the experimental results. We note that experimental friction coefficients for 34 and 52 % do not fit well any curve issued from the model. This is, undoubtedly, due to the heterogeneity of their surface compositions, see Fig. 2.11 of Chapter 2, and profiles, see Fig. 2.13 (b) and (c) of Chapter 2. Carbon fibres stick out from the surface and take the majority of the contact upon themselves, which does not leave place to epoxy/epoxy contacts. Therefore, the friction coefficient drops dramatically with regard to its epoxy/epoxy value, and the friction laws must be different from those, proposed to the composites with uniformly distributed fibres.

The hardness of carbon fibres is about 10 times higher than that of epoxy, as detailed in Chapter 2. Therefore, the assumption of an effective hardness H^* is irrelevant. This is in agreement with Fig. 4.7, where the direct proportionality law gives inadequate fit.

However, the inverse proportionality law Eq. 4.17 seems to fit the experimental results for CFRE/CFRE friction. We can estimate the effective shear stresses for the three contact types, using hardness values and local friction coefficients: $\tau_{epep} = 0.4 \cdot 240 = 96$ MPa; $\tau_{epc} = 0.46 \cdot 240 = 110$ MPa and $\tau_{cc} = 0.1 \cdot 4400 = 440$ MPa. The three values of shear stresses are of the same order of magnitude. This might explain why the inverse proportionality law coherently describes the experimental evolution of friction in the case of composite/composite contact with rather different mechanical properties of the matrix and the reinforcement.

4.6.2 CNPRE/CNPRE couples

The initial equations of CNPRE/CNPRE friction coefficient are similar to Eqs. 4.27 and 4.28 for CFRE/CFRE contact. Because of the same order of the nanopearl size and the composite surface asperities, three types of microcontact between the asperities of

two surfaces are distinguished, see Fig. 4.8: CNP/CNP, CNP/epoxy and epoxy/epoxy. The proportion between their numbers is calculated by the probabilistic approach: if two identical CNPRE are in sliding contact, the probability of CNP/CNP contacts is α_{cnp}^2, the probability of CNP/epoxy contacts is $\alpha_{cnp}(1-\alpha_{cnp})$ and the probability of epoxy/epoxy contact is $(1-\alpha_{cnp})^2$.

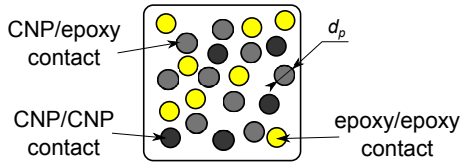

Figure 4.8: Contact area composition between two carbon nanopearl-reinforced epoxies

Thus, the contribution coefficients for these composites are similar to those from CFRE/CFRE contact:

$$\begin{cases} \alpha_{cc} = \alpha_{cnp}^2 \\ \alpha_{epc} = \alpha_{cnp}(1-\alpha_{cnp}) \\ \alpha_{epep} = (1-\alpha_{cnp})^2 \end{cases} \tag{4.33}$$

where α_{cnp} is the surface fraction of nanopearls on the composite rubbing surface.

Therefore, Eqs. 4.27 and 4.28 reduce to the following:

$$\mu = \alpha_{cnp}^2\mu_{cc} + 2\alpha_{cnp}(1-\alpha_{cnp})\mu_{epc} + (1-\alpha_{cnp})^2\mu_{epep} \tag{4.34}$$

for the proportionality law and,

$$\frac{1}{\mu} = \frac{\alpha_{cnp}^2}{\mu_{cc}} + \frac{2\alpha_{cnp}(1-\alpha_{cnp})}{\mu_{epc}} + \frac{(1-\alpha_{cnp})^2}{\mu_{epep}} \tag{4.35}$$

for the inverse proportionality law.

In order to verify the coherence between these equations and experimental results from Fig. 3.8(c), the local friction coefficients are required. The epoxy/epoxy friction coefficient is provided from our experiments, but CNP/CNP and CNP/epoxy friction coefficients are both unknown. Thus, the fittings for mean experimental values for friction coefficients by the direct and inverse proportionality laws are mathematically performed using Matlab fitting tool, see Fig. 4.9. In order to study the fitting effect on the unknown local friction coefficients, we varied the coefficients of fittings, see Table 4.2.

Both Eqs. 4.34 and 4.35 seem to fit well the experimental results. Concerning the local friction coefficients, for most of the fits, μ_{cc} and μ_{epc} are rather high with regard to μ_{epep}, as we predicted in Sec. 2.3.2. Furthermore, for both fitting equations, they are interdependent: if one grows, another falls, see Table 4.2. Nevertheless, according to the initial hypotheses of our model, an application of the direct proportionality law leads to the wrong assumption, that is to say that the hardnesses of epoxy and carbon nanopearls must be equal. We suppose, that the hardness of carbon nanopearls is close to those of carbon fibres, which differs from the hardness of epoxy at least by one order, see Chapter

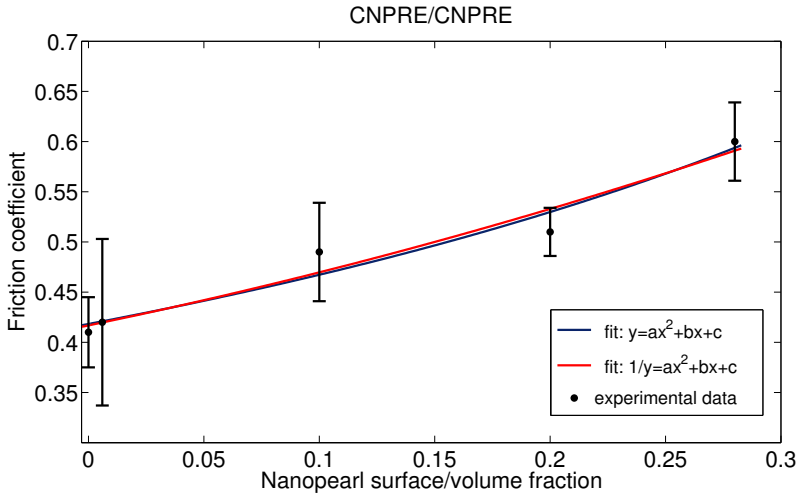

Figure 4.9: Experimental (black points with error bars) and fittings of Eqs. 4.31 and 4.32 (color lines) for CNPRE/CNPRE contact

Fit	μ_{cc}	μ_{epc}	μ_{epep}	RMSE
$y = ax^2 + bx + c$				
a=-1.5	-0.06	0.93	0.42	0.02803
a=-1	0.3	0.86	0.42	0.02447
a=-0.5	0.67	0.80	0.42	0.02156
a=-0.1	0.98	0.745	0.42	0.01989
a=0.1	1.11	0.72	0.42	0.01933
a=0.3	1.26	0.69	0.42	0.01898
a=1	1.77	0.595	0.42	0.01949
$y = 1/(ax^2 + bx + c)$				
a=-1	-0.54	0.77	0.42	0.01841
a=0.1	-9.78	0.91	0.42	0.01841
a=0.5	4.87	0.95	0.42	0.01847
a=1	1.67	1	0.42	0.01862
a=1.5	1.11	1.11	0.42	0.01886
a=2	0.77	1.18	0.42	0.01918
a=2.5	0.62	1.33	0.42	0.01959
a=3	0.5	1.43	0.42	0.02007
a=3.5	0.42	1.54	0.42	0.02063
a=4	0.37	1.82	0.42	0.02125

Table 4.2: Model fittings with corresponding local friction coefficients and root mean square errors (RMSE)

2.

Therefore, the fit by the inverse proportionality law is more reasonable. According to the hypothesis of our model, the shear stresses must be equal to a constant value τ^* for all types of microcontact. In the case, when the nanopearl contacts are plasticized, we can calculate the shear stress of epoxy/epoxy contact: $\tau_{epep} = \mu_{epep} H_{ep} = 0.42 \cdot 200\ MPa = 84\ MPa$. Since, according to Bowden and Tabor's model, we should use the hardness of epoxy to calculate both epoxy/epoxy and epoxy/carbon nanopearl shear stresses, τ_{epc} must be close to 84 MPa and the local friction coefficients for these two contact types must be close. However, no such plausible value is obtained in Table 4.2. Hence, we have to suppose that nanopearl contacts are not plasticized and the local pressure p does not reach the hardness value. In this case, we can choose the local friction coefficients $\mu = \tau/p$, expecting the local pressures $p_{cc} > p_{epc}$ due to the higher contact stiffness and lower contact area for carbon nanopearl than for epoxy contacts. If the shear stresses are equal, the local friction coefficients must be $\mu_{cc} < \mu_{epc}$. This condition is met for the inverse proportionality law with the values of fittings with $a > 1.5$, see Table 4.2.

4.7 Discussion: roughness and stress distribution for composite contact

Along with in-plane contact geometry, which we consider to be responsible for the contact area distribution between composite phases, the out-of-plane surface topography can modify this distribution, exposing some phases to the contact and hiding down others. The composite surface profiles, presented in Chapter 2, shows that this is clearly the case for CFRE of 34 and 52 % of fibres. However, even if the composite surface is uniform on the macroscopic scale, as in the case of CFRE 62 %, the roughness of the composite surface is higher than those of pure epoxy surface, and it is probable, that the polishing process worn out the epoxy matrix lying between fibres.

The topography and mechanical properties of the phases are responsible for the contact stress distribution between microcontacts, which can plasticize or not, depending on the local pressure and the elastic limit of composite phases. This shifts the composite contact closer to one of two particular cases (direct and inverse proportionality laws) of our generalized model, as we have discussed for CNPRE/CNPRE contact.

It is likely, that polymer matrix carries less of the load than carbon reinforcement due to the difference in rigidity. The idea of composite friction coefficient depending on the load carried by each composite phase and friction coefficients between these phases was proposed by Schön [95], who made the experiments on friction between CFRP under severe sliding conditions:

$$\mu = \frac{1}{P}(\mu_{mm} P_{mm} + \mu_{fm} P_{fm} + \mu_{ff} P_{ff}) \tag{4.36}$$

To estimate the local pressures in composite/composite contact, the real contact area and the rule of pressure distribution between phases are required. The finite-elements simulations were performed for sliding contact between a steel asperity and a fibre-reinforced composite by Friedrich, Varadi et al. [96,97] in order to calculate contact pressures, contact

temperatures and contact areas. An analytical solution of the anisotropic contact between a FRP and a rigid cylinder was proposed by Ning et al. [98, 99]. Unfortunately, the high rigidity of counterface does not permit us to use their conclusions for our composite contacts with a soft epoxy. This contact problem of FRP with a soft uniphase counterface material, along with more complicated problem of the contact between two FRPs, could be the subject of future research.

4.8 Conclusions

Our analytical model proposes a generalized friction law for composite/uniphase material and composite/composite sliding contacts. By application of the assumption of effective shear stresses or effective hardness, this law reduces into one of two particular laws, which are easier to apply. These composite friction laws require local friction coefficients and contribution coefficients for all phases, which, in general case, should depend on the in-plane geometry of the contact, topography of both surfaces and mechanical characteristics of the phases, which can influence the local pressures. In first approximation, these contribution coefficients are calculated for FRP/uniphase material, FRP/FRP and CNPRE/CNPRE contacts considering only the in-plane contact geometry. They found to be dependent only on the filler surface fraction on composite surface. These analytical results were compared with the experimental results, given in the previous chapter. The general conclusions are organized by the contact type and presented below.

CFRE/epoxy contact. The softer epoxy matrix is responsible for the friction of both contact types (epoxy/epoxy and epoxy/carbon fibre). Both assumptions are plausible, and both inverse and direct proportionality laws are reasonable and can be applied.

Composite/composite contact. The harder filler is responsible for the friction in both composites (CFRE, CNPRE). Filler/filler contacts seems to modify dramatically the frictional behaviour. Because of the large difference in the hardness of epoxy and carbon filler, the assumption of effective hardness can not be applied. However, estimated local shear stresses of CFRE/CFRE micro contacts are of the same order of magnitude. The micro contacts of CNPRE/CNPRE must not be plasticized to answer the assumption of the effective shear stress, which is rather plausible because of the high elastic limit of carbon filler. Therefore, in the case of composite/composite sliding contact, the inverse proportionality law should be applied.

For CFRE/CFRE contacts, **fibre orientation** was taken into account. The model concludes that it does not affect the composite interfacial friction. This is coherent with our experimental observations.

Chapter 5

Bulk frictional dissipation

In order to provide a complete study of frictional dissipation in composite materials, the interfacial friction investigation, presented in the previous chapter, is followed by the study of frictional bulk dissipation and associated wear. The experimental investigation of pure epoxy and CFRE 62% friction and wear under severe tribological conditions, i.e. high normal load and sliding velocity, is carried out and presented in this chapter.

Severe tribological conditions usually cause a surface damage and contact heating, which could increase and destabilize the frictional force. Some part of the frictional energy dissipates in the mechanical deformation, cracking, softening or wear debris formation. The types of surface damage and the severity of their consequences depend not only on normal load, sliding velocity and environmental conditions, but also on the nature of both contacting materials. The experimental wear investigations of CFRE composite issued from the literature and presented in Chapter 1 cover the wear of rather soft composite or polymer by a hard, and often sharp, metal counterface. Therefore, the involved wear mechanisms are usually abrasive, and the measured wear rates are very high.

In contrary to these studies, we are interested in frictional dissipation in polymer/polymer and composite/composite couples. Furthermore, epoxy/composite frictional couple is also tested in order to complete this investigation. Due to the similar nature of rubbing bodies, the dissipation processes are very different from those involved against hard metal.

Therefore, this chapter is organized in the following manner: it starts with a description of the experimental equipment, conditions, protocol and features, followed by the consecutive studies of epoxy/epoxy, CFRE/CFRE and CFRE/epoxy frictional dissipations. A two-scale approach is developed in our study. It involves macroscopic frictional losses, which cover mass loss measurement and friction coefficient, dissipated energy and relative contact temperature rise calculations, and microscopic surface observations in order to determine the wear mechanisms. The observation of the worn surfaces after several test durations under similar conditions allows us to distinguish wear mechanisms and to create wear history scenarios. A correlation of two-scale parameters is also discussed for all frictional couples.

Contents

5.1 Experiment description

5.1.1 Linear tribometer

This tribological study of epoxy and CFRE friction and wear under severe conditions is carried out on a linear tribometer developed in LTDS [100] and presented in Fig. 5.1.

It allows one to apply a linear or sinusoidal reciprocating motion between two samples of several geometrical configurations in ambient atmosphere or liquid lubrication environment. The main characteristics of this tribometer are summarized in Table 5.1. The linear motor on crawler tracks guides the horizontal displacement of a moving sample, providing a speed in the range from 1 to 1000 mm/s in constant or sinusoidal mode. The displacement of the moving arm is continuously measured by a sensor of the motor during an experiment. A derivation of the temporal dependence of displacement provides a velocity value at each instant.

The normal load is applied with a vertical displacement of a platform, carrying the fixed lower sample, which is guided through a screw shaft by a motor. The maximal vertical run of the platform is 10 mm. The lifting speed can be varied from 30 nm/s to 1 mm/s. The stiffness of the loading device, calculated and verified experimentally during the development of the tribometer, is about 37 MN/m, while its first natural frequency is 173.3 Hz under the load of 100 N. The normal load is continuously measured by a load cell integrated into the moving arm. In parallel with the normal force, the tangential load is also continuously measured with a piezoelectric sensor fixed on the lateral side of the platform.

The kinetic motion parameters and normal load application, as well as the measured signals, are recorded through a PC with a sampling frequency up to some kHz.

This tribometer is very versatile: it can be adapted to plane/plane, cylinder/plane or sphere/plane configurations. A rotation of an adjustable head of the slider holder in the moving arm can regulate the parallelism between two samples in plane/plane or cylinder/plane configuration.

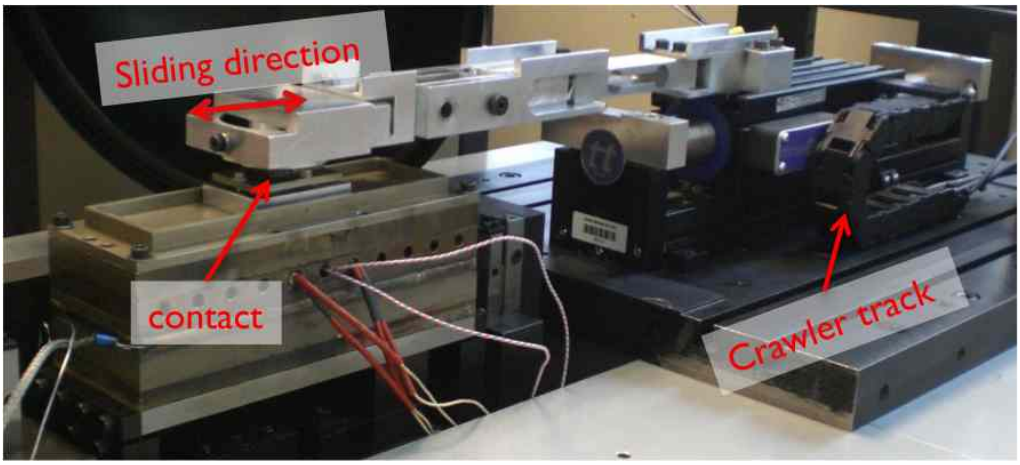

Figure 5.1: Overall view of the linear tribometer

Kinematics	Linear or sinusoidal alternative motion
Contact configuration	Plane/plane, cylinder/plane, sphere/plane
Sliding distance	From 1 mm to some cm
Speed	From 1 mm/s to 1 m/s
Normal load	Up to 100 N
Environment	Ambient air, with a possibility of the lubricant bath installation
Temperature	From $-100\,°C$ to $500\,°C$

Table 5.1: Main features of the linear tribometer [100]

5.1.2 Samples and experimental protocol

Friction experiments under severe tribological conditions are carried out on the CFRE 62 % composite and pure epoxy in different configurations. These materials, as well as their surface preparation and roughness characterization, are similar to those used in the interfacial friction study. The composite and epoxy plates were cut into rectangular samples with the approximative dimensions of $30 \times 15 \times 4$ mm^3 for tracks and $8 \times 6 \times 4$ mm^3 for sliders. While the exact track size has no importance for our frictional study, the size and shape of the sliders can possibly influence the friction or wear. Therefore, the sliding area of each slider is measured and taken into account in the following calculations.

Four tribological conditions are chosen in order to highlight an effect of normal load and sliding speed on friction and wear. A sinusoidal temporal velocity dependence is applied. This kinematic condition is characterized by an amplitude of the sliding distance and a sliding frequency. The maximal sliding distance of 10 mm and two sliding frequencies of 1 and 6 Hz are chosen. These sliding frequencies correspond to mean sliding velocity of 20 and 120 mm/s or maximal sliding velocity of 30 and 170 mm/s, respectively. The applied tribological conditions also differ by two normal forces of 20 and 50 N. These four tribological conditions are summarized in Table 5.2.

All the tests are carried out in ambient humidity ($RH \approx 50 - 60\%$) and room temperature ($\approx 20 - 25°C$).

Conditions	**1**	**2**	**3**	**4**
Normal load, N	20	20	50	50
Mean apparent contact pressure, MPa	0.7	0.7	1.8	1.8
Sliding distance, mm	10	10	10	10
Frequency, Hz	1	6	1	6
Mean velocity, mm/s	20	120	20	120
Max velocity, mm/s	30	170	30	170

Table 5.2: Applied tribological conditions

An example of one cycle of instantaneously measured frictional and normal forces and the corresponding sliding speed is plotted in Fig. 5.2. We can observe, that the normal force is rather constant with time, sliding speed is sinusoidal, and the frictional force on the forth and back passes is rather symmetrical.

5.1.3 Kinematics of slider and track

The wear characteristics are usually a function of the kinematic length. It is the distance seen by a surface point, which depends on the contact time and sliding velocities of the two contact bodies. Kinematic length L_{kM} of a point M belong to the body A can be calculated as:

$$L_{kM} = t_M(V_B - V_A) \tag{5.1}$$

where V_A and V_B are the velocities of A and B contacting bodies. $t_{cM} = b/V_A$ is a time of contact between the point M and the body B, where b is a width of contact.

The contact kinematics is schematized in Fig. 5.3. The kinematic length is similar for all points of the slider and equal to $L_{ks} = 2 \cdot l \cdot N_{cycle}$, where l is the sliding amplitude and N_{cycle} is the number of cycles. The slider kinematic length is shown with the blue line on the kinematic length/pass diagram. However, the points of track surface are under different kinematic conditions and could be divided into three zones, see the red line on the kinematic length/pass diagram. The surface points of extreme zones 1 and 3, where the contact time depends on its position on the surface, have less contact time than those of the central zone 2, where it is constant for all points. Therefore the kinematic length is not similar for these three zones. We will operate with an average kinematic length for the track, which is showed with the violet line in Fig. 5.3 : $\overline{L_{kt}} = 2 \cdot (bl)/(b + l)N_{cycle}$. The difference of kinematic length in the extreme zones will be taken into account in the worn surface study, as depicted at the bottom of Fig. 5.3.

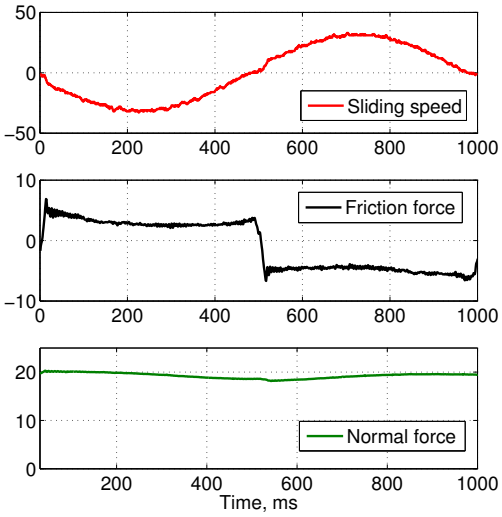

Figure 5.2: Example of the sliding speed and frictional and normal forces during one cycle continuously measured by the Linear tribometer

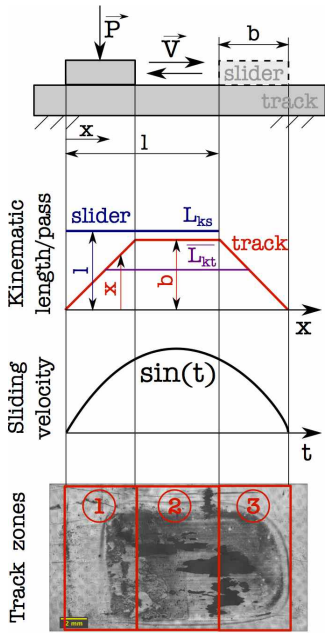

Figure 5.3: Features of the kinematic length for slider and track samples

5.2 Dissipation in polymer/polymer friction and wear

In order to study the frictional dissipation and wear of epoxy/epoxy sliding system, two approaches are developed. We will start with a macroscopic approach, which allow us to investigate parameters, such as mass loss and wear rate, evolution of friction during each cycle and throughout the whole test, dissipated frictional energy, as well as an estimate of the temperature arising in contact. This will be followed by the microscopic observations of worn surfaces after several test durations with the purpose of wear mechanisms detection and establishment of plausible wear history.

5.2.1 A macroscopic approach

5.2.1.1 Wear law

In order to study the mass loss as a macroscopic wear characteristic, all samples were weighed before and after each test. The mass losses of track and slider are plotted as a function of their respective kinematic length under four sliding conditions in Fig. 5.4 (a) and (b), respectively. We observe that all samples follow the same tendency: the mass loss ΔM increases linearly with the kinematic length L_k. Thus, we can define the linear dependency with the slope a_w, such as

$$\Delta M = a_w \cdot L_k = W \cdot \rho \cdot L_k = W_s \cdot \rho \cdot P \cdot L_k \tag{5.2}$$

where W is the wear rate, i.e. volume loss per distance unity; W_s is the specific wear rates, i.e. wear rate per normal load unity and ρ is the material density.

The slope value a_w of the slider varies from $0.10 \cdot 10^{-6}$ g/mm for the less severe conditions (20 mm/s and 20 N) to $1.3 \cdot 10^{-6}$ g/mm for the most severe conditions (120 mm/s and 50 N), while a_w of the track varies from $0.38 \cdot 10^{-6}$ g/mm to $1.88 \cdot 10^{-6}$ g/mm under similar conditions. The values of the slope are indicated on Fig. 5.4 (a) and (b).

We can notice, that for both samples, the conditions 4 produce much more mass loss, than other three conditions, under which mass loss is rather similar. Under similar conditions, the mass loss rate, i.e. the slope of the fitting curves, of the track is higher than that of the slider.

This linear behaviour seems in agreement with Archard's empirical wear law [25] postulated for metallic surfaces:

$$V_{wear} = k_w \frac{PL}{H} \tag{5.3}$$

where k_w is the wear coefficient, H is the hardness of the surface which is worn away, L is its kinematic length and P is the normal force.

Archard's wear coefficient k_w characterizes the volume loss. It is independent of velocity and normal load, but varies with the material in contact. Therefore, in order to obtain wear loss in this classical form, we divide our wear coefficients by the epoxy density. These coefficients, as well as wear rates and specific wear rates, are calculated using the values of $H = 256.7$ MPa and $\rho = 1.1$ g/cm^3 (see Chapter 2). Average wear rates, wear coefficients and specific wear rates of slider and track for four sliding conditions are reported in Table

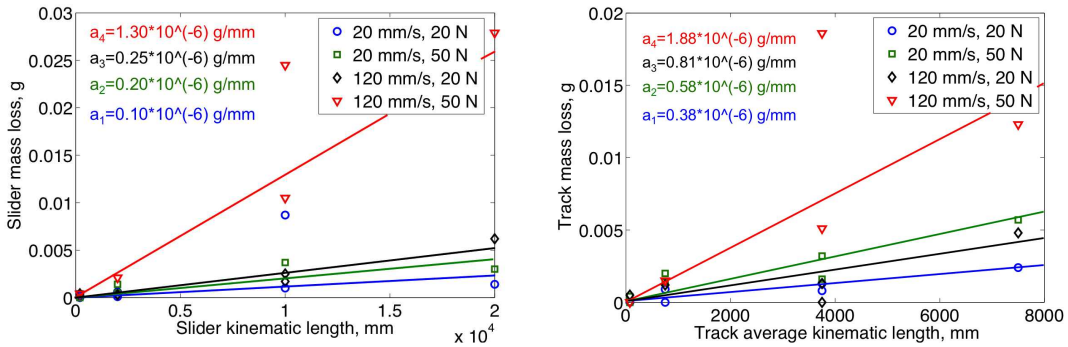

Figure 5.4: Measured mass losses of (a) slider and (b) track and their linear fits. The average sliding velocity and normal force corresponding to the four experimental conditions are presented in the legend. The slope values are indicated with the same colors as the experimental data points

5.3.

Conditions	1	2	3	4
Wear coefficient				
Slider	$1.2 \cdot 10^{-3}$	$0.9 \cdot 10^{-3}$	$2.9 \cdot 10^{-3}$	$6.1 \cdot 10^{-3}$
Track	$4.4 \cdot 10^{-3}$	$2.7 \cdot 10^{-3}$	$9.5 \cdot 10^{-3}$	$8.8 \cdot 10^{-3}$
Total	$3.1 \cdot 10^{-3}$	$1.9 \cdot 10^{-3}$	$5.5 \cdot 10^{-3}$	$10.3 \cdot 10^{-3}$
Wear rate, m^3/m				
Slider	$0.9 \cdot 10^{-10}$	$1.8 \cdot 10^{-10}$	$2.3 \cdot 10^{-10}$	$11.8 \cdot 10^{-10}$
Track	$3.5 \cdot 10^{-10}$	$5.3 \cdot 10^{-10}$	$7.4 \cdot 10^{-10}$	$17.1 \cdot 10^{-10}$
Total	$2.4 \cdot 10^{-10}$	$3.8 \cdot 10^{-10}$	$4.3 \cdot 10^{-10}$	$20.0 \cdot 10^{-10}$
Specific wear rate, m^3/Nm				
Slider	$0.5 \cdot 10^{-11}$	$0.4 \cdot 10^{-11}$	$1.2 \cdot 10^{-11}$	$2.4 \cdot 10^{-11}$
Track	$1.8 \cdot 10^{-11}$	$1.1 \cdot 10^{-11}$	$3.7 \cdot 10^{-11}$	$3.4 \cdot 10^{-11}$
Total	$1.2 \cdot 10^{-11}$	$0.8 \cdot 10^{-11}$	$2.2 \cdot 10^{-11}$	$4.0 \cdot 10^{-11}$

Table 5.3: Wear volume loss characteristics of epoxy/epoxy contact

An increase in the wear characteristics, reported in Table 5.3, with the severity of tribological conditions is observed for both samples.

We can notice, that the wear coefficients and wear rate of epoxy/epoxy are of the same order with those between identical metals, as reported by Archard [25]. He measured $k_w = 7 \cdot 10^{-3}$ and $W = 1.57 \cdot 10^{-11}$ m^3/m for mild steels and $k_w = 13 \cdot 10^{-3}$ and $W = 6 \cdot 10^{-14}$ m^3/m for hard steels. The sliding speed of 1.8 m/s and normal load of 4 N were applied. Wear tests of epoxy pin against steel disk under a normal load of 20 N and linear speed of 0.314 m/s were carried out in [101]. The authors report values of 3.5 $\cdot 10^{-12}$ m^3/Nm for the specific wear rate and 0.45 for the friction coefficient. This specific wear rate differs by 1 order of magnitude with our values. This divergence must be due

to the wear mechanisms acting in polymer/hard metal and polymer/polymer contacts. In the former, the main wear mechanisms are reported to be abrasion by hard steel asperities and formation of a polymer transfer layer. In the latter, the abrasive wear is less likely because of the similar nature and hardness of two contacting bodies.

However, although the increase of the mass loss is linear with the kinematic length, we should emphasize that, in contrast to the Archard model, our polymer/polymer wear coefficient depends on the normal load and on the velocity. This means that, in contrary to contacts obeying Archard's law, our contacts are not fully plasticized under tested conditions.

The total mass loss of both samples is presented as a function of the slider kinematic length in Fig. 5.5. It also follows an Archard-like linear dependence, which allows us to calculate wear coefficient k_w, wear rate W and specific wear rate W_s. These coefficients, presented in Table 5.3, behave similarly to those of slider or track: they increase with the sliding speed and normal load growth.

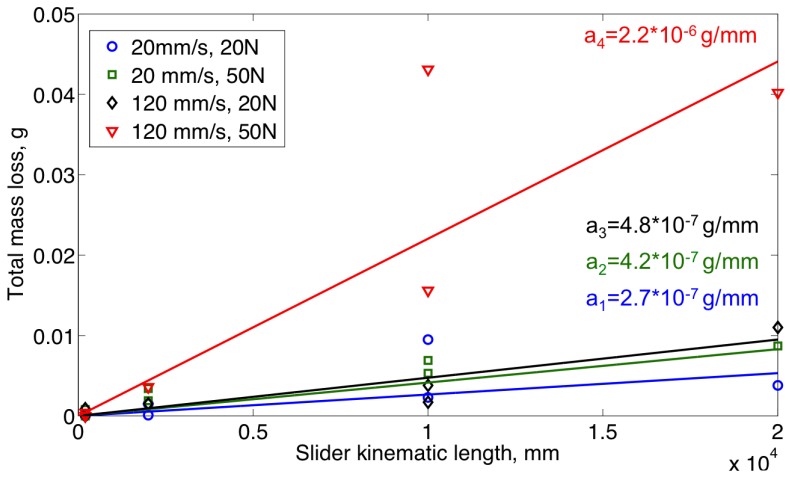

Figure 5.5: Measured mass losses of both track and slider as a function of the slider kinematic length, and their linear fits

5.2.1.2 Friction and dissipated energy

During an experiment, friction and normal forces are continuously measured at each point of the motion. Since the normal force remains constant at either 20 or 50 N, it is possible to define and calculate Coulomb friction coefficient. Resulted friction coefficients are presented in the form of maps, where $x-$axis corresponds to the cycle number, $y-$axis corresponds to the amplitude of sliding during one pass. The friction coefficient values are distinguished by color: the dark red color corresponds to the maximal value of 1.2, while the blue color indicates low friction. The relative symmetry of the friction values between back and forth passes allows us to average them for each cycle.

Four such frictional maps of 500 cycle tests for different tribological conditions are presented in Fig. 5.6. The sinusoidal velocity profile is schematized on the left of each map. It can be seen from Fig. 5.6 (a) that friction remains rather stable with the speed variation except at the end of the pass, where a blue zone, corresponding to low friction value, appears. This zone of low friction is due to a default of the parallelism between two planes and could also indicate the evacuation of the 3rd body. This behavior remains constant with time, as the number of cycles increases. An augmentation of the normal force to 50 N leads to a rather low friction coefficient on first cycles before it increases to 0.7 beyond 50 cycles, as shown in Fig. 5.6 (b). Oscillations depicted in Fig. 5.6 (c, d) at 120 mm/s are due to a tribometer instability, which occurs under high testing frequency. The frequency of this oscillation is about 156 Hz, which is close to the first natural frequency of the rig 173.3 Hz. However, a stabilized value of friction for 120 mm/s and 20 N is reached at 0.7. Under the highest sliding and loading conditions, the mean value of the friction coefficient falls to approximately 0.6 after 300 cycles. These maps seem to indicate that the friction is roughly independent of the applied normal force and of the velocity in the considered range of experimental conditions.

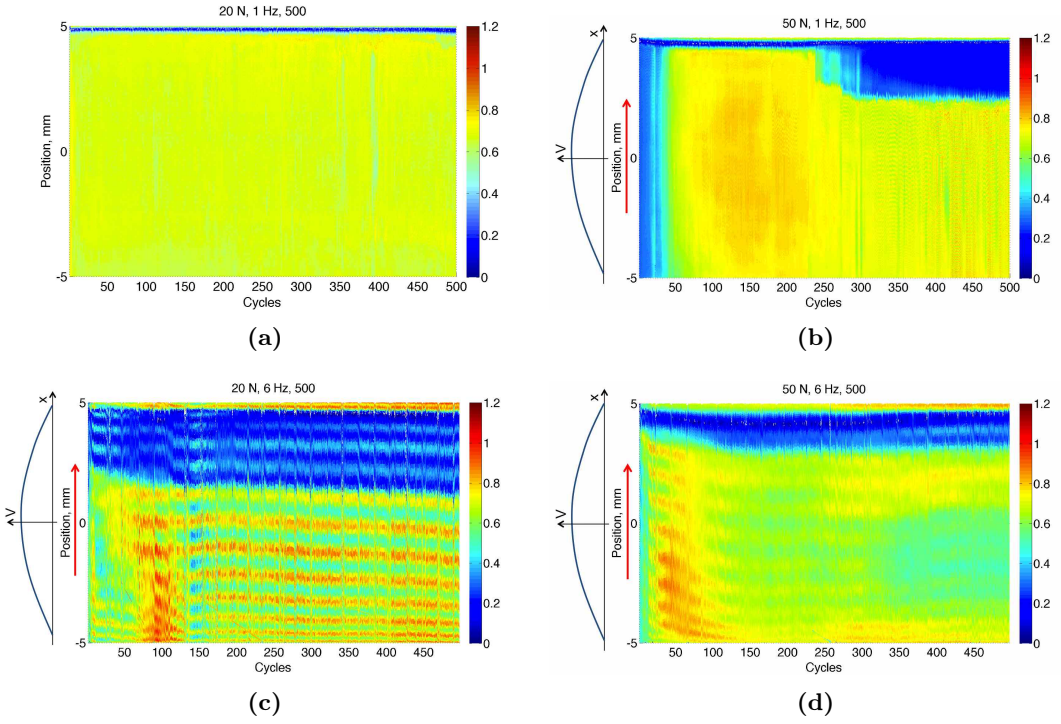

Figure 5.6: Friction maps for (a) 20 mm/s, 20 N; (b) 20 mm/s, 50 N, (c) 120 mm/s, 20 N, (d) 120 mm/s, 50 N of sliding velocity and normal force, respectively. The friction coefficient is averaged between back and forth for each cycle. The sliding distance on $y-$axis and cycle number on $x-$axis are limited by 10 mm and 500 cycles, respectively

Friction and wear processes generate frictional energy E_d, which dissipates in cracking, deformation, heating or tribochemical reactions. It can be calculated as

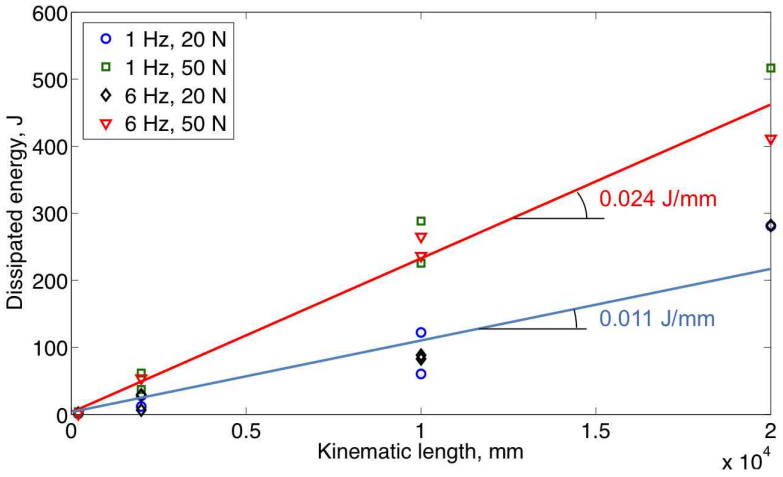

Figure 5.7: Dissipated energy as a function of the slider kinematic length for four tribological conditions

$$E_d = \int_0^{t_{exp}} F(t)V(t)dt \tag{5.4}$$

where $F(t)$ is the frictional force as a function of time, $V(t)$ is the sliding speed as a function of time and t_{exp} is the total duration of the frictional experiment.

Fig. 5.7 presents the dissipated energy calculated for four tribological conditions as a function of the slider kinematic length. We notice that it increases linearly with the slider kinematic length. Two families of experimental points can be distinguished: one for the tests under the normal load of 20 N and another for the tests under 50 N. The slopes of the linear curves, presenting these two tendencies, are approximatively equal to 0.011 J/mm and 0.024 J/mm.

Taking into account the results issued from the friction maps, we may consider that $F(t)_{av} = \mu_{av}P$ and the dissipated energy E_d becomes:

$$E_d = \sum_{i=1}^{N_{cycle}} \int_0^{1/f} F(t)V(t)dt = \sum_{i=1}^{N_{cycle}} \mu_{av}P \int_0^{1/f} |V_{max}sin(2\pi ft)|dt = \mu_{av}PL_{ks} \tag{5.5}$$

where L_{ks} is the total kinematic length of the slider. This equation validates the experimental linear dependance of the dissipated energy with the kinematic length and the strong influence of the normal force.

5.2.1.3 Correlation between mass and energy losses?

Once we have determined mass and energy losses in our epoxy/epoxy sliding system, we may wonder if these two independently measured characteristics are related. The energy-mass diagram, presented in Fig. 5.8, indicates the scatter of calculated dissipated energy as

a function of measured total mass loss of both samples. It can be seen that the dissipated energy varies linearly with the total mass loss, following:

$$E_d = a_d \Delta M = (V_0)^2 \Delta M \tag{5.6}$$

where the coefficient of proportionality a_d has the units of the square of a velocity. This critical velocity V_0 is of the order of magnitude of $5 \cdot 10^3$ m/s, and it varies with the tribological conditions.

According to Eq. 5.5 and Eq. 5.6, we can calculate that:

$$\Delta M = \frac{\mu_{av} P}{V_0^2} L_{ks} \tag{5.7}$$

This equation confirms the linear dependance of the total mass loss and the slider kinematic length. It also allows us to explain the apparent evolution of the wear coefficient with the tribological conditions (see Table 5.3) and the discrepancy with the Archard law related to the partially plastic contact.

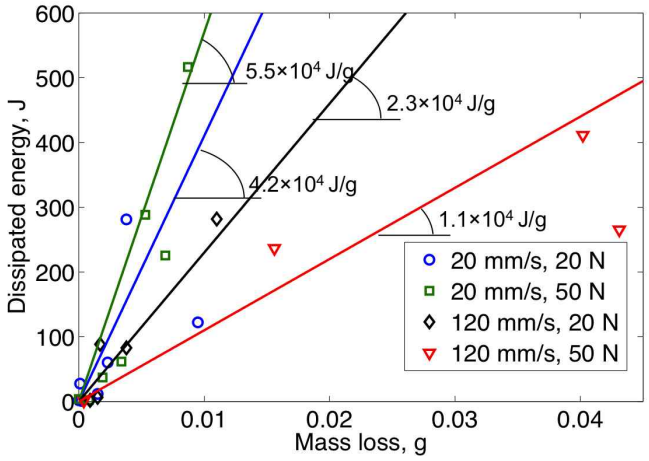

Figure 5.8: Dissipated energy as a function of measured total mass loss points. The slopes of lines are calculated for four conditions. The slope colours correspond to experimental data points colours

Therefore, by this approach we can identify the linear dependency between two independently measured macroscopic parameters, that is to say mass loss and dissipated energy. We can also notice that values of $E_d/\Delta M$ are rather large, which could indicate an influence of heating and viscoelastic dissipation, which are typical for polymers.

5.2.1.4 Contact temperature distribution

Relative motion between two bodies produces a work against frictional forces, which is mostly dissipated in heating of contact zone. Arising from real contact regions, the heat propagates into subsurface regions and create temperature gradients. The temperatures within the contact are quite difficult to measure. However, they are of great importance

because they can initiate chemical reactions of surface materials or cause softening. That is why several models of contact temperature calculation were created.

Archard [102], Jaeger [103] and Blok [104] consider the contact of two bodies: one of them, moves with a velocity V upon another, stationary one. The quantity of generated frictional heat q per surface unity and time unity is given by

$$q = \int_0^{t_{exp}} \frac{F(t)}{A_r(t)} \frac{dV}{dt} dt \tag{5.8}$$

or by its mean value:

$$q = \frac{\mu_{av} P V}{A_r} \tag{5.9}$$

where A_r is the real contact area.

The maximal temperatures arising in the contact of a short duration is called flash temperature. The real contact temperature is the sum of bulk temperature θ_b, which is ambient, and flash temperature rise $\Delta\theta$:

$$\theta = \theta_b + \Delta\theta \tag{5.10}$$

This quantity of heat is distributed between two bodies by different manner. Indeed, the problem is not symmetrical, the heat source is stationary for the moving slider and moving for the stationary track. The coefficient of heat partition δ is introduced. Let us now calculate the temperature gradients in both solids, and then this coefficient.

1. **Slider**. The heat source is stationary for the slider, therefore, its temperature gradient is calculated simply by the following equation

$$\Delta\theta_{sl} = \frac{\delta q b}{k_{sl}} \tag{5.11}$$

where k_{sl} is the thermal conductivity of the slider material and b is the characteristic length of contact.

2. **Track**. In this case, the heat source is moving, and the temperature gradient depends on the ratio between the contact time for the heat source $t_c = b/V_{sl}$ and the time of the temperature propagation in the track volume $t_d = b^2/4\chi_{tr}$. In these relations, b is the contact width, V_{sl} is the velocity of the slider, χ_{tr} is the thermal diffusivity of the track material. This ratio is introduced by the Peclet number L_P as following

$$L_P = \frac{t_d}{t_c} = \frac{V_{sl} b}{4\chi_{tr}} \tag{5.12}$$

The thermal diffusivity can be calculated as $\chi = k/\rho c_p$, where ρ is the density, c_p is the specific heat capacity, and k is the thermal conductivity. The value of this non-dimensional speed criterion can give an estimate of the heat propagation profile:

- If $L_P < 0.1$, the contact time is much higher than the time required for heat propagation. Thus, the moving heat source can be considered as stationary, and the temperature gradient is similar for both contacting bodies. It is schematically drawn

in Fig. 5.9 (a).

- $0.1 < L_P < 5$ is the intermediate mode.
- If $L_P > 5$, the contact time for the stationary body is not high enough to get the heat to propagate deeply. The temperature of the stationary body becomes higher than that of the moving one. Fig. 5.9 (b) presents a schematic temperature gradient corresponding to high Peclet values.

Therefore, the average temperature rise for the stationary body, the track, is given by [103]

$$\Delta\theta_{av} = \frac{(1-\delta)q}{k_{tr}}\sqrt{\frac{\chi_{tr} b/2}{V_{sl}}} \tag{5.13}$$

We consider that at the surface, the temperature rise is equal for both solids. Thus, we can calculate the coefficient of partition:

$$\delta = \frac{1}{2+\sqrt{\frac{V_{sl} b}{\chi_{tr}}}} = \frac{1}{2+\sqrt{2L_P}} \tag{5.14}$$

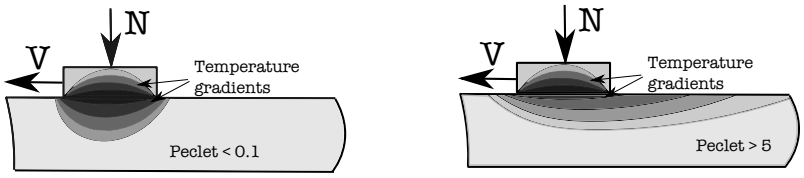

(a) (b)

Figure 5.9: Temperature gradients corresponding to (a) low and (b) high Peclet number

Thermal conductivity k, W/m K	Density ρ, kg/m^3	Specific heat capacity c_p, J/kg K	Thermal diffusivity χ, m^2/s
0.19	$1.1 \cdot 10^3$	$1 \cdot 10^3$	$0.17 \cdot 10^{-6}$

Table 5.4: Epoxy thermal properties required for flash temperature calculation

Considering the average sliding velocity $V_1 = 20$ mm/s and $V_2 = 120$ mm/s, demi contact width $b/2$ of $3 \cdot 10^{-3}$ m and thermal properties of epoxy given in Table 5.4, we obtain the Peclet numbers of $L_{P1} = 177$ and $L_{P2} = 1059$, both larger than 5. Coefficient of heat distribution between two contacting bodies is equal $\delta_1 = 0.05$ for conditions 1 and 2 and $\delta_2 = 0.02$ for conditions 3 and 4. This means that only 5 and 2 % of heat is conducted through the slider under V_1 and V_2, respectively. Therefore, the temperature gradient propagated into the fixed track is much higher. On the contrary, the temperature gradient of the slider is very low, and the temperature is ambient θ_b in the subsurface layers

of the slider. We will further calculate the contact temperature rise and its gradient in the track.

The real contact area of our plane/plane contact is unknown. Moreover, it varies significantly during the sliding process: at the beginning, it can be considered as a multiple asperity contact, whose area quickly grows as wear occurs; but it remains difficult to estimate taking into account the continuous repetitive third body formation and evacuation from the contact. We will consider two limit values for the real contact area:

1. The real contact area A_{r1} equal to the apparent one. The apparent area of slider is measured for each slider individually.

2. The real contact area A_{r2} according to Bowden and Tabor's theory: $A_r = P/H$, where P is the normal load and H is the hardness of the softest material. Therefore, for $P = 20$ N, $A_r = 20/(256.7 \cdot 10^6) = 8.8 \cdot 10^{-8}$ m^2, and for $P = 50$ N, $A_r = 50/(256.7 \cdot 10^6) = 19.5 \cdot 10^{-8}$ m^2.

The examples of quantity of heat per area unit q and relative average $\Delta\theta_{av}$ temperature rise values calculated with Eqs. 5.9 and 5.13, respectively, for a test of 100 cycles are presented in Table 5.5. The minimal and maximal values corresponding to two limit cases of real contact area are also given.

Conditions	Quantity of heat/ area unit q, W/m^2		Relative temperature rise, $\Delta\theta_{av}$, °C	
	A_{r1}	A_{r2}	A_{r1}	A_{r2}
20 mm/s; 20 N	$4 \cdot 10^3$	$3.5 \cdot 10^6$	4	2973
20 mm/s; 50 N	$13 \cdot 10^3$	$3.3 \cdot 10^6$	11	2761
120 mm/s; 20 N	$33 \cdot 10^3$	$26.6 \cdot 10^6$	12	9526
120 mm/s; 50 N	$64 \cdot 10^3$	$17.5 \cdot 10^6$	23	6261

Table 5.5: Total quantity of heat per area unit and relative average temperature rises for tracks after 100 cycles for limit cases of contact area A_{r1} and A_{r2}

The summary of relative average temperature rises for all tests under four tribological conditions as a function of the slider kinematic length is presented in Fig. 5.10(a, b). Fig. 5.10(a) presents the temperature rise calculated with the real contact area A_{r1}, while the temperature rise calculated with the real contact area A_{r2} is shown in Fig. 5.10(b). We can divide these diagrams onto two zones. The first several cycles of temperature increase represent a run-in period and are not representative of the temperature rise tendency. The second region is presented by the stabilized value of the temperature rise observed under all conditions. We notice that the temperature rise is higher for the higher sliding velocities.

Although the real flash temperature rises are unknown due to the lack of knowledge of real contact areas, they should be between the values presented in Fig. 5.10(a) and (b) and Table 5.5. The values of temperature rise calculated with A_{r2} are very high for all conditions. This can be explained by our conclusion from mass and energy loss sections: the contact area is not fully plasticized. Therefore, the equation of Bowden and Tabor

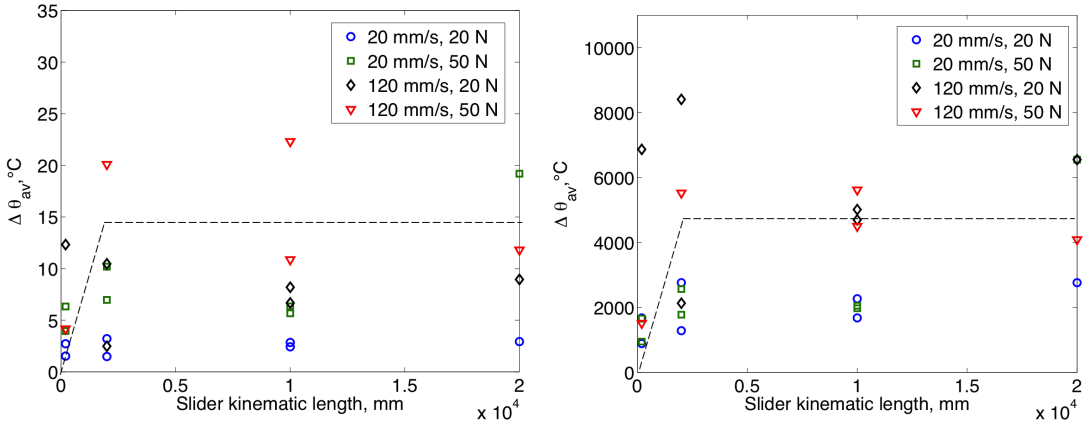

Figure 5.10: Average surface temperature rise as a function of slider kinematic length under four tribological conditions considering (a) real contact area A_{r1}, (b) real contact area A_{r2}

certainly overestimates the contact area and temperature rise. Taking into account that the glass transition temperature of epoxy is about 120 °C, such temperature rises, along with the dynamical loading, certainly change the polymer state to rubber-like, at least on local surface zones.

The track temperature gradient under 20 mm/s and 20 N, after 1000 cycles is plotted in Fig. 5.11. The real contact area calculated according to $A_r = P/H$ is considered. We assume that the bulk temperature of 25 ° C is attained in the depth of the half contact width. The temperature decreases rather quickly: at a depth of 0.75 mm, it has a half of its surface value.

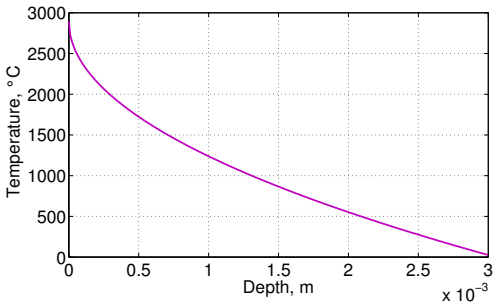

Figure 5.11: Temperature gradient for the track under 20 mm/s, 20 N after 1000 cycles, considering real contact area A_{r2}

5.2.2 A microscopic approach

The processes occurring within the plane/plane sliding contact are very complex, and the macroscopic approach only links the initial and final surface states. We may wonder what happens during sliding. What are the mechanisms at stake? In this section, we will attempt to retrace the history of the sliding contact, based on the micro and macro observations of the surfaces and their correlation to the macro parameters such as temperature, energy or mass loss.

5.2.2.1 Overview of worn surfaces

The surfaces of both slider and track are observed after each frictional test. The first overview observations allow us to notice, that the worn surfaces after the tests of 100, 500 and 1000 cycles could be distinguished into two qualitatively different types. The examples of slider and track couples, worn accordingly to these types are given in Fig. 5.12 and 5.13.

Type 1. Fig. 5.12 shows a couple of slider and track surfaces after 500 cycles under 20 N and 20 mm/s. We can see that the width of the track worn surface corresponds to that of the slider, which is not entirely worn due to the non parallelism between two planes. The length of the track worn zone is coherent to the central zone of maximal kinematic length, see Fig. 5.3. The track surface profile, following the blue arrow, is shown over its photo. The track worn zone contains several individual macrogrooves, which join to form a bigger one. The small quantity of matter piles up on several worn zone borders of both slider and track, but the borders are distinct, and a general worn surface level is lower than initial surface level. The worn zones of both solids are covered with the third body formed into rollers perpendicular to the sliding direction.

Type 2. The slider and track couple surfaces after the test of 500 cycles under 20 N and 120 mm/s are shown in Fig. 5.13. The width of the track worn zone corresponds to the length of the worn zone of the slider. The partially worn slider, as well as the asymmetry of the track worn zone, are due to the lack of the parallelism between two plane samples. However, we can notice that the worn zones look fundamentally different compared to those in Fig. 5.12. A surface profile taken along the track worn zone shows that its surface level is elevated. Due to the higher surface level, the worn zone borders present the smooth transition between two levels. Some matter quantity is collected on the left side of the worn zone, although the black areas correspond to deep hollows. Small cracks perpendicular to the sliding direction can be seen in the middle of the track worn zone. The slider worn surface resembles to the track one with the black hollows, perpendicular cracks and smooth lower border.

It is noteworthy that the surfaces presented in Fig. 5.12 and 5.13 are worn under the similar normal load and test duration, only the sliding speed is different. The similar effects are observed under other normal load after 100, 500 and 1000 cycles: the worn zones resemble to those of Type 1, as in Fig. 5.12, under mean sliding velocity of 20 mm/s and to those of Type 2, as in Fig. 5.13, under mean sliding velocity of 120 mm/s. On the other hand, the track and slider surfaces after 10 cycles are only covered by several grooves. Due to the divergence between two plane samples, the initial contact area can

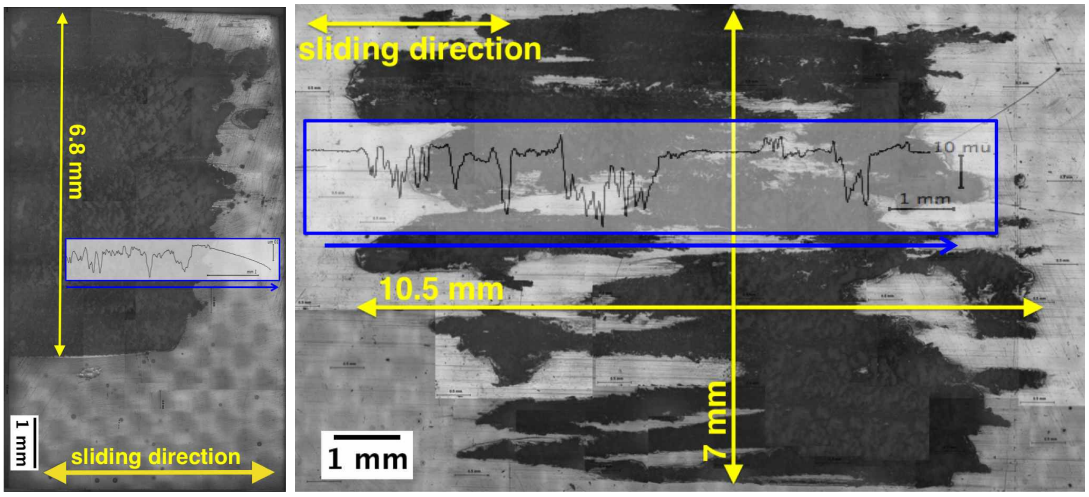

(a) (b)

Figure 5.12: Epoxy (a) slider and (b) track couple after 500 cycles under 20 N and 20 mm/s. The surface profile and the line of its measurement are shown with blue color. The visible pattern outside of the worn zone is on the back sample surface

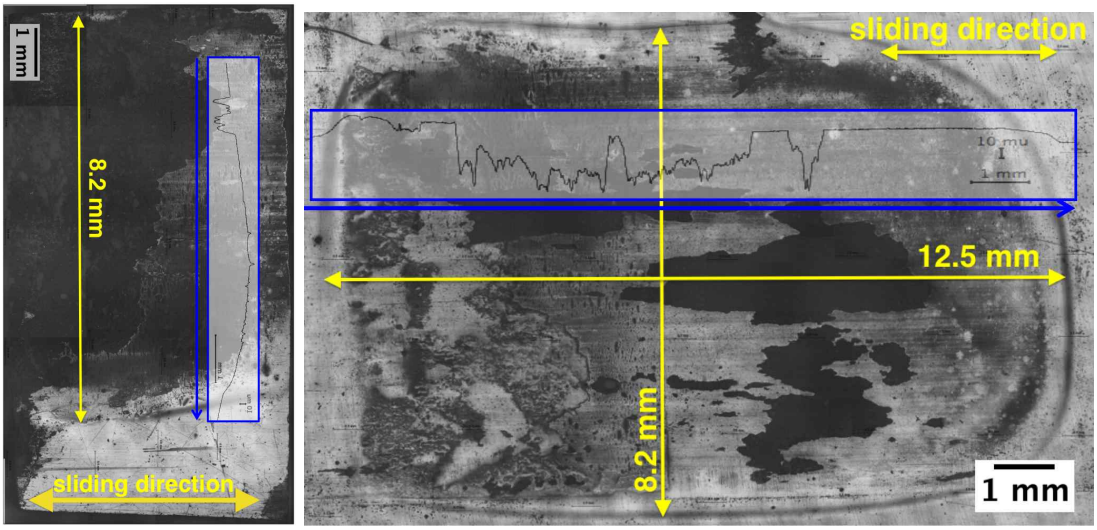

(a) (b)

Figure 5.13: Epoxy (a) slider and (b) track couple after 500 cycles under 20 N and 120 mm/s. The surface profile and the line of its measurement are shown with blue color. The visible pattern outside of the worn zone is on the back sample surface

vary dramatically between the tests. Therefore, it is difficult to judge about the conditions of the transition between the several grooves and one of discussed wear zone types, but they must be somewhere between 10 and 100 cycles, as it is schematized in Fig. 5.14.

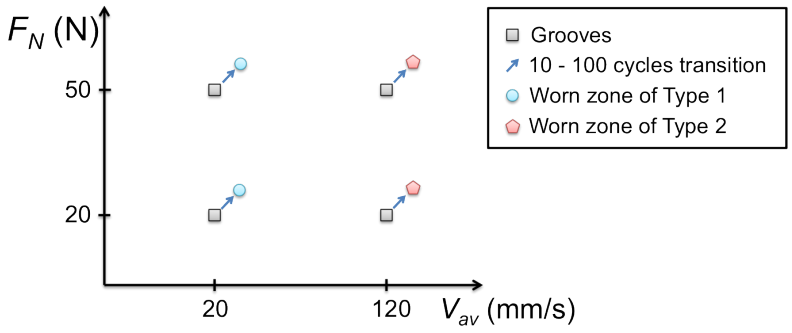

Figure 5.14: Evolution of epoxy wear modes from 10 to 100 cycles depending on normal force and average sliding velocity

The macroscopic photos of all worn track samples are treated with the software ImageJ in order to measure their worn areas. The damaged surface areas A_w are estimated after this image treatment, as it is shown in Fig. 5.15. All types of surface damage and plastic deformation are considered to be inside the worn area.

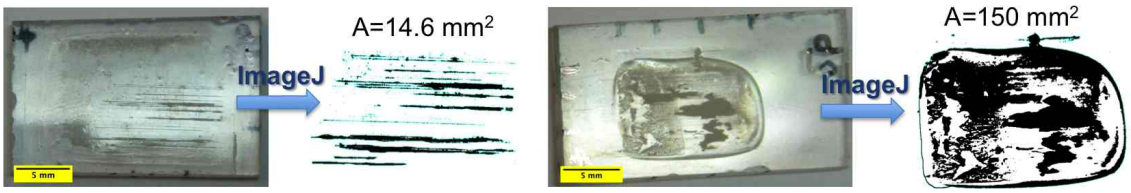

Figure 5.15: Image treatment of worn track samples and worn area estimate with the software ImageJ. The left image corresponds to a test under 20 N and 20 mm/s after 100 cycles, while the right image shows the worn area after 500 cycles under 20 N and 120 mm/s

Because of the lack of parallelism between two plane samples, the contact width is different for all the experiments. However, we can estimate the final worn area width by a measurement of the slider worn zone width. For instance, the widths of slider worn area in Fig. 5.12 (a) and Fig. 5.13 (a) are equal to 6.8 and 8.2 mm, respectively. If the worn area is represented by several individual grooves, its width is defined and measured between the two extreme grooves. This contact width is estimated on the slider photographs with the ImageJ software. Therefore, we can normalize the track worn area by its width w and theoretical track worn zone length $l + b$:

$$A_n = \frac{A_w}{w \cdot (l + b)} \tag{5.15}$$

These normalized track worn areas are plotted versus slider kinematic length in Fig. 5.16. We observe that the track worn area grows quickly at the beginning of the sliding, and more slowly after this initial period of $10 - 100$ cycles, depending on the tribological conditions. We can notice that the maximal value of normalized worn area is higher than 1. This is due to plastic deformations of its borders: the track matter is pushed by the slider. We can suppose that there is some value of the kinematic length, when the normalized worn area is maximal and similar for all the conditions. Therefore, the difference in worn area growth rate between tribological conditions should be observed only before this value. On our diagram, we can see that at $2 \cdot 10^4$ of slider kinematic length or 1000 cycles, the normalized track worn area is almost similar under all tested conditions.

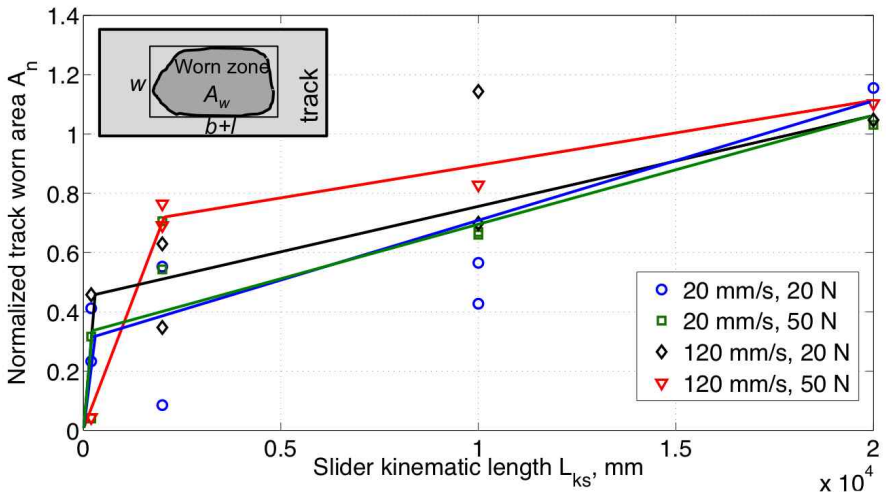

Figure 5.16: Normalized track worn area A_n versus slider kinematic length L_{ks}

5.2.2.2 Energy dissipated in surface damage

On a macroscopic approach, the dissipated energy was found to be linearly proportional to the weighed total mass loss. However, the worn surface observations and topographic measurements reveal that some parts of the track surfaces are elevated, relatively to the initial surface level. This means that some material quantity might be transferred from slider to track and remains on the track surface. This process requires energy dissipation, but is not associated with any mass loss. On the other hand, a part of the frictional energy dissipates in the surface plastic deformations also without linked material loss. Therefore, the energy dissipation should be associated not only to the mass loss, but rather to the worn zone area growth and wear mechanisms.

This analysis allows us to plot the calculated dissipated energy E_d versus the track worn area A_w under four tribological conditions, see Fig. 5.17. In this diagram, we can distinguish two regions: the initial fast growth of worn area with frictional energy until approximatively $A_w = 95$ mm^2, followed by a faster growth of the track worn area associated with an increase in dissipated energy. With little difference in the slope, the

initial linear region occurs under all tested tribological conditions. The approximative rate of dissipated energy in this zone is 0.5 J/mm^2. An increase of the number of individual grooves and their unification expand quickly the worn area. We can assume that this region corresponds essentially to the abrasion producing the grooves, as we have seen on the samples photographs. When the worn area is rather large, other wear mechanisms interfere. When the maximal damaged area is reached, the frictional process continues to dissipate energy by surface heating and eventual two or three-bodies abrasion, adhesive or fatigue wear and thermal transformation.

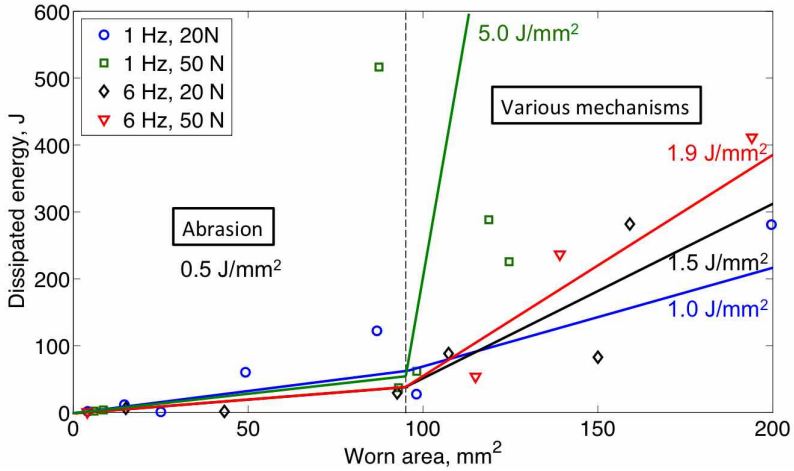

Figure 5.17: Energy dissipated in the formation of the track worn area

If the first region is rather independent on the tribological conditions, the second region seems to indicate a strong dependence of dissipated energy rate, and associated wear mechanisms, with experimental conditions. This coheres with our surface damage observations, schematized in Fig. 5.14, stated that under all conditions the first 10 cycles produce the grooves, and the following rubbing causes different wear mechanisms depending on tribological conditions.

5.2.2.3 Wear mechanisms definition and description

In this section, we will observe the worn surfaces with higher magnification in order to distinguish different wear mechanisms and to classify the observed phenomena.

We start with observations of worn grooves after 10 cycles, which we have seen on the sample macrophotographs. Fig. 5.18 (a) presents such grooves found on the track surface after a test under 50 N and 20 mm/s. The shape of worn zone borders can be associated to the ductility or brittleness of the deformed material. This brittleness is identified by the groove notched borders. The difference in groove profile and plane view of two types is schematized in Fig. 5.19. We can observe a smooth pile-up on the groove borders and its end on our photo, which indicates the ductility of these grooves. The grooves are clean, i. e. without any inserted particles. Thus, we suppose that they are produced by the hard

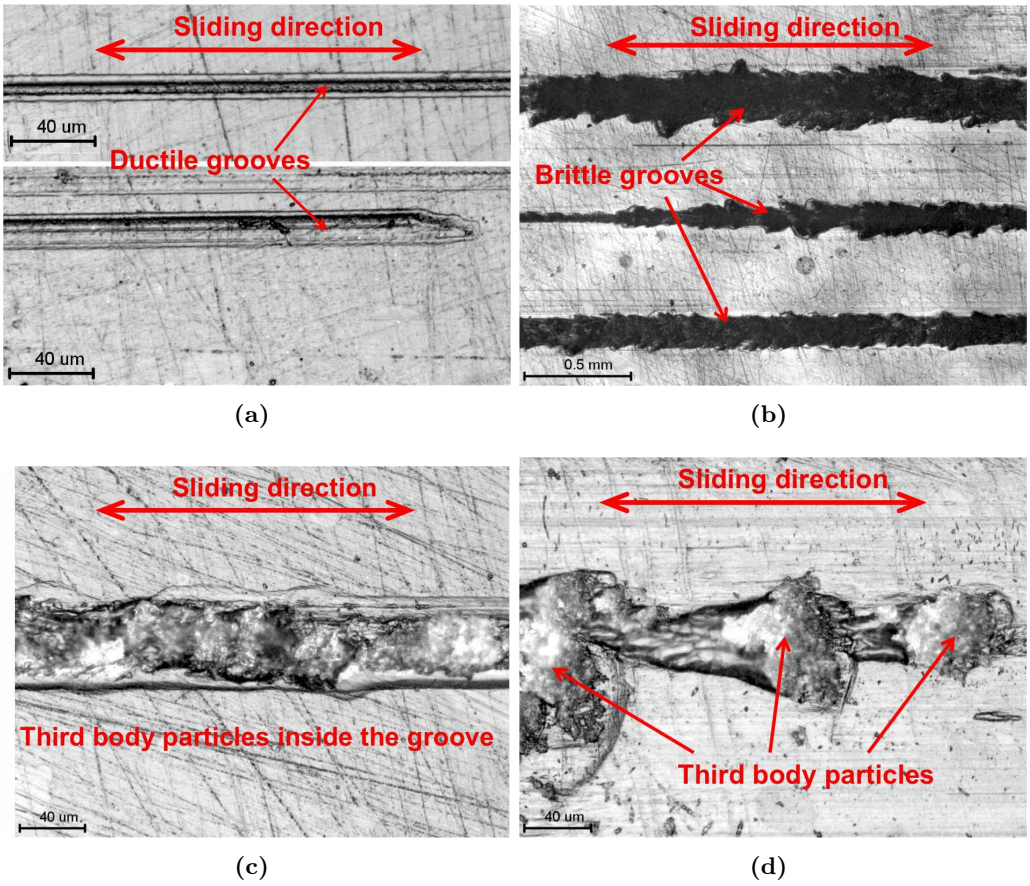

Figure 5.18: Microscopic track surface images of (a) individual ductile grooves formed under 20 mm/s and 50 N after 10 cycles (x20); (b) brittle grooves (x2.5), (c) third body particles ploughing track surface (x20); (d) third body particles remained inside a groove (x20). (b-d) images are taken on the same track sample after 100 cycles under 20 mm/s and 50 N

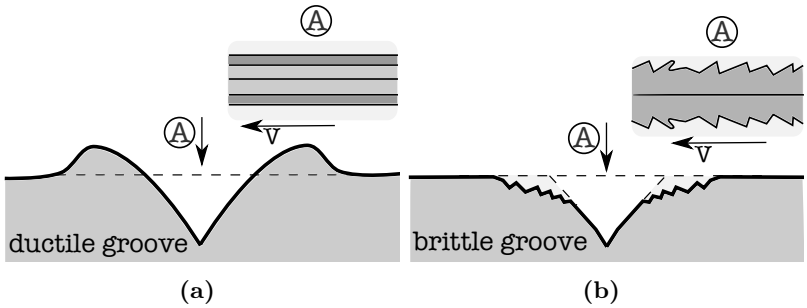

Figure 5.19: Schematized profile and inserted plane view of (a) ductile groove and (b) brittle groove

asperities or inclusions of counterbody, i. e. two-bodies abrasion.

The transition between ductile and brittle grooves can occur depending on normal and tangential forces, shape and size of the indenter, viscoelastoplastic polymer properties and environmental conditions [105]. Therefore, the larger and deeper grooves are brittle, for instance, as after 100 cycles under 20 mm/s and 50 N in Fig. 5.18 (b).

Fig. 5.18 (c) and (d) present the third body, i.e. worn material debris, particles inserted into the track surface. These particles appear and grow during the sliding and plough the counter surface. They enlarge and deepen already formed groove in Fig. 5.18 (c) and create new worn zone in Fig. 5.18 (d). We can observe smooth transitions of surface level, which indicate that the particles and the surface material are soft.

Grooves, similar to those presented in Fig. 5.18 (a), are detected on the track and slider surfaces after 10 cycles under any conditions. When the worn surfaces are larger, i.e. on Type 1 worn surfaces, as in Fig. 5.12, phenomena similar to Fig. 5.18 (b-d) are observed. However, wear mechanisms responsible to the Type 2 worn surface formation, as in Fig. 5.13, are qualitatively different. The magnified photographs of this track sample worn zone are depicted on Fig. 5.20 (a-d), a schema of their location on the worn area is drawn in the left upper corner of each image.

Adhesive forces grow under higher normal loads and sliding speeds with repeated fatigue loading and can damage the surfaces. Its consequences, such as material pull out and surface cracks perpendicular to the sliding direction, are presented in Fig. 5.20 (a, b). We notice that these cracks and craters are typical for rubber wear. Moreover, the similar nature of both contact samples and severe tribological conditions favor material transfer between the surfaces. This results in the adherence of compacted wear debris into the track surface, see Fig. 5.20 (c) or the general elevation of surface level of the worn zone, as it is emphasized on Fig. 5.20 (d).

Once the mechanisms have been defined, it is necessary to try to associate them with tribological conditions, test durations, *etc.* We have first noticed that for a low number of cycles and independently of the tribological conditions, only grooves are depicted on the surfaces. For a higher number of cycles, we have noticed that Conditions 1 and 2 cause the surface damage of Type 1, while Conditions 3 and 4 cause the surface damage of Type 2. Moreover, the worn surfaces of Type 1 are covered by a cloud of the third body particles, while Type 2 worn surfaces are rather solid and clear. Higher velocities favor the third body evacuation from the contact, while under low velocity it can remain into the sliding area and slide or roll following the slider. This induces a decrease of the real contact area and fast cooling of both surfaces. Furthermore, calculated contact temperatures show that they are generally higher for Conditions 3 and 4, than for Conditions 1 and 2 on similar contact area. On the other hand, high contact area of Type 2 surfaces and temperature growth larger for high velocity cause polymer state transformation to the rubber-like and high adhesion between the surfaces.

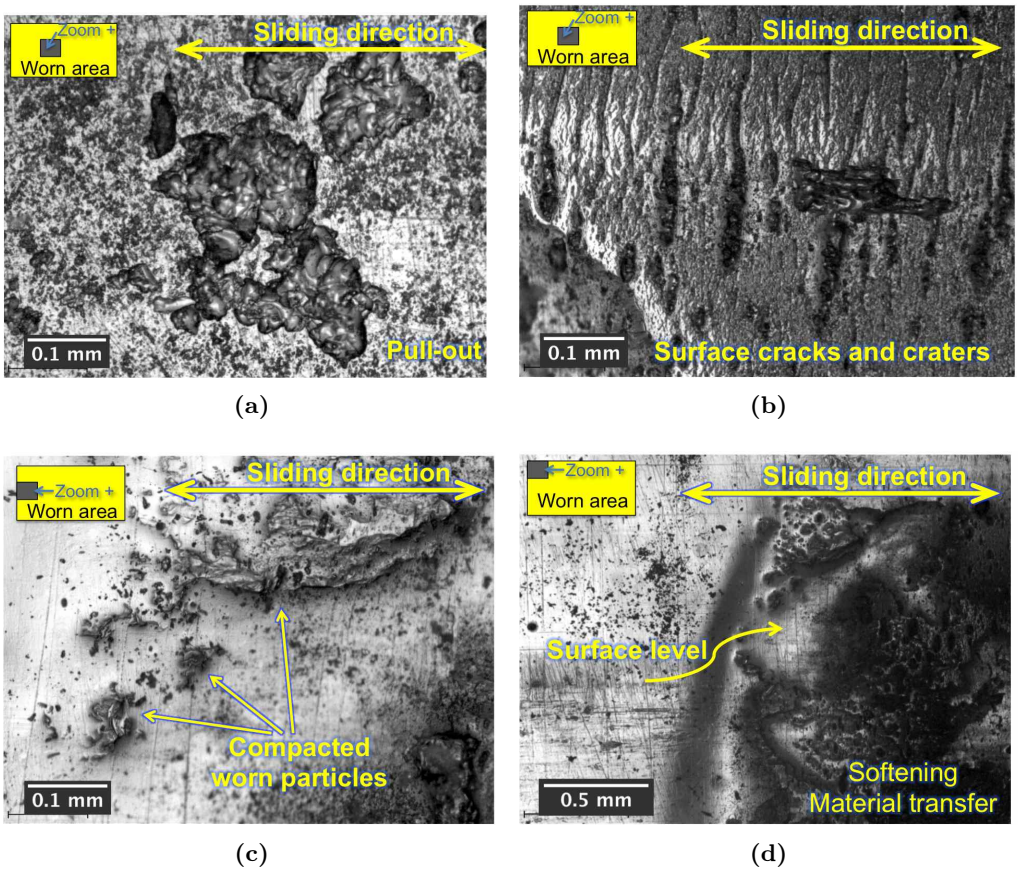

Figure 5.20: Microscopic images of the track sample after 500 cycles under 120 mm/s and 20 N. The location of zoom in is shown in the left upper corner of each image. Figures depict (a) material pull-out (x10); (b) cracks and craters on the polymer surface (x10); (c) transferred compacted material (x10); (d) material transfer and softening onto the worn zone front border (x2.5)

5.2.3 Wear retrospective: Two scenarios

In order to conclude on epoxy/epoxy wear mechanisms, we propose two scenarios of surface damage evaluation and wear history acting in the second region of diagram Fig. 5.17, where various wear mechanisms interfere. Both scenarios start with two-bodies abrasion and then develop into two branches as number of cycles increases.

1. The '*three-bodies abrasion scenario*' is characterized by the presence of micro or macro grooves on the worn surfaces, see Fig. 5.18 (a-d) and the absence of material transfer. The majority of wear debris is evacuated from the contact, while the remaining part slides or rolls inside the moving contact and entails the deepening of wear grooves by the detachment of new wear debris from their bottom and borders. The third body polishes the surfaces outside the grooves. A typical worn surface of track that underwent this scenario is described as Type 1 and shown in Fig. 5.12. This scenario occurs under low sliding velocity for both normal loads.

2. The '*Adhesion/Thermal scenario*' is characterized by two associated mechanisms: thermal deformation and adhesion. Thermal deformation is expressed in compacted material adherence into the track surface, see Fig. 5.20 (c), and material transfer from the slider to the track, as can be seen in Fig. 5.13 by the worn zone border and the track surface profile. The adhesion in this framework manifests itself by the pull-out and cracks and small craters perpendicular to the sliding direction, see Fig. 5.20 (a, b). Under high sliding velocity, wear debris detached from the slider are not evacuated from the contact, but melt and adhere to the track surface. Therefore, it elevates the track surface level. In parallel with this transfer process, the adhesion arises between two heated polymer surfaces. Some quantity of material is pulled out from the track surface, pushed by the slider to the track worn area borders and remains there as compacted wear debris. A typical example of track surface damaged according to this scenario is described as Type 2 and given in Fig. 5.13. This scenario is generally observed for the track samples that underwent high velocity loading, independently of normal load value.

These two scenarios are summarized in Fig. 5.21. We suppose that the main difference between these two scenarios is the heat-involved deformation in the surface and sub-surface layers of polymer. This hypothesis is in agreement with the contact temperature rise and its distribution into the track surface layers, calculated previously. These calculations show, that higher velocity causes higher contact temperature, and the largest part of this frictional heat (96-98 %) is dissipated into the track. This could explain the thermal processes involved into the second scenario.

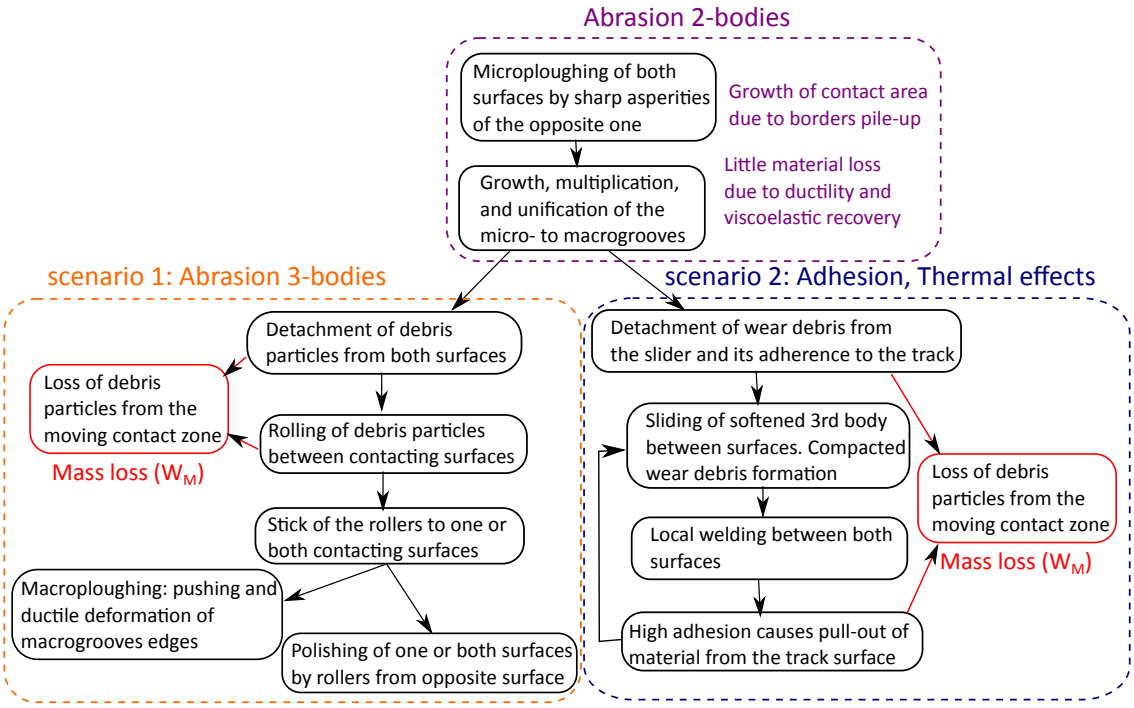

Figure 5.21: *Three-bodies abrasion* (1) and *Adhesion/Thermal* (2) wear scenarios for epoxy/epoxy sliding contacts

5.3 Dissipation in composite-involved friction and wear

In order to study the influence of carbon fibres on the composite bulk dissipation, experiments on CFRE against itself or epoxy slider are carried out under severe tribological conditions. As for epoxy/epoxy couple, several test durations, such as 10, 100, 500, 1000 and 5000 cycles, are applied. We use the similar approach based on a macroscopic point of view closely followed by a description of the wear mechanisms involved.

5.3.1 Establishment of wear laws

5.3.1.1 Wear of Epoxy/CFRE

In the case of epoxy/CFRE couple, the wear of the CFRE track remains negligible. Nevertheless, epoxy slider surface damage is observed under all tribological conditions against CFRE track. The resulted epoxy slider mass loss as a function of its kinematic length is presented in Fig. 5.22. We observe, that the mass loss increases linearly with the kinematic length. Two families seem to emerge, and the slopes are given on the diagram near each fitting curve, similarly to Fig. 5.4 for epoxy/epoxy rubbing. However, in this case, the divergence between them is more pronounced: the slider mass loss under 120 mm/s and 50 N grows rather quickly with the slope of $3.6 \cdot 10^{-6}$ g/mm, while all other tribological conditions cause very slight mass loss of about $1 \cdot 10^{-7}$ g/mm until 1000 cycles, which correspond to $2 \cdot 10^{4}$ mm of kinematic length.

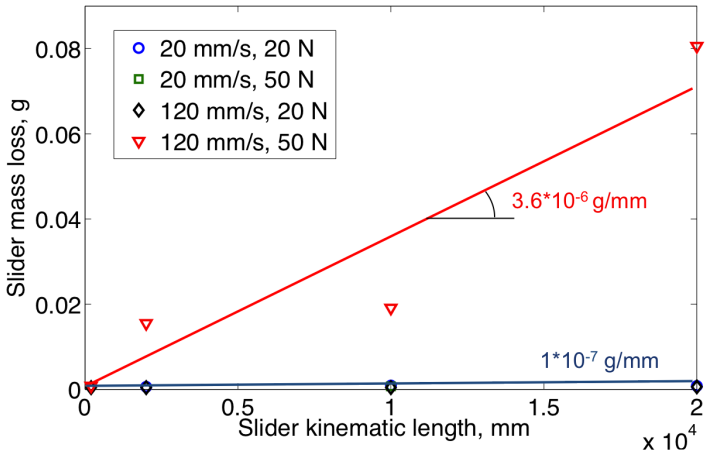

Figure 5.22: Epoxy slider mass loss as a function of its kinematic length for four tribological conditions

We calculate from the measured mass loss and epoxy density, wear coefficients, wear rates and specific wear rates of epoxy sliding against CFRE in order to verify if they follow Archard's wear law. These values are given in Table 5.6. The difference between two families is also accentuated in this table: all wear characteristics under Conditions 1, 2 and 3 are lower than those of the Table 5.3. It is noteworthy, that the wear characteristics of epoxy against CFRE under Conditions 4 are higher than those obtained for epoxy against itself. We observe that in the case of epoxy/CFRE contact, as well as for epoxy/epoxy, the mass loss does not respect the hypothesis of Archard about plastic flow into the contact. Wear coefficients vary with normal force and sliding speed.

Conditions	1	2	3	4
Wear coefficient	$1.2{\cdot}10^{-3}$	$0.5{\cdot}10^{-3}$	$1.2 \cdot 10^{-3}$	$16.8 \cdot 10^{-3}$
Wear rate, m^3/m	$0.9 \cdot 10^{-10}$	$0.9 \cdot 10^{-10}$	$0.9 \cdot 10^{-10}$	$33 \cdot 10^{-10}$
Specific wear rate, $m^3/N\ m$	$4.5 \cdot 10^{-11}$	$1.8 \cdot 10^{-11}$	$4.5 \cdot 10^{-11}$	$66 \cdot 10^{-11}$

Table 5.6: Wear volume loss characteristics of epoxy rubbing against CFRE, calculated according to Archard's wear law

5.3.1.2 CFRE wear rate

The weighing of CFRE sliders and tracks before and after each test allows us to conclude that the mass loss of CFRE is negligible in both couples under all tested tribological conditions, except for CFRE/CFRE under the highest load and sliding velocity and the longest test duration. Namely, under a normal load of 50 N, a sliding velocity of 120 mm/s and after 5000 cycles, CFRE slider loses 0.0021 grams, and 0.0007 among them are found transferred onto the CFRE track surface. Considering the composite density of 1.57 g/cm^3 (see Chapter 2), this mass loss of the slider corresponds to a wear rate of $1.3 \cdot 10^{-11}$

m^3/m and a specific wear rate of $2.7 \cdot 10^{-13}$ m^3/Nm.

Tsukizoe and Ohmae [46] measured the specific wear rate of HS CFRE against carbon steel in the order of 10^{-16} m^3/N m under normal pressure of 1.5 MPa and sliding velocity of 0.83 m/s. This value differs of 3 orders of magnitude with the one measured in our study certainly due to the counterface body hardness and heterogeneity.

5.3.2 Friction coefficient and dissipated energy

5.3.2.1 CFRE/epoxy couple

Friction maps are plotted for CFRE/epoxy frictional couple under four tribological conditions after 1000 cycles in Fig. 5.23 (a-d). The friction coefficients are indicated by color: the dark red color corresponds to the maximal value of 1. An initial period of growing friction is observed under all conditions. Then, the friction stabilizes at a steady-state value, which is fairly different depending on the conditions: 0.35, 0.68, 0.7 and 0.75 under Conditions 1 - 4, respectively. However, a drop of the friction is observed in the middle of the cycle between 300 and 600 cycles under Conditions 4. It could be explained by contact area variations and softening of the polymer. We can notice, that the similar drop after 300 cycles is observed for epoxy/epoxy friction under identical conditions. On all maps, there is a zone of low friction at the end of the sliding pass, which probably corresponds to the wear debris evacuation.

Generally, in the case of CFRE/epoxy friction, we can say that the friction coefficient increases with the severity of the tribological conditions, i.e. normal load and sliding velocity.

The dissipated frictional energy is calculated for epoxy/CFRE frictional couple according to Eq. 5.4. The resulting points for four tribological conditions are plotted in Fig. 5.24 as a function of the slider kinematic length. As for epoxy/epoxy couple in Fig. 5.7, the dissipated energy increases linearly. The slopes of each fit, varying from 0.006 J/mm to 0.027 J/mm, are also indicated on the diagram. According to Eq. 5.5, these slopes present a product of average friction coefficient and a normal load. This seems to be followed by these slope values: for example, for the lowest slope 0.006 J/mm under 20 N, the average friction coefficient is $\mu_{av} = 0.006$ J/mm/20 N$= 0.3$.

5.3.2.2 CFRE/CFRE couple

The frictional maps for CFRE/CFRE couple under four tribological conditions are plotted in Fig. 5.25 (a-d). The friction coefficients are indicated by color, and the dark red color corresponds to the maximal value of 0.8. The first figure of 20 N and 20 mm/s presents the friction during 1000 cycles, while all other maps cover the tests until 5000 cycles. Firstly, we observe an absence or insignificance of the run-in period under all conditions: the friction coefficient is rather stable even for the first cycles. Moreover, it is perfectly stable under sliding velocity of 20 mm/s during the pass of each cycle and throughout all cycles. Its average values are about 0.15 under normal load of 20 N, corresponding to the apparent pressure of 0.36 MPa, and 0.22 under normal load of 50 N, corresponding to the apparent pressure of 0.9 MPa. The absence of visible surface damage allows us to

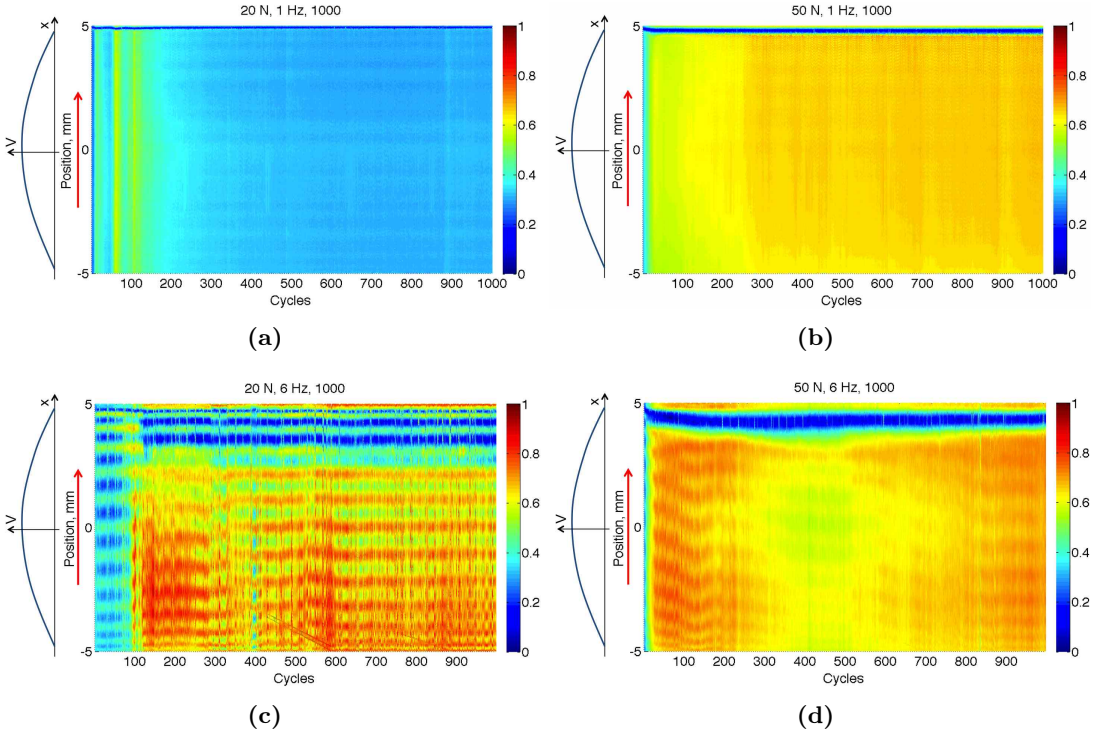

Figure 5.23: Friction maps for (a) 20 mm/s, 20 N; (b) 20 mm/s, 50 N, (c) 120 mm/s, 20 N, (d) 120 mm/s, 50 N of mean sliding velocity and normal force, respectively. The friction coefficient is averaged between back and forth passes for each cycle. The sliding distance on $y-$axis and cycle numbers on $x-$axis are limited by 10 mm and 1000 cycles, respectively

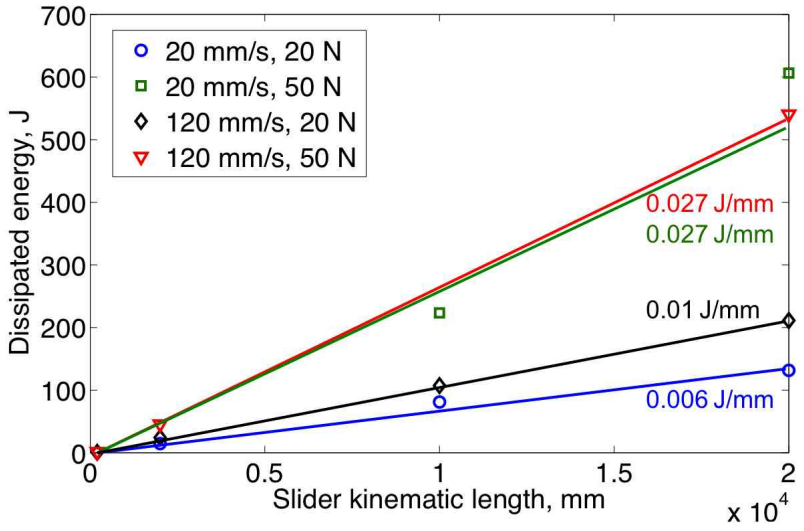

Figure 5.24: Dissipated energy evolution with slider kinematic length for four tribological conditions

suppose that the conditions 1 and 2 might be considered as interfacial. Thus, the friction coefficient values can be compared with those from Chapter 3, where under normal load of 2 N, corresponding to the apparent pressure of 6.37 kPa, and sliding velocity of 10 mm/s, the friction coefficient is equal to about 0.18.

The friction under sliding frequency of 120 mm/s, see Fig. 5.25 (c, d), is less stable throughout 5000 cycles. It is explained by surface damage, which causes contact area variation and circulation of wear debris inside the contact. Thus, the friction coefficient oscillates between 0.3 and 0.4 under 20 N and between 0.4 and 0.7 under 50 N. While the surface damage under 20 N is low, the normal load of 50 N causes serious wear, which will be presented and discussed further.

In general, the friction coefficient of CFRE rubbing against CFRE tends to increase with an increase of normal load and sliding speed.

The dissipated energy of CFRE/CFRE friction under four tribological conditions is calculated according Eq. 5.4, and the results are presented in Fig. 5.26. The perfect linear increase in the energy with time or slider kinematic length is observed under all conditions. The values of slopes are indicated on the figure near the associated lines, they vary from 0.003 J/mm to 0.023 J/mm. Exactly as we have seen for other couples, the average friction coefficient can be found from these slopes: for instance, $\mu_{av} = 0.003$ J/mm/20 N= 0.15 under Conditions 1. This is also valid for other conditions.

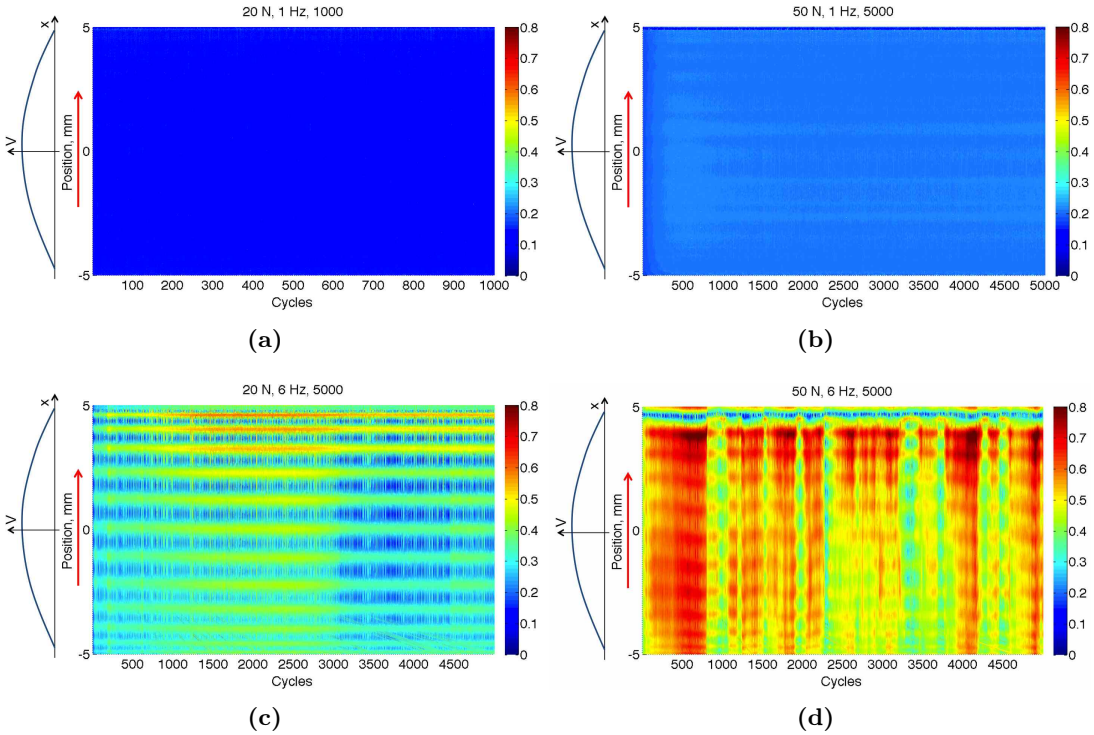

Figure 5.25: Friction maps for (a) 20 mm/s, 20 N after 1000 cycles and (b) 20 mm/s, 50 N, (c) 120 mm/s, 20 N, (d) 120 mm/s, 50 N after 5000 cycles of sliding frequency and normal force, respectively. The friction coefficient is averaged between back and forth for each cycle

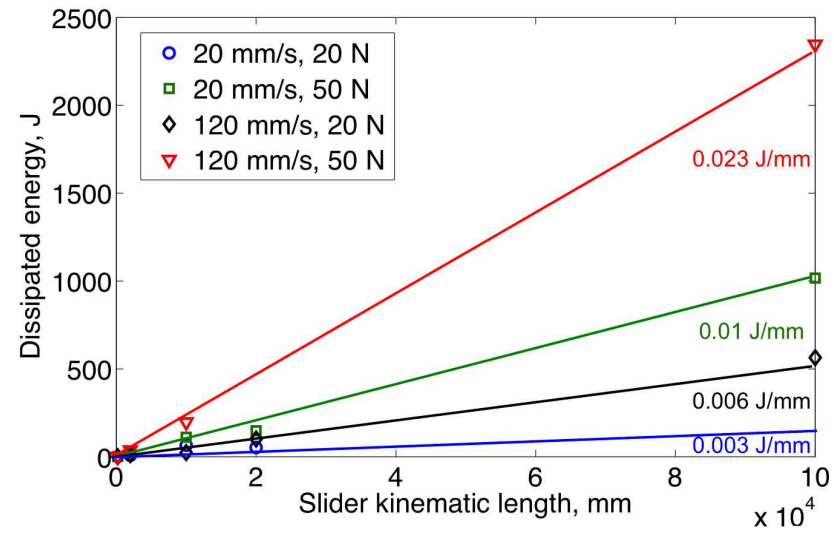

Figure 5.26: Energy dissipation of CFRE/CFRE sliding system as a function of the kinematic length for four tribological conditions

5.3.3 Contact temperature distribution

5.3.3.1 Thermal characteristics of CFRE

Heat flow distribution in composite undergoes more complicated processes because of the heterogeneous nature and anisotropy of the composite. Several studies measure thermal characteristics of CFRE by different experimental techniques and establish empirical laws [106, 107]. Others calculate them by analytical [108, 109] or numerical implementations [110]. As a first approximation, two mixture laws can be used for thermal conductivity calculation:

$$\frac{1}{k_t} = \frac{V_f}{k_f} + \frac{1 - V_f}{k_m} \tag{5.16}$$

as a lower limit of transversal composite thermal conductivity k_t. And

$$k_l = V_f k_f + (1 - V_f) k_m \tag{5.17}$$

as a longitudinal composite thermal conductivity k_l, or an upper limit of the transversal one. V_f is the fibre volume fraction, k_f is the fibre thermal conductivity and k_m is the matrix thermal conductivity.

Applying these equations to the considered composite and using the thermal properties of epoxy matrix and carbon fibres from Table 5.7, we obtain $k_t = 0.40$ W/m K and $k_l = 0.81$ W/m K.

We take the CFRE composite density equal to the prepreg density 1.57 g/cm^3, see Chapter 2, and the specific heat capacity equal to that of carbon fibres 0.8 kJ/kg K, as they are more thermal resistant. This choice is justified by experimental measurements of thermal characteristics of unidirectional carbon fibre/epoxy composites in [107] that report at 20°C values of $c_p \approx 0.8$ kJ/kgK, $k \approx 0.58$ W/mK and thermal diffusivity $\chi \approx 0.42$ mm^2/s.

The chosen thermal characteristics of CFRE composite are presented in Table 5.7.

Material	Density ρ, kg/m^3	Thermal conductivity k, W/m K	Specific heat capacity c_p, J/kg K	Thermal diffusivity χ, m^2/s
Epoxy	$1.1 \cdot 10^3$	0.19	$1 \cdot 10^3$	$0.17 \cdot 10^{-6}$
HS CF	$1.6 \cdot 10^3$	1.2	$0.8 \cdot 10^3$	$0.94 \cdot 10^{-6}$
CFRE	$1.57 \cdot 10^3$	0.6	$0.8 \cdot 10^3$	$0.48 \cdot 10^{-6}$

Table 5.7: Thermal properties of CFRE and its components

5.3.3.2 Temperature distribution in CFRE/epoxy sliding contact

We can calculate the Peclet number, describing the heat propagation profile, for two tested sliding velocities according to Eq. 5.12. The contact half-width is similar to that of epoxy/epoxy case, i. e. $3 \cdot 10^{-3}$ m, and the mean sliding velocities are 20 and 120 mm/s. The Peclet number is calculated using thermal diffusivity of the CFRE track from Table 5.7. Thus, we have $L_{P1} = 62.5$ and $L_{P2} = 375$ for V_1 and V_2, respectively.

However, as two contact surface materials have different thermal properties, the partition coefficient, can be calculated as the ratio $\delta = \Delta\theta_{sl}/\Delta\theta_{tr}$ from Eqs. 5.11 and 5.13. Thus, it depends on thermal conductivities of both materials:

$$\delta_{sl} = \frac{k_{sl}}{k_{sl} + k_{tr}\sqrt{2L_P}} \tag{5.18}$$

Therefore, epoxy slider transfers 2.8 % of the heat flow under $V_{av} = 20$ mm/s, and 1.1 % of the heat flow under $V_{max} = 120$ mm/s.

The quantities of generated frictional heat q par surface and time unity are calculated for all experiments according to Eq. 5.9. In the absence of real contact area values, two limit values are used, as previously: the apparent area of slider A_{r1} and the real contact area according to Bowden and Tabor $A_{r2} = P/H$. As we use the softest material hardness, the A_{r2} contact areas are equal to those of epoxy/epoxy contact. As both Peclet numbers are higher than 5, these quantities of heat are applied to calculate average temperature rise according to Eq. 5.13.

The resulting average temperature rises for A_{r1} and A_{r2} are plotted as a function of the slider kinematic length in Fig. 5.27 (a) and (b), respectively. As for epoxy/epoxy friction, we observe an increase of temperature rise with the increase of the tribological conditions severity. An initial growing temperature period is detected under all conditions, after which the temperature rise remains rather stable. In general, the temperature rise in CFRE track against epoxy slider is at least 2 times lower than in epoxy track against epoxy slider under all four conditions.

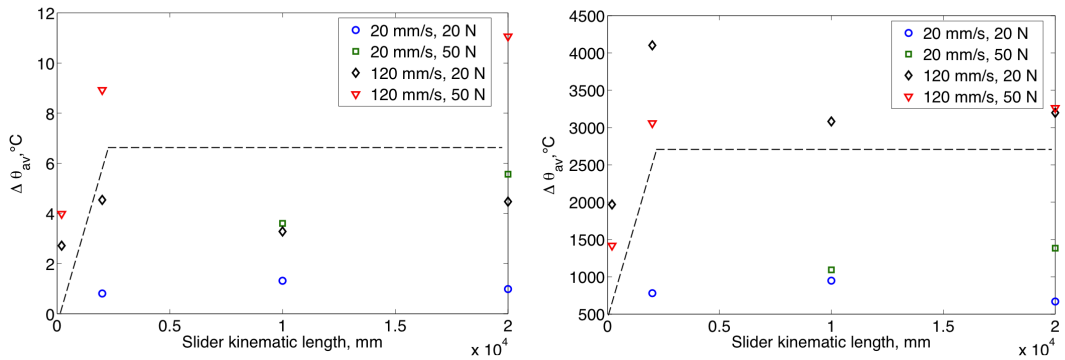

Figure 5.27: Average temperature rise in epoxy/CFRE contact under four tribological conditions considering (a) real contact area A_{r1} and (b) real contact area A_{r2}

5.3.3.3 Temperature distribution in CFRE/CFRE sliding contact

We can calculate the Peclet numbers for our sliding contact of two identical CFRE composites under $V_{av} = 20$ mm/s and $V_{av} = 120$ mm/s, using the thermal diffusivity of CFRE given in Table 5.7. The resulting Peclet numbers are equal to those of epoxy/CFRE case:

$L_{P1} = 62.5$ and $L_{P2} = 375$. As both materials are identical, we can use Eq. 5.14 to calculate the coefficient of partition of heat flow between moving and stationary bodies. Using these Peclet numbers, we obtain $\delta_1 = 7.6$ % and $\delta_2 = 3.4$ % for average sliding velocity of 20 and 120 mm/s, respectively.

As for the two other contact cases, the quantities of heat q and average $\Delta\theta_{av}$ temperature rises are calculated according to Eq. 5.9 and Eq. 5.13, respectively. Two real contact contact areas A_{r1} and A_{r2} are still considered. However, the hardness of CFRE must be used here to calculate Bowden and Tabor's contact area $A_{r2} = P/H$. This hardness will be estimated from the mixture law: $H_{comp} = H_{ep}(1 - V_{CF}) + H_{CF}V_{CF}$, where V_{CF} is the volume fraction of the carbon fibres. Taking the values of $H_{ep} = 240$ MPa, $H_{CF} = 4400$ MPa from Table 2.9 and $V_{CF} = 0.62$, we obtain $H_{comp} = 2820$ MPa. Therefore, $A_{r2} = 20$ N/2820 MPa$= 7.1{\cdot}10^{-9}$ m^2 for Conditions 1 and 3, and $A_{r2} = 50$ N/2820 MPa$= 17.7{\cdot}10^{-9}$ m^2 for Conditions 2 and 4.

The resulting average temperature rises for A_{r1} and A_{r2} are presented in Fig. 5.28 (a) and (b), respectively. We observe the strong prevalence of the temperature rise corresponding to the most severe tribological conditions. The values of temperature rise for real contact area A_{r2} are significantly higher, than those of epoxy/CFRE and epoxy/epoxy due to the lower contact area. For contact area A_{r1}, Conditions 1, 2 and 3 cause almost similar temperature rise, which are about 2 times lower than those of CFRP against epoxy. As for other cases, we observe the initial period of temperature growth and following stabilized temperature under all conditions.

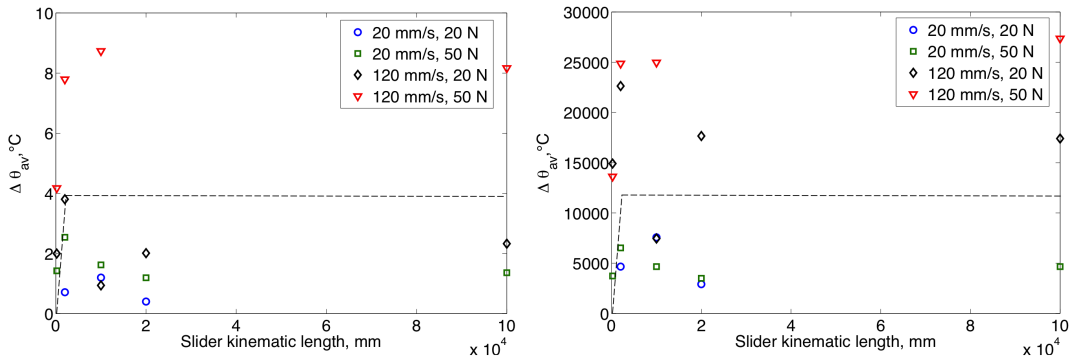

Figure 5.28: Average temperature rise in CFRE/CFRE contact under four tribological conditions considering (a) real contact area A_{r1} and (b) real contact area A_{r2}

5.3.4 Surface damage observation

5.3.4.1 Epoxy/CFRE couple

After all experiments, the surfaces of CFRP tracks and epoxy sliders are carefully observed in order to study damage mechanisms. It is interesting to compare epoxy wear mechanisms against CFRE and against itself. We have measured and discussed before the higher mass

loss of epoxy in contact with itself, than with CFRE. It is confirmed by surface wear observations: most of the epoxy sliders after friction experiment look alike the one shown in Fig. 5.29, which underwent 1000 cycles of sliding under normal load of 50 N and sliding velocity of 20 mm/s. This image shows that only a part of the slider surface is worn, the drop in surface level is depicted also by the surface profile in blue frame. If we zoom into the worn zone, we can observe abrasive grooves in the direction of sliding, see left upper frame in this figure. If we continue to magnify, we notice, that the third body remained on the slider surface contains carbon fibre debris, see left lower frame in this figure. This is also observed on a macro scale by black tint of the worn zone. We can suppose that these small hard particles, as well as long hard carbon fibres of counterbody, are responsible of the abrasive wear of epoxy slider. And, coherently to our explanations of epoxy/epoxy wear, pure abrasive wear of epoxy is the less harmful and results in less material loss.

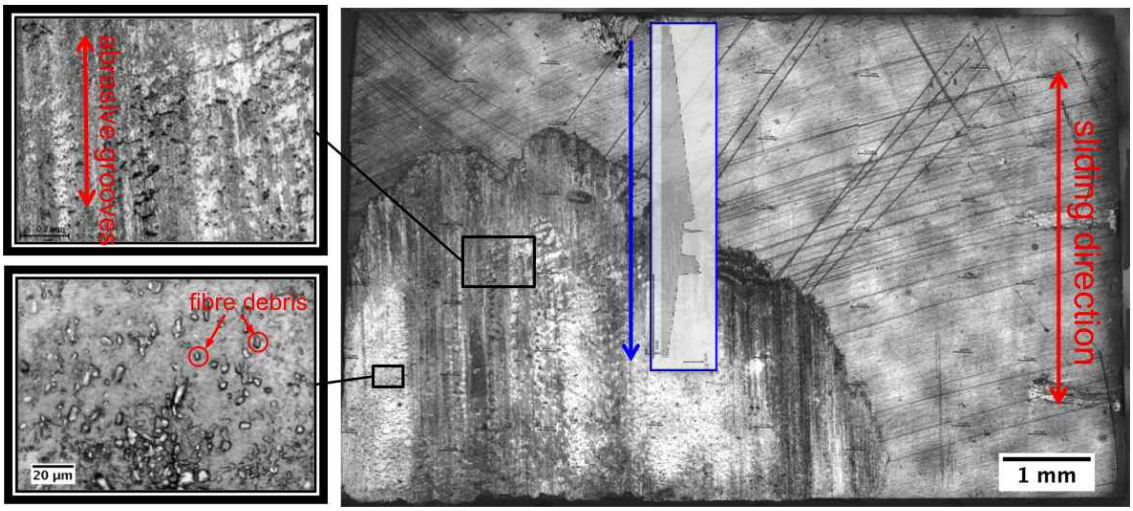

Figure 5.29: Worn surface of epoxy slider after 1000 cycles of rubbing against CFRE track under normal load of 50 N and sliding velocity of 20 mm/s. The line of surface profile measure, countered by the blue frame, is shown by the blue arrow. Visible pattern outside the worn area is on the back side of the transparent epoxy sample

Another example of worn epoxy slider, after 1000 friction cycles under 20 N and 120 mm/s, is presented in Fig. 5.30. We can notice that in contrast to the previous example, this one is worn all over its surface. However, despite observed high surface damage, its mass loss is also negligible, see Fig. 5.22. The linear surface profile is shown in the blue frame, and the line of its measurement is drawn with the blue arrow. Two magnifications of the worn surface, presented in the left of the figure, allows us to observe the abrasive grooves parallel to the sliding direction and the cracks and craters mostly perpendicular to it, that we associate with polymer fatigue.

In contrary to these two examples, the surface of the epoxy sliders after the tests under 50 N and 120 mm/s are completely damaged and resemble to those after epoxy/epoxy friction: it is covered by soft epoxy millimetric rollers, formed from wear debris. The overview of the epoxy slider and the CFRE track after 1000 cycles under normal load

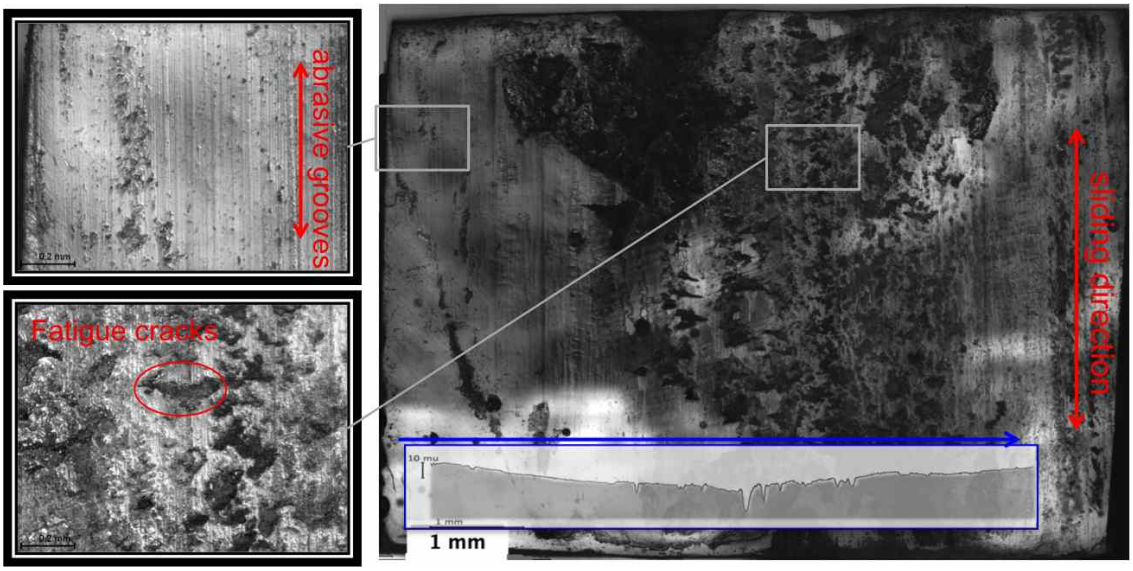

Figure 5.30: Worn surface of epoxy slider after 1000 cycles of rubbing against CFRE track under normal load of 20 N and sliding velocity of 120 mm/s. The line of surface profile measure, countered by the blue frame, is shown by the blue arrow

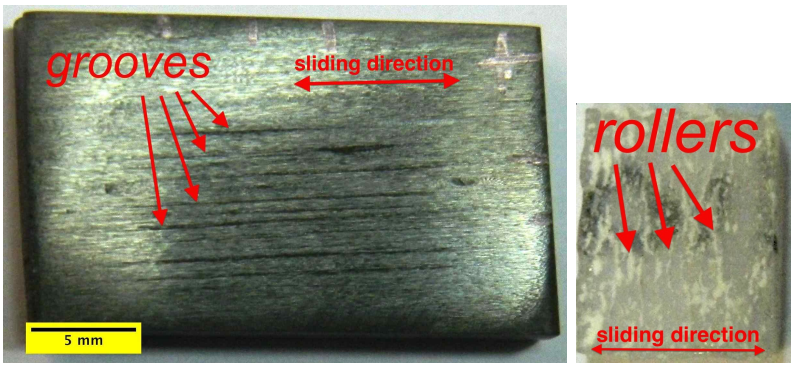

(a) **(b)**

Figure 5.31: (a) CFRE track and (b) epoxy slider after 1000 cycles of friction under normal force of 50 N and slowing velocity of 120 mm/s

of 50 N and sliding speed of 120 mm/s are presented in Fig. 5.31. The surfaces of all CFRE tracks rubbed against epoxy sliders are damaged very slightly. Under the highest tribological conditions and for the longest test, the CFRE presents only several grooves on its surface. These grooves correspond mostly to worn out epoxy, but also to several broken fibres, which we can observe in Fig. 5.29.

5.3.4.2 CFRE/CFRE couple

As we have shown before, CFRE rubbing against CFRE does not present any measurable mass loss, except under highest conditions and longest sliding duration. This is coherent with the surface observations: in most cases, either no visible surface damage or several grooves similar to those in Fig. 5.31 (a) appear on the surface after wear test.

However, the track and slider surfaces after 5000 cycles under 50 N and 120 mm/s lose several milligrams after wear test. We can observe, that both surfaces are highly damaged and worth being studied with higher magnification. The whole worn area of the track surface is presented on the left upper image in Fig. 5.32. We can distinguish the initial polished carbon fibres by gray and white unidirectional lines, and black homogeneous worn zone. The linear longitudinal surface profile is measured in the middle of the wear zone, showed by the blue arrow, and presented in the left lower image within the blue frame. It demonstrates, that wear debris are accumulated at both ends of the wear zone, and the central zone is 10 μm lower than the initial surface level. These wear debris, or third body, consist of carbon fibre pieces mixed with epoxy powder, as it is seen in the right upper microscopic image. The ways of the further propagation of the worn zone can be observed in the right lower microscopic image.

5.3.5 Synthesis

We have seen in this section, that carbon fibre-reinforced epoxy composite in configuration against itself or pure epoxy is rather wear resistant. As we expected, due to hard carbon fibre reinforcement composite mass loss is negligible under all studied conditions except the more severe. But even under these conditions, wear rate is 100 times lower than those of epoxy/epoxy under similar conditions. Friction coefficients and dissipated energy depend strongly on the applied load and sliding speed in case of CFRE/CFRE friction, as well as for epoxy/CFRE friction. This effect is more pronounced for CFRE/CFRE configuration. Frictionally generated heat flow propagates mostly into CFRE track in both configurations. Thus, due to higher thermal resistance and conductivity of the composite, the temperature rises are generally lower in CFRE than in epoxy.

Wear mechanisms observed in epoxy/CFRE configuration are:

- epoxy abrasion by harder carbon fibres of counterface;
- possible epoxy surface thermal transformation under more severe tribological conditions;
- delamination of carbon fibres from composite surface and debris formation;
- transfer and adherence of carbon fibre debris onto the epoxy slider surface;

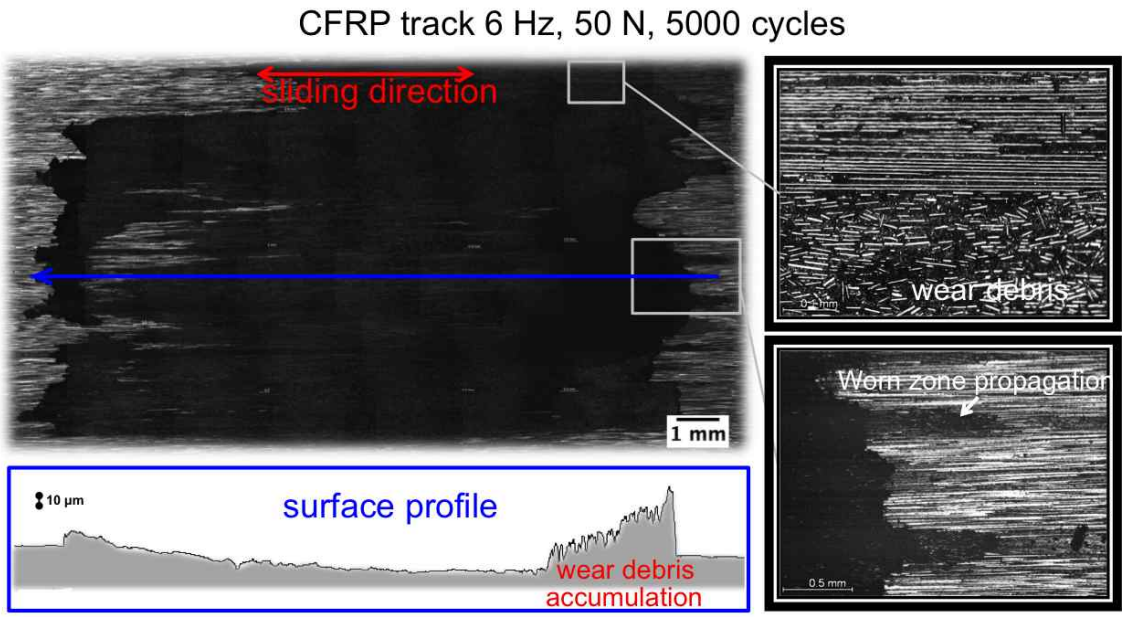

Figure 5.32: Worn surface of CFRE track after 5000 cycles of rubbing against CFRE slider under normal load of 50 N and sliding velocity of 120 mm/s

- loss of epoxy matrix lying between carbon fibres;
- when the whole surface of epoxy slider is damaged, it starts to form rollers of third body

Wear mechanisms in CFRE/CFRE configuration are:

- polishing by the opposite surface under less severe tribological conditions and lower test durations;
- delamination of carbon fibres and epoxy matrix from composite surface;
- formation of wear debris containing carbon fibre pieces and epoxy powder;
- third body abrasion by this wear debris and following delamination and worn zone propagation

5.4 Conclusions

In this chapter, the bulk energy dissipation and associated wear of pure epoxy and CFRE composite were studied under four severe tribological conditions. A two-scale approach was developed in order to quantify this dissipation and to identify wear mechanisms and their evolution. This approach and the main results and observations are summarized below.

The general observation of this study is that the epoxy/epoxy friction causes more surface damage and mass loss, than epoxy/composite friction, under three of four tested conditions. Particularly, the sliding velocity of 120 mm/s and normal load of 50 N, are much more destructive than the others: they cause 6 times higher wear rate in epoxy/epoxy couple, 37 times higher wear rate in CFRE/epoxy couple, and in CFRE/CFRE couple, it is the only conditions which cause any measurable mass loss under similar test duration. The mass loss increases linearly, but does not respect the hypotheses of Archard's model, namely, its independence of normal load and sliding velocity.

The frictional coefficient of epoxy/epoxy couple under studied severe conditions is rather high and slightly dependent on sliding velocity and normal load. However, both CFRE-involved couples present a strong dependence of the friction coefficient on normal load and sliding speed: between the lowest and the highest conditions, it increases by a factor of 2-3.

The amount of frictional energy dissipated in friction and wear is proportional to the average frictional force and kinematic length. Therefore, its slope varies with the average frictional coefficient and tribological conditions. However, we noticed that the frictional energy dissipates not only in the particle detachment and mass loss, but also in the surface plastic deformations, cracking and eventual thermal effects. Therefore, in the case of epoxy/epoxy contact, we measured the surface area concerned by all these effects, and associated the energy dissipation with this area growth. This allowed us to detect two zones of dissipation: first slow growth of the dissipated energy, which has almost similar slope under all tested conditions, and following fast growth of the dissipated energy, whose slope differs with the tribological conditions. The observations of the worn surfaces after several test durations inspired us to suppose that the first region corresponds to the abrasion, whose traces were found on the surfaces under all sliding conditions, and the second region could correspond to the three-bodies abrasion, adhesion or thermal effects, such as softening or state transition, which were observed on track surface, depending on tested conditions.

Contact temperature distribution calculations according to Archard-Jaeger-Blok theory were performed. Supposing two cases of real contact area, the apparent one and the contact area by Bowden and Tabor's theory, we calculated two limit average temperature rises under all tested conditions and test durations. It allowed us to conclude that the contact temperature rise value follows the severity of tribological conditions. The initial temperature growth and its following stabilization are observed for all tested materials. However, its magnitude is significantly lower for CFRE-involved frictional couples, than for epoxy/epoxy.

Based on this macroscopic analysis and surface observations of epoxy/epoxy couple, we proposed a wear retrospective, which describes wear modes evolution. The wear process starts with two-bodies abrasion and then ramifies into 'Three-bodies abrasion scenario' or 'Adhesion/Thermal effects scenario'. The former is observed under low sliding speed, while the latter appears under high sliding speed. The normal load does not seem to influence the wear mode evolution.

The wear mechanisms are also studied for epoxy/CFRE and CFRE/CFRE couples. They are rather different for epoxy slider against CFRE, than against itself: the wear

is mostly abrasive by the hard carbon fibres. At the same time, the wear of CFRE is initiated by surface polishing and fibres and matrix delamination, which is followed by mixed fibre-matrix wear debris formation and abrasion by this third body.

General conclusions and perspectives

The frictional dissipation of two model carbon-reinforced polymers was studied at interfacial and bulk levels. This was implemented using an experimental multi scale approach for apparent contact pressure ranging from 1.56 kPa to 800 kPa and sliding velocities from 10 mm/s to 120 mm/s. This experimental approach coupled to theoretical considerations, allows us to get a better insight into the mechanisms at stake with relation to pure polymer dissipation.

The evolution of the friction coefficient and the wear rate of epoxy/epoxy couple as a function of applied conditions, characterized using the product PV_{av} of the normal force and the mean sliding velocity, are schematized in Fig. C.1 (a) and (b), respectively. It can be seen that pure epoxy highly dissipates with values of friction at around $0.4 - 0.7$. It also experiences high wear under severe tribological conditions.

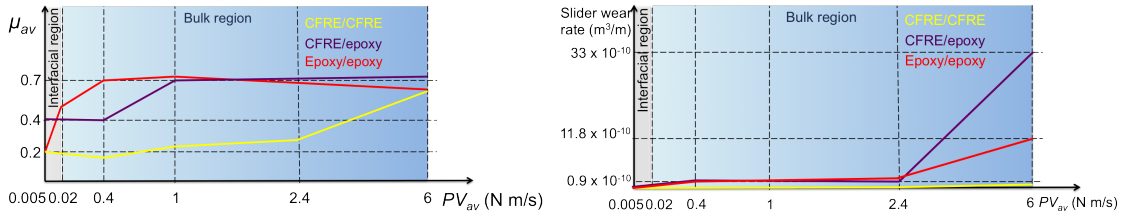

(a) **(b)**

Figure C.1: (a) Average friction coefficient and (b) wear rate of CFRE/CFRE, CFRE/epoxy and epoxy/epoxy sliding contacts under tested interfacial and bulk friction conditions

The instantaneous frictional coefficient follows wear debris formation and evacuation from the contact zone. However, we can observe that its average value is almost similar under all conditions for the epoxy/epoxy couple. The dissipated frictional energy rate depends linearly on this friction coefficient. The total of frictional energy dissipates in wear debris formation and detachment (volume or mass loss), brittle and ductile surface mechanical deformations, and heating and thermal deformations.

The area of deformed zone of the track samples was measured for epoxy tracks. The evolution of total dissipated energy as a function of this area presents two parts. The first slow growth of the dissipated energy with the worn area increases similarly under all tested conditions. After a certain value, the dissipated energy rate becomes dependent on the tribological conditions. It can be explained by the initial two and three bodies abrasion, presented under all conditions, and a further development of different wear mechanisms depending on conditions. The 10 cycles tests produce several grooves more or less developed under all conditions. The following observation of the worn surfaces, after 100 cycles and longer, identified two types of worn zones by its general shape, borders and profiles. These types of zones correspond to two sliding velocities independently of normal

load. Microscopy surface observations revealed several wear phenomena associated with the first and second types. The first type covers two and three bodies abrasion ('Abrasive wear'). The second type is presented by melting, material transfer and adherence, pull-out, surface cracks and craters perpendicular to the sliding direction ('Adhesive and Melting wear'). Due to the high number of reciprocating passages, 'Fatigue wear' can also interfere in both types. We believe that the crucial factors of formation of one or another zone are the contact temperature, polymer thermal transformation and wear debris evacuation from the contact zone. This is confirmed by the calculation of the contact temperature distribution, which dissipates mostly into the track sample and is larger for the higher sliding velocities.

What is the influence of carbon reinforcement on epoxy friction and wear? It was observed experimentally that an addition of carbon fibres or carbon nanopearls to epoxy in both contact materials changes dramatically its frictional coefficient. However, their influence differs: while carbon fibres reduce the frictional coefficient, carbon nanopearls increase it. We can also observe that under more severe conditions, CFRE/CFRE friction and wear are significantly lower than those of CFRE/epoxy and epoxy/epoxy, as shown in Fig. C.1 (a) and (b). The composite mass loss is even negligible under moderate tribological conditions.

What happens at the interfacial level? The analytical model, created to predict the friction coefficient between two composites, concludes that it depends on local friction coefficients between phases of two contacting composites and the contact geometry. Inverse or direct proportionality frictional laws are possible for composite contact, depending on the assumption made, i.e. effective shear stress for all micro contacts $\tau^* = const$ or effective hardness for all contacting materials $H^* = const$. On the other hand, in order to describe contact geometry, the filler surface fraction is required. Since filler volume fraction was known for each composite, the relation between surface and volume fibre fraction in composite is studied. A probabilistic approach, assuming a uniform distribution of fillers, was developed and resulted in the equivalence of filler surface and volume fraction $\alpha_f = V_f$. The local coefficients μ_{cc}, μ_{epc} and μ_{epep} are measured experimentally for carbon fibres and epoxy. Their application and contact geometrical characteristic α_f in the inverse proportionality frictional law fits rather well experimental measurement for carbon fibre-reinforced composites. This coheres with our main assumption for this law, i.e. the equal shear stresses of contact types are of the same order of magnitude.

The local friction coefficients of carbon nanopearl-reinforced epoxy are, a priori, unknown. However, we suppose that the nanopearl structure should favor high friction, and this is in agreement with experimental results found in literature. The fitting by inverse and direct proportionality frictional laws is made mathematically. While the hypothesis of equal hardness is irrelevant due to high difference in carbon nanopearl and epoxy hardnesses, the hypothesis of equal shear stress can be answered, if the nanopearl asperity contacts are not plasticized. This is very plausible because of their high elastic limit and low contact pressures.

Although our model seems to work rather well, we should notice that there are at least two unaccounted factors, which are known to affect composite interfacial friction.

These are composite and counterface roughness and mechanical properties of composite phases, which can affect the distribution of contact area between the phases. That is why, the contact problem of polymer composite against soft uniphase counterface material or another composite should be studied in details in perspective, experimentally as well as numerically.

What happens at the bulk level? The contact temperature of composite-involved frictional couples is lower than for epoxy/epoxy. The most part of the heat flow is also dissipated in the track, but it does not cause any thermal damage because of the high thermal conductivity and thermal resistance of carbon fibres. Wear mechanisms observed for epoxy slider, worn against composite track, differs from those against itself: the wear is mostly abrasive by hard fibres and their debris. However, polymer thermal state transformations are also possible in this configuration, because local contact temperatures can be very high. On the other hand, wear mechanisms of CFRE composite are, successively, fibre smoothening, matrix and fibres delamination, formation of the mixed third body and, finally, third bodies abrasion.

In most cases, used tribological conditions are not severe enough to cause serious damage to the composite. Therefore, it would be interesting to study its wear mechanisms formation and evolution under more severe tribological conditions. A fine descriptions of the third body dynamics within the contact would also allow us a better understanding of the wear mechanisms involved.

Appendix A

Appendix 1: Measured values of kinetic friction coefficients

Table A.1: Mean kinetic friction coefficients with standard deviations calculated for several tests

Friction couple	Kinetic friction coefficient	Normal load, N	Sliding velocity mm/s
Epoxy/epoxy	0.39 ± 0.077	0.5	10
CFRE 34%/epoxy	0.44 ± 0.068	0.5	10
CFRE 52%/epoxy	0.42 ± 0.066	0.5	10
CFRE 62%/epoxy	0.45 ± 0.076	0.5	10

Table A.2: Effect of normal load on mean kinetic friction coefficients for epoxy/epoxy and composite/composite couples

Friction couple	Kinetic friction coefficient	Normal load, N	Sliding velocity mm/s
Epoxy/epoxy	0.23 ± 0.064	0.1	10
	0.25 ± 0.052	0.2	10
	0.39 ± 0.077	0.5	10
	0.41 ± 0.035	1	10
	0.46 ± 0.032	2	10
CFRE 62%/CFRE 62%	0.21 ± 0.019	0.1	10
	0.21 ± 0.015	0.2	10
	0.19 ± 0.015	0.5	10
	0.18 ± 0.012	2	10

Table A.3: Effect of sliding velocity on mean kinetic friction coefficient for epoxy/epoxy and composite/composite couples

Friction couple	Kinetic friction coefficient	Normal load, N	Sliding velocity mm/s
Epoxy/epoxy	0.58 ± 0.012	2	1
	0.46 ± 0.032	2	10
	0.57 ± 0.012	2	20
	0.48 ± 0.073	2	40
CFRE 34%/CFRE 34%	0.23 ± 0.015	2	1
	0.21 ± 0.011	2	10
	0.23 ± 0.016	2	20
	0.23 ± 0.015	2	40
CFRE 52%/CFRE 52%	0.16 ± 0.016	2	1
	0.16 ± 0.014	2	10
	0.18 ± 0.020	2	20
	0.16 ± 0.048	2	40
CFRE 62%/CFRE 62%	0.19 ± 0.057	2	1
	0.18 ± 0.012	2	10
	0.18 ± 0.006	2	20
	0.18 ± 0.024	2	40

Table A.4: Effect of normal load on mean kinetic friction coefficient for CNPRE 1%/CNPRE 1% couple

Friction couple	Kinetic friction coefficient	Normal load, N	Sliding velocity mm/s
CNP 1%/CNP 1%	0.32 ± 0.091	0.1	10
	0.41 ± 0.074	0.2	10
	0.36 ± 0.024	0.5	10
	0.42 ± 0.083	1	10
	0.52 ± 0.065	2	10

Table A.5: Effect of sliding velocity on mean kinetic friction coefficient for CNPRE composite/CNPRE composite couples

Friction couple	Kinetic friction coefficient	Normal load, N	Sliding velocity mm/s
epoxy/epoxy	0.44 ± 0.082	1	0.1
	0.41 ± 0.007	1	0.2
	0.40 ± 0.011	1	1
	0.40 ± 0.013	1	10
	0.41 ± 0.005	1	20
	0.42 ± 0.008	1	30
	0.40 ± 0.027	1	40
CNPRE 1%/CNPRE 1%	0.66 ± 0.043	1	1
	0.52 ± 0.065	1	10
	0.66 ± 0.045	1	20
	0.53 ± 0.069	1	40
CNPRE 15%/CNPRE 15%	0.63 ± 0.026	1	0.1
	0.69 ± 0.033	1	0.2
	0.66 ± 0.024	1	0.5
	0.64 ± 0.013	1	0.8
	0.64 ± 0.040	1	1
	0.50 ± 0.049	1	10
	0.42 ± 0.038	1	20
	0.50 ± 0.038	1	40
CNPRE 28%/CNPRE 28%	0.65 ± 0.021	1	0.1
	0.66 ± 0.015	1	0.2
	0.67 ± 0.016	1	0.5
	0.65 ± 0.012	1	0.8
	0.60 ± 0.006	1	1
	0.51 ± 0.024	1	10
	0.49 ± 0.063	1	20
	0.51 ± 0.037	1	40
CNPRE 35%/CNPRE 35%	0.66 ± 0.025	1	0.1
	0.64 ± 0.013	1	0.2
	0.66 ± 0.026	1	0.5
	0.69 ± 0.009	1	0.8
	0.65 ± 0.032	1	1
	0.60 ± 0.039	1	10
	0.60 ± 0.067	1	20
	0.59 ± 0.067	1	40

Appendix B

Appendix 2: PDMS mould manufacturing process

Fabrication process of PDMS mould requires following facilities: PDMS resin, curing agent, a mould (a plastic box with objects to form the cavities), a spatula, a plastic cup, a laboratory balance, an ultra-sonic bath, a desiccator, a vacuum pump and a furnace.

Following steps are made to manufacture this mould:

1. Clean the plastic box, spatula and plastic cup;
2. Pour PDMS resin into the plastic cup placed onto the balance;
3. Add 10% by weight of the curing agent;
4. Stir the mixture with the spatula for 5 minutes;
5. Put the plastic cup containing the polymer into the ultra-sonic bath for 5 minutes with the aim to homogenize the solution and raise the bubbles from the volume up to the surface;
6. Put the plastic cup containing the polymer into the desiccator connected to the vacuum pump in order to extract residual bubbles. Leave to degas for 30 minutes;
7. At the same time, prepare the plastic box with inserted objects, forming cavities for future composites samples;
8. Slowly pour PDMS into the plastic box, avoiding air bubbles formation;
9. Carefully move the plastic box with inserted objects and liquid PDMS into the furnace;
10. Leave PDMS to cure into the furnace at 60°C for 2 hours;
11. Take out the mould from the furnace, let it cool down and carefully take out the objects. Leave the mould with the cavities into the plastic box.

Appendix C

Extended abstract in Russian

Объемная и поверхностная фрикционная диссипация в композитах

На протяжении нескольких десятилетий полимерные композитные материалы находят все больше приложений как в аэрокосмической отрасли так и в индустрии спорта и отдыха. Этот интерес вызван сочетанием отличных механических и термических свойств с малой массой этих материалов. Несмотря на то что большое количество аналитических и численных моделей для расчета механических свойств композитов предложено и используется инженерами во всем мире, их трибологические свойства остаются малоисследованными.

Эмпирические правила смесей обычно используются для расчета коэффициентов трения и износа. Тем не менее, общее понимание проблемы отсутствует. С научной точки зрения проблема диссипации вызванной трением при контакте материалов содержащих несколько компонентов является сложной задачей из-за одновременного влияния поверхностных и объемных механических, термических, химических, геометрических и других свойств каждого материала в отдельности и фаз раздела между ними. Тем более что эта проблема многомасштабная: в то время как коэффициенты трения и износа определены в макроскопическом масштабе, источники диссипации происходят из взаимодействий и особенностей материалов в нано и микромасштабах.

В этой работе была сделана попытка прояснить эту проблему на примере полимерных композитных материалов с углеродными наполнителями. Идентификация и объяснение процессов диссипации вызванной трением и механизмов трения и износа в полимерных композитах являются главной целью этой работы. Известный в трибологии полимеров подход разделения диссипации на поверхностном и объемном уровне принят в этом исследовании полимерных композитов, поэтому два отдельных исследования проведены и представлены в последующих главах.

Глава 1. Теоретические и экспериментальные основы

Эта глава представляет теоретические и экспериментальные исследования найденные в литературе, от которых отталкивается наша работа. В начале напомнены читателю

теории и основные модели сухого трения и статического и динамического контакта. Основы трибологии, а именно наиболее замечательные экспериментальные результаты и законы трения Да Винчи, Амонтона и Кулона открывают эту главу. Наблюдения фактической площади статического и скользящего контакта Боуденом и Тэйбором представлены далее. Модель Герца для абсолютно упругого контакта и ее приложение к различным геометрическим формам контакта представлены на Рис. 1.3 - 1.5 и в Ур. 1.3 - 1.13. Контакт двух шероховатых поверхностей трактован следующими двумя моделями основанными на различных подходах. Модель Арчарда (Раздел 1.1.3.3) является геометрическим расширением модели упругого контакта Герца для растущего числа микроконтактов, в то время как модель Гринвуда и Уильямсона (Раздел 1.1.3.4) использует статистический подход и представляет контакт шероховатых поверхностей как случайное распредение микроконтактов Герца. Несмотря на разницу используемых подходов, обе модели приводят к одному выводу: пропорциональности фактической площади контакта и приложенной нормальной нагрузки. Кроме того, Гринвуд и Уильямсон ввели индекс пластичности, который связывает механические свойства контактирующих материалов и топографические свойства их поверхностей и определяет порог пластичности ограничивающий использование этой модели упругого контакта (Ур. 1.20).

Введение основных теорий сухого трения завершается короткой презентацией модели Боудена и Тэейбора для пластифицированного контакта шероховатых поверхностей (Раздел 1.1.4), ключевой модели для нашей работы. Авторы этой модели предполагают что поскольку фактическая площадь контакта является очень малой частью видимой площади контакта, даже очень слабые нагрузки должны вызывать локальную пластификацию выступов поверхности. В этом случае сила трения является суммой адгезивной силы, источник которой лежит в разрыве сформированных адгезионных связей между поверхностями, и силы пропахивания, которая возникает из-за пропахивания более мягкой поверхности твердыми и острыми выступами противоположной поверхности (Ур. 1.23). Эта модель была развита Сухом и Сином, которые добавили третий компонент силы трения вызванный деформацией выступов поверхности. Значение этого компонента растет в статических условиях трения.

Секция "Диссипация при трении и износе в полимерах"начинается с объяснения другого ключевого концепта для нашей работы, а именно разделения поверхностного и объемного вкладов в диссипацию полимеров. Поверхностная диссипация происходит в слое поверхности составляющем от 10 до 100 нм. Статические и динамические силы трения в этой зоне являются адгезивными и подчиняются теории Боудена и Тэйбора представленной ранее. Поверхностное напряжение сдвига, определяющее трение согласно этим авторам, для полимеров зависит от скорости деформации и длительности контакта. Диссипация в объемной зоне, в свою очередь, управляется пластическими и вязкоупругими деформациями и соответствует компоненту пропахивания из вышеупомянутой модели. Она определяется механическими свойствами материала и геометрией двух контактирующих тел. Глубина этой зоны обычно считается сопоставимой с радиусом контакта.

Нужно заметить, что главной особенностью полимеров по сравнению с другими материалами является их высокомолекулярная структура, которая зависит от типа

полимера: термопластичный, термореактивный или эластомер. Поэтому трибологическое поведение полимеров, также как и их механические и физические свойства, определяются в первую очередь их природой и молекулярным устройством.

Раздел 1.2.2 вводит понятие износа и проблему сложности идентификации определенного режима износа из-за одновременности их действия. Множество эмпирических законов износа было предложено различными авторами, среди которых закон Арчарда (Ур. 1.31 и 1.32), наиболее известный и лучше всего функционирующий для металлов. Этот закон основан на гипотезе абсолютно пластифицированного контакта. Согласно этому закону скорость износа пропорциональна приложенной нормальной силе отнесенной к твердости материала. Коэффициент пропорциональности, названный коэффициентом износа, варьируется между 10^{-3} и 10^{-7} и является характеристикой материала. Основными режимами износа, предположительно действующими при трении полимерных композитов, являются адгезионный (Раздел 1.2.2.1), абразивный (Раздел 1.2.2.2), усталостный (Раздел 1.2.2.3) и износ из-за размягчения или плавления полимера (Раздел 1.2.2.4). Важной особенностью износа полимеров, которая должна быть учтена при работе с ними, является их способность формировать трансферный слой, который в большинстве случаев уменьшает трение. В то же время, режимы износа полимерных композитов явно зависят от их ориентации по направлению к вектору скорости, этот аспект обсуждается в Разделе 1.2.4.

Раздел 1.3 Главы 1 представляет обзор литературы на тему экспериментальных результатов по трению и износу углепластиков. Из этой массы литературы выделены эффекты материалов (углеродных волокон и полимерной матрицы), ориентации и объемной доли волокон, нормальной силы и скорости скольжения и окружающей среды. Этот обзор выявил большое количество различных экспериментальных тенденций, которые часто противоречат друг другу. Также было замечено отсутствие информации по трению композитов между собой или против более мягкого материала.

Выводы данного обзора литературы привели нас к установлению целей и научного подхода для нашей работы. Таким образом нас интересует диссипация вызванная трением при скользящем контакте типа композит/композит и композит/эпоксидная смола, которая представляет более мягкий материал. Для достижения этой цели подход разделения поверхностного и объемного вкладов в диссипацию экспериментально применен к двум модельным композитным материалам армированным углеродными волокнами или наножемчужинами. Для выявления эффекта процентного содержания наполнителя эквивалентные эксперименты проведены на чистой эпоксидной смоле. Для осуществления экспериментального исследованиея сухого безызносного трения в поверхностной зоне диссипации будут использованы слабые нагрузки и скорости скольжения. В то время как более суровые трибологические условия вызывающие износ будут применены для изучения объемной диссипации.

Глава 2. Углеродные полимерные композиты

Глава 2 посвящена описанию изготовления и характеристик композиционных материалов и их компонентов, используемых в нашем трибологическом исследовании. Усло-

вием выбора армирующих материалов для наших модельных композитов является заметный контраст трибологических свойств с полимерной матрицей и, кроме того, разница в их геометрической форме и объемной доле для изучения этого эффекта. Таким образом, три типа материалов были выбраны: чистая эпоксидная смола, эпоксидная смола армированная углеродными волокнами с 34, 52 и 62% объемной долей волокна (CFRE) и эпоксидная смола амрированная углеродными наножемчужинами с 1, 15, 28 и 35% объемной долей наполнителя (CNPRE).

Эта глава начинается с описания нано и микроструктуры углеродных наполнителей и их физических и механических свойств. Далее представлены два типа модельных композитных материалов, их производство, морфология, топография поверхности и механические свойства.

Раздел 2.1 начинается с общих сведений о кристаллических и аморфных формах углерода. Далее представлены морфология и характеристики трех основных типов углеродных волокон, то есть высокопрочных анизотропных волокон, высокомодульных анизотропных волокон и изотропных волокон с средними механическими средствами (см. Табл. 2.1). Несмотря на то что научное сообщество в основном согласно с тем, что углеродные волокна содержат главным образом турбостратный углерод (Рис. 2.2), существует несколько различных моделей структуры углеродных волокон трех типов, которые вкратце представлены в Разделе 2.1.2.2. По сравнению с другими волокнами в композитной промышленности, эти волокна имеют ряд преимуществ, в том числе отличные механические свойства, хорошую термическую и химическую стойкость, низкий коэффициент теплового расширения и др.

Затем представлены технический углерод, в некотором смысле предок углеродных наножемчужин, и они сами. Частицы обоих материалов содержат жесткое аморфное ядро покрытое слоями углерода турбостратной структуры. Эти частицы диаметром от 10 до 100 нм формируют цепи от 50 до 500 нм, называемые агрегатами, которые в свою очередь образуют агломераты микрометрических размеров (Рис. 2.7). Основным преимуществом углеродных наножемчужин по сравнению с техническим углеродом является монодисперсность их размеров (примерно 85% полидисперсности). Средний диаметр наножемчужин использованных в этом исследовании - 90 нм.

Физические и механические свойства используемой в качестве матрицы в наших композитах эпоксидной смолы собраны в Табл. 2.4. Это термореактивный полимер, обладающий хорошей адгезией и хорошей влагостойкостью, но относительно низкой температурой стеклования и, следовательно, его механических свойства заметно падают около 100 - 120°C.

Армированные углеродными волокнами композиты различающиеся объемной долей волокон, а именно 34, 52 и 62%, изготовлены по двум различным процедурам. Физико-механические свойства композита с 62% волокон, так называемого "классического"углепластика, изготовленного формованием из нескольких слоев препрега уложенных параллельно по направлению волокон, представлены в Табл. 2.5 и 2.6. В тоже время, композиты армированные 34 и 52% волокон изготовлены из углеродной ткани пропитанной эпоксидной смолой. Параллельное направление волокон в этих слоях также контролируется, в отличие от плоскости слоев. В результате структура композита довольно неоднородна и неупорядочена в объеме и на поверхности из-за

волнистости армирующих слоев. Изготовленные из этих материалов образцы представлены на Рис. 2.10 и 2.11. Несмотря на то что поверхности всех образцов были отполированы одинаковым образом, состояние результирующих поверхностей композитов и чистой эпоксидной смолы отличается. Топография поверхности всех материалов измерена с помощью тактильного профилометра. Карта шероховатой поверхности углепластика с 62% волокон (Рис. 2.12) и профили поверхностей композитов армированных 34 и 52% волокон и чистой эпоксидной смолы (Рис. 2.13) указывают, что углеродные волокна выступают на поверхности и заметно увеличивают среднюю шероховатость поверхности по сравнению с чистой эпоксидной смолой. Локальные поверхностные механических свойства углепластика и чистой эпоксидной смолы измерены с помощью метода наноиндентации. Несколько углублений выполнены на углеродных волокнах и эпоксидной матрице, а также на образце из чистой эпоксидной смолы (Рис. 2.14). Рассчитанные на основании этих измерений значения твердости и поверхностного модуля упругости для эпоксидной матрицы более чем на порядок ниже по сравнению с углеродным волокном и практически одинаковы по сравнению с чистой эпоксидной смолой (Табл. 2.9).

Композиты армированные углеродными наножемчужинами 1, 15, 28 и 35% изготовлены литьем в форму из полидиметилсилоксана в лабораторных условиях (Рис. 2.16). Процесс их изготовления описан в Разделе 2.3.2, и пример образцов из этого материала представлен на Рис. 2.17. Высокая пористость композитов с концентрацией более 1% наножемчужин наблюдаемая на Рис. 2.18 - 2.21 оценена методом обработки изображений (Табл. 2.11). Хотя измерение шероховатости этих пористых поверхностей невозможно и не имеет смысла, поверхность композита с 1% наножемчужин является относительно гладкой, и ее шероховатость сходна с шероховатостью чистой эпоксидной смолы.

Краткая информация о свойствах и особенностях двух типов композитных материалов используемых в нашем экспериментальном исследовании собрана в Табл. 2.13.

Глава 3. Поверхностная фрикционная диссипация: экспериментальное исследование

Эта глава посвящена экспериментальному исследованию трибологических фрикционных потерь в поверхностной зоне двух типов композитов и чистой эпоксидной смолы, описанных в предыдущей главе. Важнейшим условием для этого исследования является отсутствие повреждения поверхности, которое может быть достигнуто путем применения очень низких контактных давлений, то есть низкой нормальной нагрузки приложенной к большой поверхности. Для определения оптимальных трибологических условий для изучения поверхностного трения проведены предварительные экспериментальные исследования. Целью представленной в этой главе работы является экспериментальный анализ вклада углеродного наполнителя в диссипацию при трении композитов. Также исследуется влияние ориентации углеродных волокон относительно направления скольжения на поверхностное трение. Вторая часть этой главы посвящена экспериментальному изучению локального трения между уг-

леродными волокнами и эпоксидной смолой, направленное на получение локальных коэффициентов трения, которые нам пригодятся в дальнейшем теоретическом исследовании.

Экспериментальная установка, используемая в этом исследовании представлена в Разделе 3.1.1. Этот трибометр, именуемый RA, разработан в лаборатории LTDS и позволяет осуществлять возвратно-поступательное скольжение между двумя образцами относительно большой поверхности при низких нормальных нагрузках (Рис. 3.1). Длинный прямоугольный образец, называемый треком, закреплен на базовой поверхности трибометра, в то время как другой круглый образец, называемый слайдером, приводится в движение с помощью движущейся части трибометра и скользит по треку. Нормальная сила применяется с помощью груза помещенного на слайдер и может достигать 20 Н. Тангенциальная сила измеряется с помощью пьезоэлектрического датчика установленного в движущейся части трибометра. Скорость скольжения контролируется с помощью линейного двигателя и может достигать от нескольких мкм/с до 2 м/с.

Для этого экспериментального исследования, были изготовлены образцы из всех вышеописанных материалов с размерами $80 \pm 2 \times 25 \pm 2 \times 5 \pm 1$ мм^3 и $20 \varnothing \pm 2$ мм $\times 5 \pm 1$ мм для трека и слайдера соответственно. Перед каждым экспериментом поверхность обоих образцов тщательно очищается с помощью гептана, ацетона, пропанола-2 и потока азота. Все эксперименты проведены при комнатной температуре и влажности.

Каждый эксперимент представляет собой последовательность из 25 циклов скольжения (50 ходов), в течение которых тангенциальная сила измеряется с частотой сэмплирования 1 кГц и сохраняется в памяти компьютера. Средний кинетический коэффициент трения рассчитывается из этого сигнала обрезанного на 20% с двух концов, отнесенного к постоянной нормальной силе, и усредняется между двумя смежными ходами образующими цикл.

Измеренные датчиком силы трения сигналы, показаные на Рис. 3.2, более или менее стабильны в течение каждого хода, с гораздо лучшей стабильностью для пары трения CFRE 62%/CFRE 62%, чем для всех остальных материалов. При трении композитов аримированных углеродными наножемчужинами наблюдаются неустойчивости, происхождение которых можно отнести к жесткости контакта этих частиц распределенных в полимерной матрице. Кроме того, зафиксирован большой разброс коэффициентов трения в течение одного эксперимента и между несколькими экспериментами для чистой эпоксидной смолы и всех композитов кроме CFRE 62% (Рис. 3.3). Эта дисперсия, вероятно связанная со слабыми повреждениями поверхности, становится больее заметной при более суровых трибологических условиях.

Результаты исследования влияния трибологических условий, то есть нормальной силы и скорости скольжения, на трение наших материалов представлены в Разделе 3.1.4. С одной стороны, большие нагрузки и низкие скорости скольжения способствуют образованию сращиваний между двумя поверхностями и повреждению поверхностей. С другой стороны, низкие нормальные нагрузки и большие скорости скольжения могут привести к низкой площади контакта, и таким образом, к недооценке контактного давления и нагреву поверхности. Компромисс между этими условиями установлен экспериментально для каждой пары изучаемых материалов, см. Рис.

3.5 - 3.7 и Приложение 1, заключающее в себе таблицы измеренных коэффициентов трения. Значения выбранных скорости скольжения и нормальной нагрузки представлены в Табл. 3.2. Малые нормальные силы рекомендуются для пар трения с чистой эпоксидной смолой (0.5 Н) и композитов армированных углеродными наножемчужинами (1 Н) для избежания повреждения поверхности. Нормальная сила в 2 Н выбрана для пары CFRE/CFRE. Эти нагрузки соответствуют нормальному контактному давлению 1.59, 6.37 и 3.18 кПа, соответственно. Скорость скольжения постоянна для всех пар трения и равна 10 мм/с.

Эти экспериментальные условия затем применены для изучения влияния объемной доли наполнителя на поверхностную диссипацию в композитах вызванную трением (Раздел 3.1.5). Результаты этого исследования для пар трения эпоксидная смола/CFRE, CFRE/CFRE и CNPRE/CNPRE представлены на Рис. 3.8. Небольшое увеличение коэффициента трения с увеличением доли волокон наблюдается в паре эпоксидная смола/CFRE. Эта тенденция, между прочим, обратна найденной в литературе для пары CFRE/сталь определенно из-за повреждения поверхности композита более твердой сталью. В то же время, добавление волокон в эпоксидную смолу, то есть в паре трения CFRE/CFRE, уменьшает коэффициент трения более чем в два раза по отношении к паре эпоксидная смола/эпоксидная смола. Вариация объемной доли волокна от 34 до 62%, не оказывает существенного влияния на трение композитов. В отличие от углеродных волокон, армирование эпоксидной смолы углеродными наножемчужинами значительно увеличивает трение. В этом случае, коэффициент трения выше для большей объемной доли наножемчужин. Его значение для CNPRE 35% в 1.5 раза выше по сравнению с CNPRE 1% или чистой эпоксидной смолой.

Влияние ориентации волокон на поверхностное трение для пары "классических" углепластиков, CFRE 62%, изучено и представлено в Разделе 3.1.5.3. Для вариации суммарного угла между ориентацией волокон в двух образцах от 0° до 180° использовались треки с ориентацией волокон 0°, 45° и 90° по отношению к вектору скорости скольжения и вращение круглого слайдера (см. схему на Рис. 3.9). В этих условиях, средний коэффициент трения колеблется между 0.17 и 0.18 (Рис. 3.10). Теоретически, поскольку шероховатость поверхности композита в направлении перпендикулярном волокнам больше чем в параллельном направлении, трение в перпендикулярном направлении должно быть сильнее. Однако, при слабых трибологических условиях способствующих поверхностному трению, этот эффект не выражен.

Экспериментальные исследование локальных коэффициентов трения между отдельными углеродными волокнами и эпоксидной смолой также выполнено в рамках нашего исследования и представленно в Разделе 3.2. Для этого исследования был использован наноскретчер CSM Instruments со сферическим индентором радиуса 25 мм (Рис. 3.11). Этот прибор может измерять нормальную нагрузку, эквивалентную давлению 0.05 - 2 МПа, и тангенциальную силу с большой точностью и совершать скольжения в несколько нано или микрометров. В данном экспериментальном исследовании, проведенном при комнатной температуре и влажности, применены скорость скольжения 30 мкм/с и постепенно растущая нормальная сила от 1 до 50 мН, с шагом 2 мН между 1 и 20 мН, и шагом 5 мН между 20 и 50 мН.

Сферический индентор покрыт однонаправленным слоем углеродных волокон за-

крепленным по краям, как показано на Рис. 3.12 (а). Этот слайдер скользит либо по цилиндрическому образцу из эпоксидной смолы используемому как слайдер в предыдущем исследовании, либо по пучку углеродных волокон (Рис. 3.12 (б)). Во втором случае были испытаны параллельная и перпендикулярная ориентации между волокнами слайдера и стационарными волокнами.

Сила трения довольно стабильна в течение каждого прохода в 600 мкм с постоянной нормальной нагрузкой, что позволяет нам работать со средним коэффициентом трения, показанным на Рис. 3.13 в зависимости от нормальной силы. Нужно отметить, что изменения коэффициента трения с нормальным силой незначительны за исключением пары волокна/волокна при параллельной ориентации. Это можно объяснить случайным смещением ориентации между волокнами двух образцов. Полученные экспериментальные результаты сопоставлены с результатами Розельмана и Тэйбора (Раздел 3.2.3.) для отдельных углеродных волокон. Наши коэффициенты для тех же пар трения между углеродным волокном и эпоксидной смолой отличаются по сравнению с экспериментальными результатами Розельмана и Тэйбора, вероятно, из-за различных трибологических условий (см. Табл. 3.4).

Полученные в этой главе экспериментальные результаты вызывают появление ряда вопросов, на которые мы постараемся ответить в следующей главе. В частности, почему добавление углеродных волокон в один материал из пары трения увеличивает трение, в то время как в случае армирования обоих материалов коэффициент трения падает? Почему углеродные волокна и наножемчужины влияют на трение эпоксидной смолы противоположно? Каковы механизмы возникающие в трении пар из изучаемых материалов?

Глава 4. Поверхностная фрикционная диссипация: аналитическая модель

В этой главе разработана и представлена аналитическая модель поверхностного трения композиционных материалов, которая помогает ответить на вопросы поставленные в конце предыдущей главы и предсказать трение в зависимости от объемной доли наполнителя. Глава начинается с краткой презентации двух моделей на сходную тему найденных в литературе. Несмотря на их кажущуюся близость к нашей теме, обе модели были разработаны для контакта композит/более твердый однородный материал.

Первая модель, описанная в Разделе 4.1.1, основана на следующих гипотезах: площадь контакта волокон и матрицы пропорциональна общей площади контакта с коэффициентами пропорциональности объемной долей волокон и матрицы соответственно; напряжения сдвига волокон и матрицы равны; и модули жесткости волокон и матрицы также равны. Эта модель приводит к обратной пропорциональности коэффициента трения композита к коэффициентам трения его компонентов с коэффициентами пропорциональности равными объемной доле волокон и матрицы (Ур. 4.2).

Вторая модель, описанная в Разделе 4.1.2, охватывает трение между композиционными материалами и абразивным материалом. Гипотезами этой модели являются

неизменность трибологических свойств фаз композитного материала по сравнению с трением отдельных материалов и постоянность соотношения площадей контакта фаз композита при трении. В случае отсутствия износа нормальная сила распределена между фазами пропорционально поверхностым долям фаз, и значит для композита, содержащего один наполнитель и матрицу, коэффициент трения пропорционален коэффициентам трения его фаз (Ур. 4.10).

Идеи и гипотезы этих двух моделей вдохновили нас на создание новой обобщенной модели для поверхностного трения между двумя композитами представленной в Разделе 4.2. Наша модель основана на адгезивной модели Боудена и Тэйбора (Раздел 1.1.4) примененной к композитным материалам как показано на Рис. 4.2. Площадь контакта постоянно обновляется во время скольжения, но ее состав, т. е. соотношение между компонентами композита в контакте, остается постоянным. Следующие гипотезы наложены нашей моделью:

- Отсутствие повреждений поверхности и износа;
- Кулоновское трение для всех микроконтактов;
- Силы трения в микроконтактах независимы друг от друга;
- Изотропное трение для всех пар контактирующих материалов.

Согласно Боудену и Тэйбору контакт двух твердых тел состоит из множества микроконтактов, которые образуют фактическую площадь контакта. Нормальные и касательные силы распределяются между этими микроконтактами. Поскольку площадь каждого микроконтакта очень мала, давление превышает предел текучести более мягкого материала, и, значит, этот контакт можно рассматривать как пенетрацию выступов одного материала в другой. Следовательно, нормальная сила может быть найдена по формуле Ур. 4.13. Образуемые между двумя контактирующими телами при нормальной нагрузке сращивания при трении, то есть сдвиговой нагрузке, постоянно разрываются, и тангенциальная сила может быть выражена формулой 4.14. Следовательно, коэффициент кулоновского трения может быть посчитан и зависит от площади микроконтактов, сдвиговых напряжений, действующих на этих микроконтактах, и твердости материалов образующих эти микроконтакты (Ур. 4.15).

Поскольку прямое применение этого закона трения маловозможно из-за отсутствия информации о фактической площади контакта и напряжений сдвига в микроконтактах, мы предлагаем два частных граничных случая. В Случае 1 предполагается, что твердость всех фаз композита равна определенному значению эффективной твердости. В этом случае коэффициент трения может быть найден по закону прямой пропорциональности (Ур. 4.16). С другой стороны, если предположить, что касательные напряжения равны некоему эффективному значению для всех микроконтактов, как в Случае 2, то закон для коэффициентов трения имеет вид обратной пропорциональности (Ур. 4.17).

Эта модель, которая приводит к зависимости коэффициента трения между двумя композитами от локальных коэффициентов трения между их фазами и их поверхностной доли, а приори может быть применена к любому типу композитных материалов.

В продолжении этой главы результаты нашей модели сопоставлены с экспериментальными результатами полученными в предыдущей главе. В разделе 4.3 обсуждается выбор локальных коэффициентов трения на основе экспериментального исследования, представленного в Разделе 3.2 и литературе. Затем проведено исследование для определения поверхностной доли фаз композита, представленое в Разделе 4.4. В этом исследовании использован вероятностный подход, применение которого для композитного материала армированного цилиндрическими волокнами или сферическими наножемчужинами приводит к выводу, что поверхностная доля наполнителя равна его объемной доле.

В Разделе 4.5 описано применение нашей модели к контакту между чистой эпоксидной смолой и композитом на основе эпоксидной смолы армированной углеродными волокнами. Исследуются оба частные случая (Ур. 4.16 и 4.17), и результирующие кривые для коэффициента трения в зависимости от поверхностной доли волокон, также как и экспериментальные точки полученные в предыдущей главе, приведены на Рис. 4.5. Нужно отметить, что оба закона, прямой и обратной пропорциональности, хорошо следуют экспериментальной тенденции. Кроме того, изучение этого контакта позволяет выбрать лучший из локальных коэффициентов трения среди представленных в Разделе 4.3. Тот факт, что оба предложенных закона следуют экспериментальной тенденции, объяснен с точки зрения валидации гипотез эффективных твердости и напряжений сдвига для этого типа контакта.

В случае контакта двух композитов, где каждый содержит две фазы - матрицу и наполнитель, законы прямой и обратной пропорциональности принимают вид Ур. 4.27 и Ур. 4.28. Коэффициенты в этих уравнениях должны быть определены с помощью геометрии контакта для каждого типа композита отдельно. Контакт CFRE/CFRE исследуется в Разделе 4.6.1. Состав зоны видимого контакта, схематически показаного на Рис. 4.6, позволяет рассчитать коэффициенты Ур. 4.30. Полученные кривые для этого типа контакта приведены на Рис. 4.7. На этом рисунке нужно отметить, что зеленая кривая, то есть обратный закон, проходит через экспериментальную точку для "классического"углепластика с 62% углеродных волокон. Экспериментальные точки для композитов с другими концентрациями волокон не пересекаются теоретической кривой вероятно из-за нерегулярности и неоднородности состава поверхности композитов с 34 и 52% волокон. Применение прямого и обратного законов трения также обсуждается в этом случае контакта двух композитов. Выбор закона обратной пропорциональности оправдан существенным различием в твердости двух компонентов композита, в то время как оцененные величины напряжения сдвига имеют одинаковый порядок. Кроме того, применение этой модели позволило установить, что ориентация волокон, учтенная при рассмотрении геометрии контакта, не влияет на коэффициент поверхностного трения, результат подтвержденный экспериментальным исследованием представленным в предыдущей главе.

Контакт двух композитов армированных углеродными наножемчужинами рассматривается в Разделе 4.6.2. Поскольку размер наножемчужин не меньше, чем размер выступов поверхности, тот же принцип разделения микроконтактов по типу материалов их составляющих может быть применен. Коэффициенты для законов трения для этого типа контакта приведены в формуле 4.33 и равны коэффициентам кон-

такта CFRE/CFRE. Применение двух частных законов в этом случае невозможно поскольку локальные коэффициенты трения между наножемчужинами неизвестны. Несколько пар этих локальных коэффициентов предложены с помощью математической аппроксимации теоретической кривой к экспериментальным точкам, осуществленной в Matlab для обоих частных законов (Табл. 4.2). Возможности выбора этих коэффициентов обсуждены, и наиболее подходящая и правдоподобная пара коэффициентов наножемчужина/наножемчужина и наножемчужина/эпоксидная смола выбрана. Кривые коэффициента трения от поверхностной доли наножемчужин построенные для этой пары локальных коэффициенты совместно с экспериментальными точками представлены на Рис. 4.9. Как и в случае трения CFRE/CFRE, закон прямой пропорциональности не может быть применен из-за разницы между твердостью эпоксидной смолы и наножемчужин.

Представленная аналитическая модель может быть улучшена путем рассмотрения распределения площади контакта между фазами композита, которое обсуждается в Разделе 4.7. Это распределение, безусловно, зависит от шероховатости поверхностей и распределения контактного давления между фазами, то есть механических свойств контактирующих материалов.

Глава 5. Объемная фрикционная диссипация

В этой главе представлено экспериментальное исследование объемной фрикционной диссипации и возникающего при этом процессе износа, проведенное на углепластике CFRE 62% и чистой эпоксидной смоле. В данном исследовании применяются более суровые трибологические условия, при которых вырабатываемая трением энергия может быть рассеяна через различные механизмы, как нагрев, повреждение поверхности или пластические деформации, которые будут рассмотрены в этой главе. Следующий мультимасштабный подход был разработан и применен для этого исследования: для начала проводится оценка макроскопических характеристик, таких как потеря массы, коэффициент трения, диссипация энергии и нагрев, и затем проводятся наблюдения изношенных поверхностей на микроскопическом уровне с целью обнаружения признаков различных механизмов износа и корреляции условий их появления с макроскопическими параметрами.

Это экспериментальное исследование проведено на линейном трибометре также разработанном в LTDS и показаном на Рис. 5.1. Этот прибор позволяет получить коэффициент трения при возвратно-поступательном движении с синусоидальным законом изменения скорости скольжения. Нормальная сила применяется с помощью вертикального перемещения базовой плоскости трибометра, на которой укреплен неподвижный образец. Эта сила измеряется постоянно и одновременно с касательной силой и перемещением слайдера. Пример сигнала этих измеряемых величин показан на Рис. 5.2, который демонстрирует относительную стабильность сигналов сил во время проходов, что позволяет нам оперировать кулоновским коэффициентом трения. Четыре набора примененных экспериментальных условий различаются нормальной силой и скоростью скольжения, как представлено в Табл. 5.2. Для изучения эволюции режимов износа с течением времени во время скольжения продолжительность

испытания варьируется от 10 до 1000 или 5000 циклов в зависимости от материала.

Образцы для этого исследования изготовлены из чистой эпоксидной смолы и CFRE и имеют прямоугольную форму с размерами $30 \pm 2 \times 15 \pm 2 \times 4 \pm 1$ мм^3 и $8 \pm 1 \times 6 \pm 1 \times 4 \pm 1$ мм^3 соответственно. Реальная площадь поверхности слайдеров, различная для всех образцов, измеряется и учитывается во всех расчетах представленных в этой главе. Кинематическая длина для трека и слайдера рассчитана и представлена в Разделе 5.1.3, как показано на Рис. 5.3.

Результаты исследования представленного в этой главе разделены по парам материалов. Таким образом, она представляет последовательно исследование пар эпоксидная смола/ эпоксидная смола, эпоксидная смола/CFRE и CFRE/CFRE.

Изучение объемной диссипации в контакте полимер/полимер с помощью макроскопического подхода представлено в Разделе 5.2.1. Для начала на основе результатов измерения массы слайдера и трека до и после каждого испытания предложен закон износа (Ур. 5.2). Потеря массы увеличивается линейно с ростом кинематической длины для трека и слайдера по-отдельности (Рис. 5.4) и их суммы (Рис. 5.5). Несмотря на сходство с линейным законом износа Арчарда представленным в Главе 1, коэффициенты износа, посчитанные на основе наших измерений и представленные в Табл. 5.3, демонстрируют выраженную зависимость от приложенных трибологических условий. Эта зависимость противоречит закону Арчарда, который постулирует, что коэффициент износа является свойством материала и не зависит от приложенных условий. Это может означать, что контакт эпоксидная смола/эпоксидная смола в этих условиях не полностью пластифицирован.

Коэффициенты трения рассчитываются на основе измерений мгновенной нормальной и тангенциальной силы и представлены в виде карт трения (Рис. 5.6). На этих картах, ось x представляет номер цикла, ось y соответствует перемещению слайдера в течение одного прохода, и коэффициенты трения обозначены цветом. Синие области с низким коэффициентом трения, наблюдающиеся на этих картах в конце прохода, можно объяснить дефектами параллельности между двумя поверхностями и удалением третьего тела из зоны контакта. Колебания наблюдаемые на картах на Рис. 5.6 (c) и (d) связаны с недостаточной жеткостью трибометра при данных частотах нагрузки и считаются невлияющими на средний коэффициент трения. Представленные на этих картах результаты позволяют заключить, что для пары эпоксидная смола/эпоксидная смола средний коэффициент трения довольно высок и практически не зависит от приложенных условий.

Диссипация энергии рассчитана на основе силы трения и мгновенной скорости скольжения в соответствии с формулой 5.4 и построена в зависимости от кинематической длины на Рис. 5.7. На этом графике наблюдается линейная зависимость определенная нормальной силой, которая может быть объяснена преобразованием выражения для диссипации энергии в Ур. 5.5.

Найденные линейные зависимости для величин диссипации энергии и потери массы от кинематической длины позволяют определить коэффициент пропорциональности для нашего закона износа (Ур. 5.7), который зависит от силы трения и некой критической скорости, что подтверждается экспериментальными тенденциями.

Раздел 5.1.2.4 дает оценку температуры контакта в соответствии с моделью Джа-

гера-Арчарда-Блока. Сначала рассчитывается количество тепла исходя из силы трения, скорости скольжения и площади контакта (Ур. 5.8 и 5.9). Фактическая температура контакта может быть представлена как сумма температуры объема материала и кратких вспышек температуры на поверхности, которые могут принимать очень высокие значения (Ур. 5.10). Выделенное тепло распределяется между двумя контактирующими телами с коэффициентом распределения, который может быть определен по формуле 5.14. Далее в этом разделе рассчитано число Пекле, которое позволяет оценить профиль распределения тепла в двух телах. Для двух используемых скоростей высокое значение числа Пекле означает, что большая часть тепла распространяется в зафиксированном образце, и профиль его распределения неглубокий. Для оценки фактической температуры контакта предлагается рассмотреть два граничных случая площади контакта, а именно видимая площадь контакта (площадь слайдера) и полностью пластифицированная площадь контакта, рассчитанная как отношение нормальной нагрузки и твердости материала. Несмотря на то что значения результирующих температур контакта, представленные в Табл. 5.5 и на Рис. 5.10, малореальны, тенденции изменения температуры для изучаемых четырех условий одинаковы. Реальная температура контакта должна находиться между этими двумя предельными случаями ближе к нижней границе. Нужно отметить, что более высокие скорости приводят к большему нагреву. Очень высокая на поверхности температура быстро остывает на малой глубине материала, как показано на Рис. 5.11.

Микроскопический подход к изучению объемной диссипации в контакте эпоксидная смола/эпоксидная смола позволил определить два типа изношенных поверхностей показанных на Рис. 5.12 и 5.13. Было замечено, что поверхности 1-го типа появляются при низкой скорости, в то время как поверхность типа 2 характеризует скольжение при высокой скорости. Эволюция типа изношенной поверхности от отдельных царапин до поверхности типа 1 или 2 схематически показана на Рис. 5.14.

Макроскопические фотографии всех изношенных образцов обработаны с помощью программного обеспечения для обработки изображений с целью оценки площади изношенной поверхности, как показано на Рис. 5.15. Так как некоторые процессы диссипации не вызывают потери веса, но при этом деформируют поверхность, эта диссипация энергии может быть лучше прослежена через изменение фактической изношенной области, чем потерю массы (Рис. 5.17). Этот график позволяет выделить две области диссипации: мы связываем первую с чистым абразивным износом и вторую со всеми остальными механизмами износа.

Микроскопические наблюдения изношенных поверхностей позволили зафиксировать несколько механизмов износа, такие как абразивный износ двух или трех тел, адгезионый износ, размягчение полимера и перенос материала между двумя контактирующими образцами, представленные и обсуждаемые в Разделе 5.2.2.3. Различные механизмы износа наблюдаются в зависимости от типа изношенной поверхности (Типа 1 или 2) различаемых на макроскопическом уровне. Для рационализации эволюции механизмов износа, мы предлагаем ретроспективу износа в Разделе 5.2.3, которая схематизирована на Рис. 5.21. Износ всегда начинается с абразивного износа двух тел, и затем распространяется по одному из двух возможных сценариев: "Износ трех тел"или "Адгезия и тепловые эффекты".

Для изучения объемной диссипации в парах эпоксидная смола/композит и композит/композит применяется тот же подход разработанный для пары эпоксидная смола/эпоксидная смола и представленный в Разделе 5.3. Потеря массы эпоксидной смолы также увеличивается линейно с кинематической длиной (Рис. 5.22), в то время как масса композита остается неизменной при любых изучаемых условиях. Только при самых суровых трибологических условиях после 5000 циклов скольжения потеря массы композита может быть измерена и соответствует скорости износа в 100 раз меньшей, чем у чистой эпоксидной смолы при тех же условиях. Карты трения, представленные на Рис. 5.23 и 5.25 для этих пар трения, демонстрируют зависимость коэффициента трения от применяемых условий, в отличие от пары эпоксидная смола/эпоксидная смола. Зависимость диссипации энергии от кинематической длины слайдера, построенная на Рис. 5.24 и 5.26, подтверждает эту тенденцию. Термический анализ для этих двух пар, представленный в Разделе 5.3.3, дает менее глубокий профиль распространения тепла в образцах, чем для пары эпоксидная смола/эпоксидная смола. Фактические температуры контакта, приведенные на рис. 5.27 и 5.28, показывают ту же тенденцию что и для контакта полимер/полимер, но их значения ниже для контактов с композитом.

Применение микроскопического подхода к этим двум контактам позволяет выделить несколько механизмов износа. В частности, эпоксидная смола изнашивается в основном абразивно из-за более высокой твердости противоположной поверхности (Рис. 5.29 - 5.31). В этом случае, микрочастицы углеродных волокон зафиксированы на поверхности чистой эпоксидной смолы. Износ композита в этой паре трения пренебрежимо мал, но может быть замечен в углублении области матрицы (Рис. 5.31 (а)). Износ композита против композита при самых суровых применных условиях показан на Рис. 5.32. Он начинается с отделения эпоксидной матрицы от поверхности в областях между волокнами композита, эти волокна затем полируются противоположной поверхностью, и, наконец, формирующееся из смешанных частиц эпоксидной смолы и углеродных волокон, третье тело изнашивает обе контактирующие поверхности абразивно.

Выводы

Общие выводы данного исследования объемной и поверхностной фрикционной диссипации композитов армированных углеродными наполнителями и перспективы будущей работы представлены в конце этой рукописи. Обобщенная для двух регионов диссипации эволюция коэффициентов трения и износа построенна как функция от трибологических условий для трех пар исследуемых материалов на Рис. С.1. Механизмы диссипации и износа обсуждаются для каждой пары. Наше исследование выявило экспериментально, что из-за высоких тепловых и механических свойств углеродных волокон, их добавление в эпоксидную смолу увеличивает устойчивость к износу и отвод тепла и, следовательно, уменьшает нагрев контакта и изменяет режимы износа по сравнению с чистой эпоксидной смолой. В то же время, оно снижает коэффициент трения композитов сравнению с чистой эпоксидной смолой как при поверхностной, так и при объемной диссипации.

Appendix D

Extended abstract in French

Dissipation interfaciale et volumique induite par frottement dans les composites

Depuis plusieurs décades, les matériaux composites à base de polymère trouvent de plus en plus d'applications aussi bien dans l'industrie aérospatiale que dans l'industrie du sport et du loisir. Cet intérêt est dû à leurs bonnes propriétés mécaniques et thermiques associées à une masse légère. Bien que beaucoup de modèles analytiques et numériques pour le calcul de leurs propriétés mécaniques soient proposés et utilisés par les ingénieurs partout dans le monde, leurs propriétés tribologiques restent assez méconnues.

Les lois de mélange empiriques sont généralement utilisées pour le calcul des coefficients de frottement et d'usure. Cependant, la compréhension générale du problème est incomplète. D'un point de vue scientifique, le problème de dissipation par frottement dans les contacts de plusieurs matériaux reste un grande challenge à cause d'une interférence des propriétés surfaciques et volumiques mécaniques, thermiques, chimiques, géométriques et d'autres, de chaque composant du composite et de son interface. De plus, ce problème est multiéchelle : tandis que les coefficients de frottement et d'usure sont définis à l'échelle macroscopique, les origines de la dissipation se trouvent dans les interactions et particularités de matériaux à l'échelle nano- et microscopique.

Dans ce travail, nous avons tenté de clarifier ce problème appliqué aux matériaux composites modèles renforcés par du carbone. Cependant, la compréhension des processus de la dissipation induite par frottement et des mécanismes du frottement et d'usure dans les composites à base des polymères est l'objectif principal de ce travail. Une approche de séparation des dissipations au niveau interfacial et volumique, connue dans la tribologie des polymères, est adoptée dans notre étude de composites à base des polymères. Deux études indépendantes sont alors réalisées et présentées dans ce manuscrit.

Chapitre 1. Bases théoriques et expérimentales

Ce chapitre présente les bases théoriques et expérimentales trouvées dans la littérature, sur lesquelles s'appuie notre étude de dissipation par frottement dans les composites du

carbone. Tout d'abord, les théories et les principaux modèles du frottement sec et du contact statique et glissant sont rappelés. Les origines de la tribologie, les résultats expérimentaux les plus marquants et les lois de frottement de Da Vinci, d'Amontons et de Coulomb ouvrent ce chapitre. Ensuite, nous présentons les observations de l'aire réelle de contact statique et glissant par Bowden et Tabor, suivies par le modèle du contact élastique de Hertz avec son application à différentes géométries de contact (Eqs. 1.3-1.13, Fig. 1.3-1.5). Le contact multi-aspérités est traité par deux modèles basés sur des approches différentes. Le modèle d'Archard (Sec 1.1.3.3) est l'extension géométrique du modèle du contact élastique de Hertz pour un nombre croissant de contacts, tandis que le modèle de Greenwood et Williamson (Sec 1.1.3.4) utilise l'appoche statistique et voit le contact multi-aspérités comme une distribution aléatoire de microcontacts de Hertz. Malgré la différence d'approche utilisée, les deux modèles conduisent à une même conclusion : la proportionnalité de l'aire réelle de contact à la force normale appliquée. De plus, Greenwood et Williamson ont proposé un indice de plasticité qui lie les propriétés mécaniques du matériau et sa topographie de surface et définit un seuil de plasticité qui donne les limites d'utilisation de ce modèle élastique pour un contact donné (Eq. 1.20). L'introduction des théories principales de frottement sec général est conclue par présentation sommaire du modèle de Bowden et Tabor d'un contact multi-aspérités plastifié (Sec. 1.1.4), le modèle clef pour notre travail. Les auteurs supposent que l'aire de contact réel étant très petite devant l'aire apparente, même une très faible charge normale provoquerait la plastification locale des aspérités. Dans ce cas, la force de frottement est composée d'une force adhésive F_{adh}, dont l'origine est dans la rupture de l'adhésion entre deux surfaces, et une force de labourage F_{pl} qui est provoquée par le labourage de la surface plus molle par des aspérités aigües de la surface antagoniste plus dure (Eq. 1.23). Une extension de ce modèle a été développée pour le coefficient de frottement par Suh et Sin, qui ajoutent à ces deux composantes de la force de frottement une troisième composante induite par la déformation des aspérités, plus importante en condition statique.

La section 'Dissipation by friction and wear in polymers' démarre par une explication d'un autre concept clef pour notre étude, celui de la séparation des contributions interfaciale et volumique dans la dissipation dans les polymères. La dissipation interfaciale agit dans une couche de la surface d'une profondeur de 10 à 100 nm. Les forces de frottement statique et dynamique sont plutôt adhésives et obéissent la théorie de Bowden et Tabor montrée précédemment. La contrainte de cisaillement interfaciale, qui définit le frottement selon Bowden et Tabor, dépend, pour les polymères, du taux de déformation et du temps de contact. La dissipation dans la zone volumique est gouvernée par les déformations plastiques et viscoélastiques et peut être reliée à la composante de labourage du modèle de Bowden et Tabor. Elle dépend surtout des propriétés mécaniques du matériau et de la géométrie des corps en contact. Cette zone s'étend généralement d'une profondeur de l'ordre de grandeur du rayon de contact.

En général, le comportement tribologique, ainsi que les propriétés mécaniques et physiques d'un polymère dépendent fortement de sa nature, c'est-à-dire thermoplastique, thermodurcissable ou élastomère.

La section 1.2.2 introduit le terme d'usure et le problème de la complexité d'identification d'un régime d'usure particulier à cause de leur simultanéité d'action. Il existe de nom-

breuses lois d'usure, parmi lesquelles la loi d'Archard (Eq. 1.31, 1.32) est la plus connue et fonctionne relativement bien pour les métaux. Cette loi est basée sur une hypothèse d'un contact entièrement plastifié. Selon la loi d'Archard, le taux d'usure est proportionnel à la force normale appliquée, divisée par la dureté du matériau. Le coefficient de proportionnalité appelé coefficient d'usure varie de 10^{-3} à 10^{-7} pour des matériaux différents. Les régimes d'usure principaux supposés agir pendant le frottement de matériaux composites à base de polymères sont l'usure adhésive (Sec. 1.2.2.1), abrasive (Sec 1.2.2.2), usure par fatigue (Sec. 1.2.2.3) et usure à cause du ramollissement du polymère (Sec. 1.2.2.4). Une particularité de l'usure des polymères qui doit être pris en compte est leur capacité à former une couche de transfert qui, dans la plupart des cas, réduit le frottement et l'usure. En revanche, les régimes d'usure des composites à base des polymères dépendent fortement de leur orientation par rapport au sens de glissement : parallèle, antiparallèle ou normale, et sont discutés en Sec. 1.2.4.

La Sec. 1.3. du Chapitre 1 présente une revue des publications de résultats expérimentaux sur le frottement et l'usure de composites à base de résine époxy renforcée par des fibres de carbone. Les effets des matériaux (carbone et la matrice de polymère), de l'orientation et de la fraction volumique de fibres, les propriétés mécaniques et topographiques de la surface opposée, de la force normale et de la vitesse de glissement et de l'environnement sont évoqués. Il a été relevé un grand nombre de tendances expérimentales qui souvent se contredisent. Un manque d'informations sur le frottement du composite contre lui-même ou un autre matériau plus mou est également observé.

Cette revue de la littérature nous amène à définir les objectifs et les démarches de notre travail. Nous allons nous intéresser à la dissipation par frottement en contact glissant de composite/composite et composite/résine époxy, qui constitue le matériau plus mou. Pour cela, l'approche de séparation des contributions interfaciale et volumique est adoptée et appliquée expérimentalement sur des matériaux modèles composites à base d'époxy renforcés par des fibres ou nanoperles de carbone. Les expériences équivalentes sur une époxy pure seront également réalisées pour mettre en évidence l'influence du renfort de carbone. Nous allons mettre en place une étude expérimentale de frottement pur, i.e. sans usure, sous faibles charges normales et faibles vitesses de glissement et développer un modèle analytique pour étudier la dissipation interfaciale. Une étude de frottement sous des conditions tribologiques plus sévères induisant l'usure va au contraire nous donner une image de la dissipation volumique.

Chapitre 2. Matériaux composites polymères renforcés par du carbone

Le Chapitre 2 est consacré à la description, la fabrication et la caractérisation des matériaux composites et leur composants utilisés dans notre étude tribologique. Les renforts de nos matériaux modèles doivent présenter un contraste prononcé des propriétés tribologiques avec la matrice polymère, ainsi qu'une différence de leur forme géométrique et fraction volumique pour étudier l'effet de l'anisotropie. Trois types de matériaux ont été choisis : une époxy pure, une époxy renforcée par des fibres de carbone de 34, 52 et 62 % de fraction volumique de fibres (CFRE) et, enfin, une époxy renforcée par des nanoperles

de carbone de 1, 15 , 28 et 35 % de fraction volumique de nanoperles (CNPRE).

Ce chapitre commence par une description de la nano et microstructure des renforts de carbone et de leur propriétés physiques et mécaniques. Ensuite, deux types de matériaux composites modèles, leur fabrication, morphologie, topographie de surface et propriétés mécaniques sont présentés.

La Section 2.1 présente d'abord les généralités sur les formes cristallines et amorphes du carbone. Puis, la morphologie et les particularités des trois principaux types de fibres de carbone, c'est-à-dire des fibres anisotropes de haute résistance à la rupture, des fibres anisotropes de haut module élastique et des fibres isotropes avec des caractéristiques mécaniques moyennes (cf Tab. 2.1), sont présentées. Bien que la communauté scientifique soit d'accord sur le fait que les fibres de carbone contiennent principalement du carbone turbostratique (Fig. 2.2), plusieurs modèles plus ou moins récents de la structure des fibres de carbone des trois types coexistent encore et sont présentés en bref dans la Section 2.1.2.2. Par rapport aux autres fibres dans l'industrie des composites, ces fibres ont plusieurs avantages, notamment de bonnes propriétés mécaniques, une bonne résistance thermique et chimique, un faible coefficient de dilatation thermique, etc.

Les noirs de carbone, en quelque sorte les "ancêtres" des nanoperles de carbone, et ces nanoperles sont ensuite présentés. Les particules de deux matériaux ont un noyau rigide amorphe enrobé par des couches de carbone de structure turbostratique. Ces particules de 10 - 100 nm de diamètre forment des chaînes appelées agrégats de 50 - 500 nm, qui à leur tour forment des agglomérats de taille micrométrique (Fig. 2.7). Le principal avantage des nanoperles de carbone par rapport au noir de carbone est leur monodispersité, le polydispérsité est estimé à 85%. Les nanoperles utilisées dans notre étude ont un diamètre moyen de 90 nm.

Les propriétés physiques et mécaniques de la résine époxy utilisée comme matrice dans nos composites sont recueillies dans le Tab. 2.4. C'est un polymère thermodurcissable, qui a une bonne adhésion et une bonne résistance à l'humidité, mais une température de transition vitreuse relativement faible et donc une chute des propriétés mécaniques vers 100 - 120 °C.

Les composites renforcés par des fibres de carbone, distingués par la fraction volumique de fibres, i.e. 34, 52 et 62 %, sont fabriqués par deux procédures différentes. Le composite de 62 % des fibres, dit classique, est fabriqué par moulage à sec à partir des couches de préimprégné alignées avec la direction des fibres parallèle, dont les propriétés physiques et mécaniques sont présentées en Tab. 2.5 et 2.6. En revanche, les composites de 34 et 52 % de fibres sont fabriqués à partir des tissus de fibres de carbones imprégnés par la résine époxy. La direction parallèle alignée des fibres dans ces couches est également contrôlée. La structure finale de ces composites est fortement hétérogène et aléatoire en volume et en surface, à cause de la non-planéité des couches de fibres. Les échantillons fabriqués de ces matériaux sont présentés sur les Fig. 2.10 et 2.11. Bien que les surfaces de ces échantillons aient été polies toutes de la même manière, l'état de surface résultant est différent. La topographie de surface de ces composites est mesurée au moyen d'un profilomètre tactile. La carte de la surface rugueuse du composite de 62 % de fibres (Fig. 2.12) et les profils de surface des composites de 34 et 52 % et de l'époxy pure (Fig. 2.13) indiquent que des fibres de carbone dépassent de la surface et augmentent visiblement la rugosité moyenne de

surface par rapport à celle de l'époxy pure. Les propriétés mécaniques locales de surface du composite et de l'époxy pure ont été mesurées par la technique de nanoidentation. Plusieurs indentations ont été réalisées sur les fibres de carbone et la matrice époxy du composite, ainsi que sur l'époxy pure (Fig. 2.14). Les valeurs de la dureté de surface et du module d'élasticité calculées à partir de ces mesures sont plus faibles d'un ordre de grandeur pour l'époxy par rapport à la fibre de carbone et similaires pour l'époxy pure et celle du composite (Tab. 2.9).

Les composites renforcés par 1, 15, 28 et 35 % de nanoperles de carbone sont fabriqués par le moulage dans des moules réalisés au laboratoire en PDMS (Fig. 2.16). La procédure de leur fabrication est décrite en Sec. 2.3.2, tandis qu'un exemple d'échantillon est présenté en Fig. 2.17. Une porosité importante pour les composites de concentration de plus d'un % de nanoperles est observée (Fig. 2.18 - 2.21) et estimée par une technique de traitement d'image (Tab. 2.11). La rugosité de ces surfaces poreuses ne peut pas être mesurée. En revanche, les surfaces du composite d'un % de nanoperles sont relativement lisses et leur rugosité est similaire à celle de l'époxy pure.

Un récapitulatif des propriétés et des particularités des deux types de composites utilisés dans notre étude expérimentale est présentée dans le Tab. 2.13.

Chapitre 3. Dissipation interfaciale induite par frottement : une étude expérimentale

Ce chapitre est consacré à l'étude expérimentale tribologique de la dissipation par frottement dans la zone interfaciale des deux types de composites et l'époxy pure présentés dans le chapitre précédent. Une condition cruciale pour cette étude est l'absence d'endommagement de surface, qui peut être atteinte par l'application de très faibles pressions de contact, c'est-à-dire une faible charge normale appliquée sur une grande surface. Une étude expérimentale préliminaire est alors réalisée pour déterminer les meilleures conditions tribologiques pour le frottement interfacial. L'objectif de ce chapitre est d'analyser expérimentalement l'apport du renfort du carbone à la dissipation par frottement des composites. L'effet de l'orientation des fibres de carbone par rapport à la direction de glissement sur le frottement interfacial est également étudié. La deuxième partie de ce chapitre est consacrée à une étude expérimentale de frottement local entre des fibres de carbone et l'époxy pure, qui a pour but l'obtention des coefficients de frottement locaux qui vont nous servir par la suite.

Un dispositif expérimental utilisé dans cette étude est présenté en Sec. 3.1.1. Ce tribomètre appelé RA et conçu au laboratoire LTDS permet de réaliser un mouvement alternatif entre deux échantillons de surfaces relativement grandes, sous faible charge normale (Fig. 3.1). Un échantillon rectangulaire long appelé piste est collé à la surface de base du tribomètre, tandis que l'autre échantillon rond appelé glisseur est poussé et tiré par un bras du tribomètre et glisse sur la piste. La force normale est appliquée par une masse posée sur le glisseur et peut atteindre 20 N. La force tangentielle est mesurée par un capteur piézoélectrique installé dans le bras. La vitesse de glissement est contrôlée par un moteur linéaire de quelques μm/s à 2 m/s.

Les échantillons de tous les matériaux présentés dans le Chapitre 2, de $80 \pm 2 \times 25 \pm 2 \times$

5 ± 1 mm^3 et de ⌀20 mm $\times$ 5 ± 1 mm pour la piste et le glisseur respectivement, ont été fabriqués. Avant chaque expérience, les surfaces des deux échantillons sont soigneusement nettoyées avec l'heptane, l'acétone, le propanol-2 et un flux d'azote. L'expérience est réalisée à température et humidité ambiante.

L'expérience représente une séquence de 25 cycles de glissements (50 passages), au cours desquels la force tangentielle est mesurée à la fréquence d'échantillonnage de 1 kHz et enregistrée dans un PC. Le coefficient de frottement cinétique est calculé à partir de ce signal coupé à 20 % aux extrémités et moyenné entre deux passages (aller-retour) et la force normale constante.

Les signaux de frottement mesurés par le capteur présentés dans la Fig. 3.2 sont plus ou moins stables pendant chaque passage, avec une meilleure performance pour un couple de frottement CFRE 62%/CFRE 62 % que pour tous les autres matériaux. Des instabilités de frottement sont observées pour les composites renforcés par des nanoperles de carbone, dont l'origine peut être attribuée à la grande rigidité de contact de ces particules bien dispersées dans la matrice polymère. De plus, une grande dispersion des coefficients de frottement moyens entre les passages d'un test et entre plusieurs tests est observée pour l'époxy pure et tous les composites testés à part de CFRE 62% (Fig. 3.3). Cette dispersion, probablement liée au faible endommagement de surface, est plus importante sous conditions tribologiques plus sévères.

Les résultats de l'étude de l'effet des conditions tribologiques, c'est-à-dire de la force normale et de la vitesse de glissement, sur le frottement de nos matériaux sont présentés dans la Section 3.1.4. D'un côté, une charge importante et une vitesse de glissement faible favorisent la formation des jonctions entre deux surfaces et leur endommagement. D'un autre côte, une faible charge normale et une vitesse de glissement importante aboutissent à une faible aire de contact, donc une pression de contact sous-estimée, et un échauffement de surface. Un compromis pour ces conditions est trouvé dans cette étude expérimentale pour chaque couple de matériaux étudiés, cf Figs. 3.5 - 3.7 et l'Annexe 1 qui réunit les tableaux de coefficients de frottement mesurés. Les valeurs de la vitesse de glissement et de la charge normale choisies sont présentées dans le Tab. 3.2. Les faibles forces normales sont recommandées pour les couples de frottement concernant l'époxy pure (0.5 N) et les composites renforcés par des nanoperles de carbone (1 N) au regard de l'endommagement de surface observé. Une force normale de 2 N est choisie pour les couples CFRE/CFRE. Ces charges normales correspondent aux pressions de contact de 1.59, 6.37 et 3.18 kPa respectivement. La vitesse de glissement est maintenue à 10 mm/s pour tous les couples de glissement.

Ces conditions expérimentales ont été ensuite appliquées pour une étude de l'effet de la fraction volumique du renfort de composite sur la dissipation interfaciale induite par frottement, présentée dans Section 3.1.5. Les résultats de cette étude pour des couples de frottement Epoxy/CFRE, CFRE/CFRE et CNPRE/CNPRE sont présentés dans la Fig. 3.8. On observe une légère augmentation de coefficient de frottement avec l'augmentation de la fraction de fibres dans le couple Epoxy/CFRE. Cette tendance est par ailleurs opposée à celle trouvée dans la littérature pour un couple CFRE/acier certainement à cause de l'endommagement de surface du composite par l'acier. En revanche, l'ajout de fibres dans l'époxy pure, c'est-à-dire le frottement du couple CFRE/CFRE, diminue au moins

par un facteur de 2 le coefficient de frottement par rapport à celui du couple Epoxy/Epoxy. Une variation de la fraction volumique des fibres entre 34 et 62 % ne semble pas avoir une influence importante sur le frottement du composite. Contrairement aux fibres de carbone, le renfort de la résine époxy par des nanoperles de carbone augmente considérablement le frottement. Dans ce cas, le frottement est plus important pour les fractions volumiques de nanoperles plus importantes. Sa valeur pour CNPRE 35% est plus élevée d'un facteur 1.5 par rapport à celle de CNPRE 1% ou de l'époxy pure.

L'effet de l'orientation des fibres sur le frottement d'un couple de composites 'classiques' CFRE 62% est étudié et présenté dans la Section 3.1.5.3. Les pistes d'une orientation de fibres de 0°, 45° et 90° par rapport au vecteur vitesse de glissement associées à une rotation du glisseur sont utilisées pour varier l'angle total entre l'orientation des fibres dans deux échantillons de 0° au 180° (cf. schéma de la Fig. 3.9). Dans ces conditions, le coefficient de frottement moyen varie entre 0.17 et 0.18 (Fig. 3.10). La rugosité de surface du composite dans la direction perpendiculaire aux fibres est plus importante que celle parallèle aux fibres, ce qui doit impliquer un frottement plus fort. Cependant, sous conditions interfaciales, cet effet n'est pas prononcé.

Une étude expérimentale pour obtenir les coefficients de frottement locaux entre les fibres de carbone individuelles et l'époxy est également réalisée dans le cadre de notre étude et présentée dans la Section 3.2. Pour cette étude, une machine de nano-rayure de CSM Instruments avec un indenteur sphérique de rayon de 25 mm a été utilisée (Fig. 3.11). Cet appareil peut mesurer la force normale, équivalente à la pression de 0.05 - 2 MPa, et tangentielle avec une grande précision et réaliser des glissements de quelques nano- ou micromètres. Une vitesse de glissement de 30 μm/s et une force normale de 1 - 50 mN, augmentée par pas de 2 mN entre 1 et 20 mN, et par pas de 5mN entre 20 et 50 mN, sont appliquées dans cette étude expérimentale à humidité et température ambiante.

L'indenteur sphérique est couvert par des fibres de carbone unidirectionnelles attachées à ses bords comme montre la Fig. 3.12 (a). Ce glisseur frotte soit contre l'échantillon cylindrique d'époxy, utilisé dans l'étude précédente comme glisseur, soit contre une mèche de fibres de carbone (Fig. 3.12 (b)). Dans le deuxième cas, les orientations parallèle et perpendiculaire entre les fibres du glisseur et les fibres stationnaires sont testées.

La force de frottement est plutôt stable pendant chaque glissement sur la distance de 600 μm, ce qui nous permet d'opérer avec un coefficient de frottement moyen présenté dans la Fig. 3.13 en fonction de la force normale. On observe que les variations du coefficient de frottement avec la force normale sont faibles, excepté le couple fibre/fibre en orientation parallèle. On peut expliquer cela par des défauts d'alignement entre les fibres des deux échantillons. Ces résultats expérimentaux ont été comparés avec des résultats de frottement des fibres de carbone individuelles de Roselman et Tabor (Sec. 3.2.3.). Les coefficients, pour les même couples de frottement, entre des fibres de carbone et l'époxy diffèrent entre nos résultats expérimentaux et ceux de Roselman et Tabor, probablement à cause des conditions appliquées différentes (cf Tab. 3.4).

Les résultats expérimentaux obtenus au cours de ce chapitre soulèvent plusieurs questions, auxquelles nous allons tenter de répondre dans le chapitre suivant. Notamment, pourquoi l'ajout de fibres de carbone dans un matériau de couple de frottement augmente le frottement, tandis que dans le cas de deux matériaux renforcés, le coefficient de frottement

chute ? Pourquoi les fibres et les nanoperles de carbone influent-elles sur le frottement de l'époxy d'une manière opposée ? Quels sont des mécanismes du frottement impliqués pour les couples de frottement étudiés ?

Chapitre 4. Dissipation interfaciale induite par frottement : un modèle analytique

Dans ce chapitre nous allons proposer un modèle analytique de frottement interfacial des matériaux composites pour répondre aux questions posées à la fin du chapitre précédent et prédire le frottement en fonction de la fraction volumique de renfort. Il commence par une brève présentation de deux modèles de ce type trouvés dans la littérature. Malgré leur proximité avec notre sujet, tous les deux ont été conçus pour un contact composite/matériau homogène d'une dureté plus élevée.

Le première modèle, décrit en Sec. 4.1.1, est basé sur des hypothèses de proportionnalité entre l'aire de contact des fibres et de la matrice, et l'aire de contact totale, avec des coefficient de proportionnalité de la fraction volumique des fibres V_f et de la matrice V_m respectivement ; de l'égalité de contrainte de cisaillement des fibres et de la matrice; et de l'égalité des modules de rigidité des fibres et de la matrice sous la surface de contact. Ce modèle résulte en une loi de proportionnalité inverse entre le coefficient de frottement de composite et ceux de ses composants, avec des coefficients de proportionnalité des fractions volumiques de fibres et de la matrice (Eq. 4.2).

Le deuxième modèle, décrit en Sec 4.1.2, couvre le frottement d'un composite contre un matériau opposé abrasif. Les hypothèses de ce modèle sont : les propriétés tribologiques des phases d'un composite comme celles des matériaux individuels demeurent sans changement dans le composite ; et les fractions d'aire de contact des phases d'un composite restent constantes pendant le glissement. Dans le cas d'absence d'usure, la force normale est distribuée entre les phases du composite proportionnellement aux fractions surfaciques de ces phases, et donc pour un composite composé d'un renfort et d'une matrice, le coefficient de frottement est proportionnel aux coefficients de frottement de ses phases (Eq. 4.10).

Les idées et les hypothèses de ces deux modèles nous ont inspirés pour développer un nouveau modèle généralisé pour le frottement interfacial entre deux composites présenté dans la Sec. 4.2. Il est basé sur le modèle adhésif de Bowden et Tabor (Sec. 1.1.4) appliqué aux matériaux composites et illustré dans la Fig. 4.2. L'aire de contact est renouvelée continuellement pendant le glissement, mais sa composition, i.e. la proportion entre les composants du composite dans le contact reste constante. Les hypothèses suivantes sont alors imposées :

- absence d'endommagement de surface et d'usure;
- frottement de Coulomb pour tous les sites microscopiques de contact;
- forces de frottement des sites microscopiques de contact découplées;
- frottement isotrope pour tous les couples de matériaux en contact.

Selon Bowden et Tabor, le contact de deux solides est composé d'une multitude de microcontacts qui forment l'aire réelle de contact. Les forces normales et tangentielles sont distribuées entre ces microcontacts. Puisque l'aire de chaque microcontact est très faible, la pression de contact excède la limite d'élasticité et le contact peut être vu comme une pénétration d'une aspérité dans l'autre. La force normale peut être donnée par l'Eq. 4.13. Les jonctions formées entre deux corps en contact sous une charge normale sont constamment cisaillées pendant le glissement, et la force tangentielle peut être exprimée par l'Eq. 4.14. Alors nous pouvons calculer le coefficient de frottement de Coulomb, qui dépend des aires de microcontacts, des contraintes de cisaillement qui agissent sur ces microcontacts et des duretés de matériaux qui forment ces microcontacts (Eq. 4.15).

Puisque l'application directe de cette loi de frottement semble compliquée à cause de l'ignorance des aires de contact réelles et des contraintes de cisaillement, nous allons proposer deux cas particuliers limites. Dans le cadre du Cas 1, nous supposons que la dureté est égale à une certaine valeur effective pour toutes des phases du composite. Dans ce cas, le coefficient de frottement peut être trouvé par une loi de proportionnalité directe (Eq. 4.16). De l'autre côté, si nous supposons que les contraintes de cisaillement sont égales à une valeur effective pour tous les microcontacts comme dans le Cas 2, nous observons une proportionnalité inverse pour les coefficients de frottement (Eq. 4.17).

Notre modèle découle sur un coefficient de frottement entre deux composites qui dépend des coefficients de frottement locaux entre leur phases et de leurs fractions surfaciques, et peut être a priori appliqué à tous les types de matériaux composites.

Dans le suite de ce chapitre, les résultats de notre modèle sont comparés aux résultats obtenus expérimentalement dans le chapitre précédent. La Section 4.3 discute le choix des coefficients de frottement locaux basés sur l'étude présentée dans la Sec. 3.2 et la littérature. Ensuite, une étude sur la détermination des fractions surfaciques des phases du composite est réalisée et présentée dans la Sec. 4.4. Il résulte de l'approche probabiliste utilisée que pour un matériau composite renforcé par des fibres cylindriques ou des nanoperles, la fraction surfacique est égale à la fraction volumique.

L'application de notre modèle au contact entre l'époxy pure et un composite à base d'époxy renforcé par des fibres de carbone est présentée dans la Sec. 4.5. Les deux cas particuliers (Eq. 4.16 et 4.17) sont appliqués et les courbes résultantes pour le coefficient de frottement vs. la fraction surfacique de fibres, ainsi que les points expérimentaux obtenus au cours du chapitre précédent, sont tracés sur la Fig. 4.5 . On observe que les deux lois, de proportionnalité directe et inverse, suivent bien la tendance expérimentale. De plus, ce contact nous permet de valider un coefficient de frottement local entre ceux trouvés dans la Sec. 4.3. De plus, le fait que deux lois proposées suivent bien la tendance expérimentale est expliqué et discuté en termes de validation des hypothèses des duretés et des contraintes de cisaillement effectives pour ce type de contact.

Dans le cas de contact entre deux matériaux composites de deux phases chacun, nos lois de proportionnalité directe et inverse s'inscrivent dans la forme de l'Eq. 4.27 et l'Eq. 4.28. Les coefficients de contribution dans ces équations doivent être identifiés à partir de la géométrie de contact pour chaque composite individuellement. Le contact CFRE/CFRE est étudié dans la Sec. 4.6.1. La composition de la zone de contact apparent, schématisée dans la Fig. 4.6, permet de calculer les coefficients de contribution de l'Eq. 4.30. Les

courbes résultantes pour ce type de contact sont tracées dans la Fig. 4.7. On observe que la courbe verte de loi inverse passe par un point expérimental du composite 'classique' de 62 % de fibres. Les autres concentrations de fibres sont loin de cette courbe théorique certainement à cause de la composition hétérogène et irrégulière de la surface des composites de 34 et 52 % de fibres. L'application des lois directe et inverse est également discutée dans ce cas du contact entre deux composites. Le choix de la proportionnalité inverse est justifié par la différence importante des duretés des composants de deux composites, tandis que les contraintes de cisaillement estimées sont du même ordre de grandeur. De plus, l'orientation de fibres considérée dans la géométrie de contact n'affecte pas le coefficient de frottement interfacial, ce qui est en accord avec les résultats expérimentaux présentés dans le chapitre précédent.

Le cas du contact de deux composites renforcés par des nanoperles de carbone est considéré dans la Sec. 4.6.2. Comme la taille de nanoperles n'est pas inférieure à la taille des aspérités, le même principe de séparation des microcontacts par types de matériaux peut être appliqué. Les coefficients de contribution pour ce type de contact sont présentés dans l'Eq. 4.33 et égaux à ceux du contact CFRE/CFRE. L'application de nos deux lois particulières est compliqué à cause de l'ignorance des coefficients de frottement locaux entre les nanoperles. Plusieurs couples de ces coefficients locaux sont proposés par un fit mathématique des points expérimentaux réalisé avec Matlab pour deux lois particulières (Tab. 4.2). Toutes les possibilités sont discutées et un couple des coefficients nanoperle/nanoperle et nanoperle/époxy est choisi. Les courbes du coefficient de frottement vs. la fraction surfacique des nanoperles tracées pour ce couple de coefficients et les points expérimentaux sont présentées dans la Fig. 4.9. Comme dans le cas du frottement de CFRE/CFRE, la loi directe ne doit pas être appliquée à cause de la différence entre les duretés de l'époxy et des nanoperles.

Ce modèle analytique peut être amélioré par la considération de la distribution de l'aire de contact entre les phases du composite, ce qui est discuté dans la Sec. 4.7. Cette distribution dépend certainement de la rugosité des deux surfaces et de la distribution de pression de contact entre les phases, c'est-à-dire des propriétés mécaniques des matériaux en contact.

Chapitre 5. Dissipation volumique induite par frottement

Une étude expérimentale de la dissipation volumique induite par frottement et l'usure associée sur le composite CFRE 62 % et l'époxy pure est présentée dans ce chapitre. Des conditions tribologiques plus sévères sont appliquées dans cette étude. Sous ces conditions, l'énergie générée par le frottement peut être dissipée par plusieurs mécanismes, comme l'échauffement, l'endommagement ou les déformations plastiques, qui vont être étudiés au cours de ce chapitre. Une approche par deux échelles est développée et appliquée dans cette étude : dans un premier temps, les caractéristiques macroscopiques, i.e. une perte de masse, les coefficients de frottement, l'énergie dissipée et l'échauffement de contact sont estimés, et ensuite les surfaces usées sont observées au niveau microscopique et les indices des différents mécanismes d'usure sont cherchés et corrélés avec les paramètres macroscopiques.

Cette étude expérimentale a été réalisée sur un tribomètre linéaire développé au LTDS présenté dans la Fig. 5.1. Il nous a permis d'obtenir le coefficient de frottement entre deux échantillons pendant un mouvement alternatif avec une vitesse de glissement sinusoïdale. La force normale est appliquée par le mouvement vertical du plan de base qui porte l'échantillon fixe, effectué par un moteur. Cette force ainsi que la force tangentielle et le mouvement du glisseur sont mesurés instantanément pendant le glissement. Un exemple de ces grandeurs mesurées présenté à dans la Fig. 5.2 montre la stabilité des forces pendant les passages, ce qui nous permet d'opérer avec des coefficients de frottement de Coulomb. Quatre conditions expérimentales distinguées par la force normale et la vitesse de glissement utilisées dans notre étude sont présentées dans la Tab. 5.2. La durée d'essai a varié de 10 à 1000 ou 5000 cycles en fonction du matériau pour étudier l'évolution des régimes d'usure avec le temps de glissement.

Les pistes et les glisseurs en époxy pure et composite CFRE sont des plaques rectangulaires de $30 \pm 2 \times 15 \pm 2 \times 4 \pm 1$ mm^3 et $8 \pm 1 \times 6 \pm 1 \times 4 \pm 1$ mm^3, respectivement. La différence de l'aire de la surface des glisseurs est mesurée et considérée dans tous les calculs présentés dans ce chapitre. La longueur cinématique est calculée pour la piste et le glisseur dans la Sec.5.1.3 et illustrée dans la Fig. 5.3.

La présentation des résultats de ce chapitre est dictée par les couples de matériaux, c'est-à-dire que l'on présente d'abord le couple époxy/époxy et viennent ensuite les couples époxy/CFRE et CFRE/CFRE.

La caractérisation de la dissipation volumique dans le contact polymère/polymère par l'approche macroscopique est présentée dans la Sec. 5.2.1. Tout d'abord, une loi d'usure (Eq. 5.2) est proposée sur la base de mesures expérimentales de la masse mesurée avant et après chaque essai pour le glisseur et la piste. La perte de masse augmente de façon linéaire avec la longueur cinématique pour la piste et le glisseur (Fig. 5.4) et leur totalité (Fig. 5.5). Malgré une ressemblance de cette loi linéaire à la loi d'usure d'Archard présentée dans la Chapitre 1, les coefficients d'usure calculés à partir de nos mesures et présentés dans le Tab. 5.3 montrent une forte dépendance aux conditions appliquées. Cette dépendance est en désaccord avec la loi d'Archard, qui postule que le coefficient d'usure est une propriété du matériau et est indépendant des conditions. Cela pourrait signifier que le contact époxy/époxy n'est pas entièrement plastifié sous ces conditions.

Les coefficients de frottement instantanés sont calculés à partir des forces normale et tangentielle mesurées et présentées en forme de carte de frottement (Fig. 5.6). Sur ces cartes, l'axe x correspond au nombre de cycles, l'axe y correspond à la position du glisseur pendant un passage, et les coefficients de frottement sont représentés par la couleur. La zone bleue de frottement bas observée sur ces cartes à la fin de la trace peut être expliquée par les défauts de planéité entre deux surfaces et l'évacuation du 3ème corps. Les oscillations sur les cartes des Fig. 5.6 (c) et (d) sont dues à la souplesse du tribomètre et ne sont pas considérées comme le facteur influant le frottement moyen. Pour le couple époxy/époxy, le coefficient de frottement moyen est à peu près indépendant des conditions appliquées et sa valeur est assez élevée.

L'énergie dissipée a été calculée à partir de la force de frottement et de la vitesse de glissement instantanées selon l'Eq. 5.4 et tracée en fonction de la longueur cinématique dans la Fig. 5.7. L'évolution linéaire affectée par la force normale est observée et expliquée

en transformant l'expression pour l'énergie dissipée comme dans l'Eq. 5.5.

Les dépendances linéaires de l'énergie et de la perte de masse à la longueur cinématique nous permettent de déterminer le coefficient de proportionnalité pour notre loi d'usure (Eq. 5.7), qui dépend de la force de frottement et d'une certaine vitesse critique en accord avec les tendances expérimentales.

La Section 5.1.2.4 présente une estimation de la température de contact selon le modèle de Archard-Blok-Jaeger. Tout d'abord, la quantité de chaleur générée est calculée à partir de la force de frottement, la vitesse de glissement et l'aire de contact (Eq. 5.8 et 5.9). La température de contact réelle est composée de la température de volume et la température flash de durée courte (Eq. 5.10). La chaleur générée est partagée entre deux corps en contact avec le coefficient de partage qui peut être déterminé avec l'Eq. 5.14. Une grandeur nommée Le Nombre de Peclet, qui permet d'estimer le profil de la distribution de chaleur dans deux corps, est calculée pour le corps fixe. Pour deux vitesses appliquées, on obtient que la plus grande partie de la chaleur est propagée dans la piste avec un profil de distribution peu profond. Pour estimer les températures réelles du contact, deux cas limites de l'aire de contact sont proposés, à savoir l'aire de contact apparente et l'aire de contact entièrement plastifié et calculé comme la ratio de la charge normale et de la dureté du matériau. Les valeurs des températures de contact résultantes présentées dans le Tab. 5.5 et à la Fig. 5.10 ne sont pas vraisemblables, mais les tendances pour les 4 conditions étudiées sont les mêmes. La température vraie de contact doit se trouver entre ces deux cas limites. On observe que les vitesses plus élevées provoquent plus d'échauffement. Très élevée sur la surface, la température chute rapidement en profondeur comme cela est montré dans la Fig. 5.11.

L'approche microscopique de l'étude de la dissipation volumique dans le couple époxy/époxy a relevé deux types de surfaces usées illustrées dans les Fig. 5.12 et 5.13. Nous avons remarqué que la surface de type 1 apparait sous la vitesse basse, tandis que la surface de type 2 est caractéristique du glissement à vitesse élevée. L'évolution du type de surface usée, des rayures simples vers une surface usée de type 1 ou 2 est schématisée dans la Fig. 5.14.

Les photos macroscopiques de tous les échantillons usés ont été traitées avec un logiciel de traitement d'image pour estimer l'aire de la surface usée, comme dans la Fig. 5.15. Puisque certains processus de la dissipation ne provoquent pas de perte de masse, mais déforment la surface, on peut mieux étudier la dissipation et tracer l'énergie dissipée en fonction de cette aire usée plutôt que de la masse perdue (Fig. 5.17). Ce graphe nous permet de séparer deux régions de la dissipation : on associe la première avec l'abrasion pure, et la deuxième à tous les autres mécanismes d'usure.

Les observations microscopiques de surfaces usées ont relevé plusieurs mécanismes d'usure, comme l'usure abrasive à deux et trois corps, l'usure adhésive, le ramollissement du polymère et le transfert du matériau entre deux échantillons en contact, présentés et discutés dans la Sec. 5.2.2.3. Les mécanismes d'usure différents sont observés en fonction de la surface usée de type 1 ou 2 (distinguées au niveau macroscopique). Pour rationaliser l'évolution des mécanismes d'usure, une rétrospective est proposée dans la Sec. 5.2.3 et schématisée dans la Fig. 5.21. L'usure commence toujours par l'usure abrasive à deux corps et ensuite se propage par un des deux scénarios possibles : 'Abrasion à trois corps'

ou 'Adhésion et effets thermiques'.

La dissipation volumique dans les couples époxy/composite et composite/composite est étudiée exactement de la même façon que celle de l'époxy/époxy et présentée dans la Sec. 5.3. La perte de masse de l'époxy augmente également linéairement avec la longueur cinématique (Fig. 5.22), tandis que la masse du composite reste sans changement sous la plupart des conditions étudiées. Seules les conditions les plus sévères après 5000 cycles de glissement provoquent la perte de masse du composite mesurable avec un taux d'usure 100 fois moins important que celui de l'époxy pure sous des conditions identiques. Les cartes de frottement présentées dans les Fig. 5.23 et 5.25 pour ces couples de frottement montrent une dépendance de coefficient de frottement aux conditions appliquées, contrairement à celui d'époxy/époxy. L'énergie dissipée tracée en fonction de la longueur cinématique du glisseur dans les Fig. 5.24 et 5.26 confirme cette dépendance. L'analyse thermique pour ces deux couples présentée dans la Sec. 5.3.3 montre un profil de propagation de la chaleur dans la profondeur des échantillons plus plat que celui d'époxy/époxy. Les températures de contact tracées dans les Fig. 5.27 et 5.28 montrent la tendance identique à celle du contact époxy/époxy, mais leur valeurs sont moins élevées pour les contacts du composite.

L'approche microscopique appliquée à ces deux contacts permet de distinguer plusieurs mécanismes d'usure. Notamment, l'époxy est usée surtout par l'abrasion à cause de la dureté plus élevée de la surface opposée (Fig. 5.29 - 5.31). Dans ce cas, les microparticules de fibres de carbone usées sont trouvées sur la surface d'époxy pure. L'usure du composite dans ce couple de frottement est négligeable, même si certains creux peuvent être observés dans la matrice (Fig. 5.31 (a)). L'usure du composite contre le composite sous les conditions les plus sévères est illustré dans la Fig. 5.32. Tout d'abord, la matrice époxy est détachée de la surface du composite entre les fibres, ensuite ces fibres sont polies par la surface opposée, et enfin le troisième corps mélangé de particules d'époxy et de fibres abrase les deux surfaces en contact.

Conclusions

Les conclusions générales de cette étude de la dissipation volumique et interfaciale induite par frottement dans les composites renforcés par du carbone et les perspectives pour les travaux à venir sont présentées à la fin du manuscrit. L'évolution des coefficients de frottement et d'usure est généralisée pour deux régions de dissipation et tracée en fonction des conditions tribologiques appliquées pour les trois couples de matériaux étudiés dans la Fig. C.1. Les mécanismes de dissipation et d'usure sont discutés pour chaque couple. Comme notre étude a démontré, à cause de leurs excellentes propriétés mécaniques et thermiques, l'ajout de fibres de carbone augmente la résistance à l'usure, par une meilleure évacuation de la chaleur et donc une diminution de l'échauffement de contact et de la modification des régimes d'usure de l'époxy. Dans le même temps, il diminue le coefficient de frottement du composite par rapport à l'époxy pure au niveau interfacial et volumique.

Bibliography

[1] Truesdell, C.: Essays in the history of mechanics. Springer. Verlag New York Inc. (1968) (Cited on pages 4, 5 and 177.)

[2] Amontons, G.: De la résistance causée dans les machines. Mémoire de l'Académie Royale de Sciences. Paris, 206-227 (1699) (Cited on page 4.)

[3] Coulomb, C.A.: Théorie des Machines Simples, en ayant égard au frottement de leurs parties et à la roideur des cordages. Paris, Bachelier, Libraire, Quai des Augustins (1821) (Cited on pages 4, 6 and 177.)

[4] Rabinowicz, E. Friction and wear of materials. Second Edition. John Wiley & sons, Inc. Canada (1995) (Cited on page 6.)

[5] Bowden, F.P., Leben, L. The nature of sliding and the analysis of friction. Proc. of the Royal Soc. Lond. A 169 (938), 371-391 (1939) (Cited on page 6.)

[6] Bowden, F.P., Tabor, D.: The area of contact between stationary and between moving surfaces. Proc. of the Royal Soc. Lond. A 169 (938), 391-413 (1939) (Cited on page 6.)

[7] Hertz, H.: Über die Berührung fester elastischer Körper. Journal für die reine und angewandte Mathematik 92, 156-171 (1881) (Cited on page 7.)

[8] Popov, V.L.: Contact mechanics and friction. Physical principles and applications. Springer-Verlag Berlin Heidelberg (2010) (Cited on pages 7 and 8.)

[9] Johnson, K.L.: Contact mechanics. Cambridge University Press (1985) (Cited on pages 7 and 8.)

[10] Persson, B. N. J.: Sliding friction. Physical principles and applications. Second Edition. Springer-Verlag Berlin Heidelberg (Germany) (2000) (Cited on page 7.)

[11] Inglebert, G., Da Silva Botelho, T., Lemaire Caron, I.: Théorie du contact de Hertz - Contacts ponctuels ou linéiques. Techniques de l'ingénieur l'expertise technique et scientifique de référence. TRI 200. (Cited on pages 8 and 177.)

[12] Greenwood, J.A., Williamson, J.B.P.: Contact of nominally flat surfaces. Proc. of the Royal Soc. Lond. A 295, 300-319 (1966) (Cited on page 10.)

[13] Archard, J.F.: Elastic deformation and the laws of friction. Proc. of the Royal Soc. Lond. A 243, 190-205 (1957) (Cited on pages 9, 10 and 177.)

[14] Archard, J.F.: Contact and rubbing of flat surfaces. J. of App. Physics 24 (8), 981-988 (1953) (Cited on pages 9 and 16.)

[15] Greenwood, J. A.: On the area of contact between rough surfaces and flats. ASME J. of Basic Engineering, Pap. 65-LUB-10 (1965) (Cited on page 12.)

[16] Suh, N.P., Sin, H.-C.: The genesis of friction. Wear 69, 91-111 (1981) (Cited on page 14.)

[17] Briscoe, B.J., Tabor, D.: Friction and wear of polymers: the role of mechanical properties. The Br. Polym. J. **10**, 74-78 (1978) (Cited on page 14.)

[18] Briscoe, B.J.: Friction of organic polymers. in I.L. Singer and H.M. Pollock, Fundamentals of friction: Macroscopic and Microscopic Processes, 167-182. Kluwer Academic Publishers. Netherlands (1992) (Cited on page 14.)

[19] Spurr, R.T.: The friction of polymers. Wear 79, 301-310 (1982) (Not cited.)

[20] Tabor, D.: Friction as dissipative process. In I.L. Singer and H.M. Pollock: Fundamentals of friction: Macroscopic and microscopic processes. Kluwer Academic Publishers. Netherlands, 3-24 (1992) (Cited on page 15.)

[21] Blau, P.J.: Fifty years of research on the wear of metals. Tribology International 30 (5), 321-331 (1997) (Cited on page 15.)

[22] Meng, H.C., Ludema, K.C.: Wear models and predictive equations: their form and content. Wear 181-183, 443-457 (1995) (Cited on pages 15 and 16.)

[23] Stachowiak, G., Batchelor, A.: Engineering tribology. Third Edition. Elsevier Butterworth-Heinemann, Boston (2005) (Cited on pages 15, 16, 18, 19 and 177.)

[24] Hsu, S.M., Shen, M.C.: Wear mapping of materials. In Stachowiak G.: Wear – Materials, Mechanisms and Practice. John Wiley & Sons, Ltd, 369-423 (2005) (Cited on page 15.)

[25] Archard, J.F., Hirst, W.: The wear of metals under unlubricated conditions. Proc. of the Royal Soc. Lond. A 236 (1206), 397-410 (1956) (Cited on pages 16, 96 and 97.)

[26] Suh, N.P.: The delimitation theory of wear. Wear 25, 111-123 (1973) (Cited on page 18.)

[27] Ludema, K.C.: Friction, wear, lubrication. A textbook in tribology. CRC Press, Inc. USA (1996) (Cited on page 19.)

[28] Lee, H.G., Hwang, H.Y., Lee, D.G.: Effect of wear debris on the tribological characteristics of carbon fiber epoxy composites. Wear 261, 453-459 (2006) (Cited on pages 19, 20, 23, 64, 177 and 183.)

[29] Lee, H.G., Kim, S.S., Lee, D.G.: Effect of compacted wear debris on the tribological behavior of carbon/epoxy composites. Composite Structures 74, 136-144 (2006) (Cited on page 19.)

[30] Zhou, X.H., Sun, Y.S., Wang, W.S.: Influences of carbon fabric/epoxy composites fabrication process on its friction and wear properties. Journal of Materials Processing Technology 209, 4553-4557 (2009) (Not cited.)

[31] Bryant, P.J., Gutshall, P.L., Taylor, L.H. A study of mechanisms of graphite friction and wear. Wear 7, 118-126 (1964) (Cited on page 21.)

[32] Glaeser, W.A.: Materials for tribology. Tribology series 20. Elsevier science publishers. USA (1992) (Cited on page 21.)

[33] Blau, P.J., Martin, R. L.: Friction and wear of carbon- graphite materials against metal and ceramic counterfaces. Tribology International 27 (6), 413-422 (1994) (Cited on page 21.)

[34] Lancaster, J.K.: Instabilities in the frictional behavior of carbons and graphites. Wear 34, 275-290 (1975) (Cited on page 21.)

[35] Lancaster, J.K.: Transition in the friction and wear of carbons and graphites sliding against themselves. ASLE Transactions 18 (3), 187-201 (1975) (Cited on page 21.)

[36] Lancaster, J.K.: The friction and wear of nongraphitic carbon. ASLE Transaction 20 (1), 43-54 (1977) (Cited on page 21.)

[37] Tsukizoe, T., Ohmae, N.: Wear performance of unidirectionally oriented carbon-fiber reinforced plastics. Tribology International 8, 171-175 (1975) (Cited on pages 21, 23 and 24.)

[38] Giltrow, J.P., Lancaster, J.K.: The role of the counterface in the friction and wear of carbon fibre reinforced thermosetting resins. Wear 16, 359-374 (1970) (Cited on pages 21, 22, 23 and 24.)

[39] Shim, H.H., Kwon, O.K., Youn, J.R.: Friction and Wear Behavior of Graphite Fiber-Reinforced composites. Polymer Composites 11, 337-341(1990) (Cited on page 22.)

[40] Sung, N., Suh, N., Effect of fiber orientation on friction and wear of fiber-reinforced polymeric composites, Wear. 53 (1979) 129-141. (Cited on page 22.)

[41] B. Suresha, G. C., Effect of normal load and sliding velocity on friction and wear behavior of carbon fiber reinforced epoxy composites, Journal of Reinforced Plastics and Composites. 26 (2007) 1695-1703. (Cited on pages 22 and 24.)

[42] Tripathy, B.S., Furey, M.J.: Tribological behavior of unidirectional graphite-epoxy and carbon-PEEK composites. Wear 162-164, 385-396 (1993) (Cited on pages 22, 24 and 25.)

[43] Beaumont, M., Farris, T., N., Sun, C. T.: Scratch testing of advanced composite surfaces, Composites Part A. 28A (1997) 683-686. (Cited on page 22.)

[44] Chang, H.-W.: Wear characteristics of composites: effect of fibre orientation. Wear 85, 81-91 (1983) (Cited on page 22.)

[45] Friedrich, K., Reinicke, P.: Friction and wear of polymer-based composites. Mechanics of Composite Materials 34 (6), 503-514 (1998) (Cited on page 22.)

[46] Tsukizoe, T., Ohmae, N.: Friction and wear of advanced composite materials. Fibre Science and Technology 18, 265-286 (1983) (Cited on pages 23, 64, 74, 117 and 183.)

[47] Molchanov B.I., Chukalovsky V.V. et al. Carbon fiber-reinforced plastics. Moscow: Himiya, 1985. (in russian) (Cited on pages 23 and 24.)

[48] Giltrow, J.: The influence of temperature on the wear of carbon fiber reinforced resins. ASLE Transaction 16, 83-90 (1973) (Cited on pages 24 and 25.)

[49] Shim, H.H., Kwon, O.K., Youn, J.R.: Effects of fiber orientation and humidity on friction and wear properties of graphite fiber composites. Wear 157, 141-149 (1992) (Cited on pages 24 and 25.)

[50] Bernal, J. D.: The structure of graphite. Proc. of the Royal Soc. Lond. A 106, 749-773 (1924) (Cited on page 28.)

[51] Gay, D.: Matériaux composites. Paris-Londres-Lausanne: Hermes, (1987) (Cited on page 29.)

[52] Paredes, J.I., Martınez-Alonso, A., Tascon, J.M.D.: Nanometer structure of carbon fibers studied by different scanning probe microscopy techniques: a comparative investigation. Fuel Processing Technology 77-78, 293-300 (2002) (Cited on page 29.)

[53] Shim, H.-B., Seo M.-K., Park, S.-J.: Thermal conductivity and mechanical properties of various cross-section types carbon fiber-reinforced composites. Journal of Materials Science 37 (9), 1881-1885 (2002) (Cited on page 29.)

[54] http://materiaux.ecam.fr/savoirplus/mebanglais/es.html (Cited on pages 30, 32 and 177.)

[55] Liu, X., Wang, R., Wu, Z., Liu, W.: The effect of triangle-shape carbon fiber on the flexural properties of the carbon fiber reinforced plastics. Materials Letters 73, 21-23 (2012) (Cited on pages 30, 32 and 177.)

[56] Meleshko, A.I., Polovnikov, S.P.: Carbon, carbon fibers, carbon composites. Moscow: Science-press, (2007) (in russian) (Cited on pages 30, 33, 37 and 183.)

[57] Donnet, J.-B., Bansal, R.C.: Carbon fibers, Marcel Dekker, Inc.: USA. (1984) (Cited on pages 30, 31 and 183.)

[58] Ruland, W et al.: General structural features of carbon fibres. Int. Conference on carbon fibres, their composites and applications. London p.9 (1971) (Cited on page 31.)

[59] Donnet, J.-B., Bansal, R. Ch., Wang, M.-J. Carbon black. Science and Technology Second Edition, Revised and Expanded. Marcel Dekker, Inc.: USA (1993) (Cited on pages 31 and 33.)

[60] Knibbs, R. H.: The use of polarized light microscopy in examining the structure of carbon fibres. Journal of Microscopy 94 (3), 273-281 (1971) (Cited on page 31.)

[61] Barnett, F. R., Norr, M. K.: Carbon fibrer etching in an oxygen plasma. Carbon 11, 281-288 (1973) (Cited on page 31.)

[62] Diefendorf, R. J., Tokarsky, E.: High-performance carbon fibres. Polymer Engineering & Science 15 (3), 150-159 (1975) (Cited on pages 31, 32 and 177.)

[63] Maurin, R., Davies, P., Baral, N., Baley, C.: Transverse properties of carbon fibres by nano-indentation and micro-mechanics. Appl Compos Mater 15, 61-73 (2008) (Cited on pages 32, 43 and 177.)

[64] Nippon Graphite Fiber. Product data sheet (Cited on pages 32 and 177.)

[65] $HexTow^{®}AS4$ Carbon fiber. Product data sheet (Cited on pages 33 and 183.)

[66] Heidenreich, R. D., Hess, W. M., Ban, L. L.: A test object and criteria for high resolution electron microscopy. Journal of Applied Crystallography 1, 1-19 (1968) (Cited on pages 34 and 177.)

[67] Levesque, A. et al.: Monodisperse carbon nanopearls in a foam-like arrangement: a new carbon nano-compound for cold cathodes. Thin Solid Films 464-465, 308-314 (2004) (Cited on pages 34, 35 and 178.)

[68] Vu Thien, B., Levesque, A.: Method for producing graphitic carbon nanocomposites in particular nanopearls in bulk or in an individual manner. WO 2005/009900 A2 (2005) (Cited on page 34.)

[69] Bulanov I.M., Vorobey V.V. Technology of rocket and aerospace constructions of composite materials. Moscow: MGTU im. N.E.Baumana. 1998 (in russian) (Cited on pages 36, 37 and 183.)

[70] Mark, J. E. (ed.): Physical properties of polymers handbook. Second Edition. Springer Science+Buisness Media, LLC (2007) (Cited on pages 37 and 183.)

[71] $HexPly^{®}M10.1$ $120°C$ curing epoxy matrix. Product Data (Cited on page 37.)

[72] Zhandarov, S., Mader, E.: Characterization of fiber/matrix interface strength: applicability of different tests, approaches and parameters. Composites Science and Technology 65, 149–160 (2005) (Cited on page 37.)

[73] Piggott, M.G.: The effect of the interface/interphase on fiber composite properties. Polymer Composites 8 (5), 291-297 (1987) (Cited on page 37.)

[74] Piggott, M.G., Chua, P.S., Andison, D.: The interface between glass and carbon fibers and thermosetting polymers. Polymer Composites 6 (4), 242-248 (1985) (Cited on page 37.)

[75] Dong, S., Gauvin, R.: Application of dynamic mechanical analysis for the study of the interfacial region in carbon fiber/ epoxy composite materials. Polymer composites 14 (5), 414-420 (1993) (Cited on page 37.)

[76] $HexPly^{®}M10/38\%/UD300/CHS$ Epoxy Matrix. Product data sheet (Cited on pages 38 and 183.)

[77] Surface roughness terminology. Part 1. Surface and its parameters, International Standards Organization, ISO Standard 4287/1, (1984) (Cited on pages 40 and 183.)

[78] Oliver, W. C., Pharr, G. M.: An improved technique for determining hardness and elastic modulus using load and displacement sensing indentation experiments. J. Mater. Res. 7 (6), 1564-1583 (1992) (Cited on page 43.)

[79] R&G Faserverbundwerkstoffe GmbH. Technical data. Epoxy resin L + hardener S, L, EPH 161 and EPH 500 (Cited on pages 44 and 183.)

[80] Briscoe, B.J.: Interfacial friction of polymer composites. General fundamental principles, pp.25-59. In K. Friedrich (ed.): Composite material series. Volume 1. Friction and wear of polymer composites. Elsevier Science Publishers B.V. (1986) (Cited on page 53.)

[81] Tsukizoe, T, Ohmae, N.: Friction and wear performance of unidirectionally oriented glass, carbon, aramid and stainless steel fiber–reinforced plastics, pp.205-231. In K. Friedrich (ed.): Composite material series. Volume 1. Friction and wear of polymer composites. Elsevier Science Publishers B.V. (1986) (Cited on pages 64, 74 and 183.)

[82] Roselman, I. R., Tabor, D.: The friction of carbon fibres. J of Phys D: Appl Phys 9, 2517-2532 (1976) (Cited on pages 69, 70 and 83.)

[83] Roselman, J. C., Tabor, D.: The friction and wear of individual carbon fibres. J of Phys D: Appl Phys 10, 1181-1194 (1977) (Cited on pages 69, 70 and 83.)

[84] Archard, J.F.: Surface topography and tribology. Tribology International, 7 (5), 213-220 (1974) (Cited on page 69.)

[85] Bowden, F.B., Tabor, D.: Friction and lubrication of solids. Part I, Clarendon, Oxford, (1950) (Cited on pages 73 and 76.)

[86] Axén, N., Hutchings, I. M., Jacobson, S.: A model for friction of multiphase materials in abrasion. Tribology International 29, 6, 467-475 (1996) (Cited on pages 75, 76 and 179.)

[87] Axén, N., Jacobson, S.: A model for the abrasive wear resistance of multiphase materials. Wear 174, 187-199 (1994) (Cited on page 75.)

[88] Axén, N., Lundberg, B.: Abrasive wear in intermediate mode of multiphase materials. Tribology International 28 (8), 523-529 (1995) (Cited on page 75.)

[89] Hunter, C.N., Check, M.H., Hager, C.H., Voevodin, A.A.: Tribological properties of carbon canopearls synthesized by Nickel-catalyzed chemical vapor deposition. Tribology Letters 30, 169-176 (2008) (Cited on page 79.)

[90] Povirk,G. L.: Incorporation of microstructural information into models of two-phase materials. Acta Metall Mater 43 (8), 3199-3206 (1995) (Cited on page 79.)

[91] Sankaran, S., Zabaras, N.: A maximum entropy approach for property prediction of random microstructures. Acta Materialia 54, 2265–2276 (2006) (Cited on page 79.)

[92] Sun, C. T., Vaidya, R. S.: Prediction of composite properties from a representative volume element. Composites Science and Technology 56, 171-179 (1996) (Cited on page 79.)

[93] Chauveau V.: Le pouvoir lubrifiant des nanotubes de carbone. PhD Thesis (2010) (Cited on page 81.)

[94] Pierson, H.O.: Handbook of carbon, graphite, diamond and fullerenes: properties, processing and applications. Noyes Publications, Park Ridge, USA (1993) (Cited on page 81.)

[95] Schön, J.: Coefficient of friction of composite delamination surfaces. Wear 237, 77-89 (2000) (Cited on page 88.)

[96] Friedrich, K. et al.: Finite element analysis of a polymer composite subjected to a sliding steel asperity. Part II: Parallel and anti-parallel fibre orientations. Journal of Materials Science 37, 3497-3507 (2002) (Cited on page 88.)

[97] Varadi, K. et al.: The real contact area between composite and steel surfaces in sliding contact. Composites Science and Technology 61, 1853-1862 (2001) (Cited on page 88.)

[98] Ning, X., Lovell, M. R.: On the Sliding Friction Characteristics of Unidirectional Continuous FRP Composites. Journal of Tribology 124, 5-13 (2002) (Cited on page 89.)

[99] Ning, X., Lovell M. R., Slaughter, W. S.: Two-Dimensional Anisotropic Contact Behavior of Unidirectional Continuous FRP Composites. Journal of Tribology 125, 457-461 (2003) (Cited on page 89.)

[100] Guibert, M., Nauleau, B. et al.: Conception et réalisation d'un tribometre alternatif linéaire. Tribologie et couplage multiphysiques - JIFT, Lille, France (2006) (Cited on pages 92, 93 and 183.)

[101] Sinha, S. K., Chong, W. L. M., Lin, S.-C.: Scratching of polymers - Modeling abrasive wear. Wear 262, 1038-1047 (2007) (Cited on page 97.)

[102] Archard, J. F.: Temperature of rubbing surfaces. Wear 2, 438-455 (1958/59) (Cited on page 102.)

[103] Jaeger, J. C.: Moving sources of heat and the temperature at sliding contacts. Proc. of the Royal Soc. NSW 76, 203-224 (1942) (Cited on pages 102 and 103.)

[104] Blok, H.: General discussion on lubrication and lubricants. Inst. Mech. Eng. London 2, 222-235 (1937) (Cited on page 102.)

[105] Bertrand-Lambotte, P.: Sur les méchanismes de rayure des vernis de finition automobile. PhD thesis (2001) (Cited on page 112.)

[106] Wròbel, G. et al.: Determination of thermal diffusivity of carbon/epoxy composites with different fiber content using transient thermography. Journal of Achievements in Materials and Manufacturing Engineering 37 (2), 518-525 (2009) (Cited on page 121.)

[107] Kalogiannakis, G., Hemelrijck, D. V., Assche G. V.: Measurements of thermal properties of carbon/epoxy and glass/epoxy using modulated temperature differential scanning calorimetry. Journal of Composite Materials 38 (2) 163-175 (2004) (Cited on page 121.)

[108] Chen, F. C., Choy, C. L., Young, K.: A theory of the thermal conductivity of composite materials. J. Phys. D: Appl. Phys. 9, 571-586 (1976) (Cited on page 121.)

[109] Springer, G. S., Tsai, S. W.: Thermal conductivities of unidirectional materials. Journal of Composite Materials 1, 166-173 (1967) (Cited on page 121.)

[110] James B.W. et al: Prediction and measurement of the thermal conductivity of composite materials. J. Phys. D.: App. Phys. 20, 261-268 (1987) (Cited on page 121.)

List of Figures

List of Tables